DIAMAGNETIC STABLIZATION OF DOUBLE-TEARING MODES IN MHD SIMULATIONS

BY

STEPHEN RICHARD ABBOTT

B.A., Beloit College, 2005

M.S., University of Florida, 2007

DISSERTATION

Submitted to the University of New Hampshire

in Partial Fulfillment of

the Requirements for the Degree of

Doctor of Philosophy

in

Physics

September, 2015

This dissertation has been examined and approved in partial fulfillment of the requirements for the degree of Doctor of Philosophy in Physics by:

Dissertation Director, Kai K. Germaschewski
Associate Professor of Physics

Amitava Bhattacharjee
Professor of Astrophysical Sciences, Princeton University

Martin A. Lee
Professor of Physics

Joachim Raeder
Professor of Physics

Karl J. Slifer
Associate Professor of Physics

On June 23, 2015

Original approval signatures are on file with the University of New Hampshire Graduate School.

Dedication

For my family, so they may see
what ten years away from his prairie
will make of a man.

Acknowledgments

This material is based upon work supported by the following sources: the University of New Hampshire College of Engineering and Physical Sciences Graduate Fellowship; the U.S. Department of Energy, Office of Science, Office of Fusion Energy Sciences under Award Number DESC0006670; and the U.S. Department of Energy Experimental Program to Stimulate Competitive Research under Award Number DE-FG02-07ER46372.

Computations were performed using the following resources: Trillian, a Cray XE6m-200 supercomputer at UNH supported by the NSF MRI program under grant PHY-1229408; Fishercat, an IBM Blade Center H supported by the NSF CRI program under grant CNS-0855145.

This work would not have been possible without the many excellent teachers and mentors I have encountered throughout my education. I would like to express my gratitude to my supervisor, Prof. Kai Germaschewski, who has provided me with the skills to not only complete this work but to prosper as a computational scientist. I would also like to thank Prof. Amitava Bhattacharjee for providing the early impetus for this research and for many useful discussions as it evolved.

Table of Contents

List of Figures

List of Tables

Abstract

DIAMAGNETIC STABLIZATION OF DOUBLE-TEARING MODES IN MHD SIMULATIONS

by

Stephen Richard Abbott

University of New Hampshire, September, 2015

Double-tearing modes have been proposed as a driver of 'off-axis sawtooth' crashes in reverse magnetic shear tokamak configurations. The DTM consists of two nearby rational surfaces of equal safety factor that couple to produce a reconnecting mode weakly dependent on resistivity and capable of nonlinearly disrupting the annular current. In this dissertation we examine the linear and nonlinear growth of the DTM using the extended magnetohydrodynamic simulation code `MRC-3d`. We consider the efficacy of equilibrium diamagnetic drifts, which emerge in the presence of a pressure gradient when ion inertial physics is included, as a means of stabilizing DTM activity. In linear slab simulations we find that a differential diamagnetic drift at the two resonant surfaces is able to both interfere with the inter-surface coupling and suppress the reconnection process internal to the tearing layers. Applying these results to a m=2, n=1 DTM in cylindrical geometry, we find that asymmetries between the resonant layers and the presence of an ideal MHD mode result in stabilization being highly dependent on the location of the pressure gradient. We achieve a significant reduction in the linear DTM growth rate by locating a strong diamagnetic drift at the outer resonant surface. In nonlinear simulations we show that growth of the magnetic islands may enhance the pressure gradient near the DTM current sheets and significantly delay disruption. Only by locating a strong drift near the outer, dominant resonant surface are we able to saturate the mode and preserve the annular current ring, suggesting that the appearance of DTM activity in advanced tokamaks may depend on the details of the plasma pressure profile.

Introduction

Magnetic confinement of plasmas remains the best candidate for sustained fusion energy. Tokamaks, stellerators, and reverse field pinches (RFPs) use strong magnetic fields to maintain the densities and pressures necessary to achieve fusion. Stellerators have good stability but require topologically complex fields which are difficult to design and maintain. RFPs, in contrast, use relatively weak and simple fields but are prone to instability. The more successful tokamak design is a median route. Geometrically a tokamak is a torus with a strong, externally applied magnetic field around the major axis ($B_{toroidal}$). A strong internal plasma current is driven within the torus, generating a field circling the minor axis ($B_{poloidal}$). Typically the ratio B_t/B_p is of the same order as the aspect ratio, $A = R_0/a$ where R_0 and a are the major and minor radii of the torus. Together the external toroidal and self-generated poloidal fields create helical magnetic surfaces wrapping the torus that confine the hot plasma core needed for fusion.

The ITER reactor currently under construction will use a 5 T external field with a major radius of $R_0 = 6.2$ m and minor radius of $a = 2.0$ m, for an aspect ratio of approximately 3.2. An 830 m^3 volume of plasma will be confined with an average electron density 1.1×10^{20} m^{-3} at an average temperature of 8.9 keV [24]. In this regime the plasma will be dominated largely by the dynamics of the magnetic field. A good indicator of this behavior is the measure:

$$\langle \beta \rangle = \frac{p_{\text{plasma}}}{p_{\text{magnetic}}} = \frac{n k_b T}{(B^2/2\mu_0)}$$

From the above parameters, ITER is expected to operate at $\langle \beta \rangle \approx 0.014$. The device is expected to sustain 500 MW of fusion power for 400 s using an input power of 50 MW, making ITER a promising prototype for widespread fusion energy [24]. Sustained fusion is, however, still dependent on advances in material science, engineering, and plasma physics.

The presence of a current within the plasma results in the tokamak being susceptible to instabilities which can lead to disruptions. The scalar safety factor $q(r) = rB_t(r)/R_0B_p(r)$, where r is the local minor radius, is an effective measure of the susceptibility of an equilibrium to current driven instabilities. Surfaces with rational q values resonate with linear perturbations of the form $F(r, \theta, \phi) = f(r) \exp \imath(m\theta - n\phi)$, where m and n are the poloidal and toroidal modes numbers such that $q = m/n$. Generally, higher safety factors are less vulnerable to current driven modes. Unfortunately, the safety factor is lowest near the internal plasma current. If unstable modes arise in this region and disrupt the current, they can lead to a loss of plasma confinement and potentially damage the device. In this thesis we will consider one such mode.

The conventional tokamak design features a single, strong current channel which lies along the magnetic (major) axis of the torus. In such configurations the safety factor is monotonic within the plasma, rising from its lowest value near the plasma core until the edge. If q drops below one at the core it may become unstable the $m = 1$, $n = 1$ kink-tearing mode, a well understood instability. The kink-tearing mode is a reconnecting instability, meaning it is able to change the magnetic topology and release the energy stored in the field. In doing so, it disrupts the core current and allows the plasma to collapse outward, resulting in a 'sawtooth crash' [34]. When kinetic physics is included, however, the presence of a plasma pressure gradient creates equilibrium diamagnetic drifts. Such drifts interfere with the reconnection process and can stabilize the $m = 1$, $n = 1$ kink-tearing mode [41]. It is this success of diamagnetic drifts at stabilizing and even saturating the kink-tearing mode that has motivated the work in this thesis, where we examine a similar instability in tokamaks with reversed magnetic shear.

The reversed-shear configuration was developed to avoid many of the problems of conventional designs. Instead of a single plasma column, the internal current is driven in an annular ring surrounding the magnetic axis. The safety factor profile is non-monotonic with the minimum q near the current ring. This design typically results in higher minimum safety

factors, but it also results in two surfaces with the same safety factor being close to each other, bracketing the current annulus. These two surfaces may couple to form a single reconnecting instability, called the double-tearing mode (DTM). Some experimental [17, 22, 46] and numerical [17] results suggest that low mode number DTMs ($m = 2, 3$) may be responsible for 'off-axis sawteeth', in which the annular current ring is disrupted and core temperature collapses. Frequently, however, reversed-shear devices feature steep pressure profiles peaked at the magnetic axis [59], know in the literature as internal transport barriers (ITBs). These pressure profiles will result in diamagnetic drifts in the neighborhood of the annular current, and thus may impact the double-tearing mode. Motivated by similarities in the nonlinear evolution of DTMs and the $m = 1$ kink-tearing mode we have performed a simulation study to examine what role diamagnetic drift effects have in stabilizing an $m = 2$, $n = 1$ double-tearing mode in cylindrical geometry.

The dynamics of the double-tearing mode under the influence of diamagnetic drifts exhibit a complex interaction of several different mechanisms. In order to understand the final, cylindrical simulation results we will begin with the simplest manifestation of the DTM and build toward the full nonlinear behavior. Many characteristics of the double-tearing mode are poorly understood, and there are significant gaps in the existing literature. Only the simplest linear instabilities are well explored analytically. A plethora of linear and nonlinear simulation simulation studies exist, but their relationship both to each other and to the linear theory is not well defined. Therefore in order to provide sufficient context for our nonlinear simulation results, much of this thesis consists of original work interspersed with reviews of existing literature as necessary to chart a complete path. To achieve this goal, this thesis is structured as follows. Chapters 1 and 2 will review necessary background material for our study. In Chapter 1 we will introduce the the magnetohydrodynamics model implemented in our simulation code `MRC-3d` and explain its relationship to both the kinetic description of plasmas and to the two field reduced approximation commonly used for analysis. Utilizing these basic model equations, Chapter 2 will define the necessary conditions

for MHD equilibrium and introduce the magnetic configurations used for the simulations in this work. The manifestation of diamagnetic currents and drifts will follow naturally from this discussion.

Our first introduction to the double-tearing mode instability itself will be in Chapter 3, where we will review the existing boundary layer analysis of Pritchett et al. [39] in the comparatively simple force-free Cartesian slab and confirm that linear `MRC-3d` simulations of the DTM follow this theory. In Chapter 4 we will show that an equilibrium sheared flow can interfere with the coupling between the two reconnecting surfaces and slow the mode growth. We present a new boundary layer analysis that shows the emergence of a new singular layer structure, and use linear `MRC-3d` simulations to both confirm our analysis and connect it to prior linear simulation studies. In Chapter 5 we introduce kinetic physics through the Hall term and confirm that the double-tearing mode singular layers experience the same modifications with finite ion mass as do other reconnecting instabilities. We then show that the diamagnetic drifts allowed by the Hall term provide a decoupling mechanism similar to shear flow while also providing additional stabilization. We close our linear discussions in Chapter 6 by examining in what ways the cylindrical DTM does or does not resemble its more tractable Cartesian counterpart, reviewing the existing force-free linear literature and presenting new observations of ideal MHD instability and diamagnetic drift stabilization.

The nonlinear behavior of the double-tearing mode is defined largely by how it differs from other reconnecting instabilities, so in Chapter 7 we will review the fundamental terminology and classification of the more approachable single-tearing mode. With this foundation established, we will review the current understanding of nonlinear DTM evolution in Chapter 8, identifying the various phases of evolution and potential final states. We will conclude this chapter by categorizing the cylindrical DTM that is the focus of this work. In Chapter 9 we will reintroduce Hall MHD physics and present our nonlinear simulation study of the cylindrical DTM in the presence of diamagnetic drifts. Building on our linear study of Chapter 6, we will show that equilibrium diamagnetic drifts can nonlinearly stabilize the

double-tearing mode and even result in a saturated state. Their efficacy depends strongly, however, on where the pressure gradient is located.

Finally, in Chapter 10 we will summarize the important results of this thesis, and identify several avenues of research which we feel will be beneficial to understanding and stabilizing the double-tearing mode.

Chapter 1

Fundamental magnetohydrodynamics

This thesis examines the evolution of the reconnecting double-tearing mode using the magnetohydrodynamic (MHD) plasma model, which treats a plasma as a single conducting fluid. This approximation neglects significant domains of the relevant physics, in particular the two-fluid differential behavior of electrons and ions and the motions of individual particles. Despite these limitations MHD serves as a useful first order approximation in many physical systems, including magnetic reconnection. Typically the gross dynamics of reconnecting plasmas are described by the simplest magnetized-fluid model (ideal MHD) except in a very narrow region of the domain. Within this thin layer the different variants of magnetohydrodynamics implement approximations to microscopic particle physics while remaining analytically and computationally approachable.

In this chapter we will briefly review the fundamental extended-MHD model used by the simulation code `MRC-3d` and discuss its relation to the many-particle kinetic physics which more accurately describes plasmas. Particular detail will be paid to the 'generalized Ohm's law' (which governs the relationship between the electric field and plasma), and how higher order terms may have a significant effect on reconnection processes. We will then heuristically derive the common incompressible, resistive, reduced MHD (rMHD) model that we will use for linear analysis. These two discussions will form the basis of the simulation and analytic work in this thesis.

1.1 The MRC-3d model

The collective kinetic properties of a plasma can be described by the Boltzmann equation:

$$\frac{\partial f}{\partial t} + \mathbf{v} \cdot \nabla f + \frac{\mathbf{F}}{m} \cdot \nabla_{\mathbf{v}} f = \frac{\delta_c f}{\delta t} \tag{1.1}$$

which describes the evolution of a distribution function f with some collisionality described by the operator $\delta_c f/\delta t$ and under the influence of some force $\mathbf{F}$. The operator $\mathbf{F}$ typically includes the Lorentz force and (if significant) gravity. The MHD approximation can be derived from the velocity space moments of the equations governing each species s of the plasma:

$$\frac{\partial}{\partial t} \int_V \mathrm{d}^3 v \mathrm{M}^n f_s = \int_V \mathrm{d}^3 v \left(-\mathrm{M}^n \otimes \mathbf{v} \cdot \nabla f_s - \mathrm{M}^n (\frac{\mathbf{F}}{m} \cdot \nabla_{\mathbf{v}}) f_s + \mathrm{M}^n \frac{\delta_c f_s}{\delta t} \right) \tag{1.2}$$

$$\mathrm{M}^n \equiv \underbrace{\mathbf{v} \otimes \mathbf{v} \cdots \otimes \mathbf{v}}_{n} \tag{1.3}$$

The first term on the r.h.s. of Equation 1.2 results in the time evolution of the n-th moment being dependent on the moment of order $n + 1$. Thus at some point a closure must be assumed to truncate the system. The set of equations used in the MRC-3d simulation code correspond to truncation after the first order moment, leaving the 2nd order moment (or pressure tensor) undefined. We chose the common closure of a scalar pressure governed by a polytropic equation of state. This approximation, together with several concerning the electron and ion distributions that we will address later, results in a set of equations commonly termed Hall MHD.

$$\frac{\partial \rho}{\partial t} = -\nabla \cdot (\rho \mathbf{U}) \tag{1.4}$$

$$\frac{\partial \mathbf{P}}{\partial t} = -\nabla \cdot [\rho \mathbf{U}\mathbf{U} - \mathbf{B}\mathbf{B} + \mathbf{I}(p + B^2/2) - \rho\nu\nabla\mathbf{U}] \tag{1.5}$$

$$\frac{\partial T_e}{\partial t} = -\mathbf{U} \cdot \nabla T_e - (\gamma - 1) T_e \nabla \cdot \mathbf{U} \tag{1.6}$$

$$p_s = \rho T_s \tag{1.7}$$

$$p = p_e + p_i = (1 + \tau)\rho T_e \tag{1.8}$$

$$\mathbf{E} = -\mathbf{U} \times \mathbf{B} + \frac{d_i}{\rho}(\mathbf{J} \times \mathbf{B} - \nabla p_e) + \eta \mathbf{J} \tag{1.9}$$

$$\frac{\partial \mathbf{B}}{\partial t} = -\nabla \times \mathbf{E} \tag{1.10}$$

$$\mathbf{J} = \nabla \times \mathbf{B} \tag{1.11}$$

The dynamic variables are scalar fields ρ and T_e representing the mass density and electron temperature, the magnetic field $\mathbf{B}$, and the bulk plasma momentum field $\mathbf{P} = \rho\mathbf{U}$. As written this model is fully dimensionless [16], with the normalization set by choosing a characteristic length scale L, magnetic field strength B_0, and density ρ_0. Velocities are then normalized by the characteristic Alvén speed $v_A = B_0/\sqrt{\mu_0 \rho}$ and times by the Alfvén time $\tau_A = L/v_A$. Normalizations for temperature and the diffusion parameters follow from these stipulations.

Worthy of particular comment is the ion-inertial length d_i, as it is a reintroduction of kinetic physics to the MHD model. In the microscopic picture d_i represents the characteristic length scale of ion motions in response to an electrostatic perturbation:

$$d_i = \frac{c}{\omega_{pi} L} = \frac{1}{L}\sqrt{\frac{m_i^2}{\rho_0 e^2}} \tag{1.12}$$

where c is the speed of light, ω_{pi} is the ion plasma frequency, m_i is the ion mass, e is the ion charge (assuming protons), ρ_0 is the characteristic density, and L is the length scale normalization. Thus in the MHD model d_i is a characteristic length scale fixed by the ion

mass and characteristic density. In the kinetic picture any local variations in density modify the ion plasma frequency and thus formally modify the ion inertial length, but in MHD it is customary to handle these variations via the factor of $1/\rho$ in Equation 1.9.

As a final comment we note that Equation 1.5 is known as the equation of motion or the momentum equation, and is written here as a single divergence to emphasize the conservation properties. Its more common form better illustrates the balance of $\mathbf{J} \times \mathbf{B}$ Lorentz forces and ∇p pressure forces, as well as being somewhat easier to manipulate:

$$\rho \frac{\partial \mathbf{U}}{\partial t} = -\rho \mathbf{U} \cdot \nabla \mathbf{U} + \mathbf{J} \times \mathbf{B} - \nabla p \tag{1.13}$$

where $\mathbf{U}$ is the mean plasma velocity field and we have used the mass conservation equation (1.4) to re-order the time derivative. When considering reductions of this model and equilibrium conditions we will typically prefer Equation 1.13. The divergence form of Eqn. 1.5 is, however, used numerically.

The full derivation of the extended MHD equations from moments of the Boltzmann equation (1.1) is widely available in reference texts (see Ref. [25, 43], for example) and will not be reproduced here. Instead we will briefly comment on the assumptions required to achieve this comparatively simple set of equations and consider the restrictions they place on the validity of the `MRC-3d` model, and thus on any conclusions drawn from its simulations.

1.1.1 Fluid equations

The mass and momentum conservation of each independent particle species s has been reduced to the single set of Equations 1.4 and 1.5 describing the bulk plasma density ρ and momentum $\mathbf{P}$. Reducing to the form above requires assuming a plasma composed of electrons and massive ions such that $m_e \ll m_i$, which is valid in most physical domains of interest. As a consequence, the lowest order expression of the plasma momentum depends

only on the ion fluid:

$$\mathbf{P} = \sum_{s=i,e} \rho_s \mathbf{u_s} \simeq \rho_i \mathbf{u_i} \tag{1.14}$$

This reduction of the momentum contains the implicit assumption that the electron and ion densities are approximately equal. MHD validity requires that the stronger 'quasi-neutrality condition' hold across the entire domain, i.e. $q_i n(\mathbf{x})_i - e n(\mathbf{x})_e \simeq 0$ where $n_{i,e}$ is the ion/electron number density, q_i the ion charge, and $-e$ the electron charge. Quasi-neutrality removes the contribution of the electric field $\mathbf{E}$ to the momentum equation and reduces the number of dynamic variables. For this assumption to be valid, however, the scale of motions must be much larger than the Debye length $\lambda_D = \sqrt{\epsilon_0 T / n_0 e^2}$, which is the characteristic length at which electrons within a plasma screen charge inhomogeneities. MHD is valid only as at scales much larger than these microscopic variations.

With these limiting assumptions the momentum equation can be derived from the first order moments of the Boltzman equation and should contain the pressure tensor, which depends on the next highest order moment. To truncate the moment expansion the `MRC-3d` variant of MHD replaces this tensor with a scalar p, which restricts this model to isotropic pressures. Rather than evolving p directly, Equation 1.6 advances the electron temperature T_e and, together with the definitions of Eqns. 1.7 and 1.8, acts as the fluid closure. Taking the polytropic index γ to be 5/3 results in a formulation equivalent to an adiabatic equation of state. This particular choice of scalar pressure evolving adiabatically is arguably the weakest in the MHD model, as it fundamentally presumes that the plasma distribution function be sufficiently thermalized that it is approximately Maxwellian. Typical magnetospheric and (to a lesser degree) fusion plasmas are nearly collisionless and frequently magnetized, which results in strong anisotropy. Furthermore, kinetic simulations have shown that reconnection processes such as the DTM result in and are affected by these non-Maxwellian distributions.

Despite these limitations the scalar, adiabatic pressure closure has been successful in reproducing many of the observed feature of reconnection [11], and in this work we will be focusing on the large scale characteristics of double-tearing modes rather than detailed microscopic features.

The particular variant of MHD used in `MRC-3d` makes a concession to low plasma collisionality: the electrons and ions are allowed to have different temperatures via the parameter $\tau = T_i/T_e$, and thus different pressures. This ratio, however, is fixed across the entire domain and the temperatures are not allowed to evolve separately, so in practice is most useful for simulating the cold-ion regime $\tau = 0$. Note that the momentum equation (1.5) depends only on the bulk pressure $p = p_e + p_i$, and the only instance where the electron and ion pressures act separately is Equation 1.9.

1.1.2 Ohm's law

The dynamics of the fluid variables ρ, $\mathbf{P}$, and T are important to studies of magnetic reconnection, however the additional physics introduced by relaxing the assumptions discussed above typically results in higher order effects such as structural changes or stability thresholds. While these are important for accurately predicting and understanding observations, additions to Equation 1.9 directly govern (via Eqn. 1.10) the evolution of the magnetic field and have a more dramatic impact. As such, for the purpose of reconnection studies the particular 'flavor' of magneto-hydrodynamics is frequently named after which terms are included in this equation, called 'Ohm's law'. To examine the effects of the various physical processes included and omitted from the `MRC-3d` model we will consider a more generalized expression. In MHD models Ohm's law is the remnant of the electron momentum equation that was largely neglected by assuming $m_i \gg m_e$ in Eqn. 1.5. Considering higher order contributions in this limit allows the reintroduction of some kinetic physics to the system.

The most common terms are labeled below.

$$\mathbf{E} = \underbrace{-\mathbf{U}\times\mathbf{B}}_{\text{Convection}} + \overbrace{\frac{d_i}{\rho}(\mathbf{J}\times\mathbf{B} - \nabla p_e)}^{\text{FLR}} + \underbrace{\eta\mathbf{J}}_{\text{Resistive}} + \overbrace{\frac{d_e^2}{\rho}\frac{\mathrm{d}\mathbf{J}}{\mathrm{d}t}}^{\text{Electron Inertia}} - \underbrace{\eta_2\nabla^2\mathbf{J}}_{\text{Hyper-resistive}} \tag{1.15}$$

If only the convection term is present the model is labeled 'ideal MHD' and treats the plasma as a perfectly conducting fluid. This lowest order approximation results in the 'frozen-in-flux' theorem which states that the plasma and magnetic field are bound together. The Finite Larmor Radius (FLR) term relaxes this assumption by treating the ions as having finite mass, and thus they gyrate around the magnetic field with a finite radius. In particular, the Hall current term $d_i\mathbf{J}\times\mathbf{B}/\rho$ has a dramatic impact on reconnection physics [11] and we will frequently refer to inclusion of FLR effects as 'Hall MHD', although the electron pressure gradient ∇p_e must be included at this order for the approximation to be consistent.

If only these first two terms of Ohm's law (convective and FLR) are present reconnection is not possible. Due to the ideal MHD frozen-in theorem and mass conservation, the topology of the magnetic field cannot change. FLR effects only result in the field being bound to the electron fluid rather than the bulk plasma. Therefore at least one of the remaining terms (or some other physical mechanism) must be included to allow the magnetic fields to decouple from the plasma and undergo topology changes.

The resistive term is the simplest to implement but requires the assumption of some collisional process to generate a significant resistivity η, which is often not physically correct for the system of interest. A better approximation requires one to allow that electrons have finite mass, which results in the electron inertia term. The magnetic field is then no longer frozen into the electron fluid and reconnection can occur. This term is, however, computationally challenging in that the time derivative of the magnetic field $\partial_t\mathbf{B}$ acquires an implicit dependence on the convective derivative of the current $\mathrm{d}_t\mathbf{J} = \mathrm{d}_t(\nabla\times\mathbf{B})$. Furthermore, electron inertia driven reconnection occurs on the scale of the electron skin depth

$d_e = c/\omega_{pe}$, where ω_{pe} is the electron plasma frequency. The relative size of this scale compared to the ion inertial length $d_i = c/\omega_{pi}$ is directly dependent on the the ion/electron mass ratio $d_i/d_e = \omega_{pe}/\omega_{pi} = \sqrt{m_i/m_e}$. For a simple proton-electron plasma the realistic ratio $m_i/m_e \approx 1836$ results in a scale separation $d_i/d_e \approx 43$. Large scale plasma motions (such as Alfvén waves) typically occur on scales much larger than d_i, so one is required to simulate widely disparate lengths. As a consequence, it is common to use unphysical mass ratios to reduce computational costs, though more sophisticated techniques (e.g. adaptive mesh refinement) can alleviate this effect. Finally, the hyper-resitive term represents a dissipative effect that occurs near electron scales. A formal definition of the dissipative coefficient η_2 shows it depends on a viscosity coefficient and the electron mass, however this term is frequently included even when d_e is taken to be zero under the justification that η_2 can be enhanced anomalously due to small scale turbulence or magnetic stochasticity [13].

Many more minor variations on one-fluid MHD exist, and frequently the choice of model and included terms depends on what physics is expected in the problem. The current study of double-tearing mode reconnection will use Equations 1.5-1.8 for the plasma dynamic variables and Equation 1.9 to evolve the magnetic field. This variant of Ohm's law includes finite Larmor radius effects (when $d_i \neq 0$) and uses resistivity to break field lines and allow reconnection. We will refer to simulations and analysis which include these FLR effects as 'Hall MHD', and when they are not present we will refer to 'resistive MHD'. This implicit assumption of collisionality is better justified in high density fusion plasmas than other regimes (for example, magnetospheric) but the challenges of numerical simulation will frequently require unphysically large values of η. Though many of the details of the reconnection process will be incorrect, previous simulation studies [11] have shown that resistive Hall MHD is the minimal set to correctly reproduce many of the broad characteristics of fully kinetic reconnection. In particular the current sheet morphology and outflow are approximately correct, as well as potential stabilizing effects such as the diamagnetic drift that we are considering in this work. In later chapters we will show that even in this simplified model there is much

that is not understood about double-tearing mode evolution.

1.2 Reduced MHD

The full set of `MRC-3d` MHD equations describe two scalar fields (ρ and T) and two vector fields ($\mathbf{P}$ and $\mathbf{B}$) for a total of eight independent variables in three dimensions. While modern computational techniques allow the use of this full set of MHD equations in simulations, it is somewhat unwieldy for analytic work. In this section we derive a two dimensional, two field reduced MHD (rMHD) model that we will use for the linear analysis of the double-tearing tearing mode in this thesis. This rMHD model will only be valid in the presence of a large, mean magnetic field (or 'guide field') and will only encapsulate resistive MHD. Finite Larmor radius effects cannot be included in this model without introducing additional dynamic variables (see, for example, the Hazeltine four-field model [26]). The impact of FLR physics on the double-tearing mode has not (to the authors' knowledge) been addressed analytically. A rigorous derivation of the rMHD equations is somewhat involved (see Ref. [61]) and outside the scope of this work. Our goal in this section is to provide a basic understanding of the regime in which the reduced model is valid and the origin of its various components. To that end we will follow a heuristic derivation similar to that found in References [12] and [43].

We assume the plasma is embedded in a strong, nearly uniform field. For simplicity we choose to use Cartesian geometry and orient the $\hat{z}$ axis along this strong, mean, guiding magnetic field. This reduction is also appropriate to tokamak fusion devices, where the ratio of the toroidal to poloidal fields is typically on the order of the device aspect ratio. In either geometry we assume that the magnetic fields in the perpendicular (x-y or poloidal) plane are much smaller than the guide field:

$$B_z \gg B_\perp \sim \epsilon \tag{1.16}$$

Furthermore, we assume the dynamics lead to approximate equipartition of the energy sources within the plane such that:

$$\frac{|\mathbf{P}_\perp|^2}{2\rho} \sim \frac{|\mathbf{B}_\perp|^2}{2} \sim p \sim \epsilon^2 \tag{1.17}$$

In a rigorous derivation the the in- and out-of-plane derivatives can be ordered by restricting the timescales of interest [61]. We will instead consider the following heuristic argument. The magnetic field lines in this high guide field regime lie predominantly in $\hat{z}$ direction, with a small in-plane component. Imagine perturbing a field line in a fashion similar to plucking a string. The scale of motion along the guide field direction will be of a much longer wavelength than the in-plane motions. This conceptual model informs the derivative ordering ansazt:

$$\nabla_\perp \sim 1, \partial_z \sim \epsilon \tag{1.18}$$

In the presence of a strong guide field, therefore, the plasma is two dimensional to lowest order.

Equations 1.16, 1.17 and 1.18 are the fundamental ordering assumptions of reduced MHD, and are generally appropriate to the slow (compared to Alfvén wave timescales) motions of high-guide field, low β plasmas such as those found in fusion devices. We will now apply them to the MHD equations to derive the two-field model.

Any variation of the plasma in the $\hat{z}$ direction will quickly be propagated along the guide field by magnetosonic waves. Therefore we may assume that on the timescales of the in-plane dynamics the plasma maintains approximate pressure balance in the out-of-plane direction:

$$\partial_z \left(p + \frac{B^2}{2} \right) \approx 0 \tag{1.19}$$

The momentum equation (1.13) then implies that the velocity U_z in this direction is constant to lowest order, and we set $U_z = 0$ for simplicity.

We write the out-of-plane magnetic field as

$$B_z = B_{z0} + \delta B_z \tag{1.20}$$

where B_{z0} is large and constant, and δB_z is nonconstant and of (currently) indeterminate small magnitude. Expanding Eqn. 1.19 and substituting for B_z:

$$\frac{\partial}{\partial z}\left(\frac{B_\perp^2}{2} + B_z \delta B_z + \frac{\delta B_z^2}{2} + p\right) \approx 0 \tag{1.21}$$

Applying Eqn. 1.17 yields

$$\delta B_z \sim \epsilon^2 \tag{1.22}$$

We have now fixed the relative magnitudes of all the original MHD dynamic variables with the exception of the density ρ. This oversight will be address shortly. First, however, we write $\mathbf{B}_\perp$ in terms of the gradient of a scalar:

$$\mathbf{B} \approx \nabla\psi \times \hat{z} + B_z \hat{z} \tag{1.23}$$

The scalar ψ is called the magnetic flux function (or commonly just 'flux function'), and is equal (to lowest order) to the out-of-plane vector potential, i.e. $\psi = A_z + O(\epsilon^3)$. Thus this expression for the magnetic field no longer exactly satisfies the constraint that $\mathbf{B}$ be divergence free, with corrections emerging at order $\nabla \cdot \mathbf{B} \sim \epsilon^3$.

The scalar field ψ describes the in-plane magnetic configuration in rMHD, and is constant along magnetic field lines. In fact, any quantity f can be considered a 'flux function' if it is constant along field lines, $\mathbf{B} \cdot \nabla f = 0$. However generally ψ is meant by this term, as it

emerges naturally in 2D systems. Calculating the current density $\mathbf{J} = -\nabla \times \mathbf{B}$ we see that

$$J_z = -\nabla_\perp^2 \psi \sim \epsilon \tag{1.24}$$

$$\mathbf{J}_\perp \sim \epsilon^2 \tag{1.25}$$

Recall Faraday's law (Eqn. 1.10) in resistive MHD:

$$\frac{\partial \mathbf{B}}{\partial t} = -\nabla \times \mathbf{E} = \nabla \times (\mathbf{U} \times \mathbf{B} - \eta \mathbf{J}) \tag{1.26}$$

Integrating both sides and considering the in-plane components we get

$$\frac{\partial \mathbf{A}_\perp}{\partial t} = (\mathbf{U} \times \mathbf{B})_\perp - \eta \mathbf{J}_\perp - \nabla_\perp \chi \tag{1.27}$$

where $\mathbf{A}$ and χ are the vector and scalar potentials. Considering the definition $B_z = \hat{z} \cdot (\nabla_\perp \times \mathbf{A}_\perp)$, and recalling that the nonconstant portion of B_z is $\delta B_z \sim \epsilon^2$, then Eqn. 1.27 can be reduced to an ordered form:

$$\mathbf{U} \times B_{z0} \hat{z} - \nabla_\perp \chi = \epsilon^2 \tag{1.28}$$

To lowest order, therefore, the in-plane velocity can be described by a scalar stream function $\phi = \chi / B_{z0}$ such that

$$\mathbf{U}_\perp = \hat{z} \times \nabla \phi \tag{1.29}$$

Equation 1.29 implies that the plasma flow is incompressible, $\nabla \cdot \mathbf{U} = 0$. We have, therefore, ordered out the original equation of state (1.6) and replaced it with incompressibility. As a consequence, we can set the plasma density to a constant $\rho = \rho_0$ and it will not evolve (see Eqn. 1.4), and thus have removed it as a dynamic variable.

We can now return to Faraday's law (Eqn. 1.10) and consider the $\hat{z}$ component of the integrated expression:

$$\frac{\partial A_z}{\partial t} = \hat{z} \cdot (\mathbf{U} \times \mathbf{B}) - \eta J_z + \frac{\partial \chi}{\partial z} \tag{1.30}$$

Expanding in terms of ψ and ϕ and keeping only the lowest order contributions, we arrive at an expression for the time derivative of ψ involving only the reduced fields.

$$\frac{\partial \psi}{\partial t} = -[\phi, \psi] + \eta \nabla_\perp^2 \psi \tag{1.31}$$

where the Poisson bracket is defined as $[f, g] = (\nabla_\perp f \times \nabla_\perp g) \cdot \hat{z}$.

All that remains is to find a similar expression for the stream function ϕ. To do so, we take the curl of the momentum equation (1.13) and consider the out-of-plane component

$$\rho_0 \hat{z} \cdot \left[\frac{\partial \boldsymbol{\omega}}{\partial t} - \nabla \times (\mathbf{U} \times \boldsymbol{\omega}) \right] = \hat{z} \cdot \nabla \times (\mathbf{J} \times \mathbf{B}) \tag{1.32}$$

where we have defined the vorticity $\boldsymbol{\omega} = \nabla \times \mathbf{U}$ and applied the vector calculus identity

$$\mathbf{U} \cdot \nabla \mathbf{U} = \nabla (\mathbf{U} \cdot \mathbf{U}/2) - \mathbf{U} \times (\nabla \times \mathbf{U}) \tag{1.33}$$

Expanding the convective term and recalling that the velocity is incompressible ($\nabla \cdot \mathbf{U} = 0$) and confined to the plane ($U_z = 0$):

$$\hat{z} \cdot \nabla \times (\mathbf{U} \times \boldsymbol{\omega}) = \hat{z} \cdot (\boldsymbol{\omega} \cdot \nabla \mathbf{U} - \mathbf{U} \cdot \nabla \boldsymbol{\omega}) \tag{1.34}$$

$$= -\mathbf{U}_\perp \cdot \nabla_\perp \omega_z \tag{1.35}$$

A similar process can be applied to the r.h.s. of Eqn. 1.32.

$$\hat{z} \cdot \nabla \times (\mathbf{J} \times \mathbf{B}) = \hat{z} \cdot (\mathbf{B} \cdot \nabla \mathbf{J} - \mathbf{J} \cdot \nabla \mathbf{B}) \tag{1.36}$$

$$= \mathbf{B}_\perp \cdot \nabla_\perp J_z + B_z \frac{\partial J_z}{\partial z} - \mathbf{J} \cdot \nabla B_z \tag{1.37}$$

$$\approx \mathbf{B}_\perp \cdot \nabla_\perp J_z \tag{1.38}$$

where we have kept only the lowest order terms. Assembling these expansions we arrive at an equation for the vorticity

$$\rho_0 \left[\frac{\partial \omega_z}{\partial t} + \mathbf{U}_\perp \cdot \nabla \omega_z \right] = \mathbf{B}_\perp \cdot \nabla_\perp J_z \tag{1.39}$$

Using the definitions $\omega_z = \nabla^2 \phi$ and $J_z = -\nabla^2 \psi$ we can collect the vorticity equation (1.39) and the induction equation (1.31) to get a complete set of resistive reduced MHD equations in terms of the flux function ψ and stream function ϕ.

$$\frac{\partial \nabla^2 \phi}{\partial t} = -\left[\phi, \nabla^2 \phi\right] + \left[\psi, \nabla^2 \psi\right] \tag{1.40}$$

$$\frac{\partial \psi}{\partial t} = -\left[\phi, \psi\right] + \eta \nabla_\perp^2 \psi \tag{1.41}$$

where again the Poisson bracket is defined as $[f, g] = (\nabla_\perp f \times \nabla_\perp g) \cdot \hat{z}$.

Formally the model of Equations 1.40 and 1.41 is termed incompressible, low β, resistive reduced MHD. This precise name reveals what effects have been removed from the model, either by assumption or by ordering them out. The fundamental restriction of rMHD, even in a more rigorous derivation (e.g. Ref. [61]), is that the plasma is embedded in a strong mean field, or 'guide field.' To this we added the assumptions that variations along the guide field occur on a much larger spatial scale and much shorter time scale than the in-plane motions, and that the in-plane dynamics lead to approximate energy equipartition. From these constraints we were able to order out the pressure, out-of-plane magnetic field, and out-of-plane velocity, as well as show that the system is approximately 2D and introduce the

flux function ψ. As a consequence, the in-plane fluid flow is nearly incompressible and we introduced the stream function ϕ. We then manipulated the MHD induction and momentum equations (1.13) and 1.10) to arrive at the closed set of Equations 1.40 and 1.41, which are more tractable for linear analysis than the full MHD equations. We will use this model for the analytic portions of Chapter 3 and 4, and show that they accurately represent the full `MRC-3d` MHD model in the presence of strong guide field.

1.3 Discussion

In this chapter we have introduced the Hall MHD model we will use for simulation work in this thesis and discussed its relation to the fully kinetic plasma model. The `MRC-3d` model accurately represents the plasma dynamics at and above the characteristic scale of ion motions, but neglects microscopic effects related to electrons. Generally the small scale electron physics becomes important only in the immediate neighborhood of the reconnection site, and we will see in later chapters that the unique properties of the double-tearing mode occur at much larger, ideal MHD lengths. Even within the regime of resistive MHD much of the DTM behavior is currently poorly understood, and thus it is useful to examine the resistive and Hall MHD behavior of the DTM before introducing higher-order electron physics. We will see that even in Hall MHD it is challenging to accurately resolve the resistive, ion-inertial, and ideal MHD length scales, and thus future work in kinetic or two-fluid models will require the inclusion of more advanced numerical techniques (such as adaptive mesh refinement) into the `MRC-3d` code.

We have also introduced the two-field, resistive, incompressible, reduced MHD model which is used for analytic theories in both this work and the existing literature [37, 39]. This simplified model is an established tool for examining linear reconnection, and we have shown how it emerges from the full MHD model in the presence of a strong guide field with constraints on the in-plane variations. We have benchmarked `MRC-3d` against analytic

growth rates for many linear reconnecting modes and found excellent agreement, although we do not include these validation results here. In Chapter 3 we will explicitly compare the predictions of Pritchett et al.'s linear DTM theory and show that it accurately describes the DTM in `MRC-3d` simulations in the high guide field regime. Based on this validation we will propose an rMHD theory of double-tearing mode evolution in the presence of equilibrium sheared flows, and again confirm our analysis with simulation results. Thus the relatively simple reduced model given here is a good descriptor of the lowest order behavior of DTMs in the resistive `MRC-3d` model, although it must be abandoned when we introduce FLR effects in Chapter 5.

Chapter 2

Equilibrium properties

Both initial value and eigenmode simulations require establishing an equilibrium unstable to the mode of interest. As we will see in Chapter 3, reconnection is fundamentally a boundary layer problem with large scale, smooth ideal MHD processes dominating the system behavior except in a narrow region of the domain. The location of this layer is determined by where the interaction of a perturbation with wave vector $\mathbf{k}$ and the equilibrium magnetic field $\mathbf{B}$ is negligible. This requirement can be expressed as a resonance condition:

$$\mathbf{k} \cdot \mathbf{B} = 0 \tag{2.1}$$

The double-tearing mode requires that Equation 2.1 be true at two independent surfaces in the domain. In this chapter we will review the conditions that a field and plasma configuration must satisfy in order to be considered an MHD equilibrium, and define the profiles we will use in Cartesian and cylindrical geometries that satisfy the DTM resonance condition. The diamagnetic effects needed for our stabilization studies emerge from the properties of the equilibrium so we will also explain their appearance in the `MRC-3d` model and the modifications necessary to our equilibria for their inclusion.

2.1 MHD equilibrium conditions

In principle the time derivatives of the MHD dynamic variables $\mathbf{B}$, $\mathbf{U}$, ρ and T must be zero for a given configuration to be consider in equilibrium, i.e. the right hand sides of Equations 1.4, 1.5, 1.6, and 1.9 must vanish. For the slab and cylindrical geometries that we

consider in this work, however, only the momentum equation (1.5) and Ohm's law (Eqn. 1.9) are non-trivial to satisfy.

Our primary concern when constructing an equilibrium is that the total time derivative of the fluid momentum is zero. Static equilibria require that the plasma flow be zero, which reduces this requirement from $\mathrm{d}_t\mathbf{P} = 0$ to $\partial_t\mathbf{P}/\partial t = 0$. In arbitrary geometries it is difficult to prescribe flow profiles such that the convective derivative is zero, so we will generally focus on static equilibria except in Chapter 4 when we specifically consider the effects of background flow in a highly symmetric system.

From the MHD momentum equation (1.13) with $v_0 = P_0 = 0$ we derive a static equilibrium condition.

$$0 = \mathbf{J}_0 \times \mathbf{B}_0 - \nabla p_0 \tag{2.2}$$

Exploiting the constraint $\nabla \cdot \mathbf{B} = 0$ and the definition $\mathbf{J} = \nabla \times \mathbf{B}$ yields a condition for the equilibrium magnetic field B_0 and pressure p_0:

$$\nabla \left[\frac{B_0^2}{2} + p_0 \right] = -\mathbf{B}_0 \cdot \nabla \mathbf{B}_0 \tag{2.3}$$

The left hand side of Equation 2.3 is the gradient of the 'total pressure', which consists of the magnetic ($B_0^2/2$) and plasma (p_0) pressures. The ratio of these pressures is a good measure of whether the system is dominated by the dynamics of the fluid or the magnetic field, and we will reference it frequently throughout this work.

$$\beta = \frac{p}{p_B} = \frac{p}{(B^2/2)} \tag{2.4}$$

Commonly we will refer to 'force-free' equilibria that require that the plasma pressure be constant, $\nabla p_0 = 0$. When this gradient is non-zero the plasma pressure force must be

balanced by the magnetic forces, hence the term 'force-balanced'. In this work we will generally treat static force-free equilibria as our initial baseline system, as a constant background pressure simplifies much of the analytic theory and instabilities in this regime are better understood. The stabilization mechanisms we explore, however, will require adding equilibrium pressure gradients that will need to satisfy the force-balanced condition.

Ideal MHD equilibria are difficult to calculate without a convenient symmetry to exploit. In this work we are concerned with two-dimensional Cartesian and helically symmetric cylindrical configurations, which are more approachable. For a Cartesian slab we reduce the equilibrium to 1D by requiring that all dynamic variables depend only on the x coordinate which, due to the constraint $\nabla \cdot \mathbf{B}_0 = 0$, forces the $\hat{x}$ component of the field to be constant. The contribution of magnetic curvature (r.h.s. of Eqn. 2.3) is removed by setting $B_{0x} = 0$, leaving only the requirement that the total pressure $B_0^2/2 + p_0 = \text{constant}$. This freedom is not generally available in curvilinear coordinates, and the curvature must be balanced. In cylindrical geometry we will take the fields to depend only on the radius r and set $B_{0r} = 0$, so that the equilibrium condition becomes

$$\frac{\partial}{\partial r}\left[\frac{B_{0\theta}^2}{2} + \frac{B_{0z}^2}{2} + p\right] = -\frac{B_{0\theta}^2}{r} \tag{2.5}$$

Outside of these highly symmetric configurations ideal MHD equilibria become extremely difficult to calculate. For example, the study of three-dimensional tokamak equilibria is a field unto itself. To avoid these complications we will restrict our study to slab Cartesian and periodic cylindrical geometry.

Static equilibria are more complicated when physics beyond ideal MHD is included. In particular the addition of resistivity in Ohm's law (Eqn. 1.15) tends to smooth out magnetic field variations through Ohmic decay of currents. At realistic values of η this decay time is much longer than the growth time of reconnecting instabilities, but may become an issue when larger resistivities are used for numerical reasons. One means of enforcing a resistive

MHD equilibrium is by imposing an external electric field to counter balance $\eta\mathbf{J}$ in Ohm's Law. `MRC-3d` uses a mechanism built into 'the source term' to optionally provided this forced equilibrium, which is discussed in detail in Appendix A. When reporting simulation results we will note whether or not we have allowed the equilibrium to decay, as this can have an impact on long time behavior.

Additional terms in Ohm's law and the other dynamical equations can have consequences for the equilibrium. In this work, where we focus on resistive Hall MHD, we will primarily ensure the force balanced condition is met and consider whether or not resistive decay should be important. A non-zero ion inertial length does not invalidate the standard MHD equilibrium requirements but does reintroduce some kinetic physics, in particular complications related to the diamagnetic drift.

2.2 Diamagnetic systems

In the presence of magnetic fields the constituent particles of the plasma, being electrically charged, will gyrate around field lines. The magnetic moment of this motion opposes the external magnetic field, and as such plasmas are diamagnetic. In the presence of a plasma pressure gradient this can be observed by the manifestation of a diamagnetic current that has consequences for plasma flows and magnetic evolution in force-balanced equilibria.

Consider the force-balanced equilibrium condition (Eqn. 2.2) that we obtained from the MHD momentum equation (1.13) under the restriction $\mathrm{d}\mathbf{P}_0/\mathrm{d}t = 0$. Taking the cross product of this equation with the magnetic field $\mathbf{B}_0$ we obtain:

$$\mathbf{J}_{0\perp} = \mathbf{J}_0 - \frac{\mathbf{B}_0(\mathbf{J}_0 \cdot \mathbf{B}_0)}{B_0^2} = \frac{\mathbf{B}_0 \times \nabla p_0}{B_0^2} \tag{2.6}$$

This perpendicular current results from pressure gradients of the plasma and represents a reduction to the applied field compared to its force-free configuration. As such, it is known as the diamagnetic current.

The reintroduction of kinetic physics via the Hall term couples this diamagnetic current directly into the plasma motion. Considering the Hall MHD Ohm's law (Eqn. 1.9) for this force-balanced equilibrium, and recalling the definition of the bulk pressure $p = p_i + p_e$, we observe that the d_i scale contributions can be reduced using Equation 2.2.

$$\mathbf{J}_0 \times \mathbf{B}_0 - \nabla p_{e0} = +\nabla p_{i0} \tag{2.7}$$

Making this substitution, taking the cross product of the entire equation with $\mathbf{B}_0$, and reorganizing we find an expression for the plasma velocity perpendicular to the magnetic field.

$$\mathbf{U}_{0\perp} = \frac{\mathbf{E}_0 \times \mathbf{B}_0}{B_0^2} + \frac{d_i}{\rho_0}\frac{\mathbf{B}_0 \times \nabla p_{i0}}{B_0^2} \tag{2.8}$$

Here we have neglected the diffusive terms η and η_2, which are much smaller than those we have kept. The first term is present even in ideal MHD and is the fluid generalization of the $\mathbf{E} \times \mathbf{B}$ particle drift. This motion is independent of the charge of the particle, and thus both electrons and ions drift together perpendicular to any magnetic and electric fields.

The second term is of the same form as the diamagnetic current, and is known as the ion diamagnetic drift.

$$\mathbf{v}_{*i} = d_i \frac{\mathbf{B} \times \nabla p_i}{\rho B^2} \tag{2.9}$$

Because it includes the pressure gradient it is manifestly a fluid drift, but we can gain some understanding of its kinetic analog by considering how it relates to the diamagnetic current.

In a microscopic picture the current is generated by relative average motions of positively and negatively charged components of the plasma.

$$\mathbf{J} = ne(\mathbf{u}_i - \mathbf{u}_e) \tag{2.10}$$

For simplicity we have assumed the ions and electrons have charges $\pm e$ and that the number densities are approximately equal ($n_i \approx n_e \approx n$). By examining the part of this drift perpendicular to the magnetic field we can understand the relationship between the diamagnetic current, diamagnetic drift, and the Hall term.

$$ne(\mathbf{u}_{i\perp} - \mathbf{u}_{e\perp}) = \frac{\mathbf{B} \times \nabla p_i + \mathbf{B} \times \nabla p_e}{B^2} \tag{2.11}$$

In the MHD approximation the ion mass is much larger than the electron, and thus fluid flow is dominated by the mean ion velocity $\mathbf{U} \simeq \mathbf{u}_i$. In the ideal limit ($d_i = 0$) the only perpendicular fluid flow is that provided by the $E \times B$ drift, which is independent of particle type and thus cannot produce a current. As a consequence, the current is carried entirely by the electrons. Physically this corresponds to treating the ions as infinitely more massive than the electrons, i.e. it is the zeroth order approximation in the small parameter $m_e/m_i \ll 1$. For non-zero d_i, however, there is a clear association between v_{*i} and the ion pressure gradient contribution to the diamagnetic current.

$$\mathbf{u}_{i\perp} = \frac{\mathbf{B} \times \nabla p_i}{neB^2} \tag{2.12}$$

In the `MRC-3d` normalization (Sec. 1.1) the pre-factor becomes $(ne)^{-1} \rightarrow d_i/\rho$, thus establishing that

$$\mathbf{u}_{i\perp} = \mathbf{v}_{*i} = d_i \frac{\mathbf{B} \times \nabla p_i}{\rho B^2} \tag{2.13}$$

Finite d_i corresponds to the first order term in m_e/m_i, i.e. ions are treated as having finite mass while leaving electrons as a nearly massless fluid. Therefore the ions must carry part of the diamagnetic current and an equilibrium cannot be maintained without a bulk plasma velocity $\mathbf{U}_\perp = \mathbf{v}_{*i}$.

As an important consequence of this analysis we can infer the electron diamagnetic drift

velocity in the presence of a pressure gradient, even though they are not explicitly treated as a separate fluid in the MHD model.

$$\mathbf{v}_{*e} = -d_i \frac{\mathbf{B} \times \nabla p_e}{\rho B^2} \tag{2.14}$$

The addition of the Hall term adds information into the model about the motion of both the ion and electron fluids, though it is not as complete as a full two fluid theory. It is particularly important to note that the diamagnetic drifts are fluid drifts and not kinetic drifts of the particle guiding centers. The inhomogeneities the particle distribution functions that result in a pressure gradient also cause a mean velocity in the diamagnetic magnetic drift direction. The inclusion of FLR effects in Ohm's law allows this mean flow to manifest as a drift of the electron and ion fluids. These effects can have a large impact on reconnecting instabilities that we will address in Chapter 5. At present this analysis shows that if $d_i \neq 0$ then the force-balanced condition given by Equation 2.2 is not sufficient to assure equilibrium, but we must rather require that the ion diamagnetic drift v_{*i} is consistent. To avoid the challenges of guaranteeing that the convective derivative of the bulk momentum is zero we will commonly use the cold ion approximation, which assumes $\tau = T_i/T_e = 0$ and sets p_i (and thus v_{*i}) to zero. The electron drift v_{*e} is, however, accounted for by the static force-balanced condition (Eqn. 2.2) and will be treated as a property of the equilibrium configuration.

2.3 Cartesian DTM unstable equilibria

In Chapter 1 we discussed how a large guide field allows Cartesian geometry to be treated, to lowest order, as a two dimensional slab. Within this work we will take the out-of-plane field to be $B_z \approx 10$ and the in-plane fields will be order one, so that the system has (unless otherwise stated) $\beta = 0.02$. To satisfy equilibrium condition (Eqn. 2.2) we specify the in-plane field and, if appropriate, pressure profile, and vary B_z as necessary to balance the

pressures. This variational part of B_z will be small compared to the in-plane fields (see Sec. 1.2).

With the symmetry provided by the guide field the resonance condition (Eqn. 2.1) reduces to a simple constraint on the in-plane field.

$$k_x B_x(x,y) + k_y B_y(x,y) = 0 \tag{2.15}$$

We choose the x coordinate to be bound by conducting walls with periodic boundaries in y. The natural choice for the instability wave vector in such a domain is $\mathbf{k} = k\hat{y}$. Resonant layers will then occur when $B_y(x) = 0$, where we have taken the in-plane field to be one dimensional for simplicity. In Cartesian slabs we will always constrain the reconnecting field to be symmetric about $x = 0$, though this bilateral symmetry is not typically possible in more complicated geometries. Subject to these restrictions there are two equilibria which are commonly used for DTM simulation studies: a scaled sech; and the sum of two tanh functions.

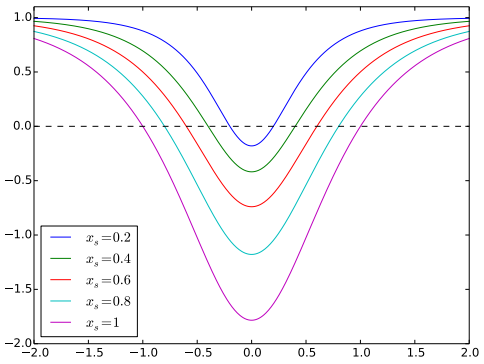

(a) The sech equilibrium excels at free modification of the tearing surface spacing x_s while keeping the local shear at each surface constant. $B'_y(\pm x_s) = \pi/2$ in all the plotted curves. It produces, however, large variations in the magnitude of the magnetic field between the surfaces, especially at large separations.

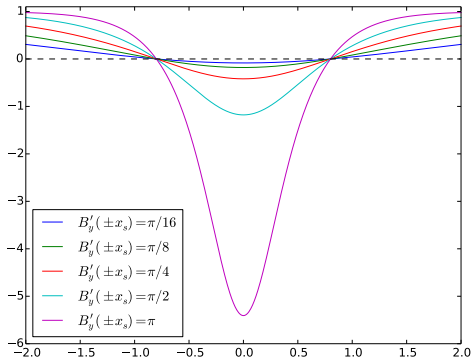

(b) Holding the tearing surface separation constant ($x_s = 0.8$ above) while changing the local magnetic shear produces large changes in the equilibrium field. This large variation in magnetic energy between the surfaces, especially at steep gradients, can be troublesome in DTM studies.

Figure 2-1: Variations of spacing and shear for the sech equilibrium.

The majority of existing simulation work uses a reconnecting field shaped as a scaled and shifted sech, popularized by the foundation linear DTM work of Pritchett et al. [39]:

$$B_y(x) = 1 - (1 + B_c)\,\mathrm{sech}(\zeta x) \tag{2.16}$$

B_c and ζ are free parameters chosen to set specific locations for the tearing layers and the magnetic shear. Specifying that tearing layers occur at $x = \pm x_s$ requires that $B_y(\pm x_s) = 0$, giving the condition

$$\zeta x_s = \mathrm{sech}^{-1}\left[\frac{1}{1 + B_c}\right] \tag{2.17}$$

The remaining parameter B_c is then calculated using a root-finding algorithm to set the derivative of the magnetic field at $x = \pm x_s$. A typical choice is $B'_y(\pm x_s) = \pm\pi/2$. Examples of this equilibrium for various scalings of separation and shear are shown in Figure 2-1 and clearly illustrate both the benefits and detriments of this choice. The equilibrium is always smooth and symmetric, and the simple inversion used to find ζ guarantees that the tearing surfaces will occur at $\pm x_s$. Increasing either the separation or the shear, however, requires also increasing the amplitude of the magnetic field between the surfaces. This restriction can make scaling studies that depend on the free magnetic energy between the surfaces difficult.

The double-tanh field is less widely used. It is based on the Harris sheet equilibrium commonly used for single tearing mode studies and is sometimes called 'double-Harris'.

$$B_y(x) = B_0\left[1 + \tanh\left(\frac{x + x_+}{\lambda_+}\right) - \tanh\left(\frac{x + x_-}{\lambda_-}\right)\right] \tag{2.18}$$

Symmetric examples of this field are plotted in Figure 2-2 with $x_\pm = \pm x_0$ and $\lambda_\pm = \lambda_0$. At wide separations (large x_0) and steep gradients (small λ_0) the asymptotic flatness of the tanh allows the free parameters to map directly to the locations of the tearing layers ($x_s \simeq x_0$) and magnetic shear ($B'_y(\pm x_s) \simeq \lambda_0^{-1}$). When this property holds the amplitude of the magnetic

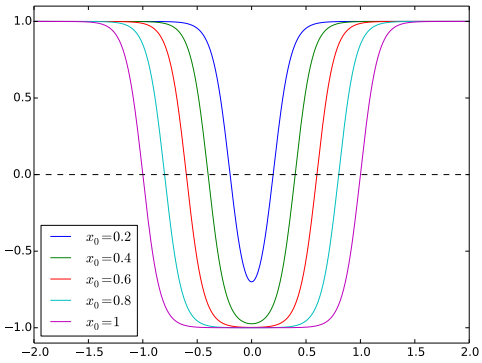

(a) At wide enough separation, variations in x_0 for the double tanh equilibrium will result in peak magnetic field and local shear that are constant outside of exponentially small corrections. The plotted curves, all using $\lambda_0^{-1} = 2\pi$, show that there is a minimum x_0 for a given λ such that $B_y'(\pm x_s) \simeq \pm\lambda_0^{-1}$ and $x_s = x_0$, and below this value the corrections at each surface from the tanh at the other become significant.

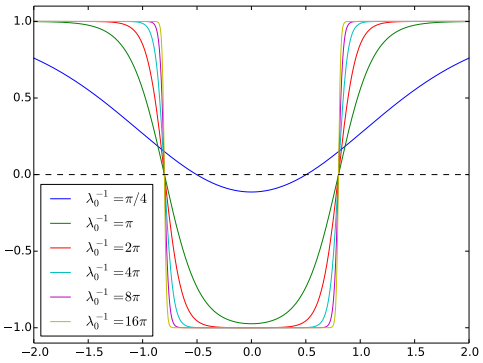

(b) The magnetic shear at each surface can be freely modified by varying λ_0 provided that the tanh centers $\pm x_0$ are large enough. In the above curves the spacing $x_s \simeq x_0 = 0.8$ is constant and the shear at each surface can be represented as $B_y'(\pm x_s) \simeq \pm\lambda^{-1}$ for steep gradients. Large values of λ, however, produce unpredictability in both separation ($x_s \neq x_0$) and shear ($B_0' \neq \lambda_0^{-1}$).

Figure 2-2: Variations of $x_\pm$ and λ for the double-tanh equilibrium.

field between the surfaces remains constant. In the opposite case, however, the nonconstant regions of each tanh overlap and these beneficial properties are lost.

The utility of an equilibrium in scaling studies depends on how easily one can change a single parameter while keeping other relevant factors constant. It will be shown in later chapters that the linear and nonlinear behavior of the double-tearing mode depends primarily on the separation of between the tearing layers, the magnetic free energy between them, and the local magnetic shear. With respect to these parameters the above two equilibria are desirable in different regimes. The sech is advisable when magnetic shears are low and layers are close together. In contrast, the double-tanh field is recommended when surfaces are far apart and the steep gradients are desired. Furthermore, the double-tanh equilibrium supports asymmetric field configurations, which is necessary for accurate comparison to tokamak plasmas. Most of the Cartesian simulations presented in this work, however, are conducted using the sech equilibrium to allow easier comparison to existing work. We will use the double-tanh only when directly comparing to cylindrical simulations.

2.3.1 Pressure gradients

To consider the effects of diamagnetic drifts we will add a density gradient that follows the symmetry of the magnetic field.

$$\rho(x) = \rho_0 + \Delta_\rho \left[1 + \tanh\left(\frac{(x - x_s)}{\lambda_\rho} \right) - \tanh\left(\frac{(x + x_s)}{\lambda_\rho} \right) \right] - \rho_{shift} \tag{2.19}$$

ρ_0 is the constant background density, which we typically take to be 1. The gradient properties are controlled by the scale height (Δ_ρ) and width (λ_ρ) of the density shear. To avoid potential issues with changing the normalization parameters within the resonant layers we add a density shift parameter ρ_{shift} that is found via an iterative method at simulation initialization to ensure that $\rho(\pm x_s) = \rho_0$. An example of this profile is shown along with a typical $x_s = 1.0$, $B_y'(\pm x_s) = \pm\pi/2$ sech magnetic field in Figure 2-3.

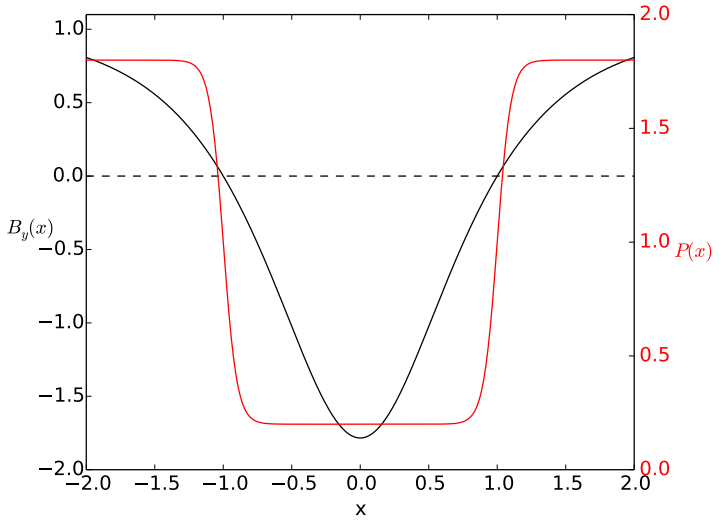

Figure 2-3: Example $x_s = 1.0$ DTM sech equilibrium magnetic field (black) and pressure gradient (red). The reconnecting field $B_y(x)$ is found from eqn. 2.16 with $B_y'(\pm x_s) = \pm\pi/2$. The pressure profile is found from 2.19 with $\rho_0 = 1$, $\Delta_\rho = 0.8$, and $\lambda_\rho = 0.1$. The density gradients are steep enough that a ρ_{shift} correction is not needed. For this plot electron temperature is constant $T_e = 1$ with cold ions $T_i = 0$.

Choosing the pressure gradient and magnetic field profiles to depend only on x results in a diamagnetic drift $\mathbf{v}_{*i}$ which automatically satisfies the convective part of the MHD equilibrium condition (i.e. $\mathbf{U} \cdot \nabla \mathbf{U} = 0$), thus it would be straight forward to include ion

drifts in these Cartesian simulations. None the less we will use the cold ion approximation ($\tau = T_i/T_e$) to eliminate the ion pressure and ion drift. Primarily we choose this regime to allow easier comparison to our later cylindrical simulations for which equilibrium flows can potentially cause numerical issues at the $r = 0$ coordinate singularity. The cold-ion limit is also more tractable analytically, though it is not strictly applicable to newer tokamak designs.

2.4 Cylindrical DTM unstable equilibria

Curvilinear field geometries do not typically feature zeros of a magnetic field component within the plasma; the tokamak configuration in particular relies on an internal plasma current to provide confinement. Thus to examine reconnecting instabilities we must consider the full $\mathbf{k} \cdot \mathbf{B} = 0$ condition for resonant modes.

The magnetic field lines in a torus lie either on a rational or irrational surface. From an initial point on a rational surface one can follow a field line and traverse the torus m times around the major axis and n times around the minor (following the helical field line) and arrive at the starting location. The ratio $\iota = n/m$ corresponds to the twist of the helical magnetic field. Following an field line on an irrational surface, in contrast, will ergodically sample points in a given region without ever returning to the starting location.

When discussing stability the inverse of the twist is commonly used, and can be calculated from the toroidal field B_t, poloidal field B_p, and major radius R for minor radius $0 \leq r \leq a$ by $q(r) = rB_t/RB_p$. The quantity $q(r)$ is called the 'safety factor' as it is a useful marker of the stability of the configuration; lower values of q are more susceptible to disruptive instabilities. The resonance condition $\mathbf{k} \cdot \mathbf{B} = 0$ can only be satisfied (for finite wave vectors) along rational surfaces, which correspond to rational values of the safety factor. (We will commonly use the terms 'rational' and 'resonant' surface interchangeably.) Perturbations resonant at a given surface $q(r) = m/n$ will have wave vectors $\mathbf{k} = m/r\hat{\theta} - n/R\hat{z}$, where θ and

z are the poloidal and toroidal coordinates respectively, leading to the common terminology of m and n as the poloidal and toroidal mode numbers. If the aspect ratio of the torus is sufficiently large (major radius R is much greater than minor radius a) the configuration can be modeled as a periodic cylinder. In this simplified geometry the helical symmetry of the field reduces (for low mode number instabilities) the available degrees of freedom and allows two dimensional simulations. Although toroidal corrections (which occur at order a/R) can have significant impacts on stability, we will use the simpler 2D cylindrical geometry in this study and leave higher order corrections for future works.

Double-tearing unstable configurations in cylindrical geometry therefore require two nearby rational surfaces of the same safety factor. Such configurations are non-trivial to derive, so our simulations use the $q(r)$ profile from Ref. [10], defined in Equation 2.20.

$$\begin{aligned} q(r) &= q_0 F_1(r) \left\{1 + (r/r_0)^{2w(r)}\right\}^{1/w(r)} \\ r_0 &= r_A |[m/(nq_0)]^{w(r_A)} - 1|^{-1/[2w(r_A)]} \\ w(r) &= w_0 + w_1 r^2 \\ F_1(r) &= 1 + f_1 \exp\left\{-[(r - r_{11})/r_{12}]^2\right\} \end{aligned} \tag{2.20}$$

Several parameters are required to determine the profile.

$$\begin{aligned} r_A &= 0.655, \quad w_0 = 3.8824, \quad w_1 = 0 \\ f_1 &= -0.238, \quad r_{11} = 0.4286, \quad r_{12} = 0.304 \end{aligned} \tag{2.21}$$

We choose to simulate a $m = 2$, $n = 1$ DTM, and q_0 may be varied near 2.5 to change the separation D between two $q = 2$ surfaces. `MRC-3d` requires the magnetic field components (rather than the safety factor $q(r)$) which we calculate by assuming $B_{z0} = R_{major} = 10$ and then performing an iterative refinement of the equilibrium fields $B_\theta(r)$ and $B_z(r)$ to converge to the input $q(r)$ over the domain $0 \leq r \leq a = 1$. This iterative method is also used to guarantee that the force-balanced condition (Eqn. 2.2) is satisfied by the final magnetic fields and, if present, the pressure gradient.

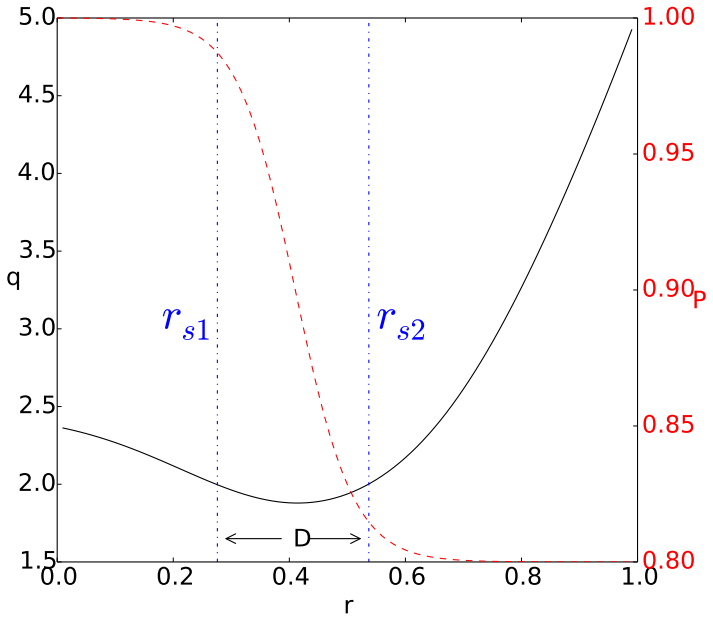

Figure 2-4: Example cylindrical safety factor(black) and pressure gradient(red) profiles. $q(r)$ is calculated using Eqn. 2.20 with the parameters 2.21 and $q_0 = 2.5$, which results in two $q = 2$ rational surfaces at $r = r_{s[1,2]}$ separated by a distance $D \approx 0.26$. The pressure gradient is found using Eqn. 2.22 with parameters $N_0 = 1$, $N_b = 0.8$, $\delta_N = 0.1$, $r_0 = (r_{s1} + r_{s2})/2$, constant electron temperature $T_e = 1$, and assuming cold ions $\tau = 0$.

For this work we fix $q_0 = 2.5$, giving $D \approx 0.26$. The resultant safety factor profile, with two $q = 2$ DTM unstable surfaces, is shown in Figure 2-4.

2.4.1 Pressure gradients

To establish the pressure gradient necessary for diamagnetic drifts we use the following density profile from Ref. [64].

$$\rho(r) = N_0 \left\{ 1 - (1 - N_b) \frac{\tanh(r_0/\delta_N) + \tanh[(r - r_0)/\delta_N]}{\tanh(r_0/\delta_N) + \tanh[(1 - r_0)\delta_N]} \right\} \tag{2.22}$$

The form of this function is designed to mimic the profile of pressure gradient structures observed in tokamak configurations, particularly reverse-magnetic shear designs, called internal transport barriers (ITBs) [59]. Typically ITBs feature both core density and temperature enhancements, but here we restrict our study to nonuniform ρ so as to avoid certain physical processes associated with steep temperature gradients that the MHD model does not

accurately capture. N_0 represents the core maximum, N_b the outer minimum, δ_N the characteristic width, and r_0 the location of peak gradient of the density profile. These parameters will be varied based on the strength and location of the desired diamagnetic drifts. An example pressure profile with the peak gradient centered between the two rational surfaces is shown in red on Figure 2-4.

Cylindrical simulations in `MRC-3d` are prone to issues near the $r = 0$ coordinate singularity when equilibrium flows are included. To avoid this problem we will restrict our cylindrical simulations to the cold-ion regime ($\tau = 0$) so that the ion diamagnetic flow (Eqn. 2.9) is zero.

2.5 Discussion

Full toroidal equilibria are significantly more complicated than those presented here, though they still must satisfy the resonance (Eqn. 2.1) and MHD equilibrium (Eqn. 2.2) conditions and will exhibit diamagnetic drift behavior (Eqns. 2.9 and 2.14). Asymmetries of the geometry and field strength generally require non-trivial equilibrium flows, and the addition of gravity further complicates the equilibrium. Our goal in using these simplified Cartesian and cylindrical field configurations is to isolate, as much as possible, the various stabilizing and destabilizing effects on the double-tearing mode. The set of equilibrium conditions and manifestation of diamagnetic effects should be taken as a minimal set necessary to establish simulation initial conditions in `MRC-3d` for these two geometries. In addition to the toroidal complications we have also avoided any discussion of kinetic or two fluid equilibrium conditions, which are required for models more advanced than MHD. The study of equilibrium reconstruction and design for fusion devices is an established field in its own right and well beyond the scope of this work. In the following we will instead restrict ourself to the simplified equilibria of this chapter and focus on the fundamental understanding of the double-tearing mode instability itself and possible mechanisms for stabilizing it.

Chapter 3

Cartesian force-free DTMs

Reconnection is fundamentally a multi-scale process whereby changes in topology within a narrow current layer produce large scale fluctuations in both the plasma and the magnetic field. This interaction between a thin active region and a global mode is an ideal system for boundary layer analysis, which is a fruitful tool for examining the linear behavior of many reconnecting instabilities. In particular the single-tearing mode [20] and the $m = 1$ cylindrical kink-tearing mode [3] have been comprehensively studied using this tool in MHD and kinetic models. In this chapter we will show the linear double-tearing mode shares many characteristics with these two systems. Depending on the spacing between the resonant surfaces the DTM may have as either as two STMs or a faster growing single kink-tearing mode. The presence of two singular layers admits a marginally stable ideal MHD mode that determines the transition between these two behaviors.

The majority of this thesis will consist of introducing different physical mechanisms, for example equilibrium sheared flows or diamagnetic drifts, in order to slow the growth of the DTM and mitigate the risk of disruption in fusion plasmas. It is important, however, to first understand why the DTM is so strongly driven and how the spacing between the two surfaces interacts with the various scales inherent to reconnection. To do so we begin with a prototype system: the linear, resistive, force-free double-tearing mode in 2D Cartesian slab geometry on a symmetric equilibrium. The asymptotic solution of this system by Pritchett et al. [39] is the fundamental framework on which most recent investigations of the DTM rely, and we will review it detail.

The analysis of this chapter relies on a simplified boundary layer method that we will compare with simulations using a linearized version of `MRC-3d`. Boundary layer theory is a

well codified method of global asymptotic approximation to ordinary differential equations, and can be viewed as a specialized application of WKB theory. We will begin with a linearized form of the reduced MHD equations (Eqns. 1.40 and 1.41) and define a new normalization based on the characteristic width of the equilibrium current channel J_{z0} of a DTM unstable system, so as to make explicit the similarity properties of the resulting solution. The key to asymptotic analysis is identification of small parameters in which the solution can be expanded, be they explicit factors or narrow regions of coordinate space. The presence of boundary layers is typically (but not always) indicated by small factors multiplying the highest derivative of an ODE, and we will identify these and predict where they will be significant. At all stages we will evaluate the 'dominant balance' of the ODE, i.e. consider the relative magnitudes of various terms so as to discard those that are not significant and to generate a solvable approximation. Outside of the boundary layers this balance will be determined by the naive limit of taking all small parameters to zero. Within the layer we will rescale the coordinates to amplify derivatives and identify a new dominant balance, thereby finding the behavior of the internal solution. The solution within and outside of the boundary layer must then be matched in some intermediate regime where the original coordinate goes to zero and the rescaled coordinate to infinity, fixing undetermined constants in the process. The final result is a description of the global mode that is uniformly asymptotic to the true solution. Our analysis of the DTM will be somewhat more complicated, as there are multiple small parameters to consider and will require several successive reductions.

3.1 Symmetric boundary layer theory

For simplicity we will assume that the equilibrium is symmetric such that $B_{y0}(\pm x_s) = 0$, which will allow for two linear eigenmodes: one which is even over the domain and one which is odd. Of these two solutions the symmetric mode is not only the fastest growing but also most easily obtainable via an asymptotic boundary layer analysis. In this section we will

review the initial theory of Pritchett et al. [39] for this even mode and explore the different domains of coupling between the two surfaces. Discussion of the antisymmetric mode, which is less well understood, will be delayed until later in this chapter.

We linearize Equations 1.40 and 1.41 and apply the assumption $\phi_0 = 0$ to consider the static, force-free, resistive DTM. In linear MHD theory it is useful to replaced the stream function ϕ with the plasma displacement ξ:

$$\mathbf{U} = \hat{z} \times \nabla\phi = \frac{\partial \boldsymbol{\xi}(x, y, z, t)}{\partial t} \tag{3.1}$$

Under the Fourier ansatz only the $\hat{x}$ component is needed, which we write as:

$$\xi(x) = -\frac{ik\phi(x)}{\gamma} \tag{3.2}$$

Working in a 2D Cartesian slab periodic in y we apply the Fourier ansatz $F(x, y, t) = f(x)\exp(\gamma t + iky)$ for the perturbed quantities. We choose as normalization parameters (Chap. 1.1) the current channel scale width a_b, constant density ρ_0, asymptotic in-plane field strength B_0, and Alvèn time $\tau_A = a_b/v_a$, and obtain the dimensionless equations:

$$\tilde{\gamma}^2(\tilde{\xi}'' - \alpha^2\tilde{\xi}) = -\alpha^2\tilde{B}_{eq}(\tilde{\psi}'' - \alpha^2\tilde{\psi}) + \alpha^2\tilde{\psi}\tilde{B}''_{eq} \tag{3.3}$$

$$\tilde{\gamma}\tilde{\psi} - \tilde{\gamma}\tilde{B}_{eq}\tilde{\xi} = S^{-1}(\tilde{\psi}'' - \alpha^2\tilde{\psi}) \tag{3.4}$$

where primes indicate differentiation with respect to the dimensionless length $\tilde{x} = x/a_b$ and the normalized variables denoted by tildes are defined as

$$\begin{aligned} \tilde{\gamma} &= \gamma\tau_A, & \alpha &= ka_b, & \tilde{B}_{eq} &= B_y/B_0 \\ \tilde{\psi} &= \psi/a_b B_0, & \tilde{\xi} &= \xi/a_b, & & \\ \tau_A &= \sqrt{\rho_0}a_b/B_0, & \tau_R &= a_b^2/\eta, & S &= \tau_R/\tau_A \end{aligned} \tag{3.5}$$

In this dimensionless form one can readily identify several indicators of boundary layer

activity. Particularly relevant to reconnection is the inverse Lundquist number S^{-1} that multiplies the highest order derivative of the flux ψ. The Lundquist number represents the relative timescales of resistive, and thus collisional, processes in the plasma compared to ideal MHD effects such as waves and fluid flows. As most plasmas are nearly collisionless we take $S^{-1} \ll 1$, and this term will only be significant in a narrow region where gradients of the eigenfunctions are large. These parts of the domain will be the diffusion regions responsible for changes in magnetic topology. We have marked the locations of this resistive region by red dashed lines on a schematic of the DTM boundary layer structure in Figure 3-1. Outside of this resistive layer the system is described, to lowest order, by the physics of ideal MHD. We will therefore begin by taking $S^{-1} \to 0$ and considering the outer region ideal solutions.

Henceforth we will discard the tildes for clarity, with the understanding that the normalized variables are used.

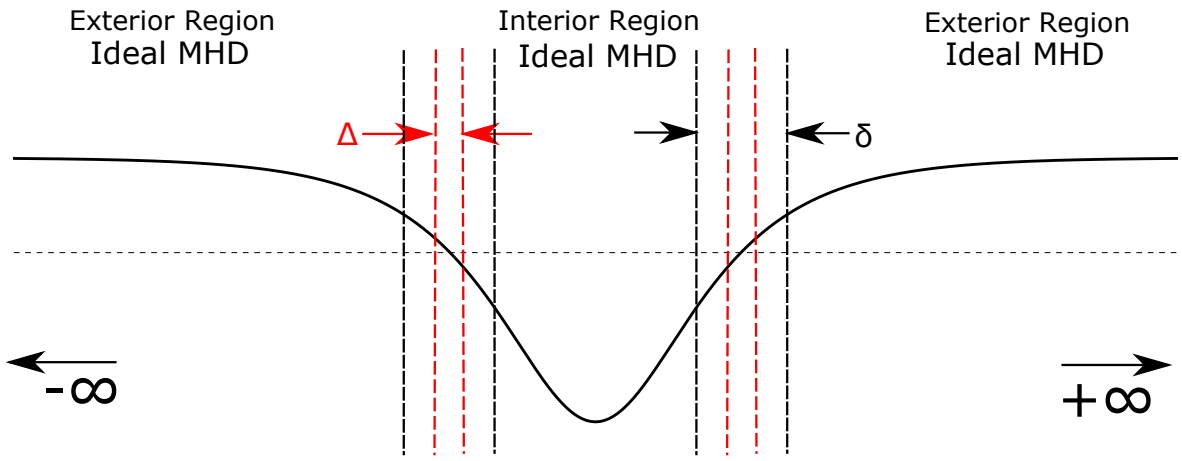

Figure 3-1: Sketch of the double-tearing mode boundary layer structure on a characteristic B_{eq} magnetic equilibrium. Away from the resonant surfaces the system is described by the lowest order ideal MHD behavior (Eqn. 3.7). The DTM differs from the single-tearing mode in having an additional ideal region between the two surfaces. Near each resonant surface two boundary layers emerge: a layer of width δ (black dashed lines) where small scale ideal MHD processes dominate (Eqn. 3.13); and a layer of width Δ (red dashed lines) where resistivity is significant (Eqn. 3.18). Note the ordering of these nested boundary layers is not necessarily as shown in this schematic.

3.1.1 Ideal regions

Neglecting the resistive term in Equation 3.4 reduces it to the relation $\psi = B_{eq}\xi$. We combine it with Equation 3.3 to form a single second order ODE for the plasma displacement

ξ describing the ideal MHD behavior of the system:

$$\frac{\mathrm{d}}{\mathrm{d}x}\left[(\alpha^2 B_{eq}^2+\gamma^2)\frac{\mathrm{d}\xi}{\mathrm{d}x}\right]=\alpha^2(\alpha^2 B_{eq}^2+\gamma^2)\xi \tag{3.6}$$

Consider the magnitude of the growth rate γ. We are searching for a reconnecting instability and the only mechanism for field line breaking is resistivity, therefore the growth rate must somehow depend on the Lundquist number. Furthermore, we are only interested in modes which grow faster than the resistive decay time, which is very long in realistic plasmas. Therefore we assume $\gamma \propto S^{-\theta}$ $(0<\theta<1)$ and as a consequence $\gamma^2 \ll \alpha^2 B_{eq}^2$ except in a narrow regions around $x=\pm x_s$ where the in-plane magnetic field approaches zero and Eqn. 3.6 becomes singular. These narrow regions form ideal MHD boundary layers, which we denote schematically as black dashed lines in Figure 3-1.

Away from the singular layers we can neglect γ to lowest order and write:

$$\frac{\mathrm{d}}{\mathrm{d}x}\left[B_{eq}^2\frac{\mathrm{d}\xi}{\mathrm{d}x}\right]=\alpha^2 B_{eq}^2\xi \tag{3.7}$$

Or, integrating both sides:

$$B_{eq}^2\frac{\mathrm{d}\xi}{\mathrm{d}x}=\alpha^2\int_0^x B_{eq}^2(X)\xi(X)\mathrm{d}X+C \tag{3.8}$$

This differential equation is not exactly solvable except for highly constrained equilibrium fields. Two possible routes for further asymptotic expansion exist. The normalized wave number α appears as an explicit parameter, and is commonly considered in single-tearing mode solutions[20]. Choosing to expand in α, however, neglects the spacing between the singular surfaces which is the defining feature of the DTM. Furthermore, assuming $\alpha \ll 1$ restricts the validity to very small wave numbers and generates a more complicated expansion with exponential tails. We instead consider that Equations 3.7 and 3.8 are valid everywhere

except in the immediate neighborhood of the singular surfaces, therefore they are also valid between the surfaces. This interior region is disconnected from the boundaries at $x \to \pm\infty$ and is unique to the DTM. We therefore expect the behavior in this interior domain to influence the global evolution of the mode when matched through the boundary layers. The appropriate expansion parameter, assuming the layers are closely spaced compared to the system size, is $\alpha^2 x_s^2$. This choice has the advantage of capturing the relative scale of variation along and between the surfaces. It abandons, however, the comparison between k and a_b, thereby neglecting the actual properties of the magnetic shear local to each surface. We will examine the consequences of this choice later in this section when considering this theory's domain of validity.

Expanding ξ in the ideal outer regions as a power series in $\alpha^2 x_s^2$ (Eqn. 3.9) and substituting into the outer region differential equation (3.8) allows us to match powers of the expansion parameter.

$$\xi = \xi_{(0)} + \alpha^2 x_s^2 \xi_{(1)} + \alpha^4 x_s^4 \xi_{(2)} + \cdots \tag{3.9}$$

To lowest order we find that $\mathrm{d}\xi_{(0)}/\mathrm{d}x = C/B_{eq}^2$. In the exterior region ($|x| > x_s$) we must choose the constant $C = 0$ to satisfy the requirement that ξ be bounded as $x \to \infty$. This condition does not apply to the interior region $|x| < x_s$. In this region, however, $C \neq 0$ would yield an antisymmetric solution for $\xi_{(0)}$, which we delay until later in this chapter. Therefore the lowest order displacement ξ_0 must be constant in both the interior and exterior ideal MHD regions. At the outer boundaries ($|x| \to \infty$) we require the eigenmode to vanish, but no such restriction exists between the two resonant surfaces.

$$\begin{aligned} \xi_{(0)} &= 0 \quad & |x| > x_s \\ \xi_{(0)} &= \xi_\infty \quad & |x| < x_s \end{aligned} \tag{3.10}$$

where $\xi_\infty \neq 0$ is a constant. This solution represents a rigid displacement of the plasma between the two tearing surfaces, similar to the $m = 1$ kink mode in cylindrical geometry [3].

Proceeding to the first order solution we again neglect the antisymmetric contribution and obtain an expression for the derivative of $\xi_{(1)}$ [39].

$$\begin{aligned}(\xi_\infty)^{-1}\left(\frac{\mathrm{d}\xi_{(1)}}{\mathrm{d}x}\right) &= \left(\frac{\alpha}{B_{eq}}\right)^2 \int_0^x B_{eq}^2(X)\mathrm{d}X \quad |x| < x_s \\ (\xi_\infty)^{-1}\left(\frac{\mathrm{d}\xi_{(1)}}{\mathrm{d}x}\right) &= \left(\frac{\alpha}{B_{eq}}\right)^2 \int_0^{x_s} B_{eq}^2(X)\mathrm{d}X \quad |x| > x_s\end{aligned} \tag{3.11}$$

The above solutions are valid far away from the tearing surfaces when $\alpha^2 B_{eq}^2 \gg \gamma^2$. Near the zeros of the in-plane field ($x = \pm x_s$) we assume that the equilibrium field is approximately linear such that $B_{eq}(x) \approx \pm B_0' (x \mp x_s)$ and, keeping factors of γ (which are now significant as $B_{eq} \to 0$), obtain an equation for the ideal MHD behavior around the $x = x_s$ singular surface.

$$\frac{\mathrm{d}}{\mathrm{d}x}\left[(x - x_s)^2 + \frac{\gamma^2}{\alpha^2 B_0'^2}\right]\frac{\mathrm{d}\xi}{\mathrm{d}x} = \alpha^2\left[(x - x_s)^2 + \frac{\gamma^2}{\alpha^2 B_0'^2}\right]\xi \tag{3.12}$$

Rescaling the coordinate x within the boundary layer such that $x = x_s + \delta\chi$ for some small parameter δ and $\chi = O(1)$ we find

$$\frac{\mathrm{d}}{\mathrm{d}\chi}\left[\chi^2 + \frac{\gamma^2}{\delta^2\alpha^2 B_0'^2}\right]\frac{\mathrm{d}\xi}{\mathrm{d}\chi} = \alpha^2\left[\delta^2\chi^2 + \frac{\gamma^2}{\alpha^2 B_0'^2}\right]\xi \tag{3.13}$$

Evaluating the dominant balance of terms in Equation 3.13 shows that the only valid scaling is $\delta^2 = \gamma^2\alpha^2 B_0'^2$. The entire r.h.s. is thus ignorable to lowest order and the zeroth order

solution within this ideal MHD layer has a closed form.

$$\begin{aligned}\xi &= \int_0^{\chi} \mathrm{d}\zeta \frac{E}{1+\zeta^2} \\ &= E \arctan(\chi) + D \\ &= E \arctan\left(\frac{\alpha B_0'(x-x_s)}{\gamma}\right) + D\end{aligned} \tag{3.14}$$

The constants E and D are fixed by taking the limits as $x \to \pm\infty$ and matching the the outer region solutions (Eqn. 3.10) to give the lowest order ideal MHD layer solution.

$$\xi(x) = \frac{\xi_\infty}{2}\left[1 - \frac{2}{\pi}\arctan\left(\frac{\alpha B_0'(x-x_s)}{\gamma}\right)\right] \tag{3.15}$$

Differentiating Equation 3.15 and matching to the first order outer region derivative found in Eqn. 3.11 results in an expression for the ideal MHD growth rate γ_H of this configuration, which can be identified as the slab double-kink mode [39].

$$\gamma_H = -\left(\frac{\pi\alpha^3}{B_0'}\right)\int_0^{x_s} \mathrm{d}x B_{eq}^2(x) \tag{3.16}$$

This mode is always stable ($\gamma_H \leq 0$). Based on the pre-factor α^3/B_0' we may observe that either decreasing α or increasing the local magnetic shear trends towards marginal ideal stability $\gamma_H \approx 0$. The integral on the r.h.s. of Equation 3.16 behaves as x_s^3 and thus the double-kink mode can approach the marginal stability threshold as $\alpha^3 x_s^3 \to 0$ [39]. This behavior strongly suggests that the closely-coupled double-tearing mode may resemble the marginally stable $m = 1$ kink-tearing mode in cylindrical geometry. The DTM is, however, always ideal MHD stable, and thus we must reintroduce resistivity to achieve growth.

3.1.2 Resistive layer

To describe the resistive layer (red dashed lines in Fig. 3-1) we replace the full magnetic field in Equations 3.4 and 3.3 with the approximate form local to the singular surface

$B_{eq}(x) \approx B_0'(x - x_s)$. Introducing the small parameters $\lambda = \gamma/\alpha B_0'$ and $\epsilon = 1/S\alpha B_0'$ this set of equations can be written as [19]:

$$\begin{aligned} \xi'' - \alpha^2 \xi &= -\frac{(x - x_s)}{\lambda^2}\left(\frac{\psi''}{B_0'} - \alpha^2 \frac{\psi}{B_0'}\right) \\ \frac{\psi}{B_0'} &= (x - x_s)\xi + \frac{\epsilon}{\lambda}\left(\frac{\psi''}{B_0'} - \alpha^2 \frac{\psi}{B_0'}\right) \end{aligned} \tag{3.17}$$

Following standard boundary layer procedure we define a scaled variable $x = x_s + \Delta\chi$ and substitute to obtain:

$$\begin{aligned} \frac{\mathrm{d}^2\xi}{\mathrm{d}\chi^2} - \Delta^2\alpha^2\xi &= -\Delta\frac{\chi}{\lambda^2}\left(\frac{1}{B_0'}\frac{\mathrm{d}^2\psi}{\mathrm{d}\chi^2} - \Delta^2\alpha^2\frac{\psi}{B_0'}\right) \\ \Delta^2\frac{\psi}{B_0'} &= \Delta^3\chi\xi + \frac{\epsilon}{\lambda}\left(\frac{1}{B_0'}\frac{\mathrm{d}^2\psi}{\mathrm{d}\chi^2} - \Delta^2\alpha^2\frac{\psi}{B_0'}\right) \end{aligned} \tag{3.18}$$

All explicit factors of α^2 are order Δ^2 and added to order one derivatives, therefore are insignificant to lowest approximation within the resistive layer. Neglecting them we obtain a compact set of equations for the displacement ξ and magnetic flux ψ which describe the lowest order behavior near the singular points.

$$\begin{aligned} \frac{\mathrm{d}^2\xi}{\mathrm{d}\chi^2} &= -\left[\frac{\Delta}{\lambda^2}\right]\chi\frac{1}{B_0'}\frac{\mathrm{d}^2\psi}{\mathrm{d}\chi^2} \\ \frac{\psi}{B_0'} &= [\Delta]\,\chi\xi + \left[\frac{1}{\Delta^2}\frac{\epsilon}{\lambda}\right]\frac{1}{B_0'}\frac{\mathrm{d}^2\psi}{\mathrm{d}\chi^2} \end{aligned} \tag{3.19}$$

The elements of Equation 3.19 which are highlighted by square brackets are pre-factors involving the scale width Δ that can be tuned to change the interaction of different terms in these equations. Unlike the ideal MHD layer (Eqn. 3.13) the appropriate expression for Δ cannot be fixed without first specifying the relative magnitudes of ξ and ψ/B_0'. Fortunately the substitutions $\xi \to -\xi$ and $\psi/B_0' \to \psi$ transform [19, 39] this set of equations into those describing the $m = 1$ kink-tearing mode resistive layer analyzed by Ara et al. in Ref. [3], in which they consider appropriate balances and complete the matching to the exterior layer. The solution and matching process is rather complicated, so we do not reproduce it here.

Instead we summarize the results of Pritchett et al. in Ref. [39] where they have performed the appropriate transformations to find two limiting expressions for γ valid within specific regimes of the DTM parameter space.

Provided that the fundamental assumption $\alpha^2 x_s^2 \ll 1$ holds, so that the outer ideal MHD solutions (Eqns. 3.10 and 3.11) are valid, and that the resistive scale width Δ is small enough to allow matching in the region between the singular layers ($\Delta \ll x_s$), the DTM dispersion relation can be expressed in terms of Γ-functions.

$$\frac{\hat{\lambda}^{5/4}\hat{\lambda}_H \Gamma\left[(\hat{\lambda}^{3/2}-1)/4\right]}{\Gamma\left[(\hat{\lambda}^{3/2}+5)/4\right]} = 8 \tag{3.20}$$

where

$$\hat{\lambda}_H = \gamma_H \left(\frac{S}{\alpha^2 B_0'^2}\right)^{1/3} \tag{3.21}$$

is a measure of the ideal MHD driving energy and

$$\hat{\lambda} = \gamma \left(\frac{S}{\alpha^2 B_0'^2}\right)^{1/3} \tag{3.22}$$

is a measure of the resistive mode instability.

By numerically mapping the dependence of $\hat{\lambda}$ on $\hat{\lambda}_H$ via the dispersion relation, approximate analytic growth rates can be found in two limits [39]. When the singular surfaces are very near to each other the slab kink-mode is marginally stable ($\gamma_H \to 0^-$, see Eqn. 3.16) and $|\hat{\lambda}_H| \ll 1$, resulting in $\hat{\lambda} \simeq 1$ and the double-tearing mode growth rate is $\gamma \simeq (\alpha^2 B_0'^2/S)^{1/3}$. The scaling of this growth rate with Lundquist number/resistivity ($\gamma \sim S^{-1/3} \sim \eta^{1/3}$) is consistent with the marginally stable $m = 1$ kink-tearing mode [3] and other such 'strongly nonconstant ψ' tearing modes. In the opposite limit, when the system is deeply ideally stable, $|\hat{\lambda}_H| \gg 1$, $\hat{\lambda} \ll 1$, and the growth rate scales like $\gamma \propto (\alpha^2 B_0'^2/S)^{3/5}$. This scaling

($\gamma \sim S^{-3/5} \sim \eta^{3/5}$) is that of a 'constant ψ' tearing mode [20], and calculations of the resistive layer width and diffusion time are consistent with this picture [39]. Mapping this deeply ideally-stable regime to the system parameters requires some care. One can conclude from Eqn. 3.16 that $\gamma_H \to -\infty$ as $x_s \to \infty$, but the dispersion relation (Eqn. 3.20) is valid only under the assumption that $\alpha^2 x_s^2 \ll 1$. Pritchett [39] considered the respective domains of validity for the $S^{-1/3}$ and $S^{-3/5}$ scaling predictions and concluded that the boundary between the two behaviors occurs in the neighborhood of $\alpha x_s \approx (\alpha^2/S)^{1/9}$. When the modes are close enough to be below this threshold they behave as coupled, reconnecting, slab kink-modes. At larger separations they resemble decoupled single tearing modes. The product αx_s can therefore be consider a sort of 'linear coupling parameter' within the domain of validity for the above boundary layer theory.

3.1.3 Domain of validity

It is important to note that we have only considered the growth rate scaling of the DTM with resistivity in two asymptotic regimes, labeled with the specialized names 'constant ψ' and 'strongly nonconstant ψ'. These terms refer to the behavior of the perturbed magnetic flux within the tearing layer, and will be used to classify tearing modes throughout this thesis. If the growth of the instability is slow compared to the resistive diffusion time across the resonant layer than the lowest order magnetic perturbation may be consider constant with the layer, i.e. one may assume constant ψ in the resistive layer. This approximation is only valid when the system is deeply ideally stable, and results in a growth rate which scales as $\gamma \sim \eta^{3/5}$. For single-tearing modes this regime typically corresponds to the large α limit near the tearing stability boundary [20]. Away from this deeply stable region the magnetic perturbation within the layer cannot be taken as constant. Such nonconstant ψ modes have growth rates which scale like $\gamma \sim \eta^{\theta}$ where $1/3 \leq \theta \leq 3/5$ depending on the instability wavenumber and equilibrium parameters. The marginally ideal MHD stable asymptotic limit corresponds to the $\gamma \sim \eta^{1/3}$ scaling and here we have used the term 'strongly nonconstant ψ'.

Isolated single tearing modes have access to these regimes based on the magnetic shear local to the resonant layer and wavenumber. The remarkable feature of the double-tearing mode is that interaction between the resonant surfaces is able to drive nonconstant ψ behavior for tearing layers which would otherwise be deeply ideally stable.

The parameter αx_s is a good indicator of the coupling strength between the two resonant surfaces, and thus of the influence of the slab-kink mode on evolution, but not sufficient to uniquely determine the growth rate scaling of the DTM. Because it is a product of the normalized wavenumber and a normalized length it no longer contains information on how the wavelength relates to the current channel width. Consider the measure of the ideal MHD driving energy $\hat{\lambda}_H$, which depends more strongly on α than on x_s:

$$\hat{\lambda}_H \sim \alpha^{11/3} x_s^3 \tag{3.23}$$

If $\alpha \ll 1$ the mode remains marginally ideally stable ($\hat{\lambda}_H \approx 0$) for all values of x_s, even if $x_s \sim 1/\alpha$ when there will be a region of exponential decay between the singular layers and we cannot reasonably expect the resonant surfaces to be coupled (see Ref. [20] for discussion of the low α tearing mode limit). Such a low α system will behave like two isolate single tearing modes, each in the strongly nonconstant ψ limit.

There exits, therefore, an important restriction on how we may appropriately use this linear analysis to categorize double-tearing modes. If the two tearing surfaces are sufficiently close that $\alpha x_s \ll (\alpha^2/S)^{1/9}$ it follows that they are strongly coupled and $\gamma \sim \eta^{1/3}$. A growth rate which scales as $\eta^{1/3}$ is not, however, sufficient to claim that the modes are strongly coupled; the value of α must also be considered. The reverse is true in the weakly coupled limit: $\gamma \sim \eta^{3/5} \implies \alpha x_s \gg (\alpha^2/S)^{1/9}$. With these considerations in mind it is generally valid to consider αx_s as a 'linear coupling parameter' with the provision that it does not uniquely determine the growth rate but, as we will show later in this chapter, describes the basic eigenmode structure.

3.2 Symmetric simulations

The scaling behavior of the linear symmetric double-tearing mode with resistivity, especially in the strongly coupled limit, has been verified in many simulation regimes [9, 10, 31, 39]. In this section we will show that the eigenfunctions and growth rates of Pritchett's analysis [39] can be reproduced in a special linearized version of `MRC-3d` with a strong guide field, thus confirming that reduced-MHD boundary layer theory represents the compressible `MRC-3d` model in this limit.

3.2.1 Linear simulation methods

The linearized version of `MRC-3d` uses the same fundamental plasma model as the fully nonlinear version. A modified version of the code generator applies the Fourier ansatz $F(x, y, t) = f(x, t) \exp(iky)$ to the fields ρ, T, $\mathbf{B}$, and $\mathbf{U}$. The real and imaginary parts of each field are stored separately and symbolic manipulation is used to generate numerical expressions discretized in x. This process is described in more detail in Appendix A.

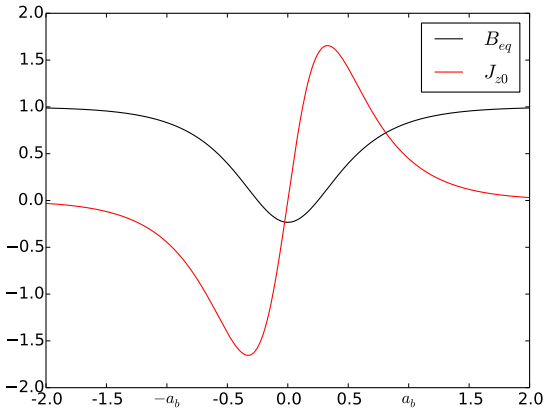

Figure 3-2: An example of the current profile for the sech equilibrium with $B_0'(\pm x_s) = \pm\pi/2$ and $x_s = 0.25$. The current (J_{z0}) channel scale width a_b is approximately 1 in `MRC-3d` coordinates.

All simulation results presented here use the 'sech' equilibrium described in Section 2.3 for the reconnecting field B_y, with the choice $\partial_x B_y(\pm x_s) = \pm\pi/2$. This configuration has the beneficial property that the current channel width at each surface is approximately equal to

one for most separations (x_s) of interest, so that the `MRC-3d` normalization closely matches that of the linear boundary layer theory, as shown in Figure 3-2. We will not exactly define or measure a_b for the simulation equilibrium as the asymptotic theory is not precise enough to require such rigor. The normalized wave number is then approximately the same as the code wave number, i.e. $\alpha \approx k = k_y$. Finally we choose the magnitude of out-of-plane magnetic field to be $B_{z0} = 10$ far away from the singular surfaces, with small variations across the domain as necessary to maintain a force-free equilibrium. At this magnitude of guide field and a constant equilibrium temperature and pressure of $T = \rho = 1$ the compressible `MRC-3d` model should behave, to lowest order, as incompressible reduced-MHD.

In choosing boundary conditions for numerical simulations one must balance the desire to minimize the length of the domain (and hence computational costs) against the need to ensure that the boundaries are far enough from the non-zero portions of the eigenmode to not influence its evolution. Unless otherwise noted simulations in this section have conducting walls at $x = \pm 4.0$. At wavenumbers on the order of $\alpha \sim 0.1$ the symmetric DTM is sufficiently well confined that this location for the boundaries does not impact the mode.

`MRC-3d` is an initial value code, even in its linearized form. As such some post processing is required to obtain growth rates and eigenfunction information. At user-defined intervals during a simulation, the code writes a sequence of diagnostic quantities to a file. The quantities include the peak values of dynamic variables, calculated currents, and the integrated kinetic energy. This diagnostic data is fitted to an exponential in time via a least-squares method provided by the `curve_fit` function of the `scipy` Python package. Because the initial perturbation is not an exact eigenmode of the system there is a period of noise early in the simulation. As time advances the fastest growing mode begins to dominate and the diagnostic output shows a steady exponential growth, from which a range is selected for fitting.

Full outputs of the simulation state at every grid point occur less frequently than the diagnostics, in order to minimize storage requirements and execution time. To compare to

the linear theory we are primarily interested in the reduced variables ξ and ψ, which must be calculated from the `MRC-3d` fields $\mathbf{P}$ and $\mathbf{B}$.

$$\xi = \frac{ik\phi}{\gamma} = \frac{P_x}{\rho_0 \gamma} \tag{3.24}$$

$$\psi = -\int_{x_0}^{x} dx' B_y(x') - \frac{i}{k_y} B_x(x) \tag{3.25}$$

$$\tag{3.26}$$

3.2.2 Simulation results

To verify the boundary layer theory we choose $\alpha = k = 0.5$, similar to Ref. [39], and tearing layer spacings of $x_s = 0.25$ and $x_s = 1.0$. Even at these relatively large values of the coupling parameter $\alpha x_s = 0.128$ and 0.5 the boundary layer theory quite accurately predicts dependence of the growth rate γ on resistivity η, which is shown in Figure 3-3. A separation of $x_s = 0.25$ produces a double-tearing mode with scaling $\gamma \sim \eta^{0.36}$, which is close to the expected $\eta^{1/3}$ behavior. Furthermore the eigenfunction (Fig. 3-4a) is approximately that of the slab-kink mode described in Section 3.1.1. At the larger spacing of $x_s = 1.0$ the mode instead scales like a constant ψ tearing mode ($\gamma \sim \eta^{3/5}$). The corresponding eigenfunction shown in Figure 3-4b behaves as a combination of slab-kink and ordinary tearing modes. To lowest order the displacement ξ between the singular surfaces is constant, as would be expected from the asymptotic analysis. Near the tearing surfaces, however, the mode begins to resemble an isolated tearing mode. From this behavior one can conclude that the two surfaces are weakly coupled, rather than entirely independent. It is important, therefore, to recognize that $\gamma \sim \eta^{3/5}$ scaling does not imply a completely decoupled double-tearing mode. In fact, we will discover in Chapter 8 that these weakly coupled modes are capable of generating strong nonlinear explosive growth.

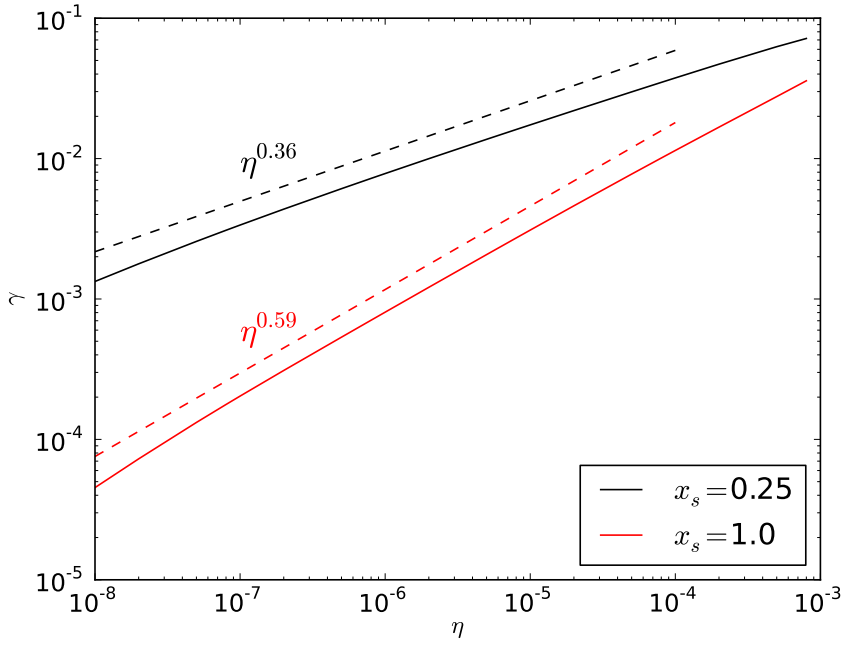

Figure 3-3: Scaling of the growth rate γ with resistivity η for the weakly coupled ($x_s = 1.0$) and strongly coupled ($x_s = 0.25$) symmetric DTM.

3.3 Antisymmetric eigenmodes

While the symmetric double-tearing mode has been extensively studied as case of fast, self-driven reconnection the antisymmetric solution has been largely ignored because the interaction between the singular surfaces does not appear to strengthen the growth, and may even slow it. As we introduce various stabilization mechanisms in the following chapters we will see that the antisymmetric DTM solution emerges as an important part of a hybrid, sheared eigenmode. In preparation for this future discussion we will briefly consider the results of `MRC-3d` simulations targeting this antisymmetric mode. The appropriate analytic solution for the odd DTM solution is not currently known.

The scaling of the antisymmetric mode growth rate with resistivity is shown in Figure 3-5 for the same values of $\alpha = 0.5$ and $x_s = [0.25, 1.0]$ as used previously. Both separations exhibit $\gamma \sim \eta^{3/5}$ behavior and have nearly identical magnitudes. As expected the growth rates are much slower the symmetric mode (Fig. 3-3) for both separations, though this disparity is less at larger x_s. The strong dependence of the growth rate on resistivity suggests

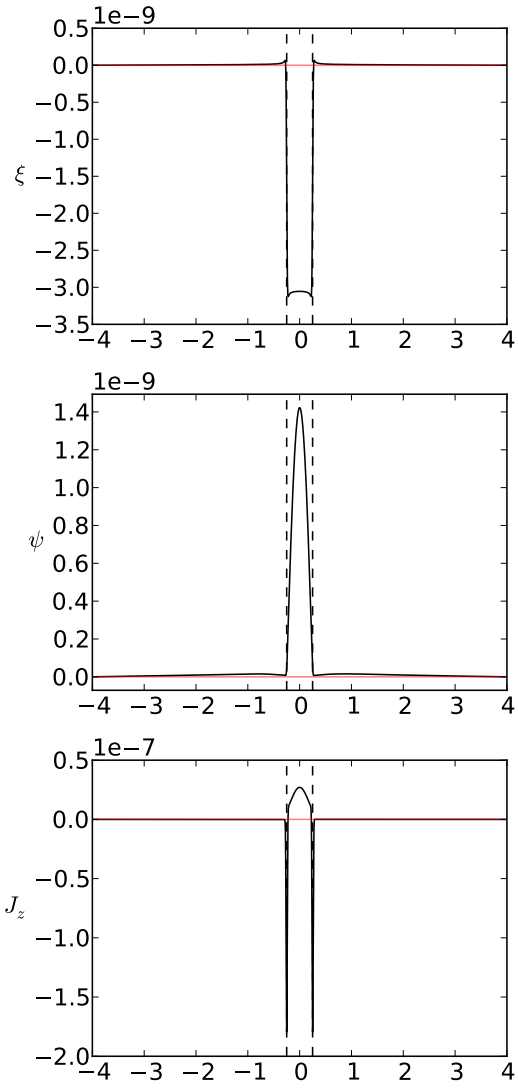

(a) $x_s = 0.25$ $\alpha = 0.5$ eigenmode at resistivity $\eta = 1 \times 10^{-7}$. Between the resonant surfaces (vertical dashed lines) the displacement ξ is non-zero and nearly constant.

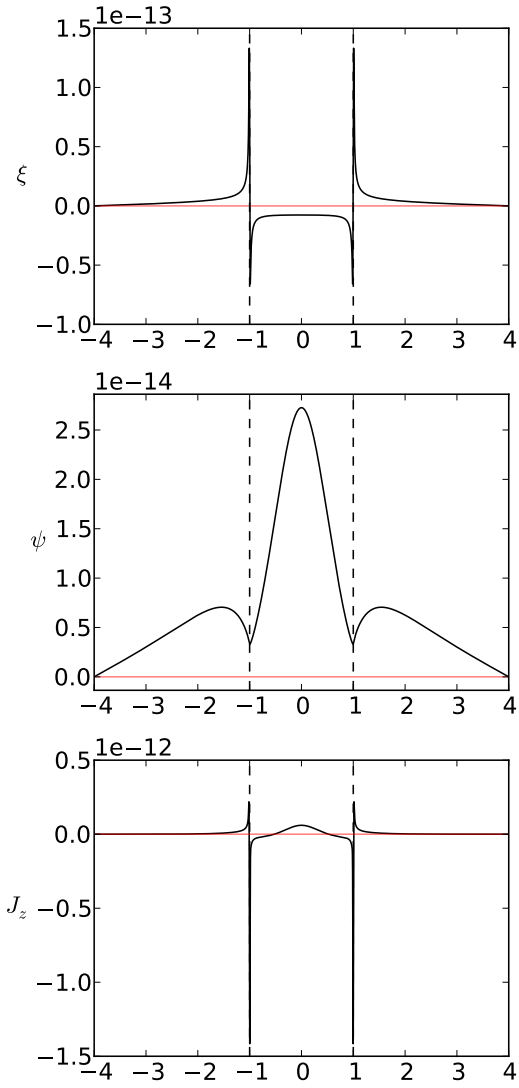

(b) $x_s = 1.0$ $\alpha = 0.5$ eigenmode at resistivity $\eta = 1 \times 10^{-7}$. The displacement between the resonant surfaces is nearly zero and constant. Near the boundary layers the displacement ξ and the magnetic flux ξ resemble single-tearing modes.

Figure 3-4: Eigenmodes for the strongly coupled (left) and weakly coupled (right) linear force-free DTM.

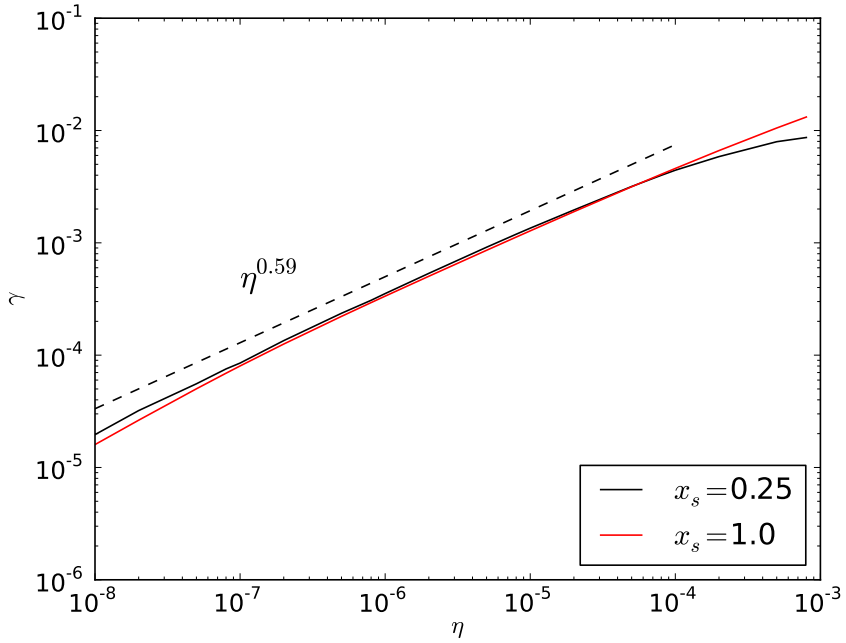

Figure 3-5: Scaling of the growth rate γ with resistivity η for the $x_s = 1.0$ and $x_s = 0.25$ antisymmetric DTMs. Both spacings have nearly the same growth rate at all resistivities, and scale like constant ψ tearing modes.

that the constant ψ assumption is valid within the resonant layers of both separations.

The shapes of the corresponding eigenmodes are shown in Figure 3-6. The regions to the left and right of the singular surfaces resemble decaying exponentials rather than constants, which is consistent with isolated single-tearing modes (which are expanded in α) rather than the symmetric DTM solution (expanded in $\alpha^2 x_2^2$). Between the layers, however, the eigenfunctions remain connected, suggesting that the two-resonance structure remains important.

These measurements of scalings and eigenmodes suggest that the antisymmetric boundary layer analysis may involve a constant ψ singular layer, a DTM like expansion between the surfaces, and a STM solution outside. The interaction between the resonant surfaces that drove the even eigenmode toward marginal ideal stability may force the odd mode deeper into the ideally stable regime.

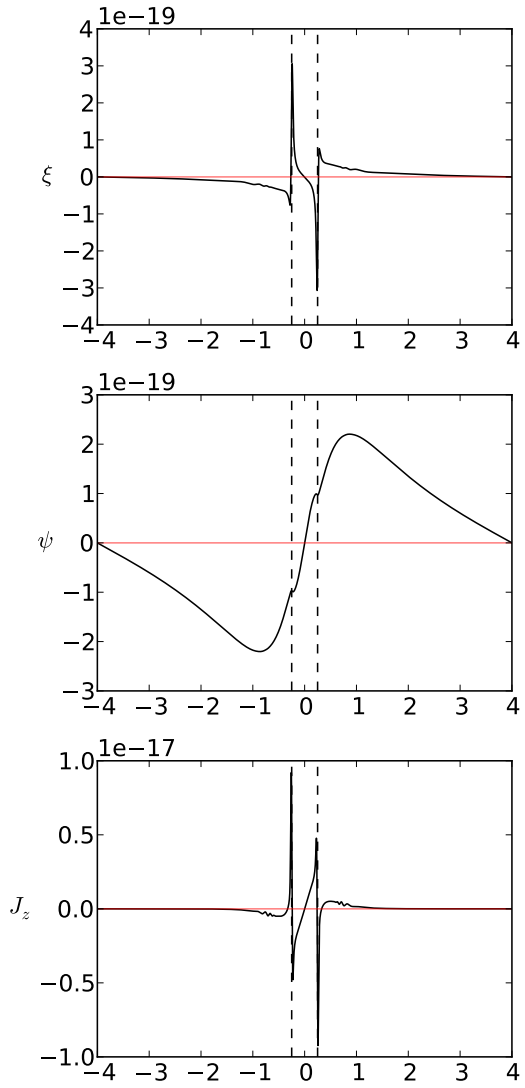

(a) $x_s = 0.25$ $\alpha = 0.5$ antisymmetric eigenmode for resistivity $\eta = 1 \times 10^{-5}$. The very slow growth rate of this instability results in some noise from the initial condition persisting in this example, but the mode behavior is clear.

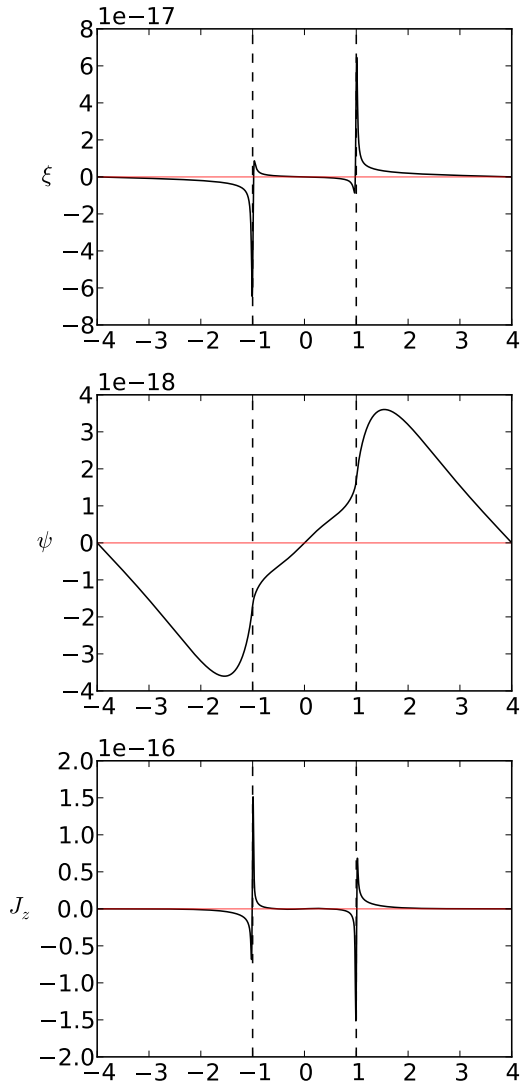

(b) $x_s = 1.0$ $\alpha = 0.5$ eigenmode for resistivity $\eta = 1 \times 10^{-5}$

Figure 3-6: Examples of linear antisymmetric double-tearing eigenmodes

3.4 Discussion

The asymptotic analysis and simulations of this chapter are not a complete description of even the force-free, resistive double-tearing mode, but they form the fundamental basis for our current understanding of this instability's self-driving behavior. Two nearby singular surfaces will couple together and form a marginally stable ideal MHD mode based on their separation and the perturbation wave number. This marginal stability results in a reconnecting mode which depends weakly on resistivity, thus making it a candidate for 'fast' field line breaking even in the absence of kinetic effects. Unless the wave number is very long the disturbance associated with strongly coupled DTMs is highly localized between the tearing layers. Nonlinearly we will see that all but the slowest growing, constant ψ double-tearing modes can results in disruptive late time behavior.

This linear theory forms the foundational understanding of the DTM that we will rely on throughout this work. Unfortunately, it lacks several key features that would aid future study of both linear stabilization mechanisms and nonlinear instability. We will see in the next chapter that the antisymmetric solution plays a key roll in determining how equilibrium sheared flows (and later diamagnetic drifts) impact DTM growth. Without an analytic understanding of the the odd eigenmode, and simulation methods better able to extract the slower growing instabilities, future progress on a linear theory of DTM stabilization will be difficult. Similarly the lack of a clear metric to define DTM stability (akin to the Δ' tearing stability index) will make the comparison of nonlinear behavior challenging. In principle the normalized wave number α and 'coupling parameter' αx_s serve as strong indicators of whether the mode behaves as constant or nonconstant ψ reconnecting mode, but they neglect the details of the magnetic field away from the layer. The ideal MHD driving energy ($\hat{\lambda}_H$) and resistive mode instability ($\hat{\lambda}$) parameters (Eqns. 3.21 and 3.22) may serve well in this respect, but their reliability as indicators of nonlinear behavior has not been explored.

In the absence of any agreed upon measure of the DTM classification we will treat the analysis of this chapter as a first indicator of coupling strength, i.e. smaller αx_s means

stronger interaction. Beyond this we will rely on subjective evaluations of the perturbed fields such as the plasma flow, linear displacement, and magnetic structure.

Chapter 4

Linear sheared flow equilibria

The interaction between two tearing surfaces causes the symmetric double-tearing mode to be less dependent on resistivity and more strongly driven than the standard single tearing mode (STM) case. In this chapter we will see our first indication that the coupling of the DTM can be suppressed by applying an equilibrium flow along the reconnecting magnetic field to shear the layers apart. The symmetric, two-boundary layer eigenmodes found in Chapter 3 will be unable to survive in the presence of this background flow and will be forced to acquire an odd component in the complex plane before completely separating into single tearing layer solutions. This effect will not, however, be sufficient to stabilize the DTM below some finite threshold, but it will be a vital component to our later application of diamagnetic drifts.

We will begin by considering the foundations of a reduced MHD boundary layer theory in the presence of equilibrium flow and mapping which regions of parameter space have interesting behavior that we should target with simulation studies. This analysis will yield several new classes of singular layers which are not present in the static DTM theory. In particular, we discover a class of singular layer that is manifestly complex, which we show is associated with a bifurcation point in linear DTM behavior caused by an antisymmetric equilibrium flow. A complete asymptotic theory is not currently available, but we will predict the approximate critical flow amplitude at which this bifurcation occurs and how the DTM eigenmodes behave above and below this threshold. These predictions will then be confirmed by linear `MRC-3d` simulations. To conclude we will sketch a road-map for the remaining theory and consider the implications for the nonlinear DTM stabilization.

4.1 Boundary layer analysis

Some preliminary understanding of the effect of shear flow on DTMs can be gained from a linear boundary layer analysis similar to that of Chapter 3. We begin by returning to the resistive reduced-MHD model of Equations 1.40 and 1.41 and linearizing, but this time retaining an equilibrium flow. In the incompressible limit the velocity must be divergence-free, and we choose to ensure this condition by requiring $\mathbf{U}_0 = v_{eq}(x)\hat{y}$ so that the equilibrium flow is parallel to the reconnecting magnetic field at all times. The linearized rMHD equations are then:

$$\partial_t \nabla_\perp^2 \phi = -v_{eq}\partial_y \nabla_\perp^2 \phi + \partial_y \phi \partial_x v_{eq} + B_{eq}\partial_y \nabla_\perp^2 \psi - \partial_y \psi \partial_x^2 B_{eq} \tag{4.1}$$

$$\partial_t \psi = -v_{eq}\partial_y \psi + B_{eq}\partial_y \phi + \eta \nabla_\perp^2 \psi \tag{4.2}$$

We again apply the Fourier ansatz $F(x, y, t) = f(x)\exp(\gamma t + iky)$ to all perturbed quantities. The normalizations listed in Equation 3.5 apply to this set of PDEs as well, though the presence of equilibrium flow requires the additional definition:

$$\tilde{\omega_0} = k v_{eq} \tau_A \tag{4.3}$$

Substituting in normalizations, and rearranging, we recover a normalized form.

$$\tilde{\gamma}(\tilde{\gamma} + i\tilde{\omega_0})(\tilde{\xi}'' - \alpha^2\tilde{\xi}) = i\tilde{\gamma}\tilde{\omega_0}''\tilde{\xi} - \alpha^2\tilde{B}_{eq}(\tilde{\psi}'' - \alpha\tilde{\psi}) + \alpha^2\tilde{\psi}\tilde{B}_{eq}'' \tag{4.4}$$

$$(\tilde{\gamma} + i\tilde{\omega_0})\tilde{\psi} - \tilde{\gamma}\tilde{B}_{eq}\tilde{\xi} = S^{-1}(\tilde{\psi}'' - \alpha^2\tilde{\psi}) \tag{4.5}$$

Henceforth we will drop the tildes for clarity.

Consider the repeating quantity $\Gamma = \gamma + i\omega_0$. Where the equilibrium flow is constant this expression would correspond to a Doppler shift of the (now complex) eigenfrequency γ, in which case we could transform it out and proceed as in Chapter 3. The more interesting case,

however, is to treat the equilibrium flow as nonconstant and sheared, such that $\omega_0 = \omega_0(x)$ and the imaginary part of Γ depends on x. It is important to remember, therefore, that while Γ may resemble an eigenvalue in the coming analysis it cannot properly be treated as such. With this identification we can further simplify this set of equations by defining a sheared form of the plasma displacement $z = \xi/\Gamma$ and, following a similar manipulation to Ofman in Reference [38], obtain a compact set of sheared equations:

$$\gamma \left[\alpha^2\Gamma^2 z + (\Gamma^2 z')'\right] = -\alpha^2 \left[B_{eq}(\alpha^2\psi - \psi'') + \psi B''_{eq}\right] \tag{4.6}$$

$$\psi - \gamma B_{eq} z = \frac{S^{-1}}{\Gamma}(\psi'' - \alpha^2\psi) \tag{4.7}$$

As before, we will begin by considering the regions outside of the diffusive layers under the assumption that $S^{-1} \ll 1$ to obtain a single ODE for z describing the ideal MHD behavior of the system.

$$\frac{\mathrm{d}}{\mathrm{d}x}\left[(\alpha^2 B_{eq}^2 + \Gamma^2)\frac{\mathrm{d}z}{\mathrm{d}x}\right] = \alpha^2\left[\alpha^2 B_{eq}^2 + \Gamma^2\right] z \tag{4.8}$$

Though this differential equation is ostensibly the same as Equation 3.6 with the substitutions $\xi \to z$ and $\gamma \to \Gamma$, it is somewhat more complicated. Firstly, because Γ is complex we cannot assume that z is purely real; in fact it most certainly will not be. Second, and more subtly, we cannot immediately identify the region where Equation 4.8 is singular. Previously we had assumed that $\gamma \ll 1$, and therefore Equation 3.6 became singular in the neighborhood where $B_{eq} \to 0$. The equilibrium flow is not, however, required to be small thus Γ can potentially have a large complex part which varies across the domain.

Because Equation 4.8 is manifestly complex we must also allow that the eigenvalue have an imaginary part $\gamma = \gamma_R + i\gamma_I$. Thus to evaluate the singular layers we must first transform to the eigenvalue rest frame. Defining the purely real growth rate $\hat{\gamma} = \gamma_R$ and Doppler shifted equilibrium flow profile $\hat{\omega}_0(x) = \omega_0(x) - \gamma_I$, we write $\hat{\Gamma} = \hat{\gamma} + i\hat{\omega}_0$ and consider the zeros of the complex function $F(x) = \alpha^2 B_{eq}^2 + \hat{\Gamma}^2$. These zeros will, in general, be complex

and so we expand $F(x)$ into its real and imaginary parts.

$$\Re\{F(x)\} = [\alpha B_{eq}(x)]^2 + \hat{\gamma}^2 - [\hat{\omega}_0(x)]^2 \tag{4.9}$$

$$\Im\{F(x)\} = 2\hat{\gamma}\hat{\omega}_0(x) \tag{4.10}$$

We assume that the instability is slowly growing compared to Alfvénic timescale such that $\hat{\gamma} \ll 1$. Furthermore, we will bound the magnitude of the equilibrium flow such that $\max|\hat{\omega}_0(x)| \lesssim O(1)$, which implies the physical restriction that the maximum flow is, at most, on the order of the maximum MHD mode in-plane propagation speed. These two assumptions force $\Im\{F(x)\} \sim \hat{\gamma} \ll 1$ across the entire domain, so that we need only evaluate the real expression.

Thus far we have only restricted the equilibrium flow profile to being sheared in x and bounded by the in-plane Alfvén speed. The case of symmetric profiles has been examined by Ofman in Ref. [38]. If the flow shear is not very large anywhere in the domain then the analysis is essentially the static solution of Chapter 3 convected with the equilibrium flow at the zeros of the in-plane magnetic field, i.e. $\gamma_I \approx \omega_0(\pm x_s)$. When the flow shear is strong near $x = \pm x_s$ the internal layer is disrupted and the DTM growth rate decreases. The velocity gradient needed for this stabilization is, however, close to the threshold for the Kelvin-Helmholtz instability. Therefore symmetric flow is not a particularly efficient or desirable method to slow DTM growth.

Antisymmetric flow profiles, such as that in Fig. 4-1, are somewhat more complicated to analyze because there is no frame where $\hat{\omega}_0(x_s) = \hat{\omega}_0(-x_s) = 0$. The analytic theory in this system has not, to the authors' knowledge, been completed. In the remainder of this chapter we will report our current work on classifying and constraining the outer region ideal MHD eigenmode solutions, then use simulation studies to predict the remaining theory. We will constrain the equilibrium flow profile $\omega_0(x)$ to be antisymmetric about $x = 0$ such that $\omega_0(-x) = -\omega_0(x)$. Unlike Ref. [38] this system will have no frame in which the flow is

stationary around both field reversal points at $x = \pm x_s$, thus we do not expect to be able to Doppler shift it away in all cases.

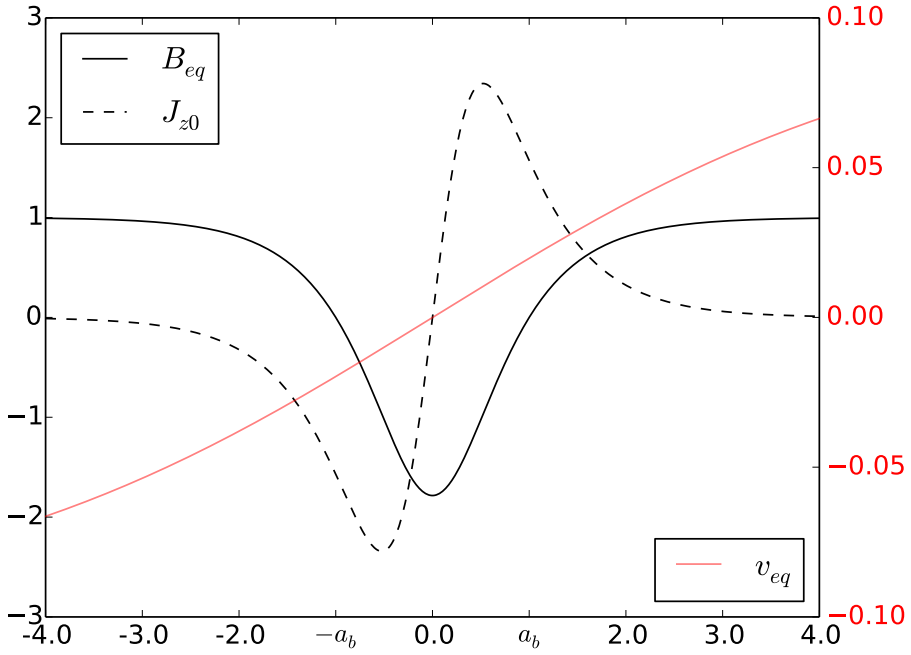

Figure 4-1: An example of an antisymmetric shear flow profile of the form $V_y = v_0 \tanh(\kappa x)$. This particular profile, with $\kappa = 2$, results in a flow difference of $\Delta\omega_0 = k_y[V_y(x_s) - V_y(-x_s)] = 0.2$ between the two zeros of the sech magnetic field at $x = \pm x_s$.

The simplest ordering to consider is that of very weak flow, $|\omega_0(x)| \ll \gamma \; \forall \; x$. In this case two tearing-like singularities are evident in the lab frame where $B_{eq} \to 0$, i.e. $x = \pm x_s$, as shown schematically in Figure 4-2a. We expect, therefore, the eigenmode to be stationary in the lab frame and resemble the static analysis of Chapter 3 with the 'sheared eigenvalue' Γ being dominantly real with a small imaginary perturbation. Provided that $\Im\{\Gamma\}/\Re\{\Gamma\} \ll 1$ this perturbation will result in higher order complex corrections within the tearing layers but not significantly change the analysis. This is the simplest case, and we will not consider it further here.

The second class of singularity to consider is the opposite limit of large amplitude equilibrium flow across the domain such that $\omega_0(\pm x_s) \gg \gamma$. In the lab frame the points $x = \pm x_s$ are not singular, thus there cannot be stationary tearing layers. Instead let us assume an

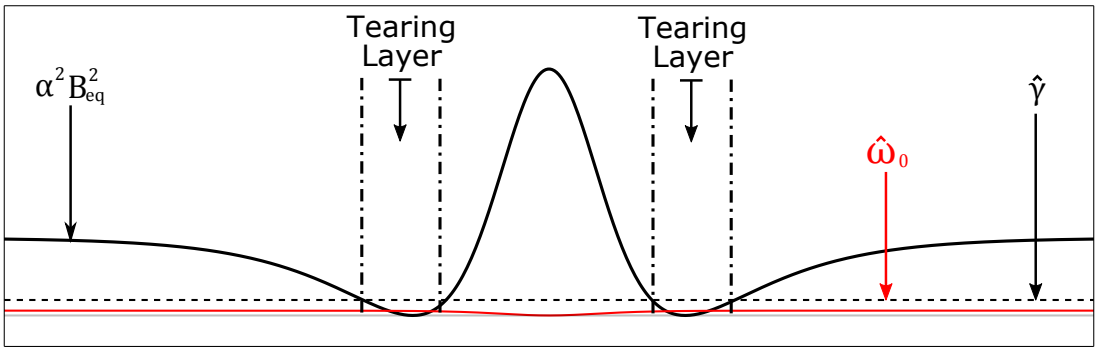

(a) When $|\omega_0(x)| \ll \gamma \; \forall \; x$ the singular layers occur at their normal DTM locations in the lab frame near zeros of the in plane field. The lab frame is pictured in this sketch.

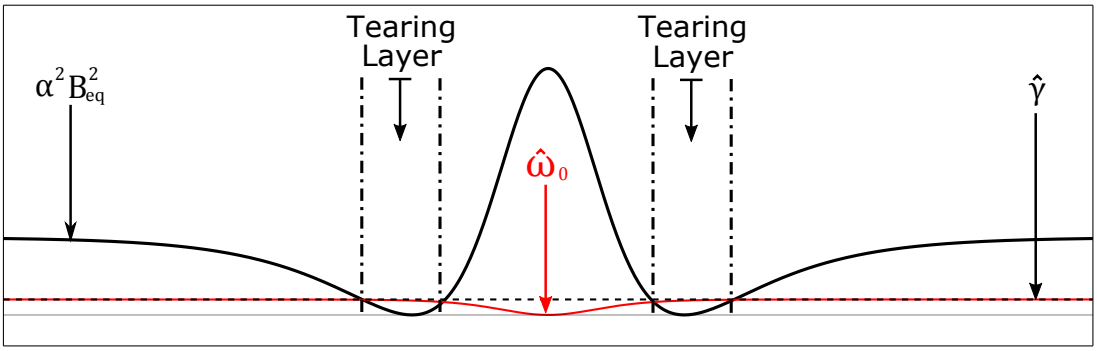

(b) When $|\omega_0(\pm x_s)| \approx \gamma \ll 1$ the singularities in the pictured lab frame occur near the usual DTM locations but include the effect of both the real γ_R and imaginary ω_0. This singularity structure is associated with the decoupling point of the DTM.

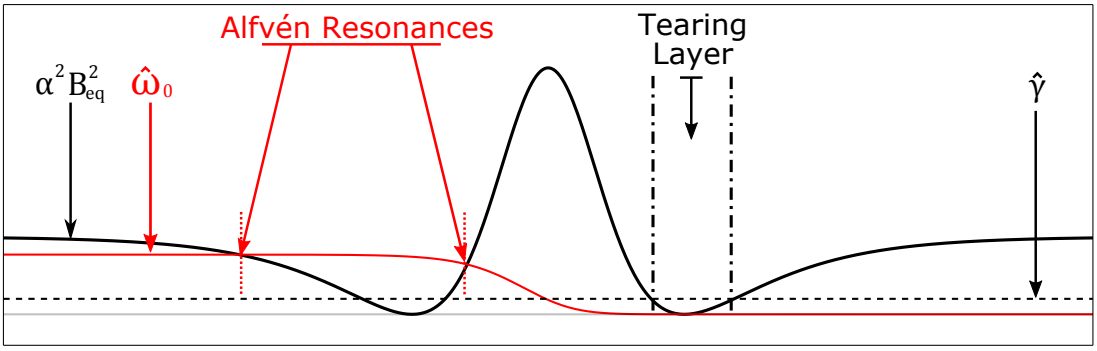

(c) When $|\omega_0(\pm x_s)| \gg \gamma$ no singularities are evident in the lab frame. This sketch instead shows a frame moving with the equilibrium flow $\omega_0(+x_s)$, where a tearing-type singularity emerges at $x = x_s$. No such singularity emerges at $x = -x_s$, however. Instead Alfvén resonance layers appear where $\alpha^2 B_{eq}^2 - \hat{\omega}_0^2 = 0$

Figure 4-2: Schematic diagrams of the three classes of singularities evident in the DTM ideal MHD equations in the presence of equilibrium sheared flow. Lines represent the relative magnitudes of the three contributions in Eqn. 4.9: the positive contributions from growth rate ($\hat{\gamma}^2$) and equilibrium magnetic field ($\alpha^2 B_{eq}^2$), and the negative contribution from sheared flow ($\hat{\omega}_0^2$). Singularities occur when the contributions add to be nearly zero.

eigenmode drifting at $\gamma_I = \omega_0(+x_s)$, so that in the eigenmode frame there is a standard tearing-like singularity at $x = +x_s$ where $\hat{\omega}_0(x_s) \to 0$, $B_{eq}(x_s) \to 0$, and $\hat{\gamma} \ll 1$. The various contributions to $\Re\{F(x)\}$ in this moving frame are sketched in Figure 4-2c. In this frame Equation 4.9 is not zero at $x = -x_s$ as $\hat{\omega}_0(-x_s) = -2\omega_0(x_s) \gg \gamma$, and we cannot expected a simple Doppler shifted DTM solution. It is, in fact, possible that the singularity at $x = x_s$ is the only one in this frame so that the eigenmode should behave like a single-tearing mode, albeit with a complicated outer region solution.

The more interesting case, however, is when the flow profile allows points of $\alpha^2 B_{eq}^2 \approx \hat{\omega}_0^2$. These singular layers are fundamentally 'Alfvén resonances' [40] and result in current singularities which can interact with the tearing layer around $x = x_s$. One might postulate, therefore, the appearance of two growing eigenmodes: one which resembles a tearing layer at $x = x_s$ propagating in the $\omega_0(x_s)$ frame and coupling to Alfén resonance layers somewhere in the $x < 0$ half of the domain; and a second tearing mode at $x = -x_s$ moving with $\omega_0(-x_s)$ and coupling to singularities in the $x > 0$ half. Recent computational studies have show this prediction is, to lowest order, correct [37]. Depending on the location of the Alvfén resonances their interaction with the tearing layer can either strengthen or weaken the instability. Linearly this type of eigenmode may have growth rates as fast or faster than the standard static double-tearing mode, which consists of two coupled reconnecting surfaces. Nonlinearly, however, Afvén resonance layers do not produce the magnetic structure needed for explosive growth and may result in stabilization [54]. The equilibrium flow profiles necessary for these structures to appear are often close to the threshold for shear-flow driven instabilities such as Kelvin-Helmholtz [37, 38, 48], and as such present their own complications. We are motivated, therefore, to find other stabilization mechanisms.

There is a clear disconnect between the global eigenmode solutions for the two classes of singularity we have discussed thus far. When $\hat{\omega}_0 \ll \hat{\gamma}$ we claimed solutions should be approximately the static eigenfunctions where the two available degrees of freedom result in a pair of even and odd global modes each with two reconnecting layers. In contrast

the opposite ordering of $\hat{\gamma} \ll \hat{\omega}_0$ produces (in the antisymmetric flow case) two modes with opposite drifts and one reconnecting layer. There must, therefore, be some transition between these two general forms. We will argue in the remainder of this chapter that this transitional behavior is associated with the third class of ideal MHD singularities.

Consider the intermediate case where $|\omega_0(\pm x_s)| \approx \gamma \ll 1$. This limit is similar to that of the standard DTM in that $F(x)$ still approaches zero in the lab frame near $x = \pm x_s$ where $B_{eq}(\pm x_s) \to 0$, shown schematically in Figure 4-2b. The 'sheared eigenvalue' $\Gamma = \gamma + i\omega_0(x)$ is, however, manifestly complex near the tearing layers, so we cannot reasonably expect the static boundary layer analysis to hold as it did in the weak flow case. Neither can we follow the strong flow case and transform to a frame where the singularity at one surface becomes that of a standard tearing mode and the other vanishes. Instead this singularity represents some sort of intermediate regime where the sheared displacement z is manifestly complex with boundary layers near $x = \pm x_s$. If, however, we assume that the eigenmode is static in the lab frame ($\gamma = \gamma_R$) then we can postulate a general outline for the analysis.

For a static mode we can take $\Gamma^2 = (\gamma_R + i\omega_0(x))^2 \to 0$ far away from the singular layers, giving an ODE for the ideal MHD outer region.

$$\frac{\mathrm{d}}{\mathrm{d}x}\left[B_{eq}^2 \frac{\mathrm{d}z}{\mathrm{d}x}\right] = \alpha^2 B_{eq}^2 z \tag{4.11}$$

This equation is fundamentally the same as the one found for the static mode in Chapter 3 with the substitution $\xi \to z$, thus we expect the same outer region symmetric and anti-symmetric solutions expanded in powers of α or $\alpha^2 x_s^2$. These must then be matched to the interior layers at $x = \pm x_s$. Consider the ideal MHD layers where $B_{eq}(x) \approx \pm B_0' (x \mp x_s)$ but we continue to ignore resistivity ($S^{-1} \to 0$). If these layers are sufficiently narrow and the equilibrium flow profile is not steeply sheared then we can expand $\omega_0(x) \approx \pm\omega_0(x_s)$ and

treat the 'sheared eigenvalue' as a constant within them:

$$\begin{aligned}\Gamma(x \to \pm x_s) &\approx \gamma_R \pm i\omega_0(x_s) \\ &\simeq \Gamma_\pm\end{aligned} \tag{4.12}$$

We can immediately see a deviation from the standard analysis. The real part of Γ is symmetric at the two singular layers whereas the imaginary part is antisymmetric. Thus for the intermediate flow region we should not expect eigenmodes to be either purely symmetric or antisymmetric, but rather some linear combination of the two.

It is currently unclear how to solve the ideal MHD layer for complex $\Gamma_\pm$, much less the resistive layer described by Equations 4.1 and 4.2. As such, we cannot carry this analysis further. This cursory examination has, however, provided several predictions as to the behavior of the double-tearing mode in the presence of antisymmetric sheared flow. We identified three different classes of singularities based of the ordering of the mode growth rate γ_R and flow amplitude ω_0. In the simplest case, when the equilibrium flow is negligible, we find singularities in the lab frame of the standard DTM type and therefore expect growing modes of the even and odd forms discussed in Chapter 3. When the plasma flow is very strong, in contrast, we observed no tearing-like singularities in the lab frame. Transforming into a frame moving with the plasma at a given zero of the in-plane magnetic field allowed us to recover a tearing layer there, but also allowed the emergence of a new class of 'Alfvén resonance' layer elsewhere in the domain. The proposed eigenmodes in these two limits have very different characteristics, and we postulated that the transition between the two forms may occur somewhere in the region where $\gamma \approx \omega_0$ and the ideal MHD outer region is manifestly complex.

Let us pause for a moment to consider the implications of these predictions in our broader discussion of the double-tearing mode, and to specifically prescribe our goals in examining these shear flow effects. The coupling between the two reconnecting surfaces of the double-tearing mode cause it to be strongly driven and weakly dependent on resistivity, even when

the magnetic shear is not large. This analysis of the singularity structure of the sheared DTM raises the possibility that by applying an equilibrium drift we can split the eigenmodes such that we produce two oppositely traveling reconnecting layers. Linearly these two eigenmodes cannot interact, thus we will have removed the coupling and potentially weakened the DTM. Going forward our goal will be twofold: first we will confirm the analysis given thus far and show that the transformation from displacement ξ to 'sheared displacement' $z = \xi/\Gamma$ is correct; second we will numerically examine the transition from coupled DTM to drifting uncoupled STM. This transition will be particularly important in later chapters when we replace the equilibrium flow with the two fluid diamagnetic drift effect.

4.2 Numerical behavior of the sheared DTM

Several recent works have performed simulation studies of double-tearing modes in the presence of shear flow, though the focus has largely been on the utility of Alfvén resonance layers nonlinearly [48, 54, 57]. In this section we will build on one of the few linear studies by Mao et al. [37] in which they have used both initial value simulations and an eigensolver to map the behavior of a slab DTM with various amplitudes of sheared flow profiles. Although our equilibria will be similar to theirs, we will focus our investigation primarily on confirming the analytic discussion of the previous section and informing its possible continuation. Ref. [37] focuses largely on strong flow effects such as the Alfvén resonance and Kelvin-Helmholtz instability, which are the best candidates for nonlinear stabilization in the purely resistive regime. Outside of verifying the emergence of these high shear effects in our linearized `MRC-3d` simulations we will focus primarily on the intermediate flow regime, specifically on understanding the transition of the sheared DTM from 'coupled' to 'decoupled' behavior. It is this small (compared to Alfvén speeds) amplitude domain of parameter space which will be most applicable to our coming diamagnetic drift investigations.

4.2.1 Equilibrium and analysis methods

As our basic magnetic equilibrium we choose to use the sech reconnecting field profile (Section 2.3) in the same configurations as our examination of the static DTM in Chapter 3.2. The magnetic shear at the tearing surfaces $x = \pm x_s$ is set at $\partial_x B_y(\pm x_s) = \pm\pi/2$ and the out-of-plane guide field is again be $B_{z0} = 10$, so that the compressible `MRC-3d` model is in the incompressible reduced MHD limit. In addition to the magnetic configuration we must also specify a profile for the equilibrium flow, which we take to be antisymmetric and parallel to the reconnecting field.

$$U_y(x) = v_0 \tanh(\kappa x) \tag{4.13}$$

Similar to Ref. [37] we fix $\kappa = 2$ and vary the amplitude v_0 to scale the shear. With these choices the native `MRC-3d` normalization is the same as that used for for the above analysis, so that we can take $a_b \approx \tau_A \approx 1$ for simplicity. Therefore the equilibrium drift is $\omega_0(x) = k_y U_y(x)$. An example of this flow profile is shown together with the magnetic field and current in Figure 4-1.

In Section 4.1 we showed that the appearance of singular layers depends on the frame in which the Doppler shifted eigenvalue $\hat{\gamma}$ and background flow $\hat{\omega}_0$ are considered. We hypothesized that if the growth rate is not purely real (i.e. if $\gamma_I \neq 0$ in the lab frame) then the eigenmodes will resemble single tearing modes convected in opposite directions with the equilibrium flow at the surfaces $x = \pm x_s$. If this is true then in the frame of the tearing layer at $x = x_s$ the appearance of a singularity at the $x = -x_s$ surface will be determined by $\hat{\omega}_0(-x_s) = (\omega_0(-x_s) - \omega_0(x_s))$, and visa-versa. Thus the behavior of the eigenmodes should be determined by the difference between the equilibrium flow at the two zeros of the in-plane magnetic field.

$$\Delta\omega_0 = \omega_0(x_s) - \omega_0(-x_s) \tag{4.14}$$

Pursuant to this presumption we will not set the amplitude of the flow v_0 directly, but rather set it from a specified value for $\Delta\omega_0$. Simulation results will also be presented in this fashion.

The analysis of Section 4.1 predicted that the type and effect of singular layers would change based on the magnitude of the equilibrium flow. Choosing the same separations of $x_s = 0.25, 1.0$ that we used in Chapter 3 allows us to compare the sheared flow cases to the better understood static regime. We set the resistivity at a relatively high value $\eta = 1 \times 10^{-4}$ for stability and computing cost reasons. The values of the growth rate γ_R are fitted from diagnostic output in much the same fashion as for the static system (Section 3.2). Calculating the imaginary part of the eigenvalue γ_I involves processing the full time-series output using a discrete Fourier transform. This method is computationally intensive and requires long simulations with a high output cadence in order to ensure both that the frequency resolution is high enough to distinguish different modes and that the Nyquist frequency of the DFT is well above γ_I. To mitigate the storage and run-time cost we only calculate γ_I for a subsample of $\Delta\omega_0$ values. Errors in the extracted frequencies are estimated by taking the larger value of the DFT resolution and fitted width of maximum amplitude γ_I peaks.

4.2.2 Numerical results

In Figure 4-3 we show the resulting values of the growth rate γ_R and oscillation frequency γ_I for increasing values of $\Delta\omega_0$ in $x_s = 1.0$ and $x_s = 0.25$ magnetic fields. For both separations the simulation results confirm one of our analytic predictions: when $\Delta\omega_0 \gg \gamma_R$ the imaginary part of the eigenvalue will be determined by the equilibrium flow at the two zeros of the in-plane field, i.e. $\gamma_I \approx \pm\omega_0(\pm x_s) = \pm\Delta\omega_0/2$. We would also expect, therefore, the appearance of Alfvén resonance layers coupled to single tearing layers. Comparison of the static $x_s = 1.0$ DTM eigenmode (provided for reference in Figure 4-4) to drifting eigenmodes confirms this prediction. Figure 4-5 shows two modes extracted via DFT from a simulation run with $\Delta\omega_0 = 0.2$. The two modes are drifting in opposite directions with $\gamma_I = \pm(0.1010 \pm 0.0034)$, which is equal to the predicted $\gamma_I = \pm 0.1$ within the DFT error.

Furthermore, the positive frequency mode exhibits a tearing-like structure in ψ surrounding the $x = +1$ surface, and likewise for the negative frequency mode and $x = -1$ surface. Examining the out-of-plane current J_z shows a strong, narrow structure at the tearing surface and two smaller peaks in the neighborhood of the opposite zero of the magnetic field. Mao et al. [37] found very similar results using a combination of eigensolver and initial value codes and determined that these secondary peaks match Alfvén resonance layers. Their proximity to and interaction with the tearing layer generates the increase in γ_R near $\Delta\omega_0 = 0.5$ shown in Figure 4-3a. This high flow regime is not particularly relevant to the diamagnetic drift mechanism which is the final purpose of this work, and is covered extensively in Ref. [37]. We consider it here only as a verification of the singularity analysis given in Section 4.1. The more tightly coupled $x_s = 0.25$ modes exhibit very similar behavior and structures, with the additional complication that γ_R increases sharply above $\Delta\omega_0 \approx 0.3$ due to the emergence of the Kelvin-Helmoltz instability at strong flow shear, which then dominates over the tearing mode behavior [37, 38, 48].

Figures 4-3b and 4-3a both show an initial drop in growth rate from the static case followed by an extended period where increasing the equilibrium flow amplitude seems only to impact γ_I. Mao et al. [37] argue that this is the region of $\Delta\omega_0$ where the Alvfén resonance points are not sufficiently close to the tearing-like layers to drive or interfere with them. As we are primarily interested in stabilization mechanisms, this flat region is not of great interest at present. The small flow regime, however, where the growth rate decreases from the static value will prove to be of vital importance. In Figure 4-6 we plot the behavior of γ_R and γ_I for $x_s = 0.25, 1.0$ in the small amplitude region using smaller steps of $\Delta\omega_0$. We are now well positioned to answer the question posed at the end of Section 4.1: How does the sheared DTM transition from a static ($\gamma_I = 0$) eigenmode with two coupled tearing surfaces into two oppositely drifting eigenmodes with one tearing surface each? It is immediately clear from these simulation results that the coupled, static mode undergoes a smooth decrease in γ_R with increasing $\Delta\omega_0$ until some critical value is reached, at which point the system transitions

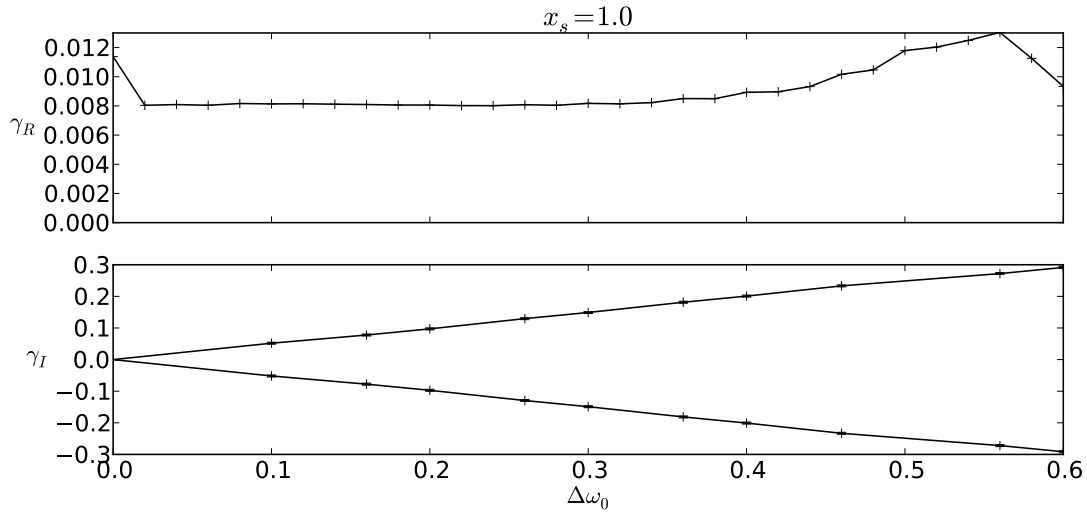

(a) Dependence of the $x_s = 1.0$ DTM growth rate γ_R and drift frequency γ_I on the equilibrium flow difference between the zeros of the magnetic field $\Delta\omega_0 = \omega_0(+x_s) - \omega_0(-x_s)$. After an initial decrease in growth at low flow amplitudes, γ_R is unaffected by increasing $\Delta\omega_0$ until Alfvén resonance interactions become significant. The drift frequencies are equal to $\gamma_I = \omega_0(\pm x_s) = \Delta\omega_0/2$ to within DFT frequency resolution. Error bars on γ_R and γ_I are too small to be observed in this plot.

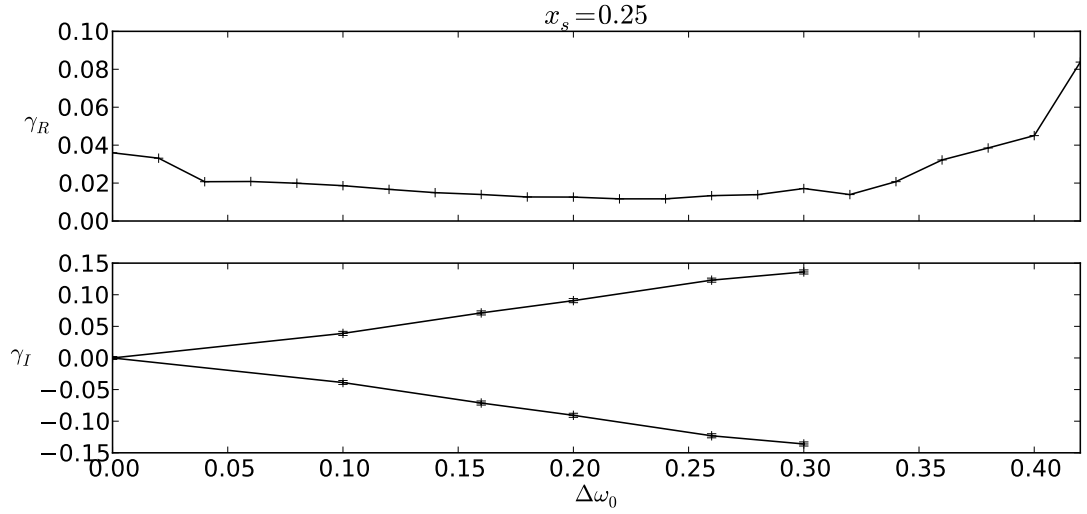

(b) Dependence of the $x_s = 0.25$ DTM growth rate γ_R and drift frequency γ_I on the equilibrium flow difference between the zeros of the magnetic field $\Delta\omega_0 = \omega_0(+x_s) - \omega_0(-x_s)$. Above $\Delta\omega_0 \approx 0.3$ the equilibrium becomes unstable to the shear-flow driven Kelvin-Helmholtz instability and γ_R increases dramatically. Below this amplitude the drift frequencies are equal to $\gamma_I = \omega_0(\pm x_s) = \Delta\omega_0/2$ to within DFT frequency resolution. Error bars on γ_R and γ_I are too small to be observed in this plot.

Figure 4-3: Behavior of the complex eigenvalue $\gamma = \gamma_R + i\gamma_I$ with changes in shear flow amplitude $\Delta\omega_0$ for $x_s = 1.0$ and $x_s = 0.25$ DTMs. All data is obtained with resistivity $\eta = 1e-4$ and wave number $\alpha = k = 0.5$

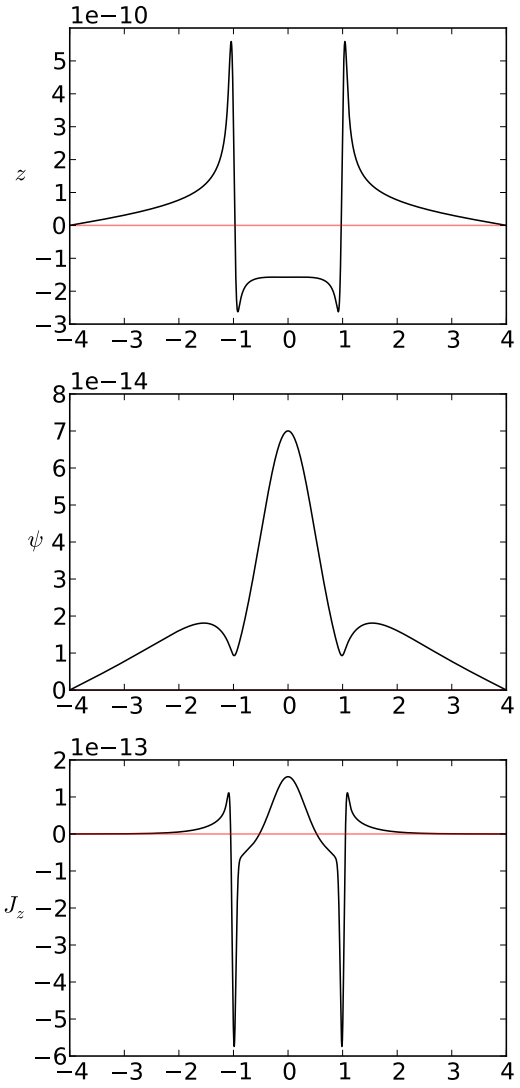

Figure 4-4: An example of the static ($\Delta\omega_0 = 0$), even, $\eta = 1 \times 10^{-4}$ DTM with separation $x_s = 1.0$. The sheared displacement $z = \xi/\Gamma$ is, in this case, merely a rescaling of the standard plasma displacement by $\Gamma = \gamma_R$. z, perturbed magnetic flux ψ, and perturbed out-of-plane current J_z are all symmetric and purely real (black lines), and thus imaginary parts (red lines) are zero.

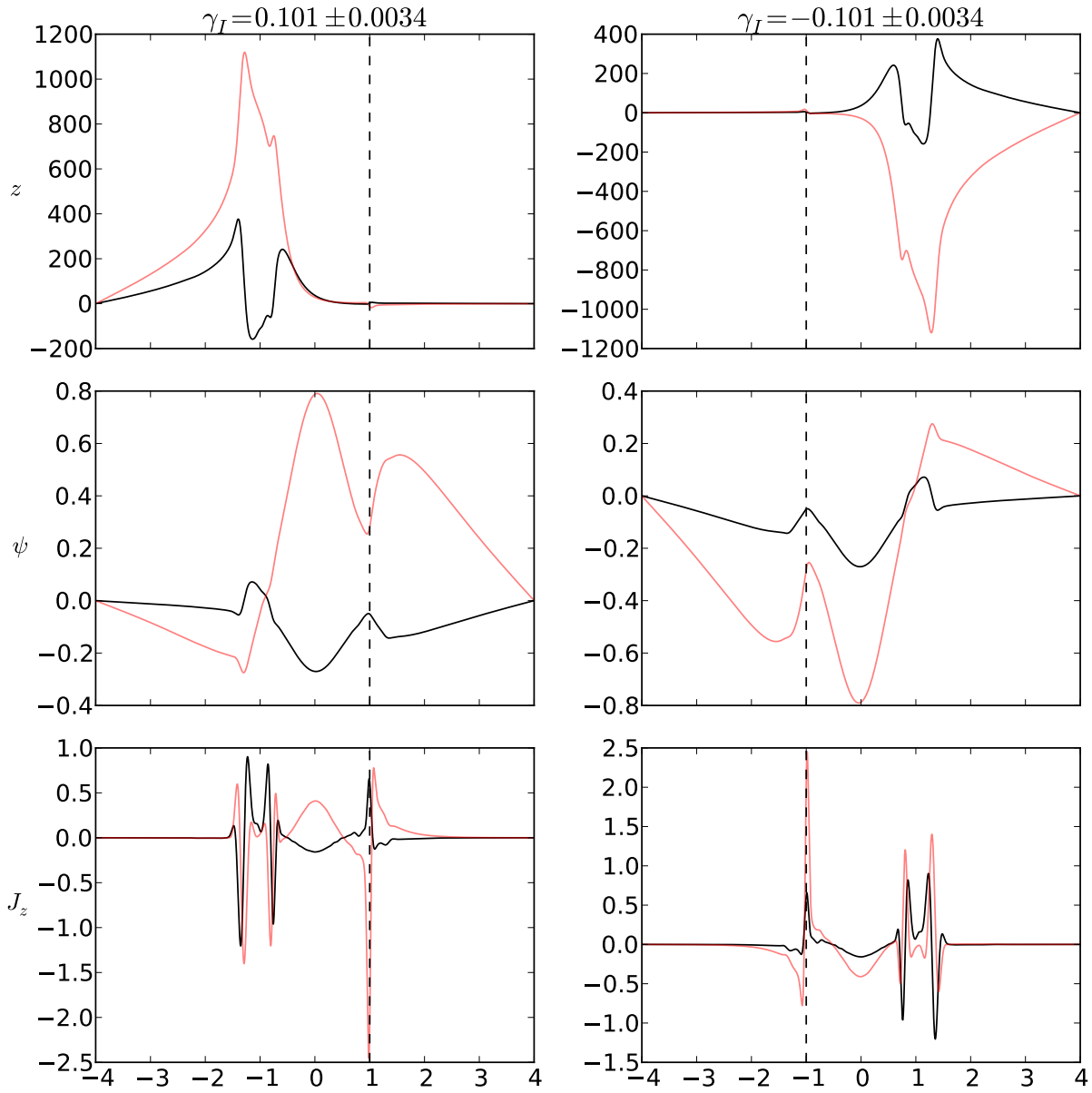

Figure 4-5: Examples of drifting, $x_s = 1.0$, $\eta = 1 \times 10^{-4}$ eigenmodes obtained via DFT from a simulation with $\Delta\omega_0 = 0.2$. Real parts of the sheared displacement z, perturbed magnetic flux ψ and out-of-plane current J_z are shown in black, imaginary parts in red. The measure drift frequencies $\gamma_I = \pm 0.1010$ are equal to the equilibrium flow at the $x = \pm x_s$ surfaces of $\omega_0(\pm x_s) = \pm 0.1$ to within the DFT error of ± 0.0034. The flux function of the positive frequency mode resembles a standard tearing mode near the $x = +x_s$ surface, and likewise for the negative frequency mode (vertical dashed lines). J_z shows the appearance of smaller Alfvén resonance current layers for each mode in addition to the tearing layer.

to the drifting states. Merely counting the number of observed eigenmodes before and after this transition reveals that our simulation results are incomplete: we are only able to resolve one type of eigenmode when $0 < \Delta\omega_0 \leq \Delta\omega_0^c$, and two after. The study of Ref. [37] using an eigensolver code demonstrates that this is a limitation of initial value methods such as `MRC-3d`. In general the fastest growing mode will dominate the simulation and thus we lose the second type of sheared DTM. The slower mode emerges from the antisymmetric static solution and the faster from the symmetric [37], therefore using our preliminary simulations from Chapter 3.3 we are able to estimate the lower branch using the static odd mode growth rate. This prediction (sketched in red on Figures 4-6a and 4-6b) cannot be verified without the use of an eigensolver code.

The observed behavior of the growth rate γ_R and mode drift γ_I strongly suggests some form of bifurcation associated with increasing flow amplitude $\Delta\omega_0$. Furthermore, we note that for both $x_s = 1.0$ and $x_s = 0.25$ this transition occurs when $\Delta\omega_0 = O(\gamma_R)$, which corresponds to the third class of singular layer we identified in Section 4.1. We also argued that in this regime the eigenmodes could not be purely even or odd. Because the equilibrium flow causes the imaginary part of the 'sheared eigenvalue' Γ to be antisymmetric across the domain we expect some mixture of the two DTM parities. To confirm this prediction we examine the magnetic flux ψ and 'sheared displacement' z for two different values of $0 < \Delta\omega_0 < \Delta\omega_0^c \approx 0.0066$ using the $x_s = 1.0$ magnetic equilibrium. Figure 4-7a is well below the decoupling threshold with $\Delta\omega_0 = 0.004$, and Figure 4-7b is just below with $\Delta\omega_0 = 0.0065$. In both cases we have seeded the simulation with an initial perturbation in ψ which is purely real and symmetric, and the real and imaginary parts of the resultant eigenmodes are shown in black and red respectively.

We first note that we have plotted the sheared displacement $z = \xi/\Gamma$ in Figure 4-7 rather than the standard plasma displacement ξ, and that for both $\Delta\omega_0 = 0.004$ and $\Delta\omega_0 = 0.0065$ the real part of z, ψ, and J_z are of same form as the static eigenmode (Figure 4-4). This correspondence is not, in general, true of ξ. The transformation $\xi \to z$ is thus the appropriate

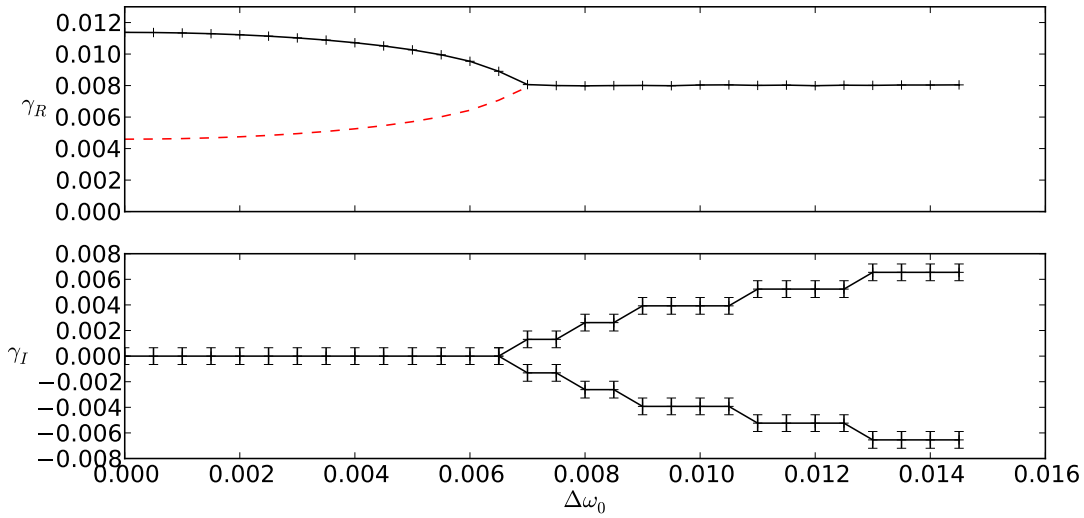

(a) $x_s = 1.0$

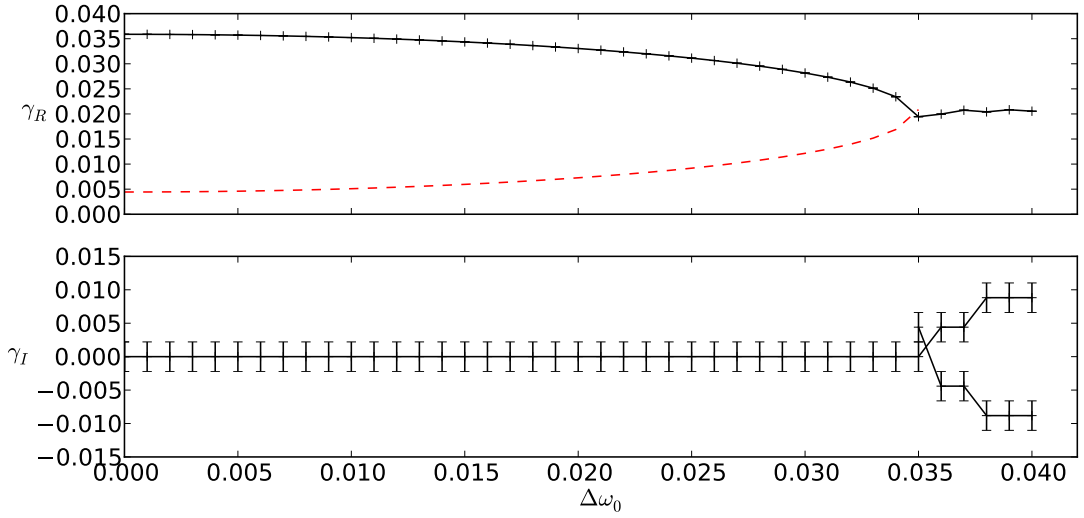

(b) $x_s = 0.25$

Figure 4-6: Behavior of the sheared DTM growth rate γ_R and drift frequency γ_I near the critical decoupling flow $\Delta\omega_0^c$ for separations $x_s = 1.0, 0.25$. Black lines represented data fitted from linear `MRC-3d` simulations. Red dashed lines are predictions of the slower, dominantly antisymmetric mode branch drawn from measurements of the static, odd DTM growth rate and the eigensolver results of Ref. [37]. The transition from opposite parity static coupled modes to isolated drifting modes resembles a pitchfork bifurcation. The critical shear $\Delta\omega_0^c$ is different for the two separations.

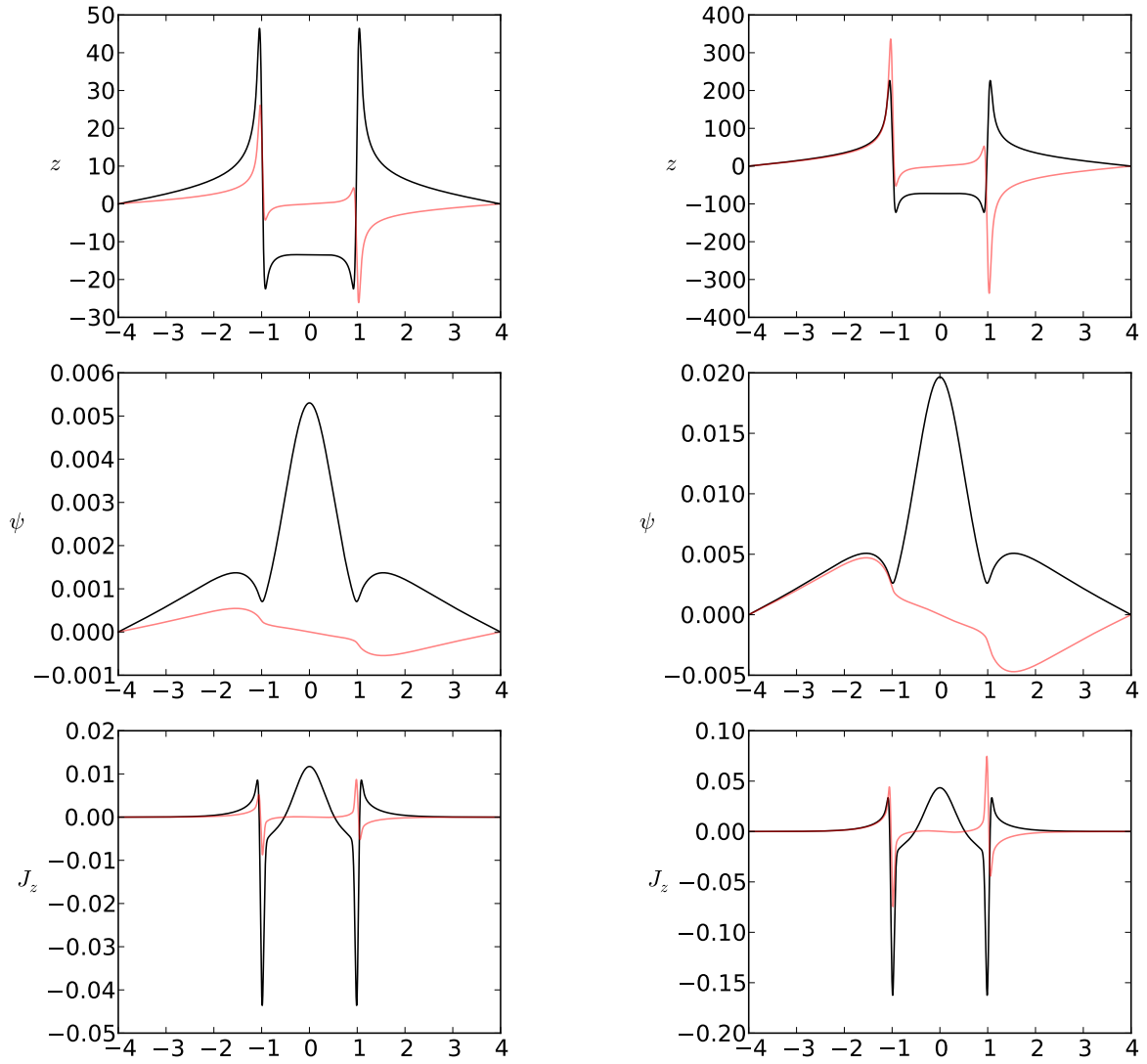

(a) The 'symmetric' branch DTM eigenmode for $x_s = 1.0$ and flow amplitude $\Delta\omega_0 = 0.004$. The real part of the sheared displacement z, perturbed magnetic flux ψ and out-of-plane current J_z are purely symmetric and shown in black. The imaginary parts (red) are antisymmetric and of a smaller amplitude. Both resemble the even and odd solutions for the static DTM.

(b) The 'symmetric' branch DTM eigenmode for $x_s = 1.0$ and flow amplitude $\Delta\omega_0 = 0.0066$, which is just below the decoupling point. The real (black) and imaginary (red) parts of the various components are of approximately the same magnitude, but remain purely even and odd respectively.

Figure 4-7: Examples of DTM eigenmodes for flow amplitudes significantly and marginally below the critical decoupling point $\Delta\omega_0^c$.

means to make contact with the original boundary layer theory of Chapter 3. Furthermore, the imaginary parts of the eigenfunctions are purely antisymmetric and resemble the odd, static DTM (see Figure 3-6). At small amplitude (Fig. 4-7a) the imaginary (odd) part is significantly smaller than the real (even) part. Near the decoupling threshold (Fig. 4-7b), however, they are approximately equal in magnitude. The eigenvalue simulations of Ref. [37] show that the reverse is true for the slower branch originating from the antisymmetric DTM: the odd part of the mode is greater than the even, with the disparity decreasing with proximity to the decoupling flow.

These simulation results present a possible explanation for the effect of antisymmetric equilibrium sheared flow on the DTM, and a possible mechanism to determine the value of $\Delta\omega_0^c$ at which the system bifurcates. Provided that the equilibrium flow is less than or on the order of the mode growth rate ($\Delta\omega_0 \lesssim \gamma_R$) the singular layers of Equation 4.8 occur in the neighborhood of the zeros of the equilibrium field, $B_{eq}(x \to \pm x_s) \to 0$. Then the only allowable solutions for z and ψ in the ideal MHD outer region that include both singular layers are of the same form as the even and odd DTM solutions found in Chapter 3 for ξ and ψ. Thus any static eigenmode with $\gamma_I = 0$ must be a linear combination of these two solutions. The real part of the 'sheared eigenvalue' $\Re\{\Gamma\} = \gamma_R$ is symmetric across the domain whereas $\Im\{\Gamma\} = \omega_0(x)$ is antisymmetric, therefore the real and imaginary parts of the outer region must have opposite parities. The relative magnitudes of the even and odd parts should be related to $\arg\{\Gamma(x = \pm x_s)\}$. We propose that the critical flow $\Delta\omega_0^c$ corresponds to the point at which the eigenmodes on the symmetric and antisymmetric become degenerate, i.e. when the dominantly even DTM has gained a significant enough odd part, and vice versa for the dominantly odd DTM, such they are related by a simple similarity transformation. At this point the system will bifurcate into two oppositely drifting modes with one tearing-type layer each. This decoupling behavior has important consequences for DTM stability, and we will now examine this bifurcation point in more depth.

4.3 Properties of the bifurcation point

If the above explanation of the sheared DTM behavior is correct then there should be a consistent relationship between the growth rate γ_R^c and equilibrium flow amplitude $\Delta\omega_0^c$ at which the modes decouple. Understanding this relationship may give us a better idea how to formulate either a bifurcation theory for the decoupling point or a complete boundary layer analysis of the sheared DTM via Equations 4.7, 4.6, and 4.8. To that end we will attempt to determine scaling of the critical decoupling growth rate and flow amplitude with resistivity η for the $x_s = 0.25, 1.0$ equilibria, thus adjusting the mode growth rate while keeping the form of the outer region solutions fixed.

4.3.1 Bisection search methodology

In order to find the approximate value of $\Delta\omega_0$ at which the sheared DTM behavior changes we exploit the interoperability of `MRC-3d` with the Python programming language. We assume that the appearance of two equal magnitude modes with non-zero drift γ_I is a sufficient indicator that a given $\Delta\omega_0 > \Delta\omega_0^c$. If a discrete Fourier transformation on the output data of a simulation shows that the largest amplitude modes have a non-zero frequency we mark them as being above the critical point. By automating the initialization and analysis of simulations we are able to use a simple bisection method to determine the value of $\Delta\omega_0^c$ for a given x_s and η within the DFT frequency resolution $\delta\omega = 2\pi/t_{max}$. Unfortunately, we cannot run the linearized version of `MRC-3d` to arbitrarily long simulation times. Though the analytic model forces the mode to evolve consistent with the linearizing assumption $\delta f \ll f_{eq}$ even when the magnitude of the state vector is, in reality, much larger than the equilibrium values, floating point precision errors cause the time integration algorithm to not converge and halt the simulation at some finite amplitude. We find the simulation time at which this occurs for the static, $\Delta\omega_0 = 0$ symmetric DTM at a given resistivity and use this as the maximum time for a subsequent sheared simulations at the

same η. Because these sheared growth rate is, for the initially even mode, less than the static γ_R we avoid non-convergence of the time-stepper while minimizing the resultant $\delta\omega$. Likewise we use our hypothesis that the critical decoupling flow is associated with the $\Delta\omega_0 \approx \gamma_R$ class of singular layer to ensure that the simulations output at a high enough cadence such that the Nyquist frequency of the DFT is well above any value of γ_I which we might encounter. In this fashion we are able to design a Python script which automatically sets up, runs, and analyzes linear `MRC-3d` simulations, performing a bisect search in $\Delta\omega_0$ over a range of η to determine the critical values $\Delta\omega_0^c$ and γ_R^c.

4.3.2 Numerical behavior of the decoupling point

The results of our bisection search are shown in Figure 4-8 for the separations $x_s = 1.0$ and $x_s = 0.25$. Two relations are important for our present discussion. The critical flow amplitude required for decoupling ($\Delta\omega_0^c$) is found to be proportional to the growth rate of the even, static ($\Delta\omega_0 = 0$) mode in both cases: $\Delta\omega_0^c = M_s\gamma_R^0$. The constant of proportionality is, however, different between the two separations: $M_{1.0} \approx 0.39$ and $M_{0.25} \approx 1.0$. This finding is primarily useful as a means to predict the necessary decoupling flow for future nonlinear studies. More relevant to understanding the bifurcation behavior is the scaling of the measured growth rate at the point of decoupling γ_R^c as a function of the critical decoupling amplitude $\Delta\omega_0^c$. For both separations the data follows linear scaling (i.e. $\gamma_R^c \propto \Delta\omega_0^c$) as shown by the dashed trend-lines. To understand the behavior of the differential equations near the bifurcation point we fit the constant of proportionality N_s between the decoupling growth rate and flow assuming that $\gamma_R^c = N_s\Delta\omega_0^c$. We find $N_{0.25} = 0.538 \pm 0.008$ for the tightly coupled $x_s = 0.25$ modes and $N_{1.0} = 1.447 \pm 0.007$ for the more weakly interacting surfaces.

It is difficult to draw any definitive conclusions from this limited sampling of the decoupling frequency and our cursory analysis. At most we can state that for a given magnetic field profile there appears to be fixed relationship between the mode growth rate and equilibrium flow amplitude at the decoupling point. This relationship is independent of the resistivity

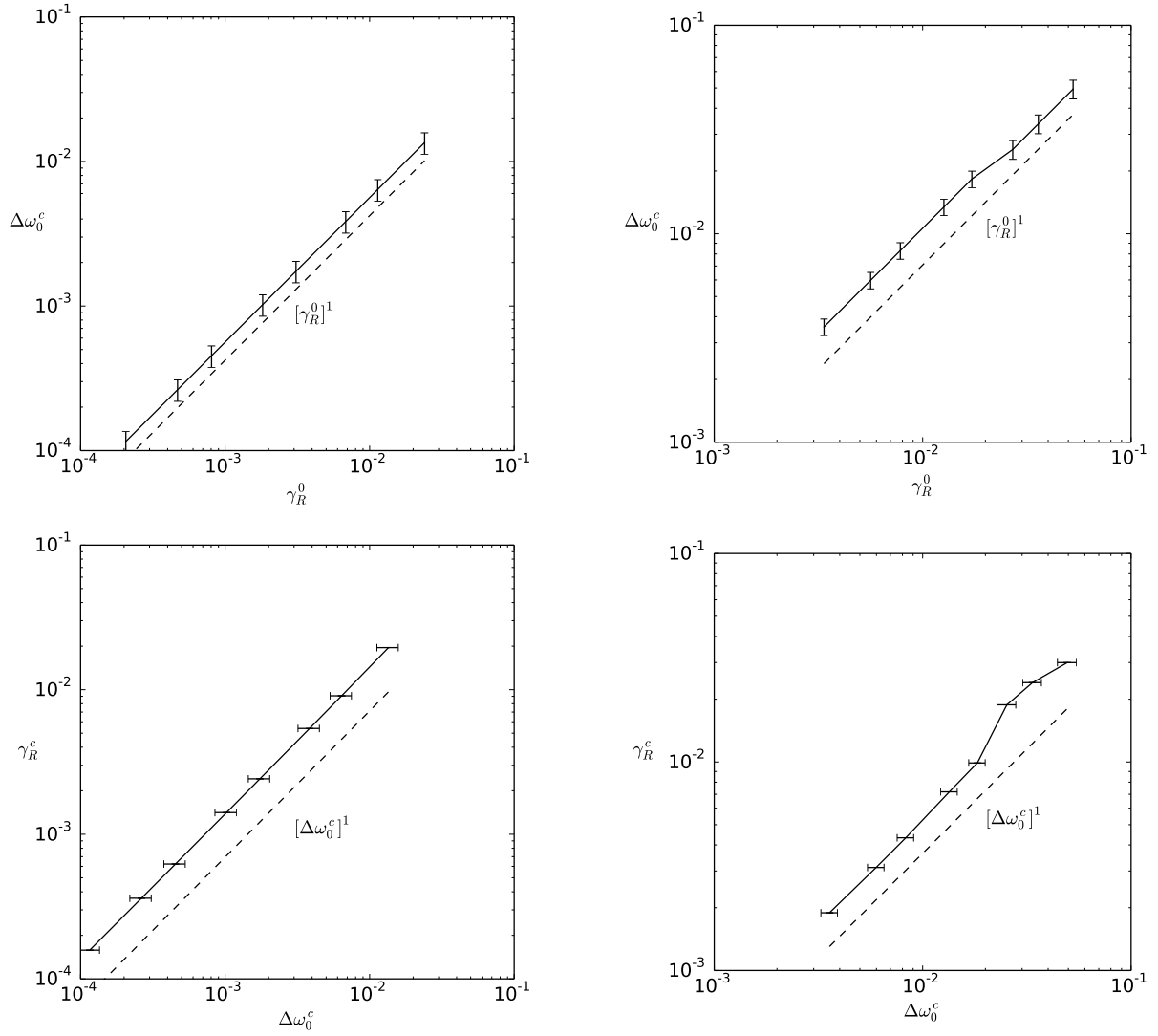

(a) $x_s = 1.0$ **(b)** $x_s = 0.25$

Figure 4-8: Preliminary results from a bisection study of the $x_s = 1.0$ (left) and $x_s = 0.25$ (right) double tearing mode decoupling points. Plotted are the scaling behavior of the critical flow amplitude $\Delta\omega_0^c$ with the maximum (static) symmetric DTM growth rate γ_R^0(top) and relationship of the growth rate at the decoupling point γ_R^c to $\Delta\omega_0^c$ (bottom). In all cases the behavior is approximately a linear relationship, shown by the dashed trend-lines, though the constants of proportionality are different in each instance. At larger growth rates the $x_s = 0.25$ results show significant deviation from the trend, suggesting that in these higher η values the resistive boundary layers are too large for a standard boundary layer analysis to be valid.

(and thus actual measured grown rate) in the simulation. Let us presume, for the moment, that this statement is true, and consider it's implications on the boundary layer analysis we began in Section 4.1. Based on our examination of sheared eigenvalues (Sec. 4.2.2) we proposed the decoupling point is related to the argument of the complex sheared eigenvalue at the tearing surfaces $\Gamma_\pm = \gamma \pm \omega_0(x_s)$. In our numerical study we found that the growth rate and equilibrium sheared flow at the decoupling point are directly proportional, $\gamma_R^c = N_s \Delta\omega_0^c$, with the constant of proportionality N_s that depends on x_s but not η. This behavior suggests that the bifurcation behavior emerges from the ideal MHD regions of the boundary layer theory, and it may not be necessary to solve the resistive layer equations (Eqn. 3.17) for a complex eigenvalue. The linear relationship between γ_R^c and $\Delta\omega_0^c$ also confirms our hypothesis that decoupling depends on the ratio $\Re\{\Gamma_\pm\}/\Im\{\Gamma_\pm\}$, although there is some additional contribution which varies based on the equilibrium field properties.

Ultimately, we expect that to understand the decoupling process we will need to complete the boundary layer analysis at least as far as the ideal MHD layer. In doing so we might find a threshold where the solutions within the layers cannot be matched to the outer regions without a nonzero drift, or the emergence of an additional singularity which results in bifurcation. Completing this task would require, however, first understanding the full antisymmetric DTM solution encountered in Chapter 3 and then considering the internal layer solutions to Equations 4.6 and 4.7. For the purposes of our current work it is sufficient to have determined that, within an order one constant of proportionality, the flow amplitude needed for decoupling is approximately the static, symmetric DTM growth rate. This will allow us to initialize nonlinear simulations that are initially coupled or decoupled and examine their differing evolution.

4.4 Discussion

In Chapter 3 we showed how the coupling between the two singular layers of the double-tearing mode drive each other to produce an instability which depends weakly on resistivity. In later chapters we will observe how nonlinearly this interaction can result in explosive growth and catastrophic disruption. Any mechanism which can interfere with the coupling between the two surfaces should be explored as a useful stabilization mechanism, and the addition of antisymmetric equilibrium sheared flow is our first indication that such a decoupling is possible. We have presented the foundations of a linear theory to describe the various behaviors observed in the sheared DTM including the appearance of Alfvén resonance layers and the changes in eigenmode behavior. Recent work has explored the stabilization properties of Alfvén resonances nonlinearly [48, 54], however these effects require relatively large equilibrium flows or self generated drifts and thus present their own complications. For our coming application of kinetic effects via the diamagnetic drift we are more interested in the apparent bifurcation point at which the eigenmodes transition from global modes spanning both zeros of the magnetic field into drifting single-tearing layers.

In this discussion we have characterized the behavior of the sheared, coupled DTM as a mixing of symmetric and antisymmetric modes in the complex plane. This approach makes explicit the relationship between γ_R^c and $\Delta\omega_0^c$ and will provide the best framework for understanding the bifurcation behavior. An equivalent (and perhaps more physically intuitive) description is to view the linear modes in 2D space. In Figure 4-9 we have plotted the linear, complex, 1D eigenmodes of the flux function ψ from Figs. 4-4, 4-7a, and 4-7b as contours in the $x - y$ plane, as well as an example of the static, odd eigenmode from Chapter 3. The composite sheared eigenmodes on the symmetric DTM branch resemble the static even eigenmode sheared in y between the two surfaces, with the amplitude of this shift increasing with $\Delta\omega_0$. Mao et al. [37] found similar behavior along the antisymmetric branch, and concluded that the decoupling point occurs when the phase shear between the surfaces is the same for the even and odd branches. It may be more natural, in this framework, to

examine the balance between the convective forces that attempt to drag the singular surfaces along with the equilibrium flow and the coupling forces that keep them locked together, and to derive some relation for the maximum shear Θ^c. It should be clear, however, that this view of sheared 2D eigenmodes is entirely equivalent to the approach we have taken above, which relates the bifurcation of the mode to the argument of the complex sheared eigenvalue Γ. The primary difference between these conceptualizations is that they lend themselves more readily to different analysis frameworks.

Ultimately our analysis of the influence of equilibrium sheared flow on the linear DTM is not our end in and of itself, but rather a means to understand processes we will see when kinetic effects are introduced. Once the critical shear is achieved and the surfaces are decoupled, further increases in $\Delta\omega_0$ do not have any effect until flows large enough to produce Alfvén resonance coupling are present. As we will see in the next chapter, diamagnetic drifts are able to produce this same decoupling. They will also continue to slow the growth past the bifurcation point, which results in them being a much more effective stabilization mechanism.

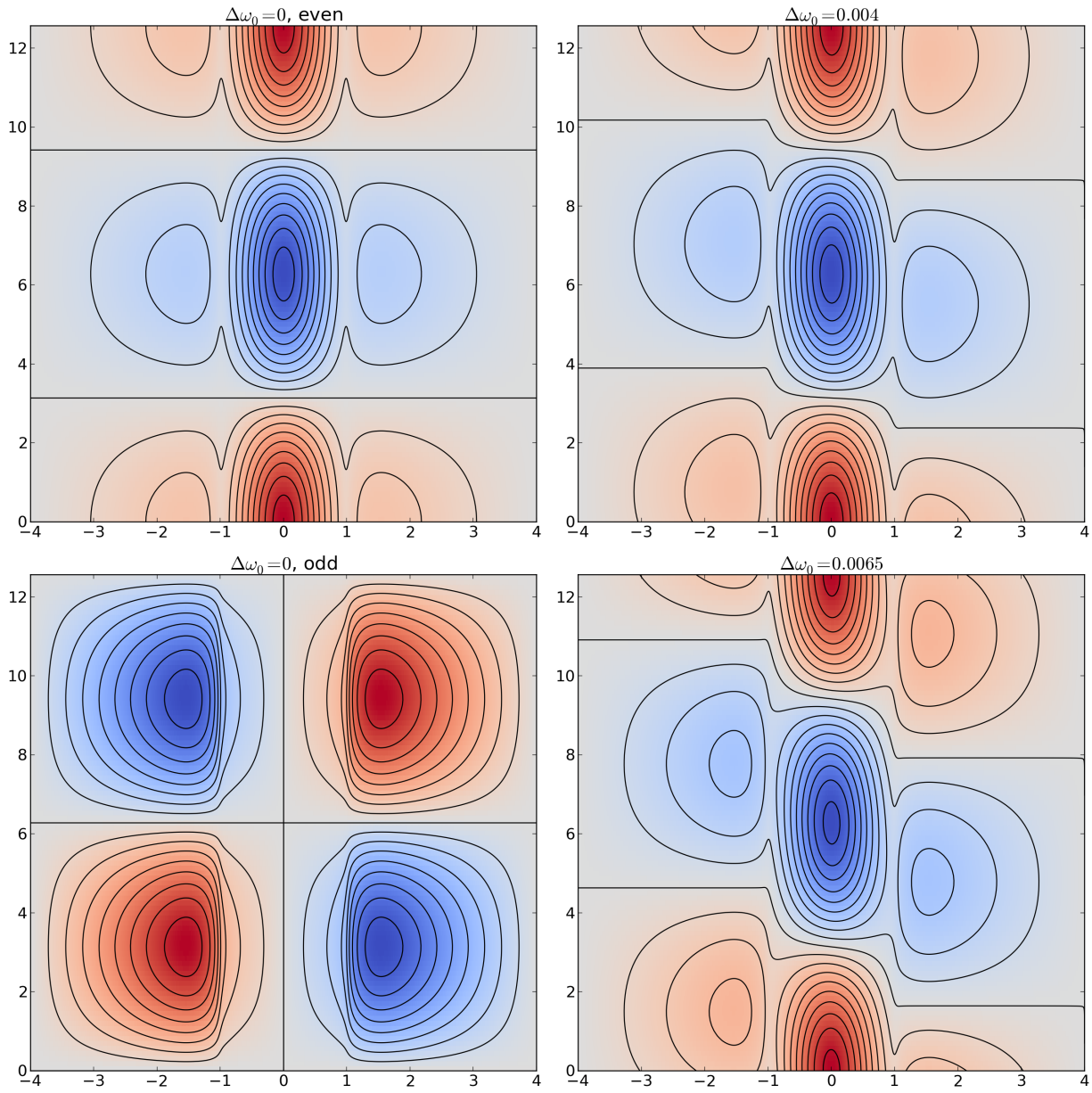

Figure 4-9: Projection of the ψ component of the 1D linear eigenmodes plotted in figs. 4-4, 4-7a, and 4-7b onto the 2D plane, as well as an equivalent static odd DTM at the same resistivity $\eta = 1 \times 10^{-4}$ and separation $x_s = 1.0$. The static DTM appears to be sheared between the two tearing surfaces, with this effect increasing at higher $\Delta\omega_0$.

Chapter 5

FLR effects on the linear DTM

The simplest means to reintroduce some kinetic plasma behavior to the resistive MHD model is to keep the d_i scale contributions in the generalized Ohm's law (Eqn. 1.15), which are the Hall and electron pressure gradient terms. In terms of physical ordering this corresponds to the first order term of an expansion in the electron-ion mass ration m_e/m_i, and can be conceptualized as allowing the ions to have a small, finite mass while the electrons remain massless. As a consequence, the ions have a finite gyro-radius in the presence of a magnetic field, leading to the common name 'Finite Larmor Radius' (FLR) effects.

This closer approximation to the true kinetic model allows for physical processes which are excluded from the standard MHD model. For example, in ideal MHD the wave behavior is dominated by the Alvén wave dispersion relation at all values of the wave number k and frequency ω. FLR effects allow the emergence of the whistler wave branch of the dispersion relation, although this branch continues as $k, \omega \to \infty$ rather than saturating at the electron-cyclotron resonance. Electron resonance behavior requires finite electron mass, which is excluded from the Hall MHD description. This partial step towards kinetic physics is, however, enough to introduce two new processes critical to accurate reconnection modeling. Firstly, if the characteristic scale of ion motions is larger than the reconnecting current layer, the ion fluid cannot participate in the reconnection process. In systems without an out-of-plane equilibrium field this decoupling occurs at the ion inertial length d_i (see Chapter 1.1). If a mean, 'guide' magnetic field is present the ions will gyrate around it, and the characteristic scales becomes the ion gyro- or 'Larmor' radius ρ_i. Finally, if the guide field is very strong compared to the pressure and in-plane fields such that the ratio of the bulk

plasma pressure to magnetic pressure $\beta = 2p/B^2$ is much less than one, then the magnetosonic mode is the fastest wave in the system [13] and the ion decoupling scale becomes the ion-sound Larmor radius [60]:

$$\rho_s = \frac{c_s}{\Omega_{ci}} = \sqrt{\beta} d_i \tag{5.1}$$

where c_s is the sound speed and Ω_{ci} the ion gyro-radius. The latter low-β, strong guide field limit is that most applicable to tokamaks. Linearly this decoupling creates a nested boundary layer structure which increases the growth of the reconnecting instability and triggers a nonlinear collapse of the current sheet into a compact point. Although this effect aids the reconnection process it is not sufficient to produce it alone; the magnetic fields remain tied to the massless electron fluid and some additional mechanism, such as resistivity, is required to change the magnetic topology.

Not all FLR effects are beneficial to the reconnection process; the diamagnetic drift effects discussed in Chapter 2.2 can inhibit growth. When ions are allowed to have finite mass they must also participate in carrying the diamagnetic current, and thus the ion diamagnetic drift $\mathbf{v}_{*i} = d_i \mathbf{B} \times \nabla p_i / B^2 \rho$ is required in the model. This addition indirectly couples the electron drift $\mathbf{v}_{*e} = -d_i \mathbf{B} \times \nabla p_e / B^2 \rho$ into the MHD equations. These drifts are able to reduce the growth rate of reconnecting instabilities; equivalently represented as a forced mixing of the mode in the complex plane [3] or as an interference with the re-coupling of the electron flow to the ion flow in the down-stream regions of reconnection sites [44]. These diamagnetic drift stabilization mechanisms are critically important in the understanding of the $m = 1$ kink-tearing mode in cylindrical geometry [3, 41], and are capable of completely saturating the instability and leaving finite sized islands nonlinearly [34]. Because of the similarities between double-tearing eigenmodes and $m = 1$ kink-tearing modes (Chap. 3) v_* effects are a strong candidate for DTM stabilization.

Our primary goal in this chapter is to understand how the introduction of diamagnetic

drifts will affect the linear double-tearing mode in Cartesian geometry. To accomplish this task we will rely almost entirely on simulation results from the linearized version of `MRC-3d`. Because drift stabilization requires $d_i \neq 0$, the Hall effect beneficial to reconnection growth will also be manifest. To separate the growth enhancing properties from the v_* suppression we will first consider the scaling of growth rate with d_i and the impact on resistivity dependence. After isolating the enhancing properties we will replicate the sheared scaling studies of Chapter 4 using an electron diamagnetic drift frequency $\omega_{*e} = kv_{*e}$ in place of the equilibrium flow. We will see that the general trend of mode mixing and bifurcation remains, however the diamagnetic effects local to the tearing layer will continue to slow the growth after decoupling is achieved.

5.1 Force-free Hall

In this section we will focus specifically on the effects of the Hall term on the Cartesian double-tearing mode in the presence of a strong out-of-plane magnetic field B_z. In the linear phase the growth rate behavior is largely dependent on the ordering of the various boundary layers, specifically the ion-sound Larmor radius ρ_s, which represents the characteristic scale of ion motions about the guiding magnetic field, and the resistive layer width δ_η, which we first encountered as the inner-most layer width Δ in Chapter 3.1.2. For the kinetic effects to have a significant impact on the mode, the ion fluctuations must occur on a scale larger than the tearing layer so that the ion fluid is decoupled from the reconnecting magnetic field. Thus the strong Hall regime is characterized by $\rho_s \gg \delta_\eta$, the weak Hall regime by $\rho_s \ll \delta_\eta$, and the 'moderate' Hall regime when they are approximately equal and the boundary layers cannot be considered strictly nested.

In the strong guide field regime ($B_z \approx 10B_{eq}$) the ions have a small gyroradius around the large out-of-plane magnetic field and the plasma beta ($\beta = B^2/2p$) is likewise small, therefore ρ_s is very small unless d_i is large. As a consequence it is difficult to observe the

strong Hall regime of the double-tearing mode while keeping the separation x_s larger than the layer widths unless the Lundquist number is very large ($S^{-1} \ll 1$) so that the resistive layer is very small. To illustrate the FLR transition we use a small resistivity ($\eta = 1 \times 10^{-7}$) and step d_i to generate the scalings in Figure 5-1. Our equilibrium for these examples is the same as that used in Chapter 3.2, which has $\beta = 0.02$ so that $\rho_s \approx 0.14 d_i$.

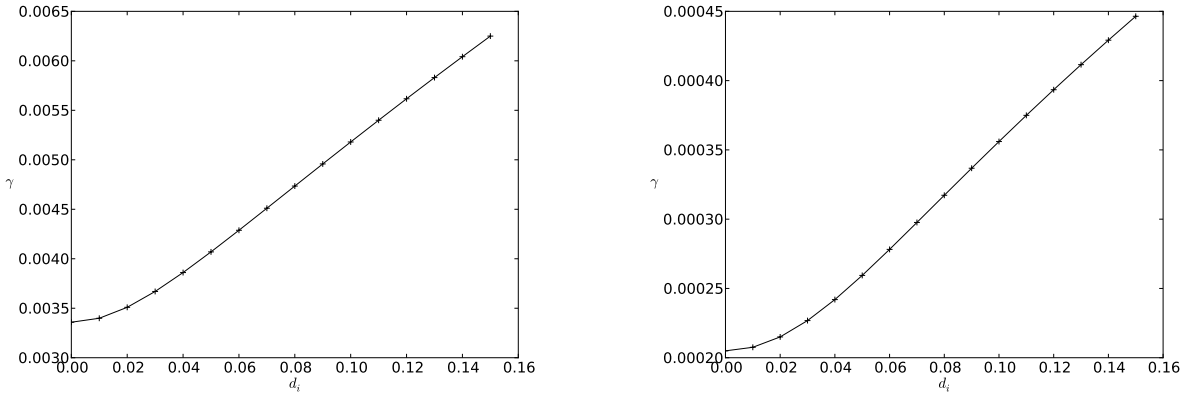

(a) $x_s = 0.25$ **(b)** $x_s = 1.0$

Figure 5-1: The growth rate γ of the symmetric double-tearing mode increases with increasing ion inertial length d_i. At low values ($d_i < 0.04$) the resistive layer is much larger than the ion-sound gyro-radius $\rho_s = \sqrt{\beta} d_i$ and γ is weakly effected by the Hall term in Ohm's law. The transition between moderate and strong Hall regimes is not readily apparent in the scaling of γ with d_i.

Both the $x_s = 0.25$ (Fig. 5-1a) and $x_s = 1.0$ (Fig. 5-1b) double-tearing modes exhibit an increase in linear growth rate as d_i is increased. The transition from weak to moderate Hall behavior occurs in the neighborhood of $d_i = 0.04$ for this equilibrium and resistivity. Below this value the mode is not strongly impacted by changes in the ion-inertial scale. The boundary between moderate and strong Hall is not readily apparent in the d_i scalings during the linear phase. Comparing the plasma displacement (ξ) near the boundary layers of the $x_s = 1.0$ DTM for $d_i = 0$ and $d_i = 0.15$ shows the appearance of a nested structure when ρ_s becomes significantly larger than the resistive scale (Fig. 5-3), which indicates that the transition does occur. The out-of-plane current J_z becomes more strongly peaked when FLR effects are present, which explains the increase in the linear growth rate γ as the diffusive ηJ term in Ohm's law is the mechanism responsible for field-line breaking and reconnection.

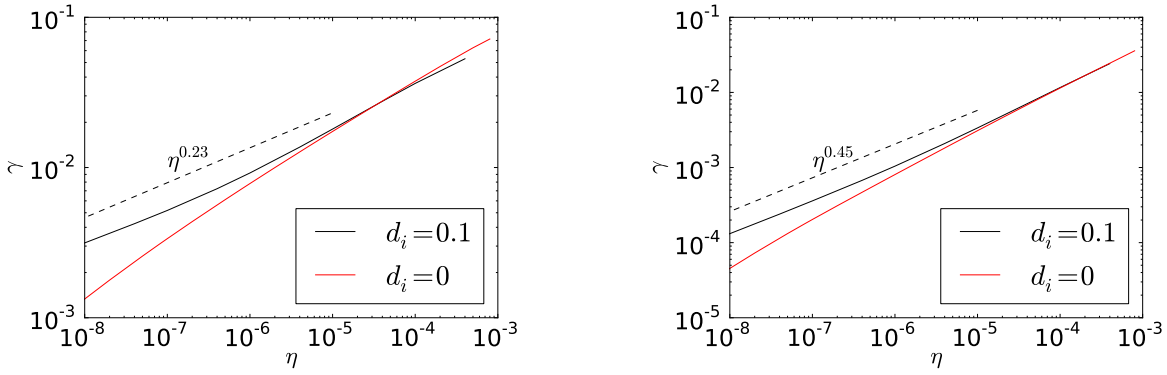

(a) $x_s = 0.25$ **(b)** $x_s = 1.0$

Figure 5-2: When the ion sound Larmor radius ρ_s is larger than the resistive layer the DTM growth rate γ depends less strongly on the resistivity η. For an ion inertial length of $d_i = 0.1$ ($\rho_s = 0.014$) this transition occurs near $\eta = 1 \times 10^{-6}$ for both the $x_s = 0.25$ (left) and $x_s = 1.0$ (right) separations. At larger resistivities the modes are in the weak Hall regime and the growth rates behave as in resistive MHD (red lines).

This nested boundary layer structure disconnects the internal resistive layer from the outer ideal MHD regions. The dependence of the growth rate on resistivity is modified based on the relative ordering of FLR and diffusive terms. Fixing $d_i = 0.1$ ($\rho_s = 0.014$) we scale the resistivity for both the $x_s = 0.25$ (Fig. 5-2a) and $x_s = 1.0$ (Fig. 5-2b) DTMs. At low resistivities ($\eta \lesssim 1 \times 10^{-6}$) the dependence of γ on η is significantly reduced from the purely resistive case ($\gamma_{x_s=0.25} \propto \eta^{0.23}$ compared to $\eta^{1/3}$ for the resistive, and likewise $\gamma_{x_s=1.0} \propto \eta^{0.45}$ rather than $\eta^{3/5}$). This weakened dependence indicates that the resistive layer is much smaller than the FLR layer and the system can be considered in the 'strong Hall' regime. At very large values of η the growth rate begins to follow the standard resistive behavior (shown in red for both separations in Fig. 5-2), indicating a transition to the 'weak Hall' behavior.

For the remainder of this chapter (and all future Hall MHD simulations) we will use this value of $d_i = 0.1$ and a resistivity on the order of $\eta \approx 1 \times 10^{-5}$. This value of the ion inertial length, and the corresponding ion-sound Larmor radius, is (when translated to dimensional coordinates) at least an order of magnitude larger than that expected in actual fusion plasmas [24]. Our choice of this value is largely motivated by the numerical challenges of simulating small resistivities. A large value of η allows for less computationally

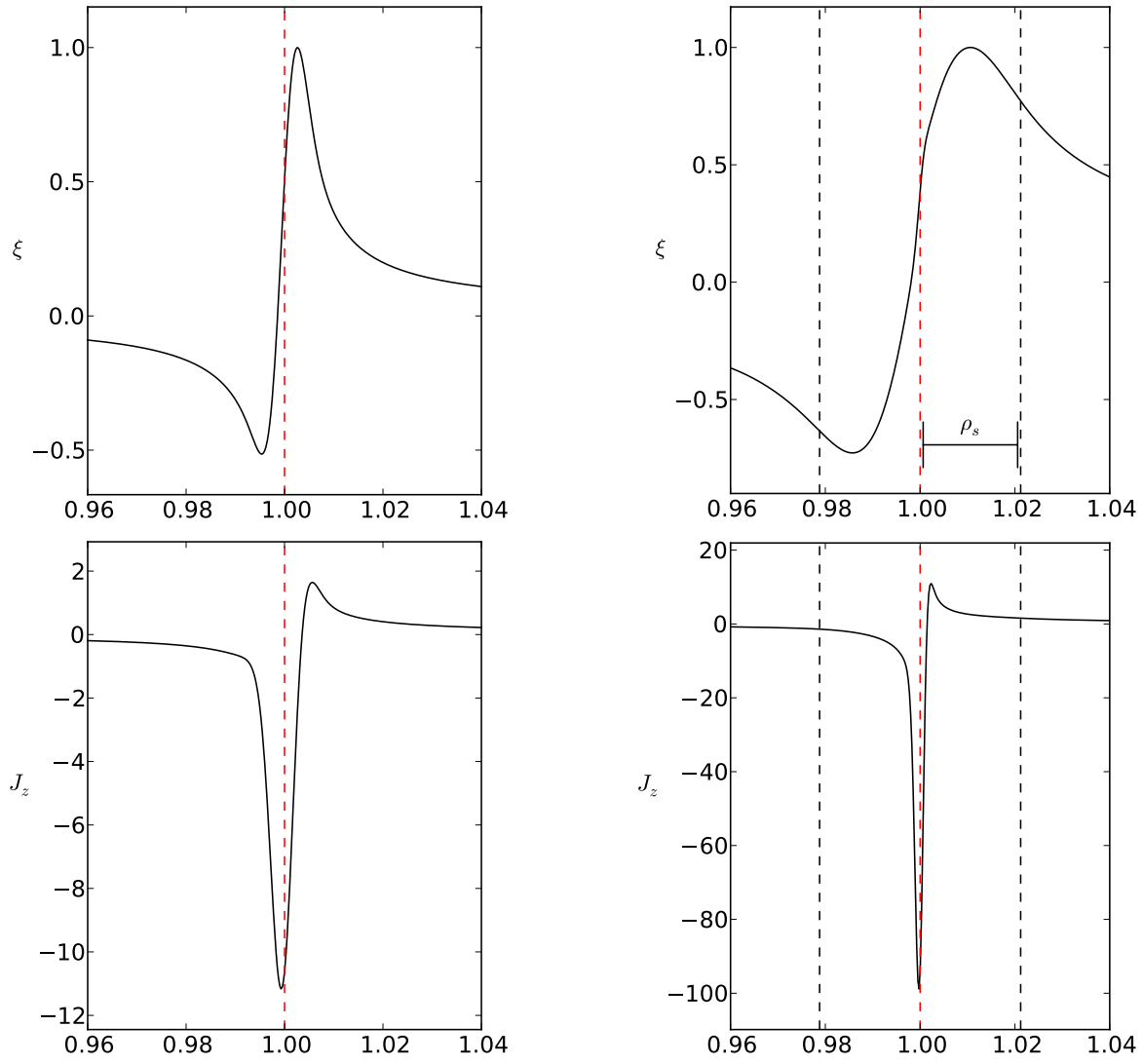

(a) $d_i = \rho_s = 0$ **(b)** $d_i = 0.15$, $\rho_s = 0.015$

Figure 5-3: The introduction of FLR effects results in a nested boundary layer structure. When $d_i = 0$ the singular layer of an $x_s = 1.0$ DTM exhibits one boundary layer transition (left). A ion inertial length of $d_i = 0.15$ introduces an outer boundary layer at ion-sound gyro-radius scales $\rho_i = \sqrt{\beta} d_i = 0.021$ with the resistive layer nested inside (right), visible predominantly in the linear plasma displacement ξ. The perturbed out-of-plane current J_z is much more strongly peaked than in the purely resistive case. In order for this nested structure to be clearly visible, ρ_s must be significantly larger than the resistive layer width. Thus we have used a small resistivity $\eta = 1 \times 10^{-7}$ to generate these examples.

expensive simulations, however a larger value of d_i is required for FLR effects to be significant. We require, however, that the ordering of ρ_s be less than the spacing between the tearing surfaces x_s so that there is an asymptotically ideal MHD region between the two DTM nested boundary layers, thus d_i cannot be arbitrarily large. Based on the scaling studies of Figures 5-1 and 5-2 this combination of d_i and η results in a 'moderate Hall' mode where the FLR effects are significant and the linear mode growth is increased, but the scale separation will not cause numerical issues.

5.2 Diamagnetic drift effects

The addition of a pressure gradient to a Hall MHD system introduces an equilibrium diamagnetic drift for both the ions and electrons by forcing the ions to participate in the diamagnetic current, as discussed in Chapter 2.2. Within the MHD model the ion drift manifests as a bulk fluid flow, and thus can advect eigenmodes in the same fashion as an externally applied flow (Chap. 4). In this work we will, however, choose to work in the cold-ion approximation ($T_i = p_i = 0$) for analytic and numerical simplicity. The ion diamagnetic drift will not appear in our simulations. Although the electron fluid is not strictly present in Hall MHD, the d_i scale terms in Ohm's law couple the diamagnetic current directly into the advancement of the magnetic field. As we will see in the following simulations, this results in the magnetic modes acquiring a drift determined by the electron diamagnetic frequency. In this sense the Hall MHD model is a half-step between two fluid models, for which a mode can formerly be considered as advected with the electron fluid [3, 41], and the resistive MHD model where diamagnetic drifts are absent.

Our goal in this section is to demonstrate linear stabilization of the DTM through electron diamagnetic drift effects. This task has two components. Firstly, by establishing the electron drift in opposite directions at the two singular layers we will demonstrate that the mode decoupling first observed with sheared equilibrium flows (Chap. 4) can also occur as a

consequence of v_{*e} drifts. Secondly, we will demonstrate that diamagnetic drifts can continue to stabilize the reconnection process after decoupling. In this sense they are more effective than equilibrium sheared flows. Strongly coupled modes, however, may require extremely steep pressure gradients to achieve appreciable stabilization, and these large shears may lead to other instabilities. The nature of these instabilities is outside the scope of this work, but we will show that for the most nonlinearly dangerous class of modes (moderately coupled DTMs) there is an extended range of pressure profiles where the tearing surfaces are decoupled and the growth rate is strongly suppressed.

A globally sheared diamagnetic drift of the same form as as the tanh equilibrium sheared flow profiles used in Chapter 4 is not physically or numerically realistic, as it would require an unbounded pressure profile. Fortunately the decoupling behavior of the DTM, which occurs in the low amplitude regime, depends on the drift local to the two resonant surfaces (see the analysis of Sec. 4.1 and simulation work of Ref. [37]). To generate peaked drift profiles local to the layers we use the double-tanh density profile describe in Section 2.3.

$$\rho(x) = \rho_0 + \Delta_\rho \left[1 + \tanh\left(\frac{(x - x_s)}{\lambda_\rho} \right) - \tanh\left(\frac{(x + x_s)}{\lambda_\rho} \right) \right] - \rho_s \tag{5.2}$$

The equilibrium electron diamagnetic drift frequency in `MRC-3d` can be calculated from this gradient, assuming a strong guide field $B_z(x)$, reconnecting field $B_y(x)$, and constant electron temperature T_0, and is confined to the $\hat{y}$ direction.

$$\omega_{*e} = \mathbf{k} \cdot \mathbf{v}_{*e} = -k d_i \frac{T_0 B_z \partial_x \rho}{\rho B^2} \tag{5.3}$$

In following with the sheared flow study, we will define the parameter $\Delta\omega_*$ as the difference between the electron diamagnetic drift at the two surfaces.

$$\Delta\omega_* = |\omega_*(x_s) - \omega_*(-x_s)| = 2|\omega_*(x_s)| \tag{5.4}$$

This difference is an effective marker of decoupling and drift behavior for the symmetric pressure profile we use. Unlike the sheared flow case, however, we cannot take this to be a generic indicator of the DTM response for arbitrary drift profiles. The interaction of the diamagnetic drift with the reconnecting mode is not a simple advective process [3] but rather involves a more complex interaction between the current, electric, and magnetic fields. As a consequence we cannot Doppler shift to an arbitrary frame without introducing an additional equilibrium electric field that will have an effect on the mode growth. The parameter $\Delta\omega_*$ can therefore only be taken as a characteristic measure for this symmetric pressure where $\omega_*(x_s) = -\omega_*(-x_s)$. We will not explore any additional profiles in Cartesian geometry, but this distinction will be important in cylindrical equilibria when symmetric profiles are not possible.

One limitation of the high guide field regime is that the drift frequency varies inversely with B_z so that large drifts require steep pressure gradients. To mitigate this we will use, for this Cartesian study, a larger electron temperature of $T_0 = 10$. This change will increase the plasma β to 0.2, as opposed the $\beta = 0.02$ we used in the previous chapters. While still small, this may present a further complication for any direct comparison of these simulation results to some future analytic theory. In simulation work the important impact is that increased β at the current layer will cause an increase in the measured growth rate both due to changes in normalization and because of an increase in $\rho_s = \sqrt{\beta} d_i$. These changes will need to be more carefully accounted for if, at some future point, we are able to compare to theoretical predictions.

An example drift profile along with the pressure gradient that generates it is plotted in Figure 5-4. Holding d_i and $\rho(\pm x_s)$ fixed, we decrease λ_ρ to increase the pressure gradient and generate the desired differential drift $\Delta\omega_*$, similar to the sheared flow scalings of Chapter 4.

The mode shearing and decoupling effects of the diamagnetic drift, together with the additional plasma waves allowed by the FLR terms in Ohm's law, have an unfortunate tendency to introduce and support small scale spurious oscillations which can cause numerical

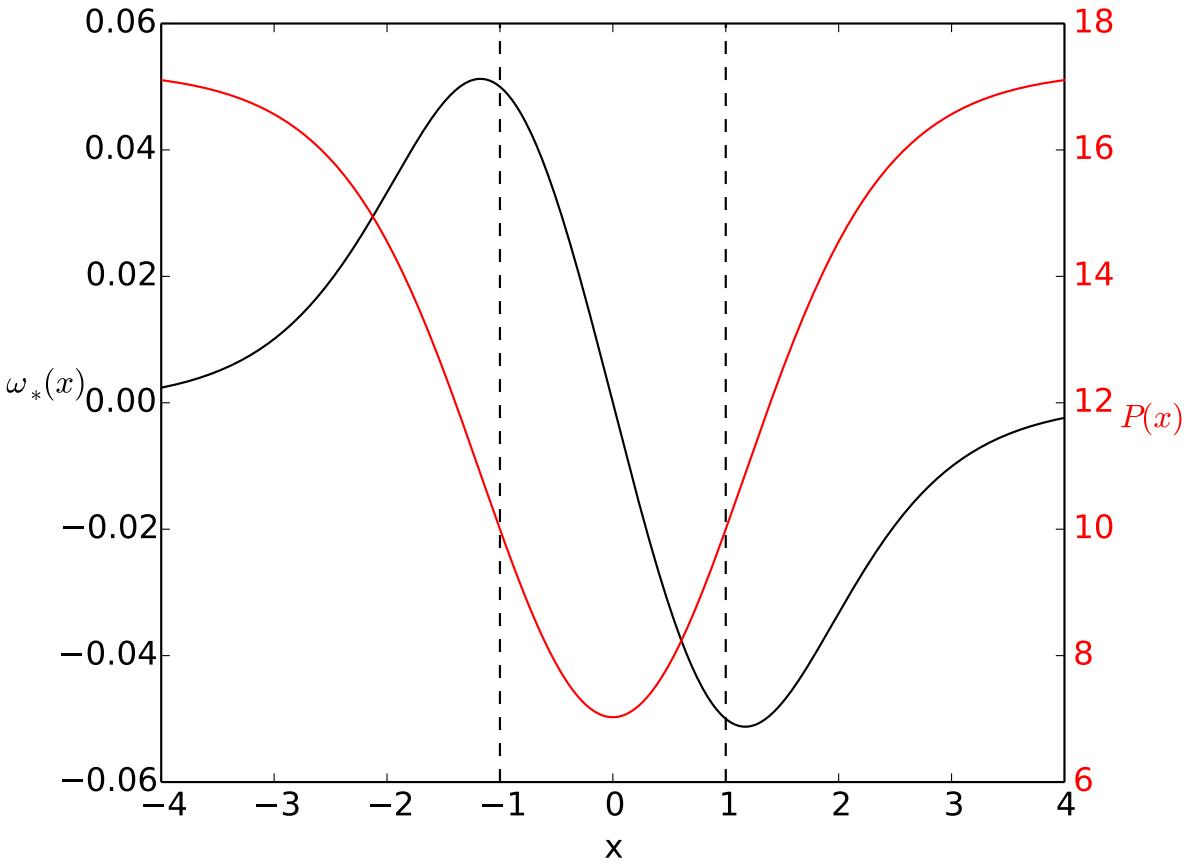

Figure 5-4: Example pressure gradient (red) formed by a density given by Eqn. 5.2 with $\rho_0 = 1.0$, $\Delta\rho = 0.8$, $\lambda_\rho = 1.32$, and $\rho_{shift} = 0.074$, multiplied by a constant electron temperature of $T_0 = 10$. When $d_i = 0.1$ and there is a strong guide field $B_z = 10$ this profile results in an equilibrium electron diamagnetic drift ω_* (black) which is antisymmetric across the domain.

instability even in linear simulations. At larger resistivities ($\eta \gtrsim 1 \times 10^{-4}$) these oscillations are quickly damped, however the resistive boundary layer is too large in this region to allow sensible study. To allow simulation at lower values of η we use the additional dissipation terms in the `MRC-3d` model: the particle diffusivity D (Eqn. 1.4); viscosity ν (Eqn. 1.5); and temperature diffusivity DT (Eqn. 1.6). While these parameters are less important to the reconnection process than resistivity, we further reduce their impact by setting them an order of magnitude lower than η:

$$D = \nu = DT = 10^{-1} \times \eta \tag{5.5}$$

In our experience this ordering is sufficient to damp spurious oscillations in linear simulations while minimally effecting the growth rate of the tearing mode.

The effects of the differential diamagnetic drift $\Delta\omega_*$ on $x_s = 1.0$ and $x_s = 0.25$ double-tearing modes for parameters $\eta = 1 \times 10^{-5}$ and $d_i = 0.1$ are shown in Figures 5-5 and 5-9 respectively. Both separations experience a reduction of the growth rate and decoupling behavior which was observed with the equilibrium sheared flow (Figure 4-6). There are, however, some substantial differences. In order to illustrate the variations we will conduct a detailed comparison between the two stabilization mechanism in three regimes of the $x_s = 1.0$ DTM: near decoupling (small $\Delta\omega$); decoupled (moderate $\Delta\omega$); and strong drift (high $\Delta\omega$).

5.2.1 Near decoupling

In order to compare the effects of diamagnetic drifts and sheared equilibrium flow we run a subset of the scaling from Chapter 4 using a force-free equilibrium with $T_0 = 10$ and the same resistivity and ion inertial length as used for the ω_* runs. The estimated critical decoupling frequencies $\Delta\omega^c$ and growth rates γ_R^c are shown in Table 5.1 for both ω_* drifts and sheared flow. For the $x_s = 1.0$ DTM the equilibrium diamagnetic drift is less effective at decoupling the modes than plasma flow and requires a frequency difference of $\Delta\omega_* =$

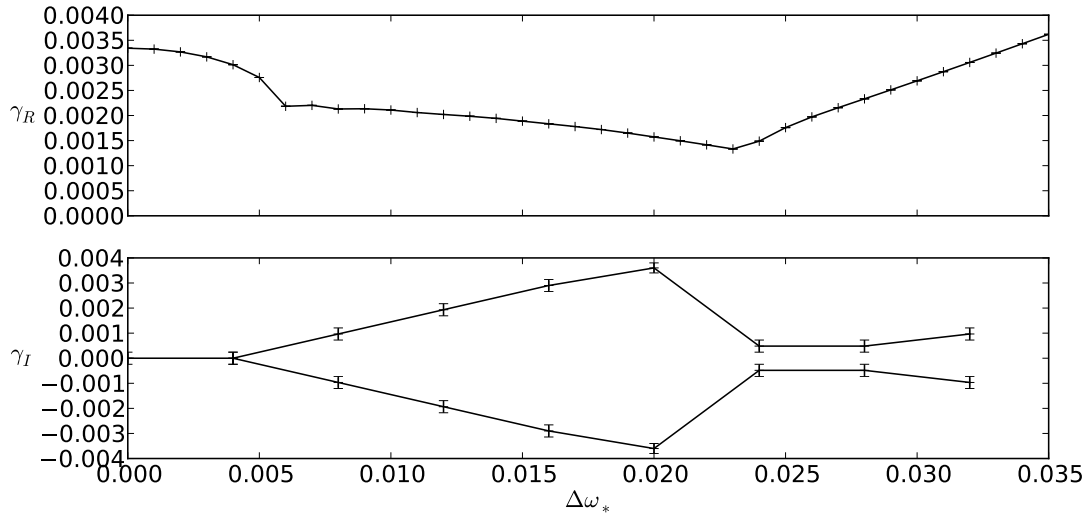

(a)

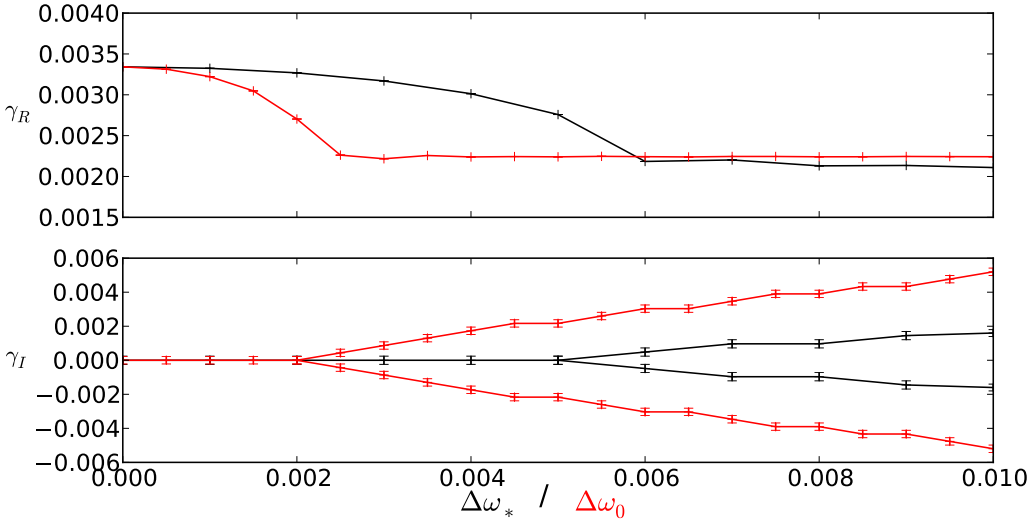

(b)

Figure 5-5: (Top): Increasing differential diamagnetic drift $\Delta\omega_*$ continues to decrease the growth rate γ_R of the $x_s = 1.0$, $\eta = 1 \times 10^{-5}$, $d_i = 0.1$ DTM after decoupling until a new type of instability triggers at large drifts. Comparing the diamagnetic drift (bottom, black) to an equilibrium sheared flow differential (bottom, red) reveals that the diamagnetic effects are less effective at mode decoupling. The decoupled mode frequencies γ_I are less than the ω_* drift local to each surface, which is consistent with the decreased decoupling efficiency.

Run Type	$\Delta\omega^c$	γ_R^c
Diamagnetic (ω_*)	$6 \times 10^{-3} \pm 0.5 \times 10^{-3}$	$2.18 \times 10^{-3} \pm 0.28 \times 10^{-3}$
Sheared Flow (ω_0)	$2.2 \times 10^{-3} \pm 0.25 \times 10^{-3}$	$2.26 \times 10^{-3} \pm 0.06 \times 10^{-3}$
Resistive Prediction	$\approx 2.0 \times 10^{-3}$	$\approx 2.8 \times 10^{-3}$

Table 5.1: Comparison between decoupling points for the differential diamagnetic drift and sheared flow mechanisms for $x_s = 1.0$, $\eta = 1 \times 10^{-5}$, $d_i = 0.1$ DTMs with initial, force-free growth rates of $\gamma_R^0 = 3.34 \times 10^{-2}$. Values for the critical frequency difference $\Delta\omega^c$ and growth rate γ_R^c are estimated from Figure 5-5b. For comparison we also include the predicted values using the resistive, sheared flow bisection study (Fig. 4-8a).

0.006, roughly three times larger than the flow value of $\Delta\omega_0 = 0.0022$. The post-decoupling measurements of the eigenmode frequencies γ_I (Fig. 5-5a) show that after separation the two layers drift with frequencies less than the local equilibrium diamagnetic drift. Both the larger decoupling frequency and lower eigenmode drift are consistent with the more complicated means by which the perturbation couples to the electron diamagnetic frequency. As mentioned previously, the diamagnetic drift is not a simple advective process but rather a higher order effect and therefore the local equilibrium ω_* value does not map directly to the expected frequency of a given mode and cannot simply be Doppler shifted away. A more detailed reconciliation of the critical decoupling drifts and eigenmode frequencies would require a Hall MHD analysis of the DTM boundary layer problem in force-balanced equilibria, which is unavailable at this time.

Despite the differences in decoupling drift $\Delta\omega^c$, the growth rate of the DTM at decoupling (γ_R^c) is approximately the same for both the diamagnetic and sheared flow mechanisms. The structure of the eigenmodes before (Fig. 5-6) and after (Fig. 5-7) decoupling follows the behavior established in Chapter 4 for the sheared flow decoupling mechanism, i.e. mixing of the symmetric and antisymmetric solutions prior to decoupling and isolation of the tearing layers after. This correspondence seems to indicate that although the interaction of the equilibrium diamagnetic drift with the perturbation is more complicated than in the sheared flow case the fundamental physical process behind DTM decoupling and the linear mode bifurcation is the same.

5.2.2 Decoupled

The major advantage of equilibrium diamagnetic drifts as a stabilization mechanism appears after the $x_s = 1.0$ mode is decoupled. As the drift increases in the range $0.005 < \Delta\omega_* < 0.024$ the growth rate γ_R continues to decrease. This behavior is preferable to that of the equilibrium flow, which cannot influence the growth rate post-decoupling until Alfvén resonances become important (Chap. 4). The diamagnetic drift local to each decoupled tearing layer has a stabilizing effect on the reconnection process [3, 41] that is absent for equilibrium plasma flow.

5.2.3 Strong drift

At large diamagnetic drifts ($\Delta\omega_* \gtrsim 0.024$) the eigenmodes transition to a new regime. The growth rate γ_R begins to increase with increasing equilibrium drift and the mode frequencies decrease to follow a new trend line (Fig. 5-5a). We have conducted sufficient convergence testing to ensure that this behavior is not numerical. The eigenmodes in this regime extracted via Fourier analysis are shown in Figure 5-8 and exhibit very strongly defined singular layers. Several mechanisms may be responsible for this change in the mode characteristics. The most likely candidate is a transition to a DTM analogue of the drift-tearing regime [23] where the electron diamagnetic drift becomes strong enough to alter the nature of the singular layers. In this case the extra dissipation coefficients we are adding for numerical stability (Eqn. 5.5) may be driving the mode growth at these high $\Delta\omega_*$ values. Alternatively, the density profile needed to produce the strong drift may be causing some pressure driven instability. In either case, our present understanding of the double-tearing mode in the model and equilibrium conditions necessary to achieve this faster growing mode is inadequate to determine the physical mechanism. For the purposes of this thesis we will restrict our consideration to the moderate drift regimes where the diamagnetic drift is sufficient to decouple the DTM and slow its growth but not to initiate this new instability.

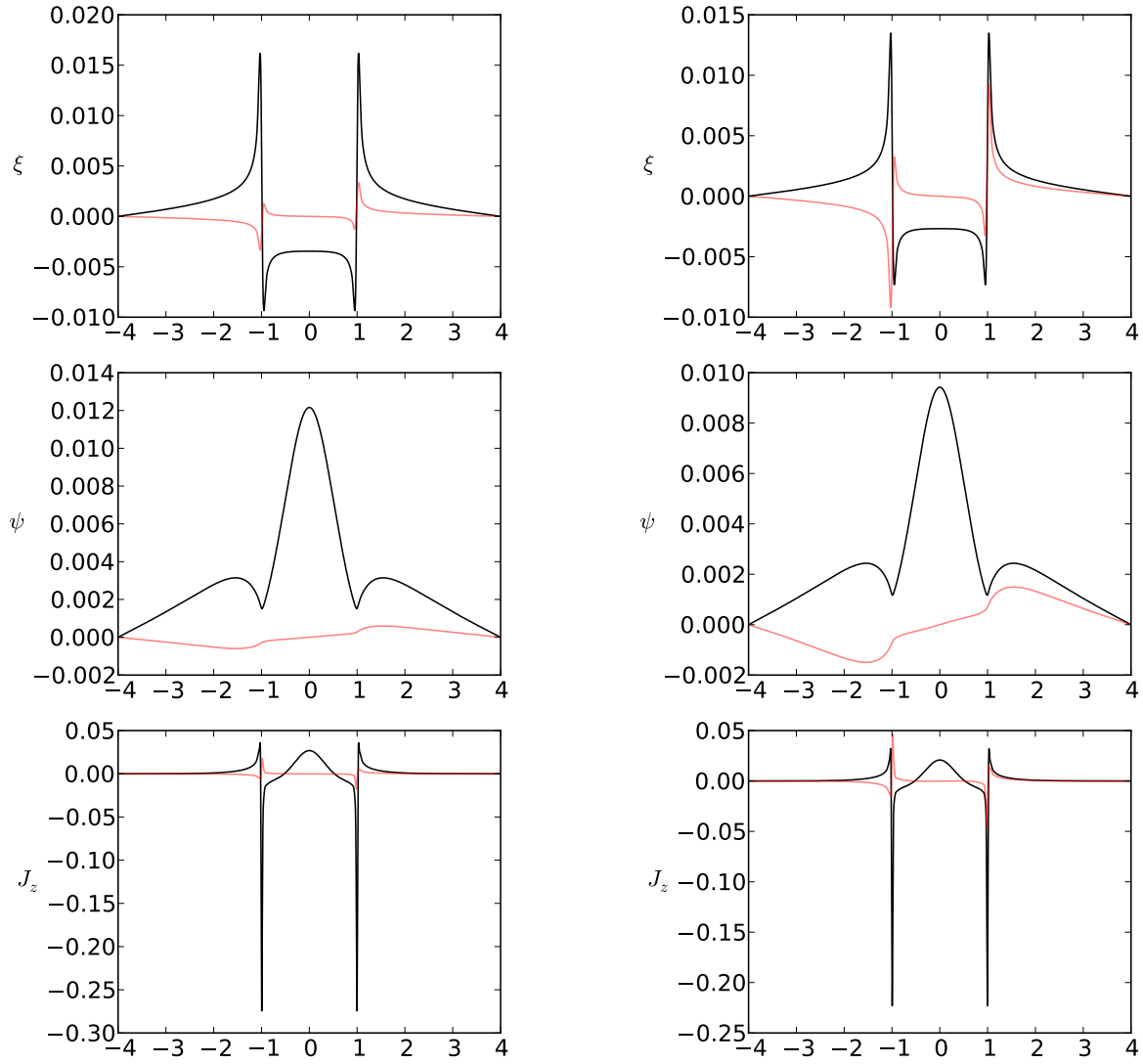

(a) $\Delta\omega_* = 0.002$ **(b)** $\Delta\omega_0 = 0.005$

Figure 5-6: Differential diamagnetic drift ($\Delta\omega_*$) produces the same mixing of symmetric and antisymmetric DTM eigenmodes seen for equilibrium sheared flows in Chap. 4. Near decoupling (right) the antisymmetric, imaginary part of the mode (red) is closer in magnitude to the symmetric, real part (black) than for smaller values of $\Delta\omega_*$ (left). Note that the functional form of the plasma displacement ξ is the same as for force-free DTMs (Chap. 3) suggesting that the transformation to a 'sheared displacement' z (Chap. 4) is not appropriate for equilibrium diamagnetic drifts.

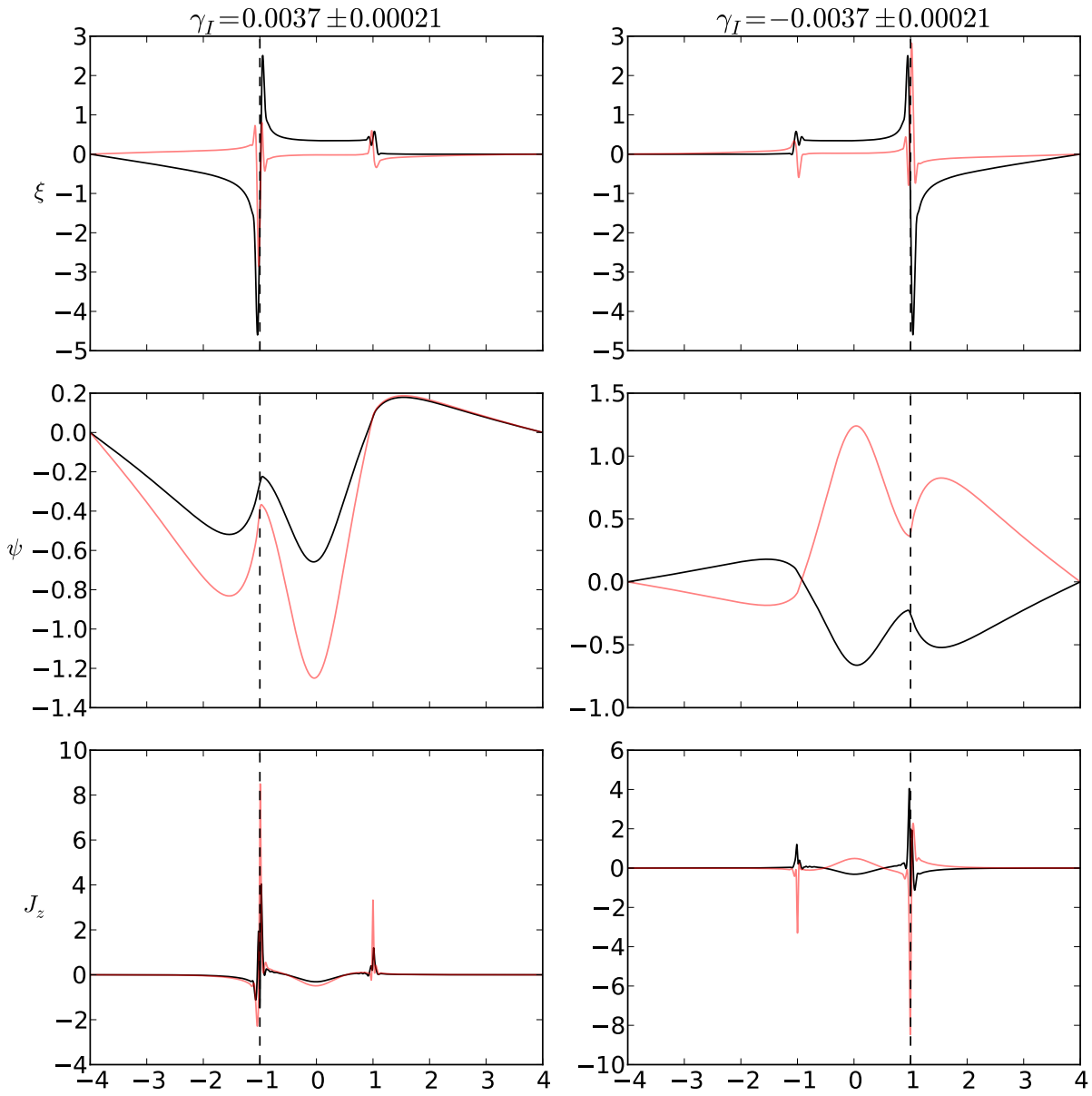

Figure 5-7: $x_s = 1.0$, $\eta = 1 \times 10^{-5}$, $d_i = 0.1$ eigenmodes decoupled by a differential diamagnetic drift of $\Delta\omega_* = 0.02$ show the same isolated tearing layer structure with finite mode frequency as observed for equilibrium sheared flow DTMs in Fig. 4-5. The plasma displacement ξ and current j_z tearing layers (marked with vertical dashed lines) are strongly enhanced by FLR effects. The mode measured frequency $\gamma_I = 0.0037$ is less than the $\omega_* = 0.01$ drift local to each tearing layer.

At smaller, more realistic resistivities the DTM growth rate will be small enough that this desirable regime should be broader than for our current large η simulations.

5.2.4 $x_s = 0.25$ variations

The above characteristics of the widely separated double-tearing mode also apply to the strongly coupled $x_s = 0.25$ DTM. The closely spaced surfaces have, however, a stronger growth rate with a weaker dependence on resistivity. Due to the higher growth rate, equilibrium diamagnetic drifts are a much less effective stabilization mechanism. The scaling results in Figure 5-9 show that the differential drift $\Delta\omega_*$ necessary for decoupling is so large that once the surfaces are separated they immediately transition into the high drift instability. The intermediate regime, where the tearing surfaces have been separated and the growth rate decreases with increasing drift, is completely absent. In contrast, the better decoupling properties of equilibrium shear flow result in more effective stabilization at low $\Delta\omega_0$. Similar to the widely spaced mode, the differential drift needed for decoupling is also much larger that the differential flow (Table 5.2). The growth rate of the closely coupled DTM depends very weakly on resistivity, especially when FLR effects are included (Fig. 5-1a), so the diamagnetic drift does not appear to be an effective stabilization mechanism for double-tearing modes with small inter-resonant distances.

We note an unexpected feature of the sheared flow scalings (red line) in Fig. 5-9: the growth rate continues to decrease past decoupling with increasing $\Delta\omega_0$. The mechanism behind this decrease, and the large flow behavior, is not currently understood. Two likely candidates are modification of the Alfvén resonance locations due to changes in the plasma β, or a more complicated interaction between the various singular layers when FLR effects are included. This behavior suggests that future examination of sheared flow equilibria in two-fluid models might yield new means of stabilizing the strongly coupled DTM.

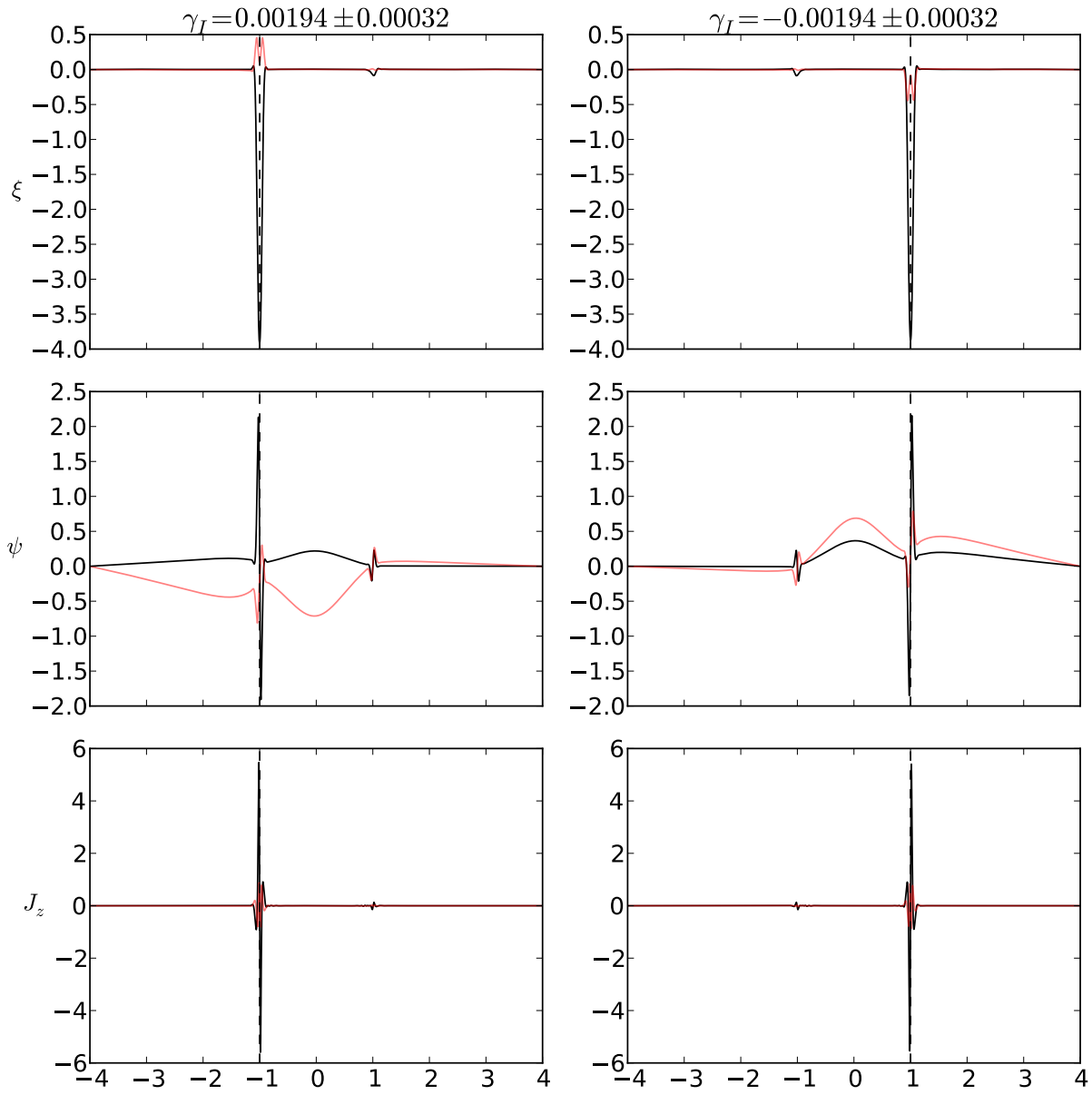

Figure 5-8: At large values of the diamagnetic drift ($\Delta\omega_* = 0.050$ for this $x_s = 1.0$, $\eta = 1 \times 10^{-5}$, $d_i = 0.1$ example) the system eigenmodes change to some currently unidentified form of instability that grows with increasing drift. The layers at the rational surface with the same sign as the local ω_* drift (marked with dashed vertical lines) are strongly enhanced.

Run Type	$\Delta\omega^c$	γ_R^c
Diamagnetic (ω_*)	$6.4 \times 10^{-2} \pm 0.1 \times 10^{-2}$	$1.09 \times 10^{-2} \pm 0.05 \times 10^{-2}$
Sheared Flow (ω_0)	$2.25 \times 10^{-2} \pm 0.25 \times 10^{-2}$	$1.3 \times 10^{-2} \pm 0.2 \times 10^{-2}$
Resistive Prediction	$\approx 2.12 \times 10^{-2}$	$\approx 1.2 \times 10^{-2}$

Table 5.2: Comparison between decoupling points for the differential diamagnetic drift and sheared flow mechanisms for $x_s = 0.25$, $\eta = 1 \times 10^{-5}$, $d_i = 0.1$ DTMs with initial, force-free growth rates of $\gamma_R^0 = 2.12 \times 10^{-2}$. Values for the critical frequency difference $\Delta\omega^c$ and growth rate γ_R^c are estimated from Figure 5-9. For comparison we also include the predicted values using the resistive, sheared flow bisection study (Fig. 4-8b).

5.3 Discussion

In introducing finite Larmor radius effects we have moved a step closer to understanding the behavior of the linear double-tearing mode in an actual fusion plasma. The additional layer scale generated by the Hall term in Ohm's law increases the growth rate of the DTM and decreases its dependence on resistivity, consistent with other, better understood reconnecting systems. Moving to force-balanced equilibria, we have demonstrated that equilibrium diamagnetic drifts can slow the instability through a combination of global mode shearing and layer-local effects. These ω_* drifts are, however, not as efficient at decoupling the two tearing surfaces as the equilibrium sheared flows of Chapter 4, and have the potential to enhance the growth of the instability when steep pressure gradients are required. If the critical decoupling differential drift $\Delta\omega_*^c$ is sufficiently small compared to the point at which the high-drift instability triggers, such as for the $x_s = 1.0$ mode we have examined above, the diamagnetic drift can slow the growth of the separated, drifting, tearing surfaces. In this regime the diamagnetic drift is preferential to the equilibrium sheared flow. When the tearing surfaces are strongly coupled, such as for the $x_s = 0.25$ DTM considered above, the eigenmodes follow the faster, high-drift instability growth everywhere above $\Delta\omega_*^c$. The equilibrium sheared flow is, overall, a much more effective stabilization mechanism for these strongly coupled modes. If the source of this high-drift instability can be identified, however, it may be possible to design pressure profiles that are recover the beneficial ω_* effects.

We neglected many potential avenues for interesting future work. The Hall MHD code we have used to conduct our simulations is the minimal model to exhibit diamagnetic effects. It is reasonable to expect two-fluid and kinetic physics to have an impact on these results, though we believe the lowest order behavior is exhibited here. Even within this model one could move outside of the cold-ion approximation and allow $T_i \neq 0$, thus introducing ion diamagnetic flows. This additional differential shearing could improve the decoupling efficiency, as it would combine both the internal layer stabilizing effects of ω_* drifts and the large scale advective properties of an equilibrium sheared flow. The results of Section 5.2

suggest that a combination of using sheared flows to decouple the DTM and diamagnetic drifts to continue stabilization may be the most effective route. This combination may also avoid the new class of instability which emerges at high $\Delta\omega_*$, which we have not explored in depth and currently places limits on how low the growth rate can be decreased for a given equilibrium. A better understanding of the analytic theory, both of sheared flow decoupling and two-fluid DTMs, would significantly aid determining the best stabilization mechanism.

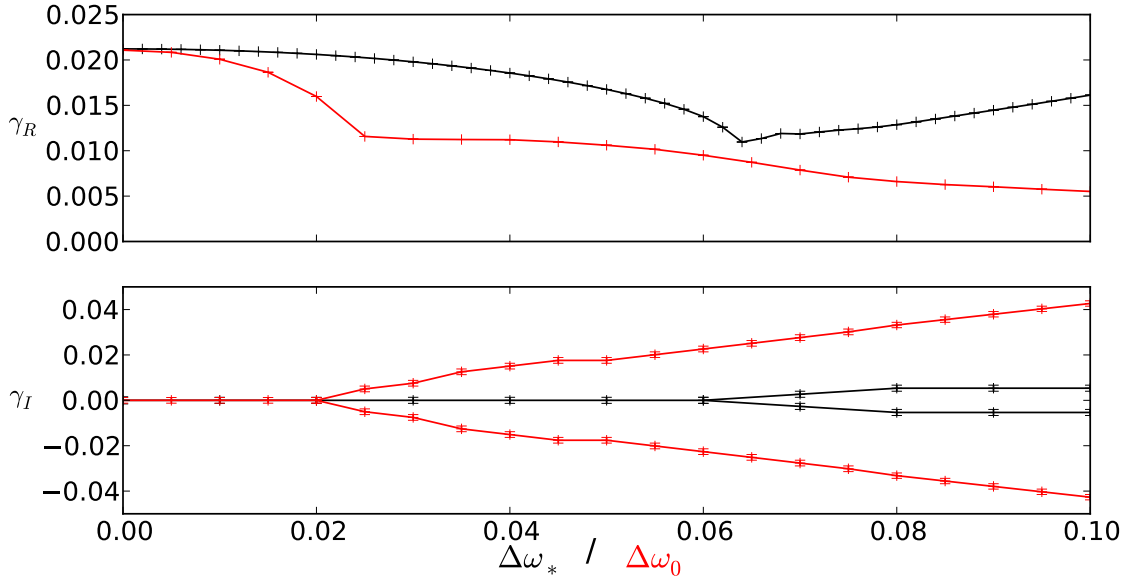

Figure 5-9: Differential electron diamagnetic drifts (black) are less effective decoupling a $x_s = 0.25$, $\eta = 1 \times 10^{-5}$, $d_i = 0.1$ DTM than equilibrium sheared flows (red). Immediately after decoupling the growth rate γ_R begins to increase with increasing $\Delta\omega_*$, indicating the onset of the high drift instability and removing the stabilized region of decoupled tearing surfaces observed in more widely separated modes.

Chapter 6

Linear cylindrical modes

Our discussion of the double-tearing mode thus far has been confined to Cartesian slabs. DTMs have been most widely studied in this geometry and the fundamental properties, including the sheared flow/diamagnetic drift decoupling mechanism, can most easily be understood in highly symmetric equilibria. Tokamak devices are, in contrast, toroidal systems with many asymmetries. Defining equilibria in full three dimensional device simulations is a difficult process, and they are generally unstable to a wide variety of modes. Our focus in this work is, however, to study the influence of equilibrium diamagnetic drifts on the nonlinear DTM, which will require variation of the pressure gradient and magnetic field profile. Performing this scaling study in periodic cylindrical geometry allows for greater flexibility than in toroidal, as well as being more numerically tractable. Even in devices for which the central plasma core is sufficiently confined to resemble a cylinder there will be higher order toroidal contributions which we cannot capture in `MRC-3d`. We will discuss the possible neglected effects in more depth at the end of this chapter.

In preparation for our later nonlinear, cylindrical simulations this chapter will be devoted to translating our previous discussions of the double-tearing mode to cylindrical geometry. To do so, we must first define the two dimensional plane in which rMHD is valid. In periodic cylindrical geometry we do not assume that the $\hat{z}$ derivative is zero, but rather that the system is symmetric along a helix defined by the invariant

$$u = \theta - \frac{n}{m}\frac{z}{R} \tag{6.1}$$

where n is the axial (toroidal) mode number, m the poloidal mode number, and $2\pi R$ the length of the cylinder along the axis (which approximates a torus of major radius R). Perturbations have wave vectors $\mathbf{k} = m/r\hat{\theta} - n/R\hat{z}$ (Chap. 2.4), where $0 \leq r \leq 1$ is the minor radius of the cylinder. Locations where the resonance condition $\mathbf{k}\cdot\mathbf{B} = 0$ is satisfied will not, generally, be zeros of B_θ. While analysis is possible in this coordinate system, it is simpler to define the helical coordinates:

$$\hat{r} = \hat{r} \tag{6.2}$$

$$\hat{u} = \frac{1}{\sqrt{1 + \frac{n^2}{m^2}\frac{r^2}{R^2}}}\left[\hat{\theta} - \frac{n}{m}\frac{r}{R}\hat{z}\right] \tag{6.3}$$

$$\hat{h} = \frac{1}{\sqrt{1 + \frac{n^2}{m^2}\frac{r^2}{R^2}}}\left[\hat{z} + \frac{n}{m}\frac{r}{R}\hat{\theta}\right] \tag{6.4}$$

which we will henceforth refer to as the radial, poloidal, and axial directions respectively. The axial B_h is the equivalent of the Cartesian guide field B_z, thus the perpendicular (or poloidal) plane is that defined by $\hat{r}$ and $\hat{u}$. The poloidal field B_u will be zero at resonant surfaces, and it is in these helical coordinates that we can compare to the Cartesian examples. We define the helical flux function ψ^* as:

$$\mathbf{B}_\perp = \nabla\psi^* \times \hat{h} \tag{6.5}$$

The other variables needed for comparison to slab geometry are the linear displacement $\xi = U_r/\gamma$ and axial current $J_h = -\nabla^2\psi^*$. For our equilibrium (Fig. 6-1) the poloidal field B_u is positive between the two resonant surfaces and negative outside, opposite our standard Cartesian sech equilibrium. Thus the relationship between ξ and ψ^* ($\psi^* = B_{eq}\xi$, Sec. 3.1.1) will be reversed in plots compared to the Cartesian examples. With these basic definitions, we can now examine the correspondence between the cylindrical DTM and the Cartesian theory.

We will first show that for nearby rational surfaces the force-free cylindrical DTM follows

the behavior of Chapter 3 with the modification that the equilibrium shear at the tearing layers is asymmetric. The addition of a pressure gradient will, however, introduce an ideal MHD instability that is not present in slab modes. We will then move directly to the impact of finite Larmor radius effects on the cylindrical DTM, showing that both the Hall enhancement effects and diamagnetic drift stabilization are present. Sheared flow equilibria are more challenging in curvilinear simulations, and as they are not directly germane to the goal of this thesis we will not examine them for cylindrical modes. We will see that the electron diamagnetic drift is an effective means of slowing double-tearing mode growth in cylindrical geometry, however due to asymmetric equilibria and the presence of an ideal instability the impact varies greatly with the location of the pressure gradient.

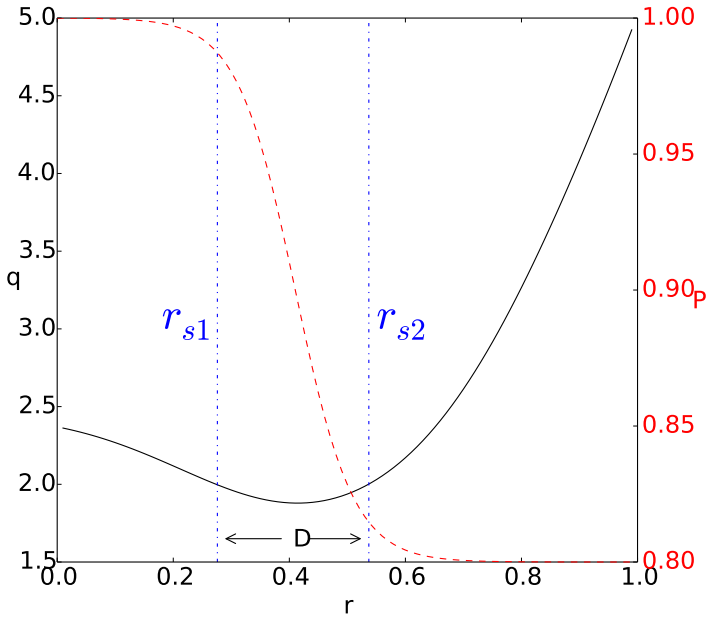

Figure 6-1: Example cylindrical safety factor(black) and pressure gradient(red) profiles. $q(r)$ is calculated using Eqn. 2.20 with the parameters in Eqn. 2.21 and $q_0 = 2.5$, which results in two $q = 2$ rational surfaces at $r = r_{s[1,2]}$ separated by a distance $D \approx 0.26$. The pressure gradient is found using Eqn. 2.22 with parameters $N_0 = 1$, $N_b = 0.8$, $\delta_N = 0.1$, $r_0 = (r_{s1} + r_{s2})/2$, constant electron temperature $T_e = 1$, and assuming cold ions $\tau = 0$.

6.1 Force-free resistive

The resistive double-tearing mode is strongly localized, provided that the surfaces are sufficiently close to each other that the analysis of Chapter 3 holds. Our cylindrical equilibrium, described by Equation 2.20 and shown in Figure 6-1, has two $q = 2$ surfaces at r_{s1} and r_{s2} which will be unstable to $m = 2$, $n = 1$ resonant modes. If the separation between these two surfaces is sufficiently small compared to the minor radius of the cylinder ($D = r_{s2} - r_{s1} \ll 1$) then between the surfaces the system will be Cartesian to the lowest order with curvilinear corrections. Cylindrical modes will then resemble the slab DTM solution wrapped around an annulus. To better illustrate this, we have used a 2D plot of the widely spaced, symmetric double-tearing mode flux function and projected it on the annulus of a cylinder (repeated twice to account for the $m = 2$ mode number) using image manipulation software. Figure 6-2 shows the original slab mode and its cylindrical projection, and will serve as prediction of the cylindrical eigenmode.

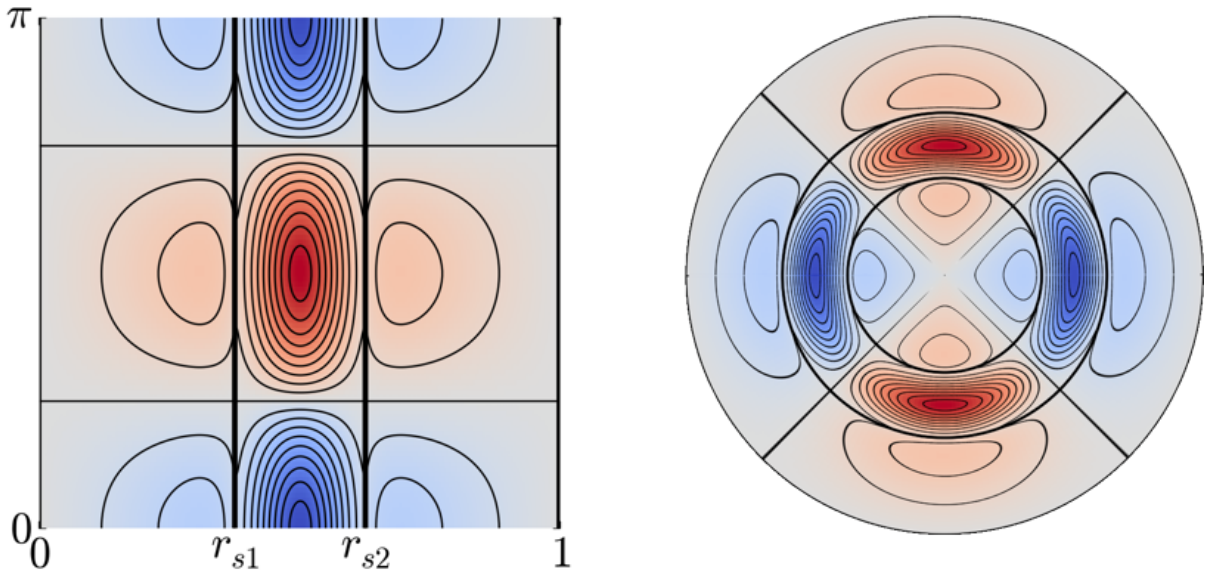

Figure 6-2: The perturbed flux function ψ of a widely space ($x_s = 1.0$) slab DTM (Chap. 3) is mapped onto the annular region of a cylinder bound by the $q = 2$ rational surfaces as a prediction of the cylindrical DTM eigenmode. To lowest order this transformation reproduces the actual cylindrical result (Fig. 6-3).

In practice the largest deviation from the previous analytic theory emerges from the

asymmetry of the system. For simplicity the boundary layer theory assumed that the equilibrium magnetic field, and thus the singular layers, were symmetric [39]. The safety factor profile we have chosen (Fig. 6-1) has steeper shear at the outer (r_{s2}) surface than the inner (r_{s1}). This asymmetry is common to the tokamak design due to the use of a hot, core plasma current to generate the poloidal magnetic field. Despite this imbalance several simulation studies have established that cylindrical and toroidal double-tearing modes exhibit the same coupling and scaling behavior as the slab theory, i.e. the dependence of the growth rate scales with resistivity like $\gamma \sim \eta^{\alpha}$ for $1/3 \leq \alpha \leq 3/5$ based on the coupling parameter kD, where the system asymmetry requires that the full inter-resonant spacing D replace symmetric current sheet space x_s [9, 10, 64].

With regard to these studies we note that the $\gamma \sim \eta^{3/5}$, constant ψ DTM behavior, which we observed in Cartesian geometry with widely separated modes, is rarely the fundamental (lowest m) instability in the system. It may instead be present as a higher harmonic. The constant ψ approximation requires both widely spaced modes and low magnetic shear such that the system is deeply ideally stable. In curvilinear configurations the confined geometry restricts the maximum spacing, thus one must rely on large wave numbers in order to achieve this regime. In our helically symmetric system, however, k is dependent on the mode number m and n, and thus directly proportional the safety factor $k \propto q = m/n$. Therefore the dependence of the mode on resistivity increases with increasing m. The magnetic shear reversal, which allows two nearby surfaces with the same safety factor, typically occurs (in tokamaks) near the center of the plasma where q is small, thus the lowest m on a rational surface is generally not a constant ψ DTM mode. Our equilibrium has two $q = 2$ surfaces spaced a distance $D \approx 0.26$ apart, which results in the fundamental $m = 2$, $n = 1$ mode being the fastest growing instability. The growth rate of this DTM is somewhere in the intermediate regime with $\gamma \sim \eta^{0.48}$ (Fig. 6-4).

The intermediate coupling regime of this DTM results in a mode which is more tightly confined between the two rational surfaces than the prediction made in Fig. 6-2 using a

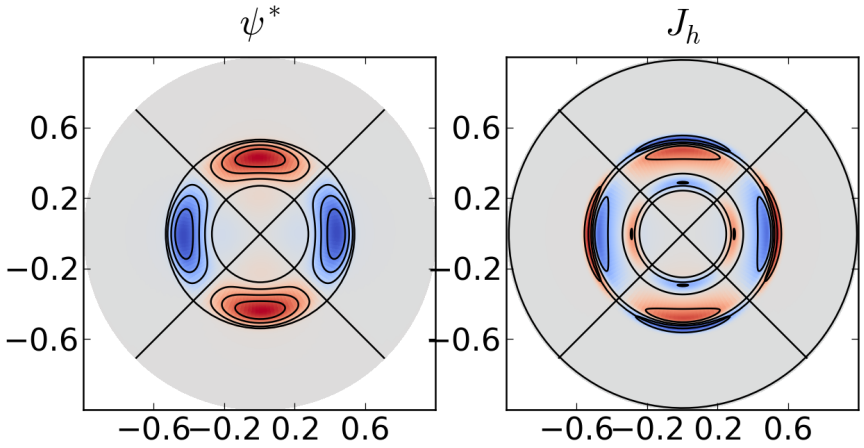

Figure 6-3: The helical flux function ψ^* and axial current J_h of a force-free, $m = 2$, $n = 1$ double-tearing eigenmode in cylindrical geometry with an inter-resonant distance of $D \approx 0.26$. The larger equilibrium magnetic shear at the outer resonant surface results asymmetry in the eigenmode favoring the r_{s2} layer. This example is in the intermediate DTM coupling regime, resulting in a more localized mode than the prediction drawn from the $x_s = 1.0$ slab DTM in Figure 6-2.

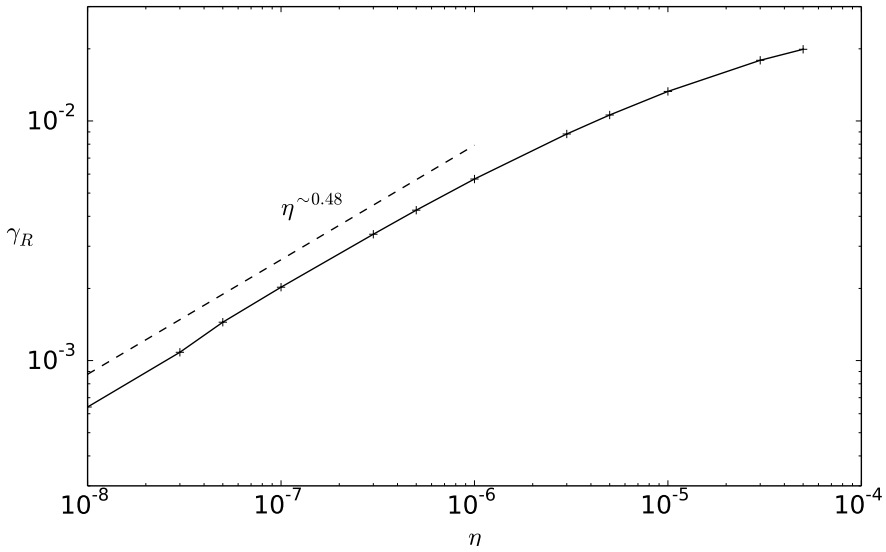

Figure 6-4: Resistive scaling of the force-free cylindrical double-tearing mode with spacing $D \approx 0.26$. At this inter-resonance distance the growth rate γ_R increases with resistivity η as $\gamma_R \propto \eta^{0.48}$, placing it in the intermediate coupling regime when compared to the boundary layer theory of Chapter 3.

Cartesian $x_s = 1.0$ mode, however the large scale features of the actual helical eigenmode (plotted in Fig. 6-3) are consistent with our claim that the cylindrical, force-free DTM is, to lowest order, described by the slab theory. The flux function ψ^* shows a clear asymmetry favoring the outer surface, which we expect based on the steeper shear of the safety factor profile at r_{s2}. To better examine the mode structure, Fig. 6-5 compares the 1D linear eigenfunctions of plasma displacement ξ, flux ψ^*, and out-of-plane/axial current J_h for the close and wide symmetric slab double-tearing mode and the $D = 0.26$, $m = 2$, $n = 1$ cylindrical DTM. The asymmetric cylindrical eigenmode shares characteristics with both Cartesian separations. The weaker shear at the inner most cylindrical surface has the features of the constant ψ $x_s = 1.0$ Cartesian mode, whereas the outer surface more closely resembles the nonconstant ψ $x_s = 0.25$ mode. In cylindrical geometry the eigenfunction is weighted toward the surface with greater magnetic shear, but despite the asymmetry the mode evolution is consistent with the boundary layer theory of the symmetric Cartesian DTM.

6.2 Ideal instability

The primary goal of tokamak research is to achieve fusion by confining a hot, dense core of plasma using magnetic fields. Pressure gradients naturally occur in the plasma as a necessary byproduct. Such profiles are generally peaked in both density and temperature at the central core of the plasma column and fall off toward the edge of the device. In this work we approximate this pressure curve with the density gradient plotted in red on Fig. 6-1 and of the tanh form introduced in Equation 2.22, reproduced below:

$$\rho(r) = N_0 \left\{ 1 - (1 - N_b) \frac{\tanh(r_0/\delta_N) + \tanh[(r - r_0)/\delta_N]}{\tanh(r_0/\delta_N) + \tanh[(1 - r_0)\delta_N]} \right\} \tag{6.6}$$

This function is modeled after that in Ref. [64] and designed to resemble the profiles which are seen to accompany internal transport barriers (ITBs) in reverse-shear devices [59]. For this

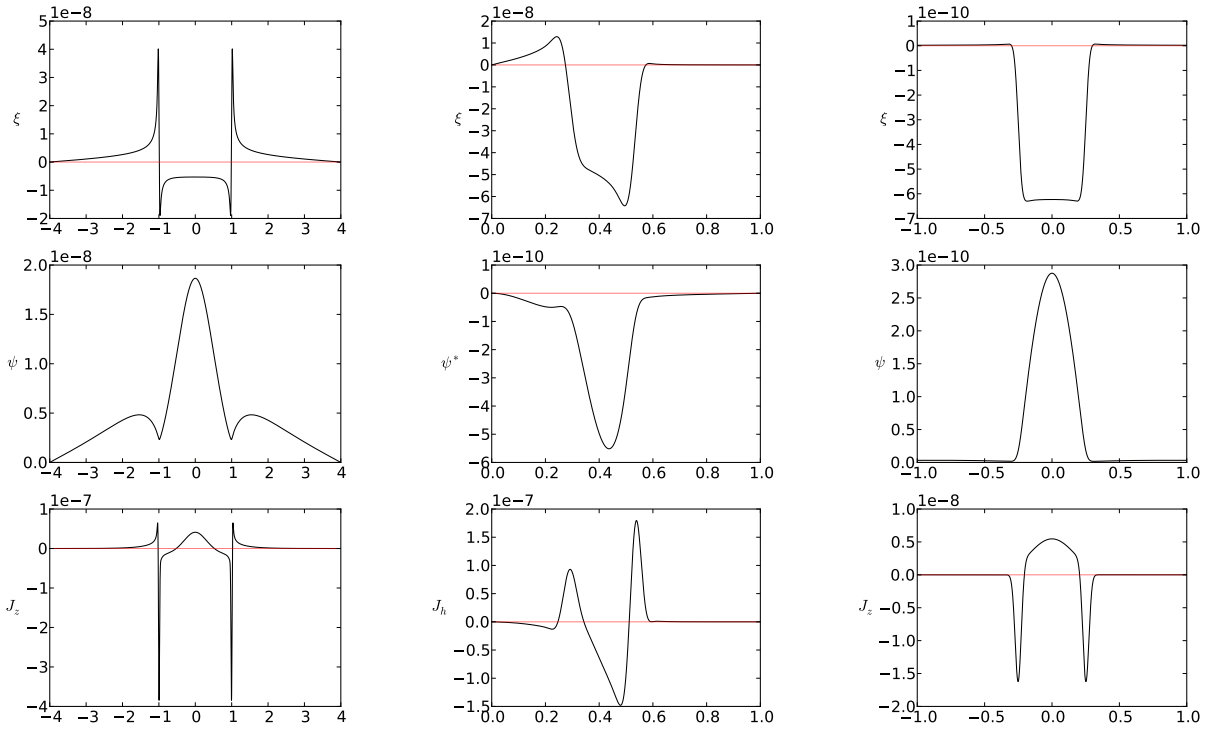

(a) $x_s = 1.0$ Cartesian **(b)** $D = 0.26$ Cylindrical **(c)** $x_s = 0.25$ Cartesian

Figure 6-5: Near the inner surface the cylindrical DTM eigenfunction (center) has features of the constant ψ Cartesian singular layers (left). The outer surface, which has greater magnetic shear, more closely resembles the closely coupled, nonconstant ψ slab mode (right). Globally the eigenfunction is a combination of the two, with the stronger nonconstant ψ features dominating.

study we work in the cold-ion regime ($\tau = 0$) and take the equilibrium electron temperature to be constant. This configuration sacrifices some features of the observed device profiles (particularly finite ion temperature and temperature gradients) in favor of better numerical stability and greater flexibility to conduct scaling studies. The cold ion approximation is chosen to avoid equilibrium plasma flows when the diamagnetic drift is introduced, which are numerically challenging in the `MRC-3d` code. Equilibrium electron temperature is taken as a constant both to allow easier shaping of the pressure profile (since p will depend only on $\rho(r)$) and to avoid certain classes of high wavenumber instabilities which can be driven by steep temperature gradients. These approximations are not expected to impact the general results of our DTM analysis, though they will not allow direct comparison to experimental data.

In Cartesian geometry introducing a pressure gradient within the framework of resistive MHD may impact the reconnection process by changing the normalization or causing asymmetries in the plasma flow, but the character of the instability is not significantly affected. The variable curvature of the equilibrium magnetic field in cylindrical geometry may, however, interact with a pressure gradient to form an unstable ideal MHD mode. Our reversed shear DTM equilibrium appears to be unstable to such an ideal instability.

The prototype example of the interaction between an ideal MHD instability and a reconnecting layer is the $m = 1$ kink-tearing mode [3, 60]. This particular instability plays a large role in the 'sawtooth oscillation' process commonly observed in conventional tokamaks with core safety factors less than $q = 1$, and has been extensively studied. Fundamentally the linear instability is composed of two parts: the current driven ideal MHD kink mode (which is marginally stable when force-free and driven unstable by a finite pressure gradient) and the resistive tearing mode. The interaction between these two mechanisms can, in the linear phase, be interpreted as an ordering of two boundary layers. The kink mode has a singular layer width of λ_H, which can be calculated in a fashion similar to the ideal region analysis of the double-tearing mode in Section 3.1.1. In fact, the outer region analysis of the Cartesian

boundary layer theory is based on treating the DTM as a slab-kink mode. We had found that the slab-kink mode was always stable, $\gamma_H \leq 0$. The opposite is true for the $m = 1$ kink mode in cylindrical geometry. It is, in the absence of a pressure gradient, marginally stable ($\gamma_H = 0$), which corresponds to a layer width $\lambda_H = 0$. A non-uniform pressure profile results in a finite layer and growth rate, so that $\lambda_H \geq 0$. When resistivity η is finite, therefore, the evolution of the mode is governed by the ordering of the resistive layer width δ_η and the ideal kink mode layer width λ_H. If $\lambda_H = 0$ the kink mode is marginally stable, the mode growth is governed entirely by the resistive tearing mode, and we recover the $\gamma \sim \eta^{1/3}$ nonconstant ψ scaling. If, however, λ_H is larger than δ_η the width of the current layer is determined by ideal instability alone and the growth rate of the mode is independent of resistivity ($\gamma \sim \eta^0$). The latter case allows us to develop an effective marker of ideal MHD instability using resistive scaling studies; if at some finite value of resistivity the growth rate and current sheet width no longer change with variations in η then the system is ideal MHD unstable. Furthermore, if the mode is driven unstable by the pressure gradient we expect that variations in the density profile will change the η cutoff point and current sheet width.

Introducing a pressure profile to our cylindrical DTM equilibrium shows clearly, based on the above criterion, the emergence of an ideal MHD instability. With the center of the pressure gradient between the two surfaces at $r_0 = (r_{s1} + r_{s2})/2$, we run a full resistivity scaling at several different values of the pressure gradient width δ_N. The density scale height is held fixed at $N_b = 0.8$, and the electron temperature is a constant $T_0 = 2.0$ (for this section only). Figure 6-6 shows the results of this scaling study. For each given pressure profile, as denoted by the gradient width δ_N, there is a clear cutoff η below which the growth rate does not depend on resistivity. The measured asymptotic ideal growth rates increase as the steepness of the pressure gradient increases (δ_N decreases). This independence from resistivity can also be observed when comparing the scaling of the outer resonant surface current layer with η for the force-free and $\delta_N = 0.05$ equilibria (Fig. 6-7). Whereas the force-free layer continually narrows with decreasing η, in the presence of a pressure gradient

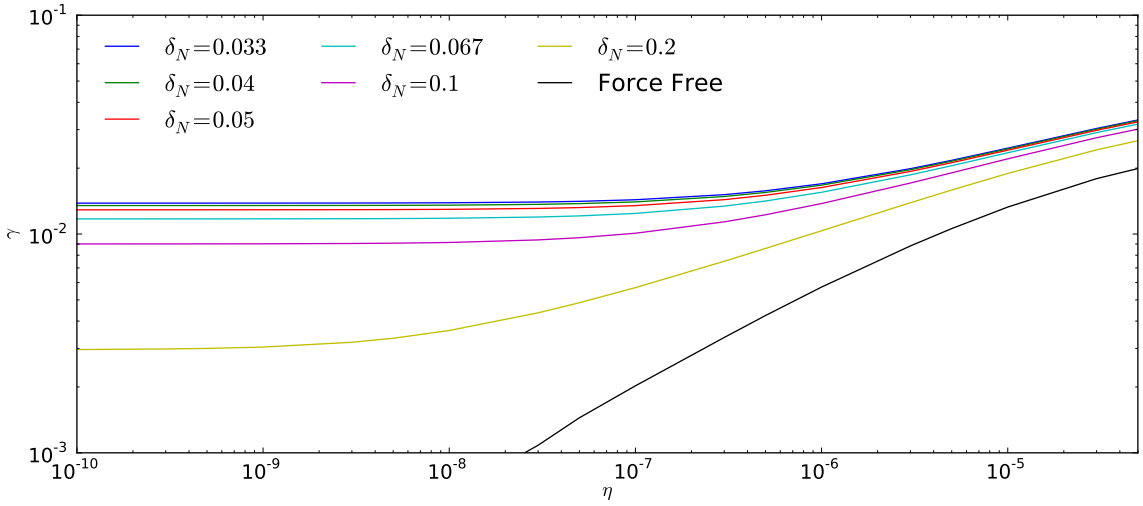

Figure 6-6: Measured linear growth rates of the resistive, $D \approx 0.26$ cylindrical DTM in the presence of a pressure gradient centered between the two surfaces at $r_0 = (r_{s1} + r_{s2})/2$. At low resistivities γ no longer depends on resistivity, suggesting an ideal MHD instability. The location and magnitude of the asymptotic ideal growth rate increase with increasing pressure gradient (decreasing gradient width δ_N).

a minimum width is evident. This width is analogous to the λ_H parameter of the $m = 1$ kink mode.

Based on analogy to the $m = 1$ kink-tearing mode, it is clear that the introduction of a pressure gradient to our cylindrical, reversed shear equilibrium couples the $m = 2$, $n = 1$ double-tearing mode to some form of ideal MHD instability with the same mode numbers. At present the nature of this instability is not understood, nor the mechanism by which it couples to the resistive DTM. A sample eigenmode (Fig. 6-8) appears to be fundamentally of the same form as the standard DTM mode, with several modifications. The inner resonant surface now bears more resemblance to a nonconstant ψ tearing mode than in the force-free DTM (Fig. 6-3) and the eigenfunction between the layers is closer to the strongly coupled $x_s = 0.25$ slab DTM. These changes reinforce the analysis of Chapter 3, which concluded that the DTM coupling is related to the stability of an ideal MHD kink mode.

The discovery of this ideal MHD mode complicates but does not invalidate possibility of FLR effects stabilizing the double-tearing mode. Diamagnetic drifts have been shown to be strongly nonlinearly stabilizing for the ideally unstable $m = 1$ kink-tearing modes around which we have framed this discussion [41], and are a likely candidate for DTM stabilization

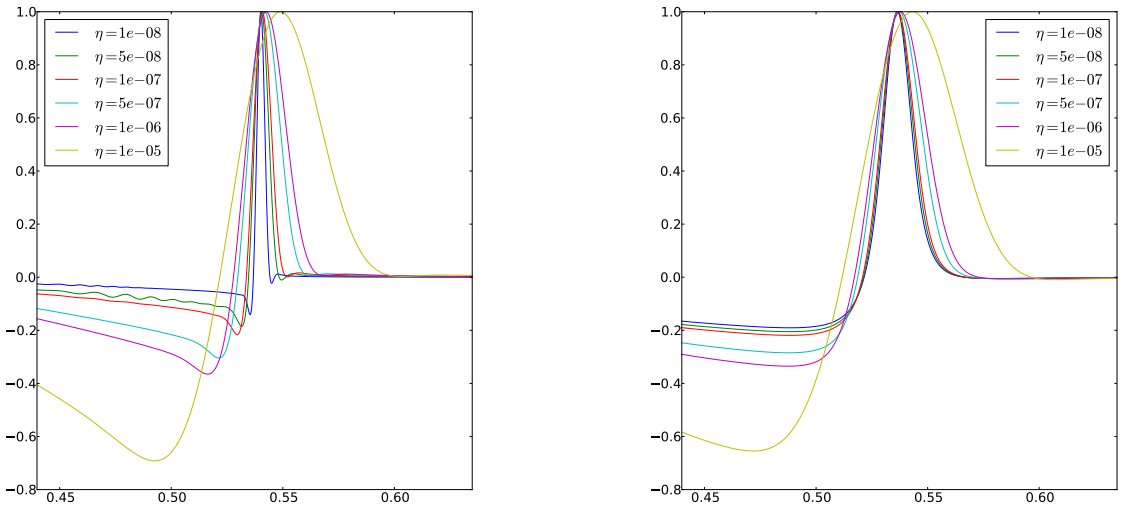

(a) Force-free (constant pressure)

(b) $\delta_N = 0.05$

Figure 6-7: In the presence of a pressure gradient the singular layers of the cylindrical DTM exhibit a minimum, ideal layer width for decreasing resistivity(right). The force-free layers (left) to not show this saturation. These plots show the layers via the axial current J_h at the outer $q = 2$ rational surface (r_{s2}, though the same behavior is evident in the dynamic variables ξ and ψ^* and at the interior surface (r_{s1}).

as well.

6.3 Diamagnetic drifts

Now that we have established the similarities and differences between our $m = 2$, $n = 1$ cylindrical DTM and the Cartesian boundary layer theory, we are prepared to reintroduce FLR effects and consider the effect of diamagnetic drifts. Due to the inherent radial asymmetry between the $q = 2$ resonant surfaces we need to account for three important factors not present in the symmetric slab analysis of Chapter 5. First we must contend with the differing magnetic shears, and thus singular layer characteristics, at the inner and outer $q = 2$ rational surfaces. Secondly the ω_* drifts resulting from the monotonic pressure profile (Fig. 6-1) will all be counter-clockwise poloidal rotations with a single peak frequency:

$$\omega_*(r) = \boldsymbol{k} \cdot \boldsymbol{v}_{*e} = -\frac{m d_i T_0 B_h}{r \rho B^2} \frac{\partial \rho}{\partial r} \tag{6.7}$$

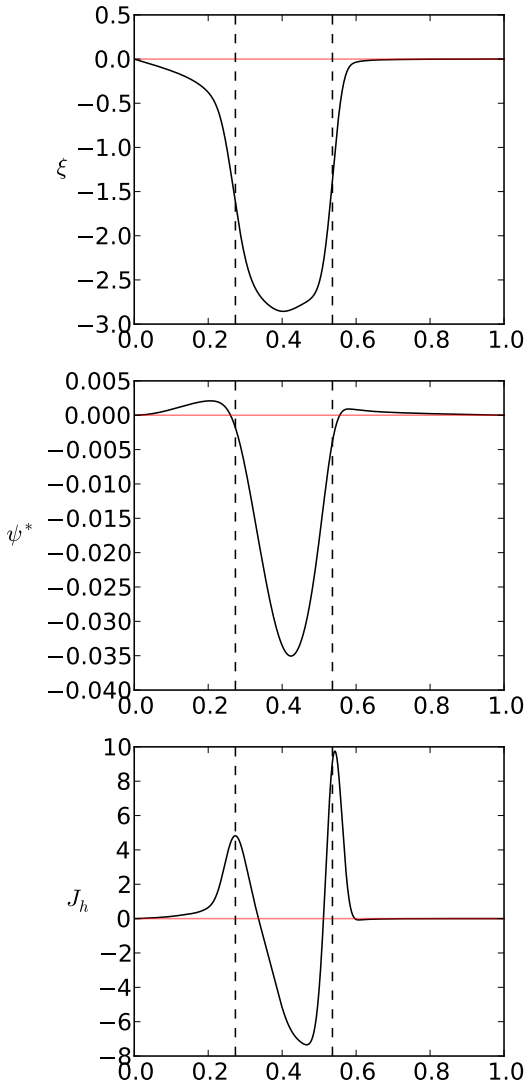

Figure 6-8: Linear eigenmodes for the $D \approx 0.26$, $\eta = 1 \times 10^{-5}$ DTM in the presence of a $\delta_N = 0.05$, $N_b = 0.8$ density gradient centered at $r_0 = (r_{s1} + r_{s2})/2$. The presence of an ideal instability causes this mode to more closely resemble the closely coupled Cartesian slab DTM.

Note that to an order r/R correction the poloidal unit vector $\hat{u}$, in which direction the mode rotates, is aligned with the coordinate unit vector $\hat{\theta}$ (see Eqn. 6.3). Thus we cannot produce a differential drift $\Delta\omega_*$ without also having the magnitudes of the drifts be different at each surface. Finally, any modifications to the pressure profile (necessary to produce variable ω_* at fixed d_i) will also modify the characteristics of the underlying ideal MHD instability.

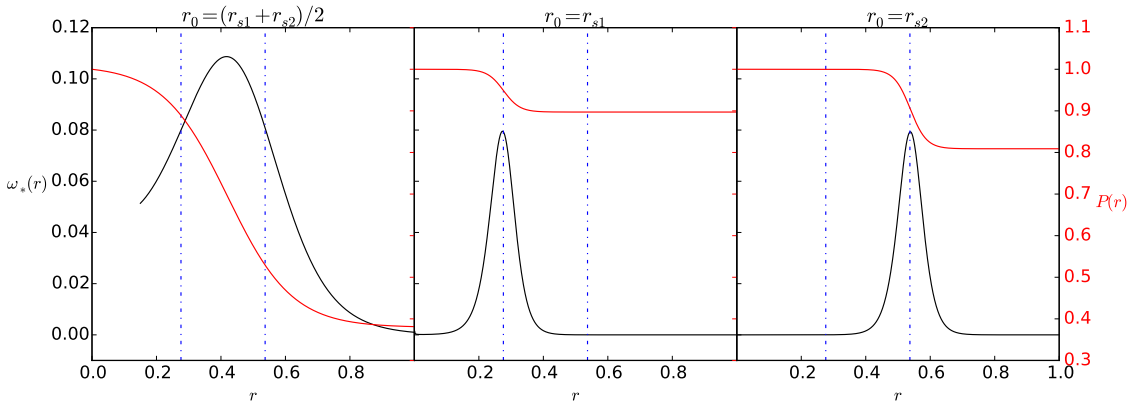

Figure 6-9: Example electron diamagnetic drift profiles (black lines) and the pressure profiles (red lines) that produce them. Type 1 profiles (left) produce equal drifts at both surfaces; type 2 (center) only produce significant drift at the inner surface; type 3 (right) only produce significant drift at the outer surface. All pictured pressure gradients are chosen to produce a drift of $\omega_* = 0.04$ at the specified surface(s) when $d_i = 0.1$.

In order to simplify our analysis we will consider only three possible locations for the center, and thus maximum gradient, of the $P(r)$ pressure profile: (1) equidistant between the two rational surfaces ($r_0 = (r_{s1} + r_{s2})/2$); (2) centered on the inner resonant surface ($r_0 = r_{s1}$); and (3) centered at the outer resonant surface ($r_0 = r_{s2}$). To be consistent with our study in slab geometry (Chap. 5) we will maintain the definition of the differential drift as the magnitude of the ω_* difference between the two surfaces, i.e. $\Delta\omega_* = |\omega_*(r_{s1}) - \omega_*(r_{s2})|$. Only profiles of type (2) and (3) can generate appreciable differential drift, and to minimize the necessary pressure gradients we will focus on tightly confined profiles with δ_N values of 0.1 and 0.05 that result in negligibly small ω_* values at the surface opposite the gradient peak, i.e. a density shear centered at $r_0 = r_{s2}$ will produce a negligibly small diamagnetic drift at r_{s1}. Profiles of type (1) cannot produce significant differential drift and we will instead use a wide value of $\delta_\rho = 0.2$ to set $\omega_*(r_{s1}) \approx \omega_*(r_{s2})$, allowing a comparison between

the efficacy of differential drift versus uniform diamagnetic stabilization. Examples of all three types of profile are plotted in Figure 6-9.

The exact equilibrium pressure profiles for our study are generated via an iterative initialization script. The core plasma density (maximum of the profile) is held fixed at $N_0 = 1.0$. We choose the cold ion regime ($\tau = 0$) with a constant electron temperate of $T = 1.0$ and ion skin depth of $d_i = 0.1$. For each of the profiles described above δ_N is held fixed and N_b is chosen to give the desired values of $\omega_*(r_{s1})$ and $\omega_*(r_{s2})$. As the dependence of the ideal MHD instability (Section 6.2) on the pressure profile is not well understood, we also run each profile in the resistive MHD regime ($d_i = 0.0$) to separate diamagnetic effects from the pressure driven behavior. The results of this study for the equal drift (type (1)) and differential drift (type (2) and (3)) profiles are shown in Figures 6-10, 6-11, and 6-12 respectively.

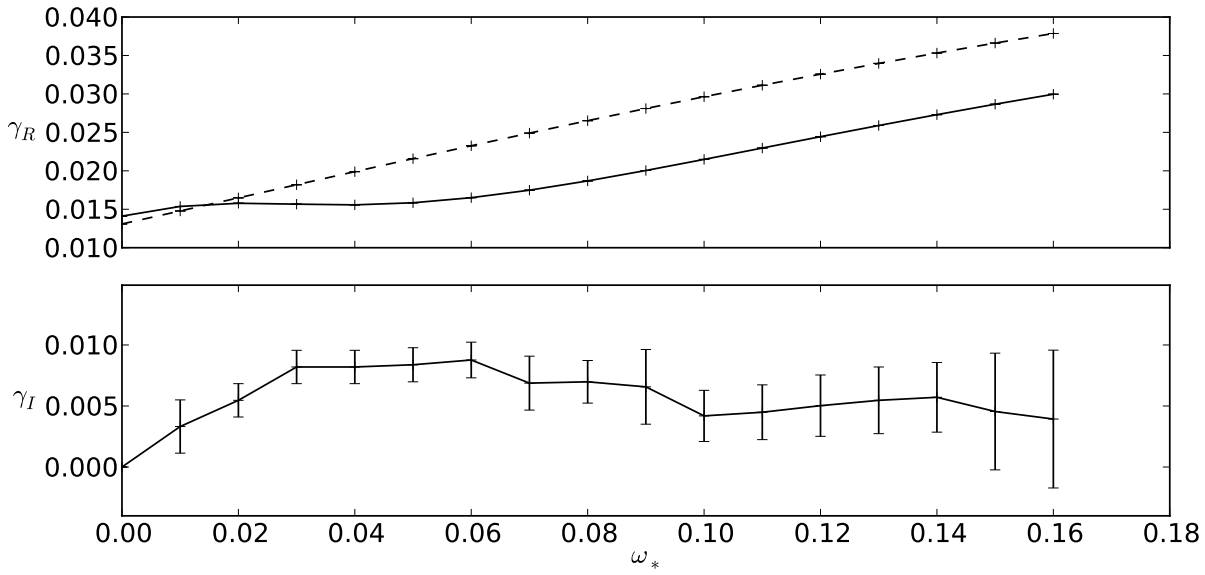

Figure 6-10: A pressure profile with $\delta_N = 0.2$ centered between the two rational surfaces at $r_0 = (r_{s1} + r_{s2})/2.0$ results in an equal diamagnetic drift at both layers. The solid lines are fitted growth rates (γ_r) and eigenmode drifts (γ_I) of simulations with increasing pressure gradient for $d_i = 0.1$, plotted as a function of the resultant drift at the layers (ω_*). The stabilizing FLR effects within the singular layers result in a uniformly lower growth rate compared to the resistive MHD modes for equivalent pressure gradients (dashed lines), which are dominated by enhancement of the ideal MHD instability.

Only by centering the pressure profile at the outer r_{s2} resonant surface are we able to achieve any appreciable decrease in the growth rate γ_R. In all three cases there is an apparent competition between the stabilizing effects of the diamagnetic drifts and the destabilization

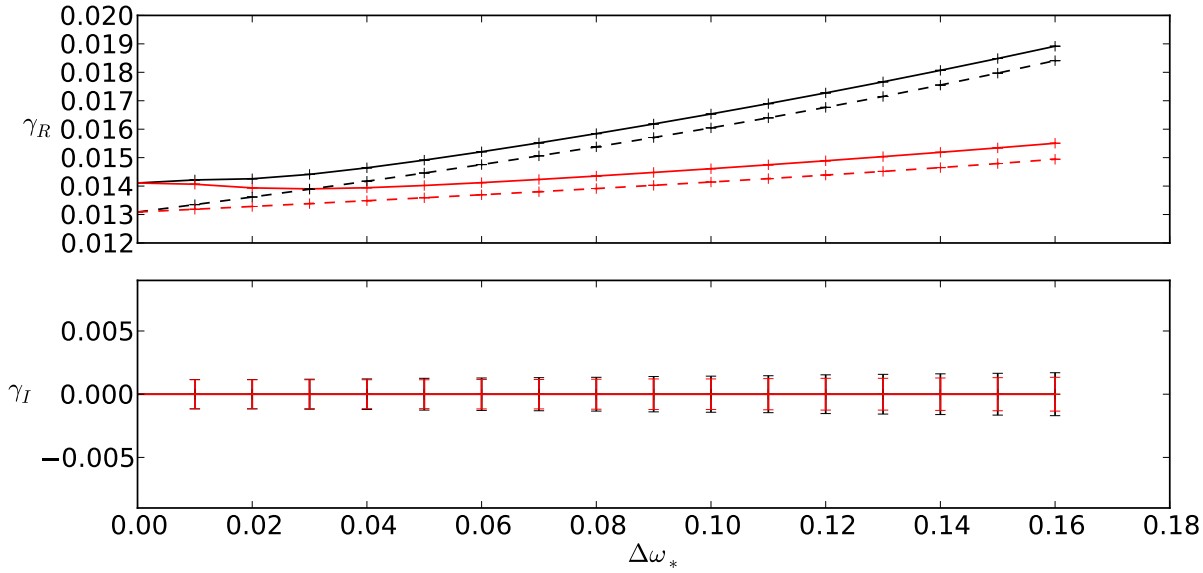

Figure 6-11: Pressure profiles centered at the inner resonant surface ($r_0 = r_{s1}$) with narrow widths $\delta_N = 0.1$ (black lines) and $\delta_N = 0.05$ (red lines) produce, for $d_i = 0.1$ (solid lines), a differential diamagnetic drift between the two surfaces of $\Delta\omega_*$. Compared to the resistive MHD ($d_i = 0$) growth rates for equivalent pressure profiles (dashed lines) the growth rate γ_R is enhanced by FLR effects. Only the inner, weaker surface experiences any stabilizing diamagnetic drift, thus the dominant outer surface is enhanced by the nonzero d_i and increases the mode growth.

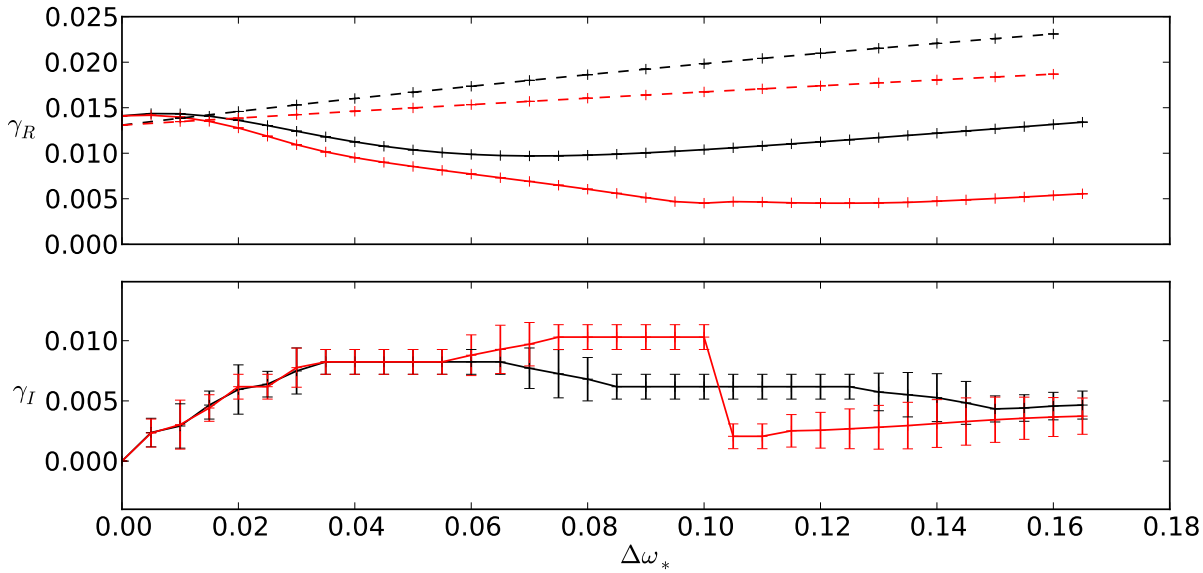

Figure 6-12: Pressure profiles centered at the outer resonant surface ($r_0 = r_{s2}$) with narrow widths $\delta_N = 0.1$ (black lines) and $\delta_N = 0.05$ (red lines) produce, for $d_i = 0.1$ (solid lines), a differential diamagnetic drift between the two surfaces of $\Delta\omega_*$. The fitted growth rates γ_R feature an inflection point in the neighborhood of $\Delta\omega_* \approx 0.03$, suggesting decoupling of the resonant surfaces. By locating the diamagnetic drift at the stronger, outer singular layer we are able to achieve substantial reductions in the growth rate compared to equivalent pressure profiles in resistive MHD ($d_i = 0$, dashed lines).

of the ideal MHD mode with increasing pressure gradient. Above some value of the imposed drift the variation in growth rates tracks that the of the resistive mode, for which the ω_* effects are absent. The critical ω_* at which this transition occurs is different for each profile type. Equal drifts exhibit a flat growth rate up to $\omega_* \approx 0.06$, and the Hall MHD growth rates are uniformly lower than their resistive counterparts for the same equilibrium. When the drift is centered at the inner surface, however, γ_R is dominated by the scaling of the pressure driven mode above $\Delta\omega_* \approx 0.03$, and the FLR growth rates are uniformly higher than their resistive counterpoints. Only drifts centered at the outer rational surface exhibit behavior similar to that observed in slab, with a smooth decrease in the growth rate until a large pressure gradient is present.

When examining the force-free resistive instability (Sec. 6.1) we noted that the eigenmodes favored the outer most rational surface, and that this was consistent with the shear (and thus magnetic free energy) being stronger near r_{s2}. The observed differences between centering the diamagnetic drift at each surface may also be explained by this asymmetry. When the inner, weaker surface is suppressed the increasing pressure gradient strengthens the outer layer and the growth rate increases. Locating the drift at r_{s2}, however, stabilizes the primary driving surface of the instability and results in a significant decrease in γ_R. At large drifts ($\Delta\omega_* \gtrsim 0.1$), however, the pressure driven mode seems to again control the instability, though at a greatly reduced growth rate compared to the resistive MHD counterpart.

In slab geometry we concluded that decoupling of the two tearing layers is a crucial element of any stabilization mechanism. The eigenmode drift frequencies γ_I extracted via Fourier analysis (lower plots in Figs. 6-10, 6-11, and 6-12) show, however, evidence of only a single drifting mode. For profiles without any differential drift (type (1)) this behavior is expected as there is no decoupling mechanism. The single mode behavior of type (2) and (3) differential drift profiles is again a consequence of the magnetic asymmetry; when the modes are decoupled the outer, more strongly sheared surface has a much larger growth rate and thus is the only mode observed in the initial value simulations of `MRC-3d`. The dominance of

the outer r_{s2} surface can be seen clearly in γ_I measurements for the differential drift profiles. When the peak diamagnetic drift is located at the inner surface (Figure 6-11) the drift at the outer surface is negligible and thus the measured eigenmode frequency of the most unstable mode remains at 0 for all profiles. In contrast, when the peak ω_* is at the outer surface (Figure 6-12) a finite γ_I appears.

The diamagnetic drift effects on the eigenmodes are significantly more complicated than in the symmetric slab case, and cannot be easily parsed in the context of odd and even parity mixing until some bifurcation point is reached. Much can be learned, however, by comparing the Hall MHD eigenmodes for a given pressure profile to their resistive counterparts.

The most straight-forward case is the equal drift (type (1)) modes, shown in Figure 6-13. The general form of the eigenfunction is the same for both the resistive and Hall MHD modes. Some variations are evident near the current layers due to finite Larmor radius effects. Without a differential drift between r_{s1} and r_{s2} the diamagnetic drift can, to lowest order, only impact the internal layer solution. The observed deviations near the resonant surfaces are therefore a combination of ρ_s scale enhancements and local ω_* interference.

When the pressure gradient is centered at the outer resonant surface the fitted growth rates γ_R show an inflection point in the neighborhood of $\Delta\omega_* \approx 0.03$ (see Fig. 6-12), which is the asymmetric cylindrical analog to the decoupling point observed in slab geometry. In support of this interpretation, Figure 6-14 compares the resistive and Hall MHD modes for the more localized $\delta_N = 0.05$ profile at a differential drift of $\Delta\omega_* = 0.02$, below the inflection point. In the presence of FLR effects the resistive eigenfunction remains the dominant contribution to the DTM, though due to finite rotation frequency it appears as the imaginary part of the eigenmode (extracted via Fourier analysis). Taking the place of the antisymmetric mode is a new form with two peaks near the resonant surfaces for all the dynamic variables but a reduced connection between the two layers. This double peaked structure may be a slower growing eigenmode of the system, as we found in slab geometry, or may indicate a more complicated decoupling mechanism in asymmetric configurations.

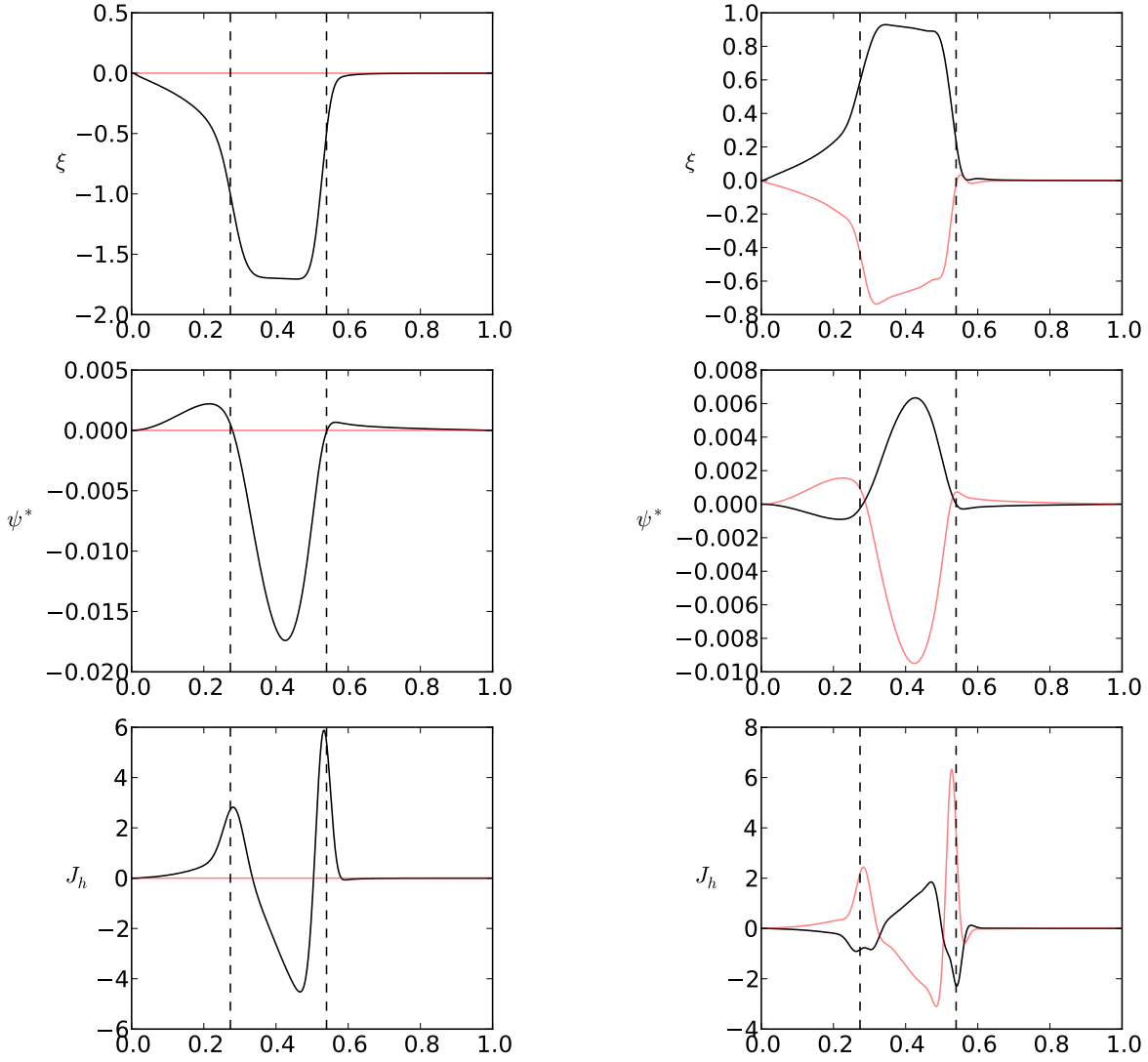

(a) Resistive eigenmode

(b) $d_i = 0.1$ eigenmode

Figure 6-13: Resistive (left) and Hall MHD (right) DTM eigenmodes in the presence of a pressure gradient centered between the two rational surfaces at $r_0 = (r_{s1} + r_{s2})/2$ with $\delta_N = 0.2$ and $N_b = 0.381$. For $d_i = 0.1$ this produces a diamagnetic drift of $\omega_* = 0.08$ at both singular layers. The drifting eigenfunctions are largely the same as the resistive except near the resonant layers where FLR effects are significant. The eigenmode frequency of the Hall MHD mode, extracted via Fourier analysis, is $\gamma_I = 0.007 \pm 0.002$, significantly less than the equilibrium drift.

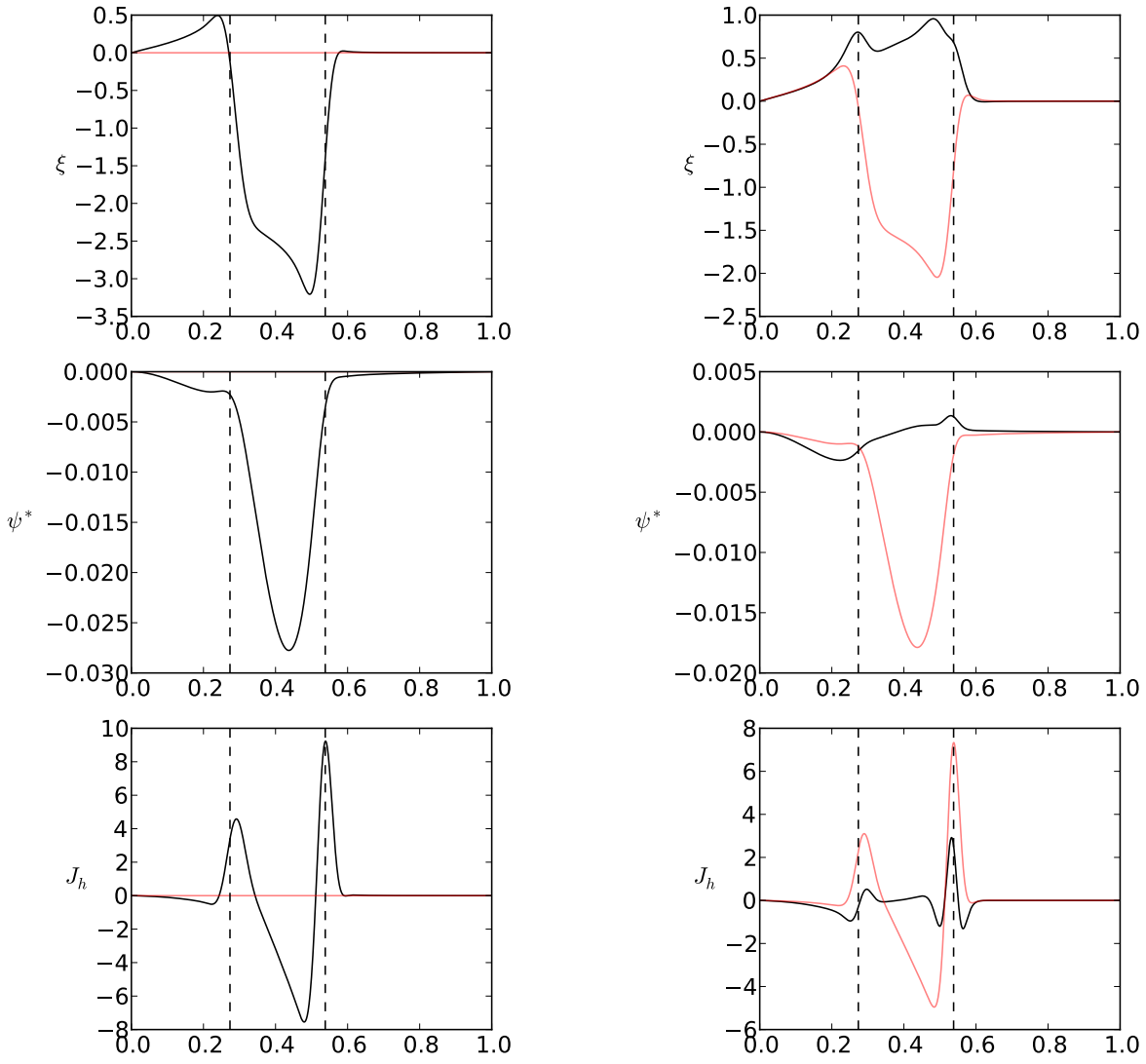

(a) Resistive eigenmode

(b) $d_i = 0.1$ eigenmode

Figure 6-14: Resistive (left) and Hall MHD (right) DTM eigenmodes in the presence of a pressure gradient centered at the outer rational surface $r_0 = r_{s2}$ with $\delta_N = 0.05$ and $N_b = 0.949$. For $d_i = 0.1$ this produces a diamagnetic drift of $\omega_* = 0.02$ at the outer layer and no drift at the inner, resulting in a differential drift of $\Delta\omega_* = 0.02$. The imaginary part of the drifting eigenmode (red) is of the same form as the resistive, and the real (black) shows a new behavior with less coupling between the surfaces, suggesting the asymmetric cylindrical analog to the pre-decoupling sheared modes of Chapters 4 and 5. The Hall eigenfunction has a measured mode frequency of $\gamma_I = 0.006 \pm 0.001$.

Figure 6-15 shows a strongly stabilized DTM with the pressure gradient at the outer surface and a differential drift of $\Delta\omega_* = 0.08$. The eigenmodes show a strong departure from the resistive modes in the same pressure profile, analogous to the 'decoupled' regime. Unlike the slab modes, however, the inner surface still features a current layer of the same order of magnitude as the outer. The flux function ψ^* near r_{s1} is, for the Hall mode, substantially different than its resistive counterpart, indicating that the character of this singularity has changed. Although the layer at the r_{s2} surface has been strongly stabilized by the local diamagnetic drift it still resembles, locally, the nonconstant ψ tearing layer seen in the resistive simulation, and it is unclear how the steeper magnetic shear and coupling to an ideal MHD instability affect the 'coupled' and 'decoupled' transition and layers.

To better understand how the DTM decoupling might manifest in this equilibrium, Figure 6-16 shows a sample of the resistive and Hall MHD modes for $\Delta\omega_* = 0.08$ when the pressure profile is centered at the inner resonant surface. In this case the outer surface, which has no local diamagnetic drift, strongly resembles its resistive counterpart, as does the mode in the ideal MHD region between the two layers. The eigenfunction at the inner layer is, however, substantially different and no longer presents the characteristics of either a constant or nonconstant ψ tearing layer, though it does share some characteristics with the inner layers from Fig. 6-15. Based on this comparison, this mode is also a 'decoupled' DTM. Because the stronger, outer surface is not stabilized it maintains many of the characteristics of its undrifted form.

Two clear conclusions can be drawn from our growth rate scaling studies and the eigenmode examination. The outer surface is, as expected from the steeper magnetic shear, the dominant layer in the system. Substantially decreasing the linear growth rate requires some disruption of the resonant layer at r_{s2}. Our most effective results come from combining the stabilization of the outer surface with the mode decoupling effects initially observed in Cartesian geometry. Applying an equal drift at both $q = 2$ rational surfaces does counterbalance the pressure driven component of the mode, leaving the growth rate γ_R constant with

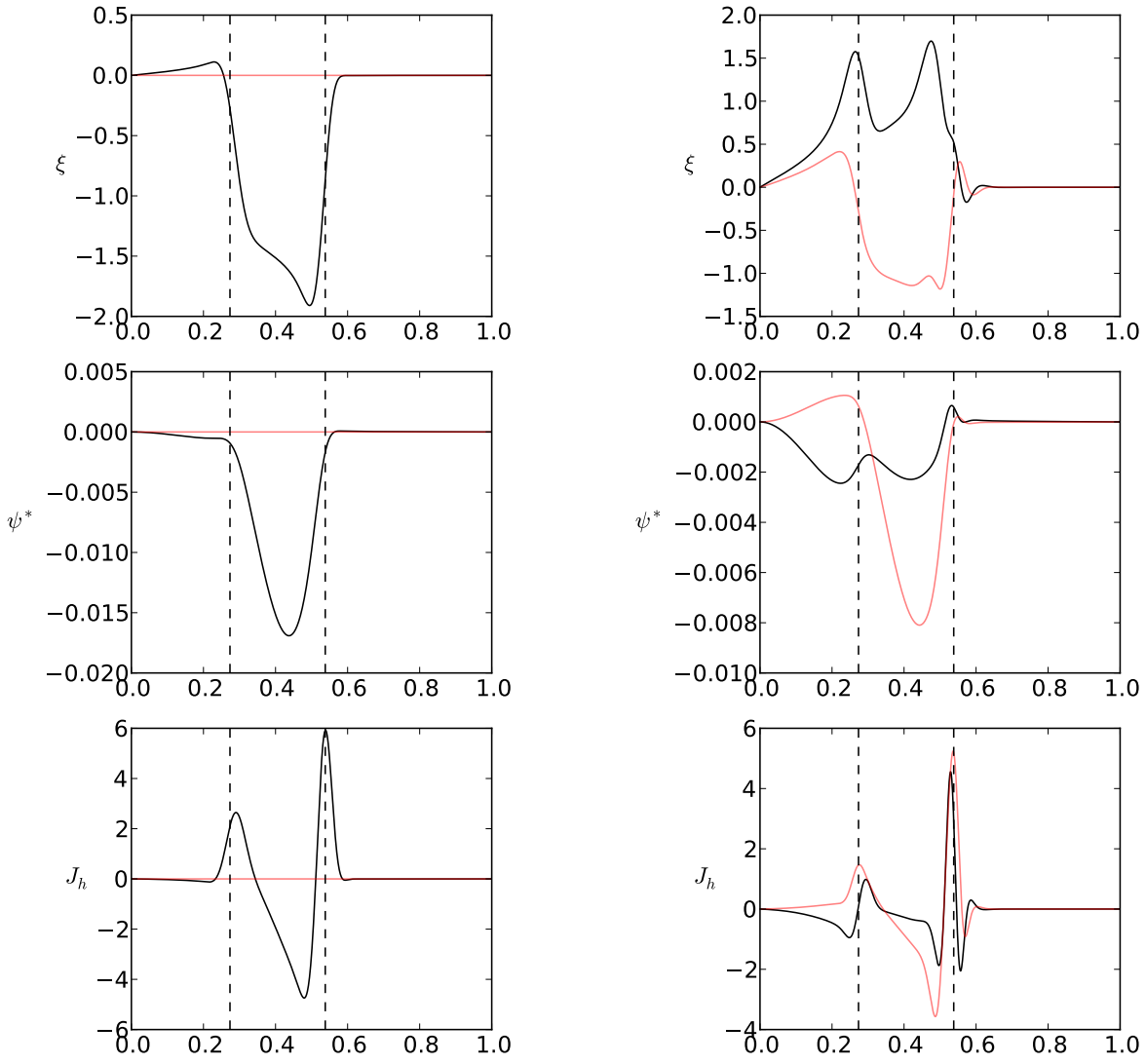

(a) Resistive eigenmode

(b) $d_i = 0.1$ eigenmode

Figure 6-15: Resistive (left) and Hall MHD (right) DTM eigenmodes in the presence of a pressure gradient centered at the outer rational surface $r_0 = r_{s2}$ with $\delta_N = 0.05$ and $N_b = 0.81$. For $d_i = 0.1$ this produces a diamagnetic drift of $\omega_* = 0.08$ at the outer layer and no drift at the inner, resulting in a differential drift of $\Delta\omega_* = 0.08$. Neither the real (black) nor imaginary (red) parts of the drifting eigenmode are of the same form as the resistive mode except in a localized region near the outer resonant surface. This mode is of the 'decoupled' form, though the dominant outer layer is also strongly suppressed by the diamagnetic drift within the layer. The Hall eigenfunction has a measured mode frequency of $\gamma_I = 0.010 \pm 0.001$

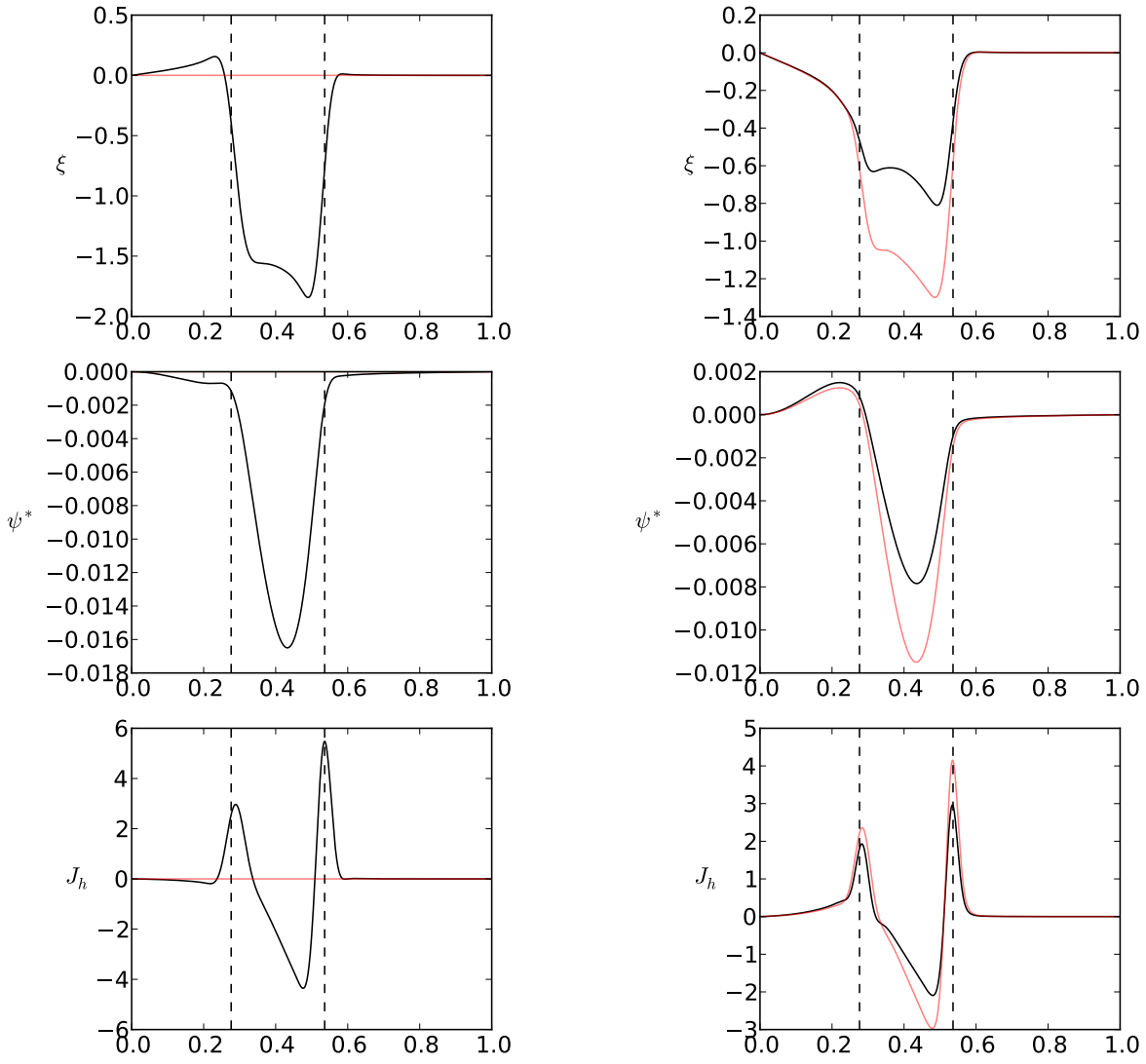

(a) Resistive eigenmode

(b) $d_i = 0.1$ eigenmode

Figure 6-16: Resistive (left) and Hall MHD (right) DTM eigenmodes in the presence of a pressure gradient centered at the inner rational surface $r_0 = r_{s1}$ with $\delta_N = 0.1$ and $N_b = 0.81$. For $d_i = 0.1$ this produces a diamagnetic drift of $\omega_* = 0.08$ at the inner layer and no drift at the outer, resulting in a differential drift of $\Delta\omega_* = 0.08$. Because the outer, dominant surface does not experience any diamagnetic drift the fastest growing eigenmode does not have a finite frequency ($\gamma_I = 0 \pm 0.001$). Hall eigenfunction shows little variation from the resistive near the r_{s2} surface but the inner r_{s1} layer is significantly modified, suggesting that this mode is in the 'decoupled' DTM regime.

increasing gradient for a short range of ω_*. This local stabilization is not, however, sufficient to reduce the DTM growth rate from its force-free value, either due to stronger driving of the ideal instability for pressure gradients located between the two surfaces or because of the absence of surface decoupling.

6.4 Discussion

The cylindrical $m = 2$, $n = 1$ double-tearing mode shares many of the fundamental features of the slab DTM we examined in previous chapters. The inherent asymmetry of the magnetic geometry causes, however, several significant differences. We have clearly identified that the singular layer at the outer rational surface is the strongest driver of the instability, which results in fundamentally asymmetric eigenmodes and requires any stabilization mechanism to target this surface in particular. Unlike the slab mode, therefore, the details of the pressure profile must be understood in order to predict DTM stability.

The coupling of an ideally unstable mode to the DTM for finite pressure gradients is a further complication for our diamagnetic drift study. Understanding the nature and behavior of this ideal instability should be a primary goal of any future work. In Chapter 3 we noted that the Cartesian force-free DTM is coupled to a slab kink mode which can, in the strongly coupled case, be only marginally stable ($\gamma \to 0^-$). Given the similarities between the slab and force-free cylindrical DTMs (Section 6.1), and the connections between our observed force-balance DTMs and the $m = 1$ kink-tearing mode (Section 6.2), we suspect the underlying ideal instability is a cylindrical kink-mode. Beyond understanding the dependence of the ideal growth rate on the pressure profile two important questions remain. Firstly, is this ideal instability particular to the $m = 2$, $n = 1$ equilibrium we use in this simulations? We have conducted preliminary studies not reported here that show the pressure driven mode persists regardless of the spacing of the tearing surfaces, but it is possible that higher mode number instabilities will not feature this instability. Were this the case the diamagnetic

drift stabilization mechanism may be more effective in equilibria with larger safety factors. The second question is fundamentally more important: does this ideal instability persist in toroidal geometry or is it particular to periodic cylindrical? Though toroidal corrections to the cylindrical model are (in the small aspect ratio/high guide field regime) small, they are known to impact the stability of ideal MHD kink modes [14]. Answering both these questions will require both analysis and simulation outside the scope of this thesis, but are important to understanding the actual impact of DTMs in fusion devices. We note, however, that even if the ideal MHD mode stability is impacted by higher safety factor equilibria or toroidal geometry, the pressure gradient will likely remain a source of destabilizing free energy and the DTM growth rate may be enhanced in a fashion similar to our study here.

We have observed that in cylindrical geometry the differential drift remains an important factor in slowing the growth of the reconnecting DTM, although the system asymmetry results in a less clear distinction between coupled and decoupled modes. A combination of equilibrium flows and diamagnetic drifts will likely be the most effective route to stabilization. This combination may, in fact, be naturally realized in toroidal geometry as the system asymmetry tends to drive intrinsic plasma rotation. The best understanding of double-tearing mode stabilization in reverse-shear tokamaks would, therefore, come from fully toroidal simulations that take into account both the intrinsic plasma motion and FLR effects.

In this chapter we have established the commonalities and differences between the well studied slab and more complex cylindrical double-tearing modes, and shown that diamagnetic drifts can (for certain pressure profiles) slow the growth of the linear instability. With this foundational understanding of the interaction (and decoupling) of the two resonant surfaces, we will proceed to the nonlinear regime where the DTM takes on a more disruptive character.

Chapter 7

Nonlinear reconnection processes

Linear analysis is import to understanding general stability thresholds and to ascertain the dominant behavior but evaluating the disruptive potential of a mode requires understanding its nonlinear development. Reconnection is not, however, an instability type in-and-of itself, but rather a physical mechanism by which an unstable plasma can transit to a lower energy state. The included physical processes, topology, symmetry, and magnetic configuration can all have a dramatic effect on the manifestation of reconnecting modes. To better navigate the complicated DTM parameter space we will first establish what features are common to all two dimensional tearing-mode type reconnecting modes, and establish a link between certain nonlinear characteristics and our prior boundary layer theory. Finally, we will consider the substantial impact of finite ion mass on nonlinear tearing modes. Our goal in this chapter is not to provide an exhaustive account of reconnection physics but rather to lay the groundwork for later discussions of the unique double-tearing mode features.

The bulk of this chapter will feature examples and descriptions of isolated single tearing modes simulated from a two dimensional Cartesian 'Harris sheet' reconnecting field.

$$B_{y0}(x) = B_0 \tanh\left(\frac{x}{\lambda}\right) \tag{7.1}$$

We will embed this profile in a guide field with asymptotic strength $B_z = 10B_0$ so that the reduced MHD approximation is valid, and will largely consider force-free configurations with constant $\rho = T = 1.0$, so that $\beta = 0.02$. The Harris sheet equilibrium is popular because it is possible to construct an equivalent form that is an exact kinetic equilibrium, thus it allows

for easy comparison between different models. Furthermore, the inherent symmetries make this something of a minimal example to discuss common features.

7.1 General characteristics of 2D reconnection

As reconnection is a change in magnetic topology it is natural to characterize the nonlinear state by the apparent magnetic structures. In two dimensions this is best accomplished by examining the scalar 'flux function', which we encountered in the rMHD approximation.

$$\mathbf{B} = \nabla\psi \times \hat{z} + B_z\hat{z} \tag{7.2}$$

Mathematically the reduction of the magnetic topology to a scalar component (ψ) describing the reconnecting field and another (B_z) describing the guide field is always possible when there is an inherent symmetry in the problem to reduce the number of degrees of freedom. Note that henceforth we use ψ to represent the total flux function, i.e. the sum of the perturbation and equilibrium. Nonlinearly these are, by assumption, of the same order. Thus in the remaining chapters the distinction between equilibrium and perturbation will not be useful, and all variables are to be considered representative of the total quantities unless otherwise stated. Lines of constant flux function $\psi(x, y)$ represent projections of magnetic field lines onto the plane. For clarity we will henceforth refer to these projections as 'field lines', though it should be understood that in the presence of a guide field the actual field lines have an out-of-plane component.

As the linear instability grows the magnetic flux of the equilibrium field lines, which are initially parallel, is reconnected within the singular tearing layer and stored within magnetic islands. An example of this structure can be seen in the late time state of a nonlinear Harris sheet tearing mode, plotted in Figure 7-2. The island is bound by a separatrix, indicated by a solid black line. The place at which the two branches of the separatrix meet is the diffusion region where the ideal MHD frozen-in condition breaks down and reconnection is possible.

This region is the nonlinear manifestation of the singular, resonant surface that enabled our prior boundary layer analysis.

Consider a fluid packet on an unreconnected field line at point 'A' in Figure 7-2. In this outer region the plasma is governed, to lowest order, by ideal MHD and thus the fluid packet is frozen onto the field line. Together they are advected toward the point 'x', which lies on the separatrix within the diffusion region. As they enter this layer the resistivity η allows plasma and magnetic field to decouple and reconnection to occur. The fluid packet is carried downward toward point 'B' by the strong outflow jets emerging from the diffusion region. During this journey downstream the branches of the separatrix widen, the strong gradients defining the diffusion region flatten, and ideal MHD again becomes the dominant physical ordering. Thus the plasma and magnetic field recouple and advect together into the magnetic island. This continuing reconnection process causes the magnetic island to grow until the forces exterior to separatrix surface balance those within and the instability saturates.

All tearing modes will have the above fundamental characteristics. More generally any 2D nonlinear reconnection site will consist of an inflow domain feeding a diffusion region where field line breaking occurs. The energy released by reconnection generates the outflow jets, which recouple to the magnetic field downstream. The topology of the separatrix surface between reconnected and unreconnected flux (and thus inflow and outflow plasma) will not, however, necessarily be describable as an island. In particular, magnetic islands themselves may be reconnected to produce lower energy parallel magnetic field configurations. This secondary process is not possible for an isolated single tearing mode, but will emerge at late times for the DTM. Whatever the initial and final magnetic configuration, the structure of the diffusion region and separatrix are critical to the reconnection process and therefore an area of intense study. Certain common terminology has emerged for 2D systems. The point at which the two branches of the separatrix meet within the diffusion region is known as the 'X-point', and is a saddle point of the global flux function $\psi(x, y)$. Note that the term

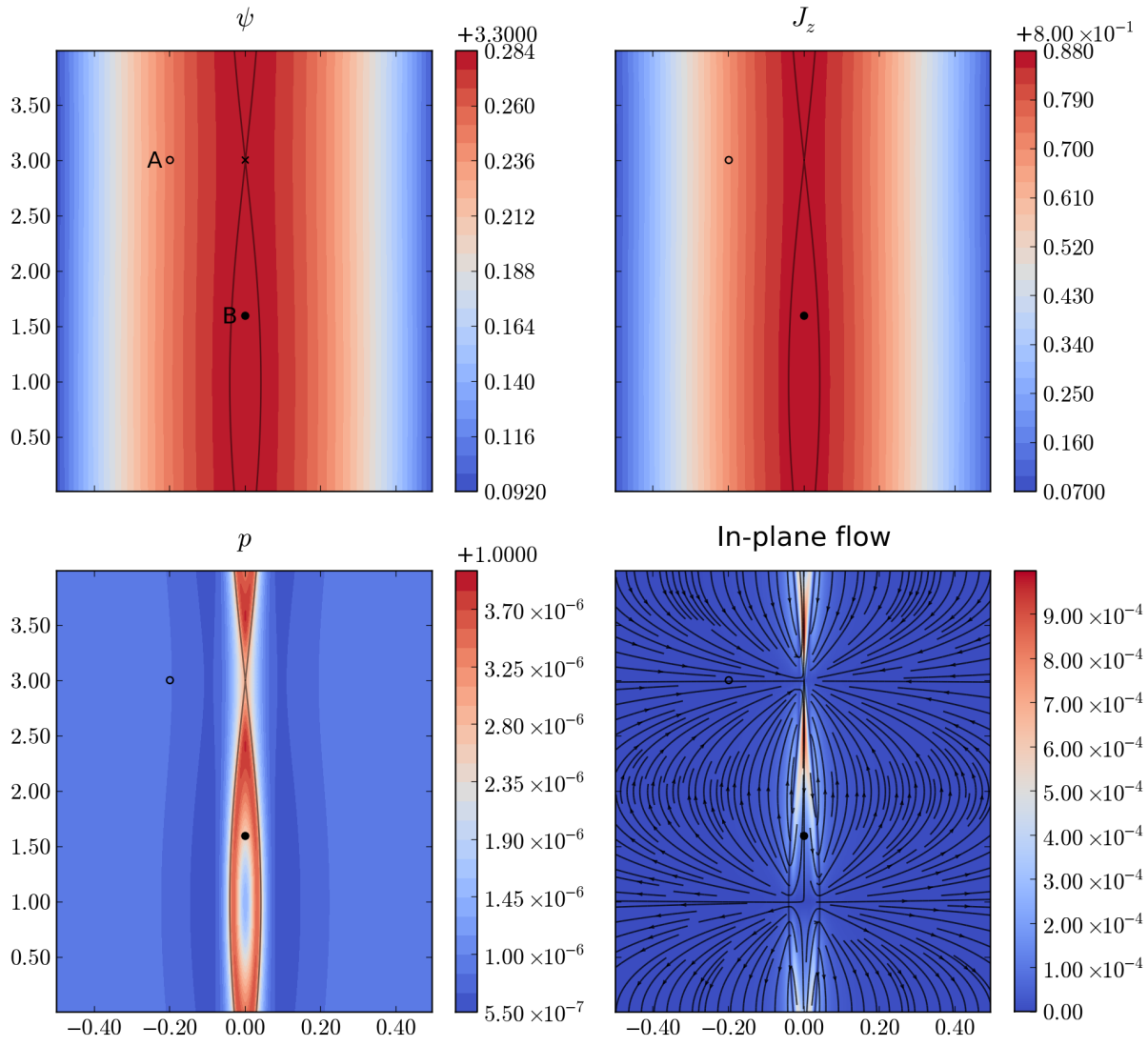

Figure 7-1: A nonlinear constant ψ tearing mode from a Harris sheet equilibrium with $\lambda = 0.6$. The out-of-plane current J_z is a function of the flux ψ at all points, and the separatrix (black line) has an X-point geometry. Point A lies upstream of the reconnection site; point B downstream.

'X-point' is also commonly used in the literature to describe the global separatrix geometry. We will endeavor to make it clear by context whether we are describing the saddle point of the flux function or separatrix morphology. A saddle point of the stream function must also occur within the diffusion region and is called the 'stagnation point'. For symmetric configurations the X-point and stagnation point are typically co-located, however they may be offset from each other (within the diffusion region) when asymmetries exist [15]. The center of the magnetic island is the 'O-point' and is an extremum of ψ. Other important boundaries and characteristics emerge when physics beyond resistive MHD is considered, and in three dimensions the taxonomy of reconnection sites becomes much more complex, but for the purposes of this work the above is sufficient.

7.2 Classification of tearing modes

The symmetry of the single tearing mode configuration has allowed the development of quasilinear theories that relate the nonlinear diffusion region structure to the linear boundary layer theory. Specifically, the separatrix morphology and appearance of an extended current layer near the reconnection site can be associated with whether the linear instability is in the constant or nonconstant ψ regime. Both these characteristics are of critical importance to the triggering (or absence) of an explosive growth regime for the nonlinear double tearing mode, so we will briefly review the quasilinear theory of single tearing modes. In this section we focus on the analyses of Rutherford [42] and Waelbroeck [49] that address slower constant ψ and faster nonconstant ψ STMs respectively.

As discussed in Chapter 3, when the growth time of the instability is sufficiently small compared to the time for the perturbation to diffuse across the singular layer the flux function can be treated as constant within. Use of this constant ψ assumption results in a growth rate that depends strongly on resistivity as $\gamma \sim \eta^{3/5}$. This assumption can be extended nonlinearly to estimate the growth rates of magnetic islands. During the linear phase the

separatrix is contained entirely within the singular tearing layer and the growth of the instability is determined by the balance of first order magnetic forces and the bulk fluid inertia. As the magnetic island grows larger than the singular layer the inertia term is replaced by higher order magnetic forces due to nonlinear eddy currents. To lowest order, therefore, the out-of-plane current J_z is a function of the total magnetic flux $\psi(x, y)$:

$$J_z(x, y) \approx J_z(\psi) \tag{7.3}$$

This relation must hold everywhere except on the singular surface where $J_z(\psi)$ is not analytic, i.e. the magnetic separatrix. Using the constant ψ approximation, however, one can match the solutions along this layer to those within and outside the island and directly calculate the current via averaging Ohm's law along flux surfaces [42]. The nonlinear perturbations in this system remain dominated by the fundamental harmonic of the system, resulting in islands that span the entire resonant surface and meet only at a single point. An example of this type of nonlinear, constant ψ tearing mode is shown in Figure 7-1. Note, in particular, the sharp X-point configuration of the magnetic separatrix and direct mapping of the current J_z to the flux ψ at all points. Both these features are hallmarks of nonlinear constant ψ tearing modes. In this regime the growth of the magnetic perturbation changes from exponential to algebraic such that the perturbed flux function ψ_1 grows like t^2. The width w of the corresponding magnetic island then grows like $w \propto \eta t$ [42]. This behavior continues until the island saturates at finite amplitude due to the balancing of forces interior and exterior to the magnetic island [56].

The constant ψ approximation is valid only for the most slowly growing tearing modes, and outside of this domain we must seek additional simplifications in order to perform nonlinear analysis. One such method involves considering the magnetic helicity K, which is a measure of field complexity defined as the product of the magnetic field and vector

potential integrated around a region of closed field or 'flux tube'.

$$K = \int \mathbf{A} \cdot \mathbf{B} \mathrm{d}V \tag{7.4}$$

Waelbroeck [49] used the hypothesis that helicity is conserved during reconnection to extend Rutherford's description into the 'nonconstant ψ' tearing mode regime. In this more general theory the higher order harmonics of the system are not ignorable, and consequentially the islands do not span the entirety of the resonant surface. Instead they span a fixed length Δy such that $k\Delta y < 2\pi$. The space between these endpoints, along which the separatrix lies, then forms a current layer as seen in Figure 7-2. This layer is a clearly defined diffusion region where reconnection can occur, and the separatrix geometry in this class of tearing mode is commonly considered to be two 'Y-points' fixed to either end of a current sheet. A prediction of the island growth can be found by assuming this current sheet is described by the Sweet-Parker model such that $\dot{\psi}_1 \propto \eta^{1/2}$. From this one can find the nonlinear behavior of the magnetic island width to be $w \propto \eta t^2$ [49].

Both these nonlinear, algebraic island growth regimes, while analytically tractable, are difficult to realize in practice for single tearing modes. The constant ψ approximation applies only to a narrow region of the STM dispersion relation, specifically equilibria which are deeply ideally stable ($\Delta' \to 0^+$) and produce slowly growing instabilities. Furthermore, Rutherford type islands generally saturate at small amplitudes [56] and thus are not typically responsible for large scale disruptive behavior. Nonconstant ψ tearing modes that follow Waelbroeck's description are nonlinearly faster growing, and have a greater impact on the equilibrium plasma. As a consequence, however, they tend to rapidly evolve outside this theory's validity, due either to geometric changes triggering non-algebraic growth [51], triggering of secondary instabilities (such as plasmoid tearing), or onset of two fluid reconnection effects (see below). Together, however, these theories provide a framework for relating the linear boundary layer properties to nonlinear island morphology. In Chapter 8 we will see that understanding

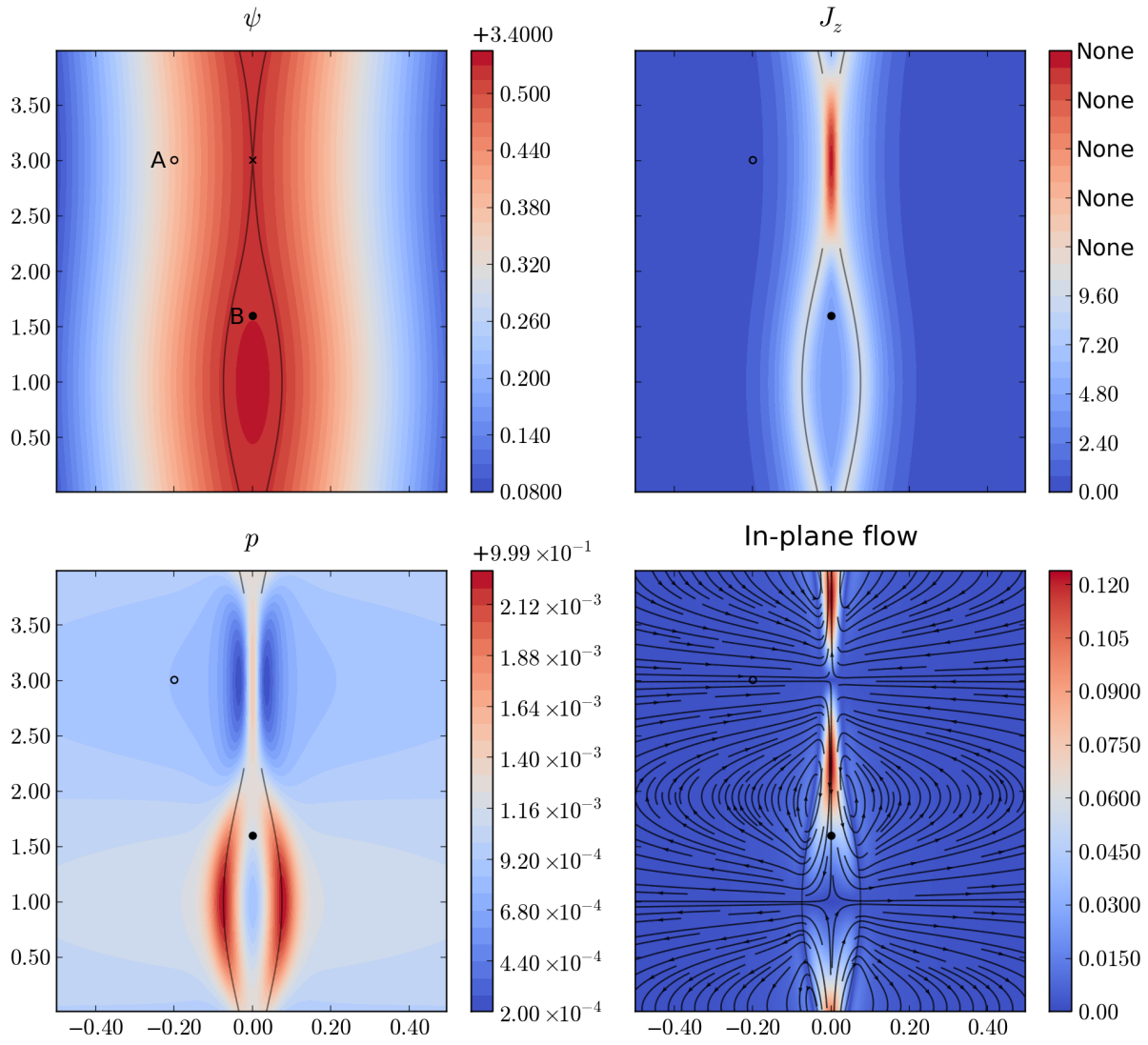

Figure 7-2: A nonlinear nonconstant ψ tearing mode from a Harris sheet equilibrium with $\lambda = 0.1$. The magnetic island does not span the entirety of the resonant surface, resulting in an extended current sheet defining the diffusion region. The separatrix (black line) forms a Y point configuration on either end of the current sheet and delineates the inflow (A) and outflow (B) regions.

the development of magnetic islands in the double tearing mode is a critical component of predicting the nonlinear stability, and that the Rutherford and Waelbroeck nonlinear theories will be an important tool to this end.

7.3 Hall MHD reconnection

Nonlinear single tearing modes, especially those that form an extended current sheet in the resistive regime, are strongly impacted by the addition of finite Larmor radius (FLR) effects. In Chapter 5 we showed how the additional ion inertial length scale d_i results in a nested boundary layer surrounding the resonant surfaces. The introduction of a secondary layer of thickness ρ_s (for non-zero guide field) decoupled the innermost, reconnecting layer from the outer, ideal MHD region and allowed for steeper gradients and enhanced out-of-plane current density (Fig. 5-3). These enhancements caused the growth rate to increase compared to resistive MHD and to be less dependent on η (Fig. 5-2).

Nonlinearly this nesting occurs in the neighborhood of the current sheet, which is the remnant of the singular layer. The magnetic field decouples from the upstream ion fluid at the ion-sound Larmor radius (ρ_s) scale and is advected into the diffusion region by the electrons. The reconnected magnetic fields must then recouple to the ion fluid downstream of the current sheet. This process results in an enhancement of the magnitude of the current sheet and a collapse of the separatrix geometry from a Y-point towards an X-point. At sufficiently large values of d_i the current layer begins to resemble a current point [36]. A combination of effects results in Hall MHD nonlinear tearing modes having significantly higher reconnection rates than their resistive counterparts (Figure 7-4). Predominantly the enhancement of the current layer due to the ion decoupling enhances the resistive ηJ field line breaking in Ohm's law (Eqn. 1.9). Furthermore, the shortening current layer results in the Hall MHD separatrix having a larger opening angle than resistive islands of the same width, resulting in broader outflow jets and thus a greater mass flow rate through the reconnection

site. Both these effects are evident when comparing the state of the single tearing mode for equivalent island widths in the resistive (Figure 7-2) and Hall MHD (Figure 7-3) simulations.

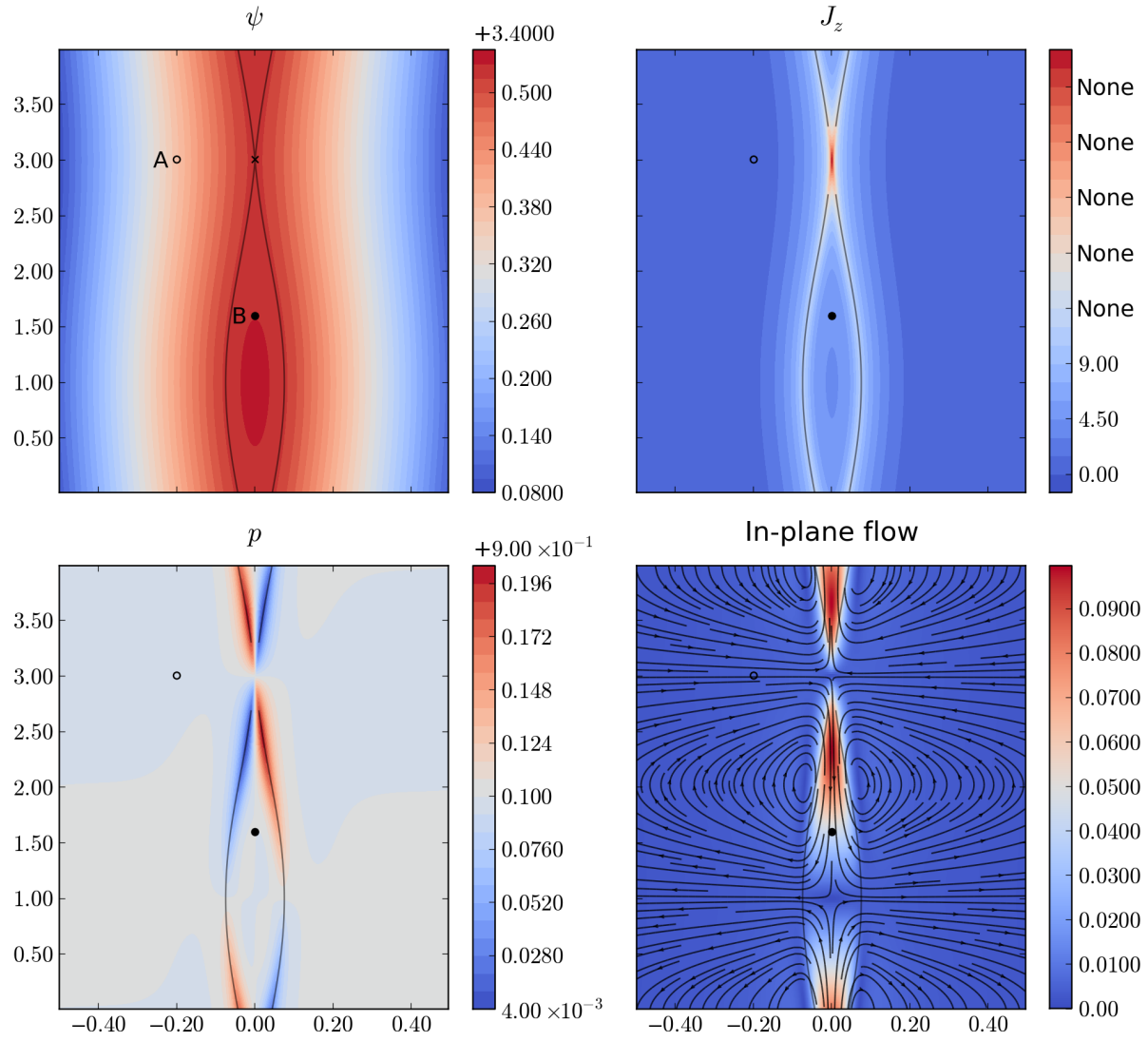

Figure 7-3: When Hall MHD physics is included ($d_i = 0.2$) the growth of $\lambda = 0.1$ tearing mode is significantly enhanced compared to resistive simulations (Fig. 7-2). The FLR effects result in a collapse of the current sheet toward a current singularity, and the separatrix (black line) approaches an X point geometry. The broader opening angle of the separatrix allows for wider outlow jets into the magnetic island, and faster reconnection.

We note that although the X-point separatrix structure of the nonlinear Hall tearing mode is topologically similar to the deeply ideally stable tearing modes of Rutherford's theory (Fig. 7-1) the two regimes are fundamentally different. Nonlinear constant ψ STMs exhibit an X-point because the out of plane current remains, at all times, a function of the

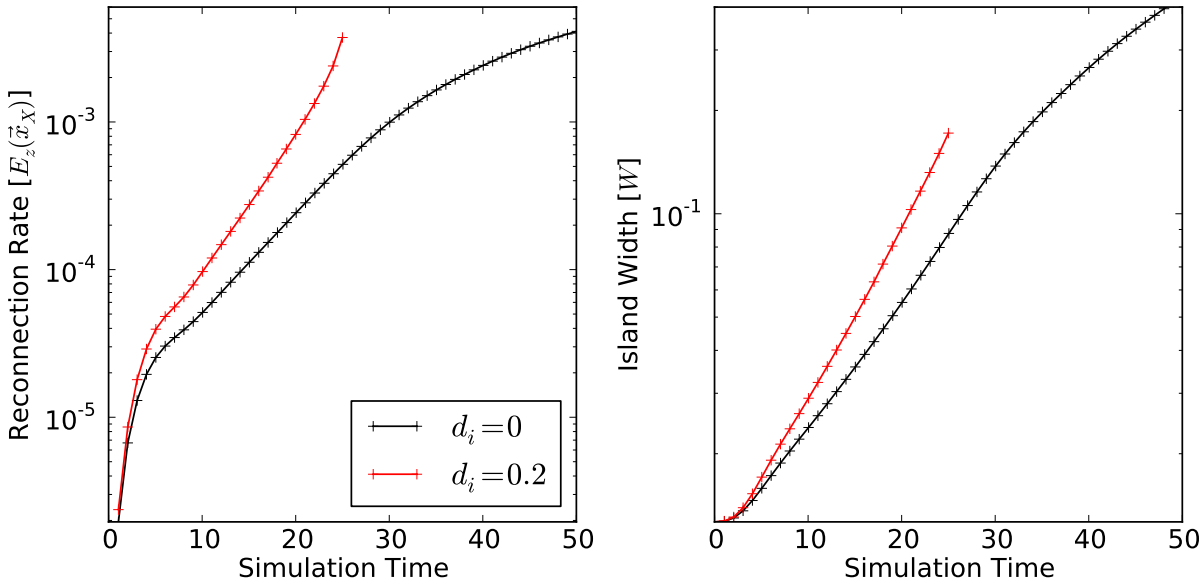

Figure 7-4: The addition of FLR effects when $d_i = 0.2$ allows for larger reconnection rates, as shown by the out-of-plane electric field at the X point $E_z(\vec{x}_X)$ (left). As a consequence, the width of the islands, measured as the distance between the separatrix branches at the O point (right), grows significantly faster.

magnetic flux. This property does not hold for the Hall tearing mode, as indicated by the presence of a current singularity at the reconnection site (Fig. 7-3). In principle, therefore, one cannot treat the morphology of the separatrix as a sufficient indicator of the type of nonlinear reconnection. In practice, however, because constant ψ tearing modes saturate at relatively small amplitudes, have slow growth rates, and occupy a very narrow region of the dispersion relation they are rarely important for nonlinear reconnection studies. Thus the distinction between Y-point separatrices with extended current sheets and X-point topologies with current singularities is a good indicator of ion inertial effects being significant.

7.4 Discussion

In this chapter we have focused on the general features of nonlinear tearing mode reconnection that are most essential to our discussion of double tearing modes. Nearly all of the elements described above for STM examples will persist when a second tearing surface is added, however we have isolated them here to better distinguish the characteristics unique

to the DTM. Pursuant with this goal we have neglected a substantial body of work on nonlinear reconnection. The topic is a very active area of research, and even a cursory summary is well beyond the scope of this work. We do wish, however, to briefly mention two topics, guide field and asymmetric reconnection, that have not been extensively studied as a factor in DTM evolution but are likely important.

The theories described in this chapter and all accompanying simulations have assumed a strong guide field regime. This limit is that most applicable to rational surfaces near the plasma core in tokamak devices, and is the limit in which our prior reduced MHD linear work is valid. We have neglected, therefore, a wide variety of important effects which are suppressed by the guide field. In particular, we have omitted discussion of the quadrupolar magnetic field which is a hallmark of FLR effects in the small B_z regime [11]. The Hall magnetic field (or rather, its absence) is merely one of many modifications that a strong out-of-plane magnetic field imposes on 2D reconnection. Because we are focused primarily on applications to tokamak configurations we will forgo this discussion.

Considering an individual resonant surface (rather than, for example, the two layer DTM system) asymmetries in magnetic field and plasma density on either side of the current sheet have a significant impact on the nonlinear reconnection rate and development of islands. A magnetic asymmetry, for example, can modify the observed reconnection rate for resistive Sweet-Parker like current sheets and cause the islands to bulge preferentially toward the weak field side [15]. The double tearing equilibria we use in this work feature this field asymmetry across each layer as a fundamental element, as well as an additional density inequality in our force-balanced systems. Except in strongly constrained systems this cross-sheet asymmetry cannot be removed. Such highly symmetric systems are unlikely to occur in reality, especially in curvilinear geometries. For this reason our study (and the bulk of currently published research) does not explicitly examine the nonlinear DTM variation with cross sheet imbalances, focusing instead on the coupling between the two layers. It is likely, however, that a full understanding of DTM behavior will require accounting for asymmetric

reconnection effects.

Excluding these two topics, we have now broadly characterized the features of single tearing mode reconnection that are essential to our study of nonlinear DTMs. We will now proceed to examine how the addition of a second resonant surface can produce large scale disruptive behavior.

Chapter 8

Force-free nonlinear DTMs

In the linear theory of the double-tearing mode we focused primarily on the interaction of boundary layers in asymptotically strongly and weakly coupled systems, where the analysis is tractable. Nonlinearly the important dynamics occur when the two tearing surfaces are only intermediately coupled. Analysis in this regime is much more difficult and current understanding is drawn almost entirely from numerical studies. In this chapter we will describe the simplest and best understood nonlinear configuration, the force-free ($\nabla p = 0$), resistive double-tearing mode in 2D Cartesian slab geometry. We will show that there are significant parameters space boundaries where the nonlinear behavior of the DTM changes, and summarize the current understanding of these domains. Using this information we will then classify the nonlinear state of the cylindrical $q = 2$ mode that we introduced in Chapter 6.

Most works on nonlinear DTM evolution [27, 29, 55] characterize the mode primarily by the behavior of the total kinetic energy of the system and the magnetic energy stored in the perturbation.

$$E_k = \int \frac{1}{2}\rho \mathbf{U} \cdot \mathbf{U} d\mathrm{V} \tag{8.1}$$

$$E_m = -\int \frac{1}{2}\left(\delta\mathbf{B} \cdot \delta\mathbf{B} + 2\delta\mathbf{B} \cdot \mathbf{B}_0\right) d\mathrm{V} \tag{8.2}$$

Here $\mathbf{U}$ is the plasma velocity field, ρ the density, $\mathbf{B}_0$ the equilibrium magnetic field, and $\delta\mathbf{B}$ the perturbed magnetic field. We will use the evolution of E_k (which is outputted as a diagnostic in `MRC-3d`) to categorize both the stage and type of double-tearing mode, and examine E_m (which is obtained via post-processing) as a marker of island development.

The prototype DTM in Figure 8-1 shows the multi-stage evolution of E_k and E_m in a system that exhibits a pronounced 'explosive growth' phase. Contours of the flux function $\psi(x, y)$ are inset to show the state of the magnetic islands at each stage of the kinetic energy evolution. As the widths of the islands become comparable to the singular layer width the growth of the kinetic energy decreases sharply. The evolution of the magnetic fields decouples from that of the plasma flows, as shown by the evolution of the kinetic (solid line) and magnetic (dashed line) energies between points B and C on Fig. 8-1. For many systems this process is similar to that seen in single tearing instabilities [42, 49]. Certain classes of equilibria, however, maintain their exponential linear growth even as nonlinear islands develop. We will discuss these variations of the 'island growth regime' in Section 8.1. Following the period of slow growth the DTM suddenly releases a large burst of kinetic energy and undergoes significant qualitative change (points C, D, and E). This 'explosive regime' is the feature most responsible for the recent interest in the double-tearing mode, since it represents not only the potential for damaging disruptive events in fusion plasmas but also an occurrence of self generated fast reconnection. It can be observed in resistive MHD without kinetic effects (such as ion or election inertia) or external driving. In Section 8.2 we will discuss a how this phase is triggered and summarize the available (and conflicting) studies examining the dynamics of fast reconnection during explosive growth, and propose a connection between explosive and exponential types of nonlinear DTMs. When all the available equilibrium free energy between the surfaces is consumed, either via an explosive phase or through steady reconnection, the plasma is characterized by strongly sheared flows and intermittent reconnection activity as the islands are consumed and the magnetic field profile is flattened between the two surfaces. We will briefly describe this final state in Section 8.3. In Section 8.4 we will use this discussion of DTM evolution to classify our $m = 2$, $n = 2$ cylindrical DTM. Finally, we will conclude this chapter by discussing the outstanding issues that should be resolved in order to better understand the nonlinear DTM.

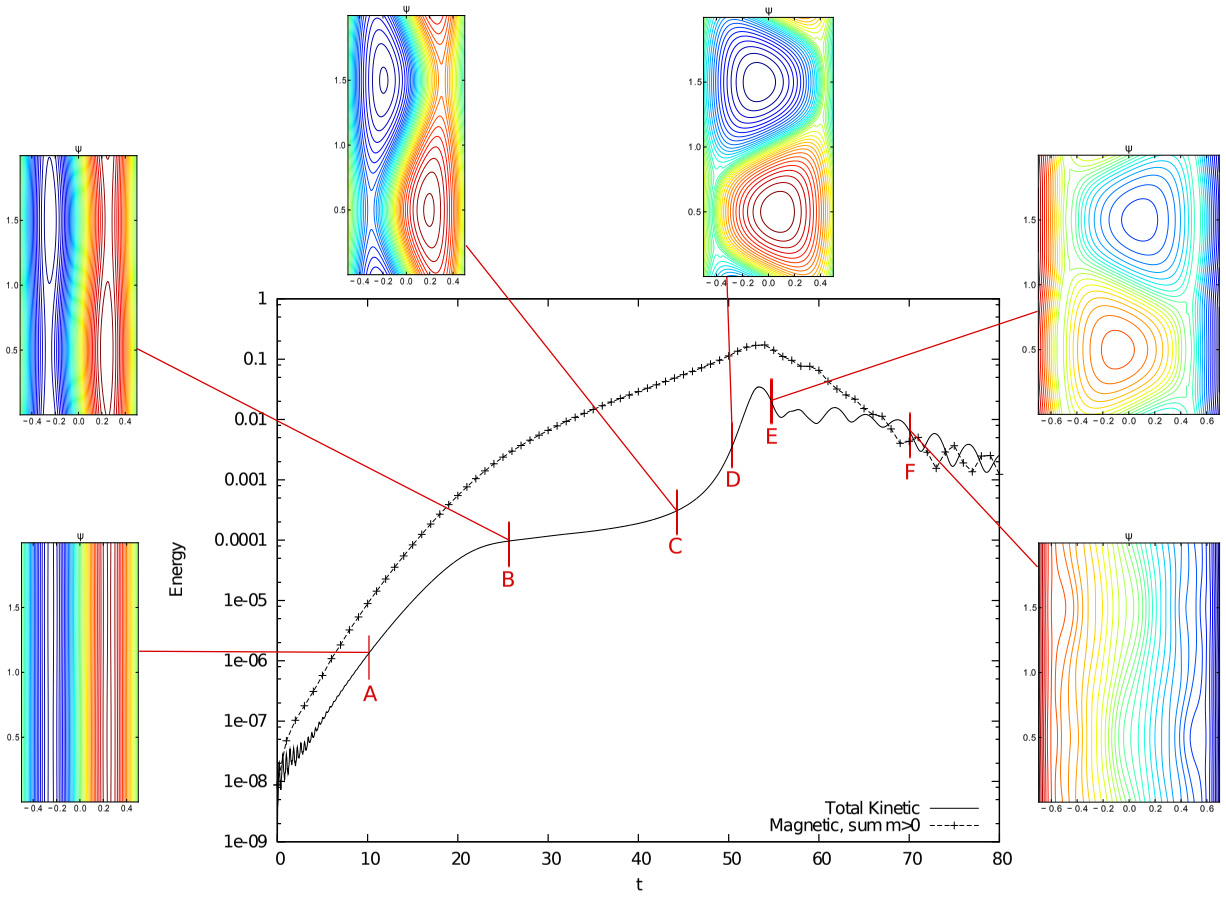

Figure 8-1: The evolution of an explosive-type Cartesian DTM is well illustrated by system kinetic (solid line) and perturbed magnetic (dashed line) energies as functions of time . Pullout plots are of the in-plane magnetic flux, contours of which serve as proxies for magnetic field lines: A) Linear – reconnection sites and magnetic islands are too small to appear over the background; B) Early Nonlinear – kinetic energy growth slows as equilibrium magnetic energy is spent deforming the magnetic surfaces, macroscopic islands appear; C) Onset of Explosive Phase – large islands and well defined current sheets become unstable and trigger a release of kinetic energy; D) Explosive Phase – Islands drive into current sheets causing significant plasma motion; E) Post Collapse – islands begin reconnecting at current sheets on the opposite tearing surface, the separatrix is broken and redefined; F) Approaching Final State – the system is nearing complete reconnection as resistive decay becomes the dominant process. This prototype example is generated using a double-tanh equilibrium with $\lambda = 0.075$, $k = \pi$, and $x_s = 0.25$ yielding a moderately coupled nonconstant ψ DTM. (resistivity $\eta = 2 \times 10^{-4}$, $D = DT = \nu = 0.1\eta$)

8.1 The island growth regime

The development of large magnetic islands is believed to be a crucial factor in the onset of explosive growth in the nonlinear double-tearing mode. In this section we will use the quasilinear framework established in Chapter 7.2 to examine several different DTMs during the 'island growth regime' that immediately follows the linear phase for moderately coupled modes (between points B and C in Fig. 8-1). The detailed behavior of the mode growth during this period has only been studied in a limited regime of parameter space [31, 58], so our description of this phase will rely largely on `MRC-3d` simulations of characteristic modes. We will begin with an example of a weakly coupled DTM and progress toward strongly coupled modes. The most interesting class of nonlinear double-tearing mode occurs somewhere between these two extremes.

The examples we present in this section will (unless otherwise noted) use a sech type equilibrium (Chap. 2.3) with resonant surfaces at $\pm x_s = \pm 0.8$ and a magnetic shear of $B_0'(\pm x_s) = \pm\pi/2$. We change the length of the simulation domain in y to set the wavenumber k and simulate DTMs with different coupling parameters kx_s while keeping the inter-resonant spacing and magnetic shear constant. As per our discussion in Chapter 3.2, decreasing k will also force the layer at each resonant surface into the nonconstant ψ regime. This method of varying the wavenumber (and leaving the surface separation constant) is common in nonlinear DTM simulation studies and we use it here to make contact with the existing literature. We will leave discussion of the consequences of this choice until the end of the chapter.

In the large k regime the DTM behaves as two very weakly coupled single tearing modes and the nonlinear mode growth is approximately that of a constant ψ, Rutherford-like [42] island. Janvier et al. [31] mapped a stability threshold in k and x_s above which the island growth halts at finite time without triggering the explosive phase. An example of a DTM just above this boundary with $k = 1.43$ and $x_s = 0.8$ is shown in Figure 8-2, with energy evolution as plotted in Figure 8-6. The asymmetric magnetic field on either side of each

resonant layer causes significant changes in the mapping of the out-of-plane current J_z to the flux function $\psi(x, y)$ when compared to the symmetric constant ψ tearing mode (Fig. 7-1). The separatrix structure is, however, X-point shaped and a visible current sheet does not develop at the reconnection site. These features suggest that the current remains a piece-wise function of the flux function everywhere in the domain (i.e. $J_z(x, y) = J_z(\psi)$) even along the singular layer. This function is not, however, analytic along the separatrix. The STM Rutherford solution has all these same properties [56] but they are accentuated by the system asymmetry in Fig. 8-2. It is expected, therefore, that a systematic study of this weakly coupled, nonlinearly saturated DTM regime would show the $w \approx \eta t$ island width growth found by Rutherford [42]. To the authors' knowledge such a study has not been conducted. Ref. [32] conducted a survey of saturated DTM island widths for fixed k and variable separation and found that the maximum island width increases linearly with x_s, suggesting that for widely spaced modes the coupling between the two resonant surfaces still plays a role in the nonlinear island growth. The STM quasi-linear theories of growth [42] and saturation [56] would therefore likely need to be modified to account for the magnetic free energy between the tearing layers.

Decreasing the wavenumber to $k = 1.0$ pushes the DTM below the stability threshold. During the island growth regime, plotted in Figure 8-3, the separatrix at each surface maintains its X-point like structure. Close examination of the current near the reconnection site reveals, however, a slight increase in the axial current of about 15% when the separatrix enters the resonant layer. The current is not, therefore, everywhere a function of the magnetic flux. Streamlines of the in-plane plasma velocity in Fig. 8-3 show significantly more flow between the two resonant surfaces than in the saturated mode (Fig. 8-2). This DTM is not, therefore, strictly within the constant ψ, Rutherford nonlinear regime. These deviations are, however, small enough that to lowest order one expects the island growth to have the same characteristics the previous, saturated mode, with the clear exception that the triggering of an explosive growth regime is evident in the kinetic energy (Fig. 8-6).

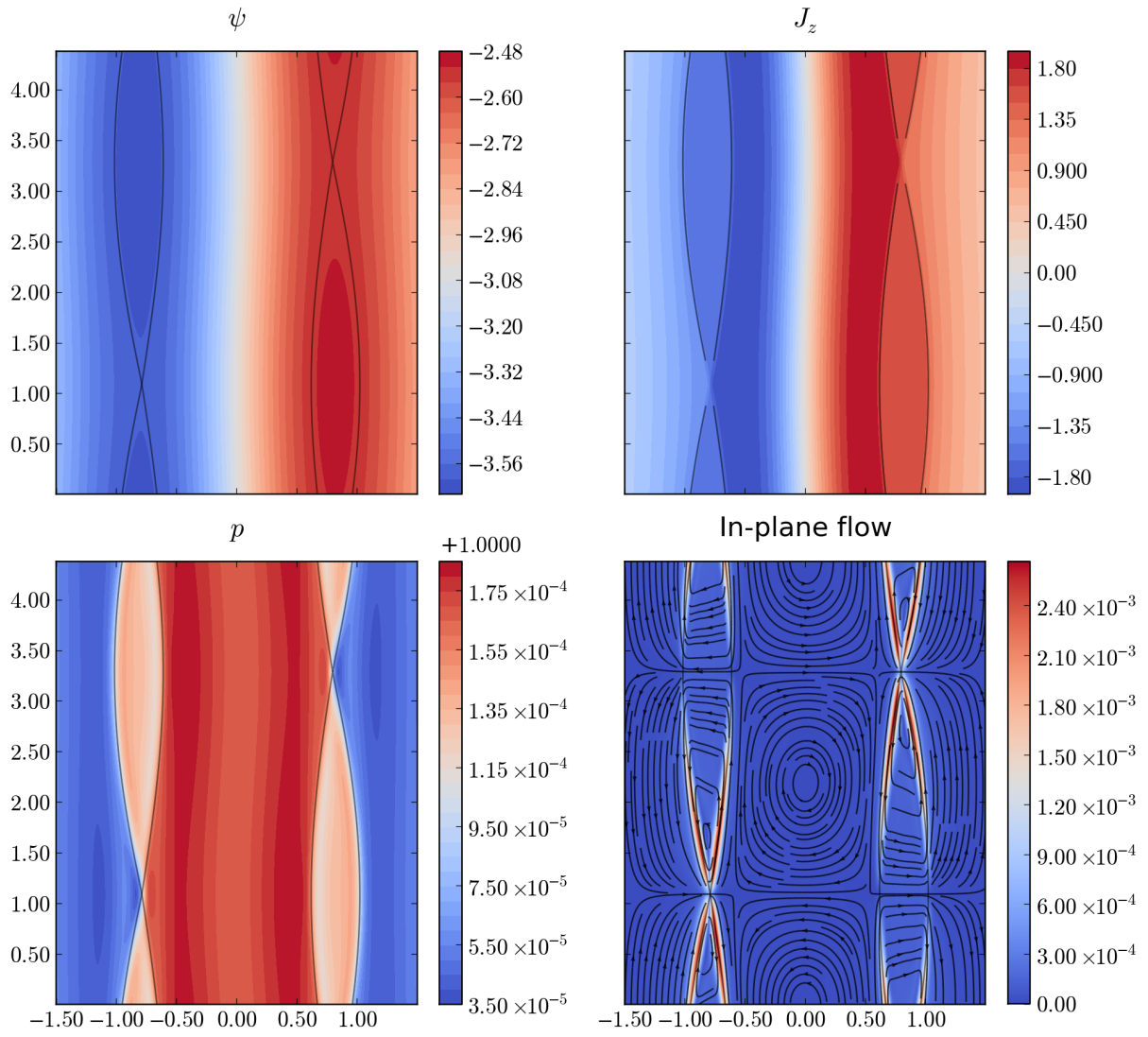

Figure 8-2: In a sech type equilibrium with $x_s = 0.8$ a DTM with wavenumber $k = 1.43$ saturates during the island growth regime. The separatrix (black line) has been masked in the region of the X-point on the J_z current plot to show the absence of any current sheet structure, suggesting this mode is an asymmetric, DTM generalization of the Rutherford [42], constant ψ quasilinear STM theory. Note the absence of strong plasma flow between the two resonant surfaces. (simulation time $t = 8800$, resistivity $\eta = 1 \times 10^{-4}$, $D = DT = \nu = 0.1\eta$)

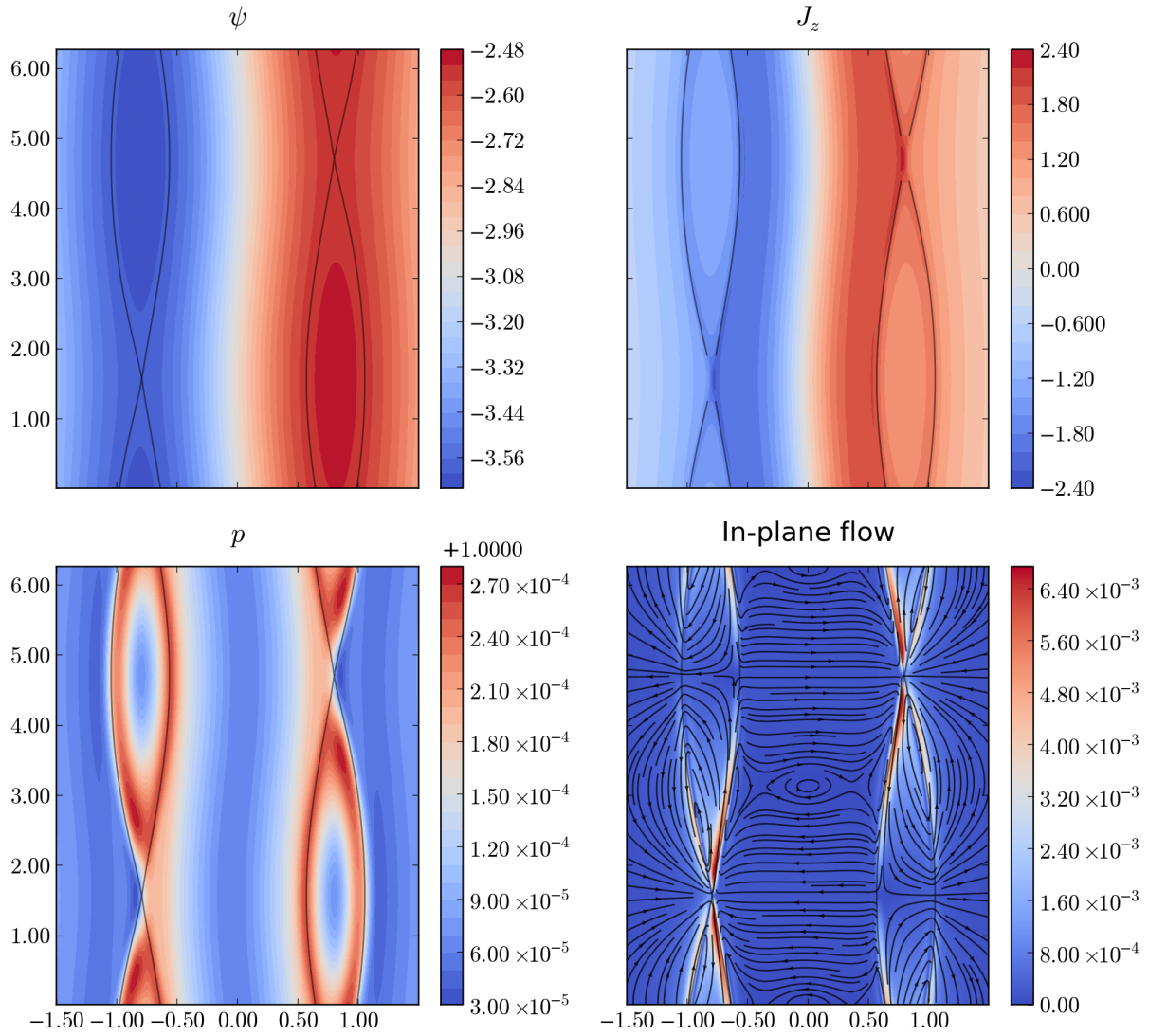

Figure 8-3: When the wavenumber is decreased to $k = 1.00$ the explosive phase will be triggered when the magnetic structure develops sufficiently. During the island grown regime the separatrix (black line) has an X point structure similar to a Rutherford mode but an enhancement of the current J_z is evident at the reconnection site, indicating that the constant ψ approximation is not valid. Streamlines of the plasma flow show weak coupling between the two resonant surfaces. (simulation time $t = 925$, resistivity $\eta = 1 \times 10^{-4}$, $D = DT = \nu = 0.1\eta$)

The classification of the DTM changes substantially when $k = 0.67$. In Figure 8-4 it is evident that an extended current sheet has formed at the reconnection site and the separatrix is trending towards a Y-point geometry. The example plotted in Fig. 8-4 shares many features with the nonconstant ψ, Waelbroeck STM (Fig. 7-2) with the additions of coupling between the tearing layers and asymmetry across them. Streamlines of the plasma velocity show that there is significant flow between the two tearing layers and the outflow jets are biased toward the interior region. It is not reasonable, therefore, to expect that these islands follow the Rutherford growth behavior. The flow between the two surfaces suggests, however, that the Waelbroeck $w \sim t^2$ solution is not appropriate either, as it assumes a Sweet-Parker current sheet [49] that does not account for either the magnetic asymmetry or the outflow from each surface driving inflow at the other. Whatever the details of the analytic theory, it is clear from the appearance of a current sheet that the constant ψ nonlinear scaling theory no longer applies.

The three previous examples are DTMs which show a pronounced island growth regime in their kinetic and magnetic energies with a much lower growth rate than the linear phase. With the exception of the $k = 1.43$ saturated case they also develop into a disruptive explosive growth phase, as shown on Figure 8-6. Very strongly coupled surfaces, however, lead to complete reconnection without passing through these phases. Instead they develop large islands while the growth of the kinetic energy remains linear. Examining the islands during this exponential nonlinear phase shows structure that does not clearly fall into the establish STM categories. To achieve this regime we use an equilibrium known from our linear study (Chap. 3) to result in a strongly coupled mode. Figure 8-5 represents the state of a DTM on a sech equilibrium with $x_s = 0.25$ and $k = 0.5$ at time $t = 140$, which shows exponential growth of E_k in Fig. 8-6. The out-of-plane current J_z is not a function of ψ except far away from the resonant surfaces where ideal MHD dominates. There is not, however, any clearly defined current sheet. Instead the mode exhibits a large region of enhanced current near the X point and a decrease in J_z within the islands. Thus this mode can be consider

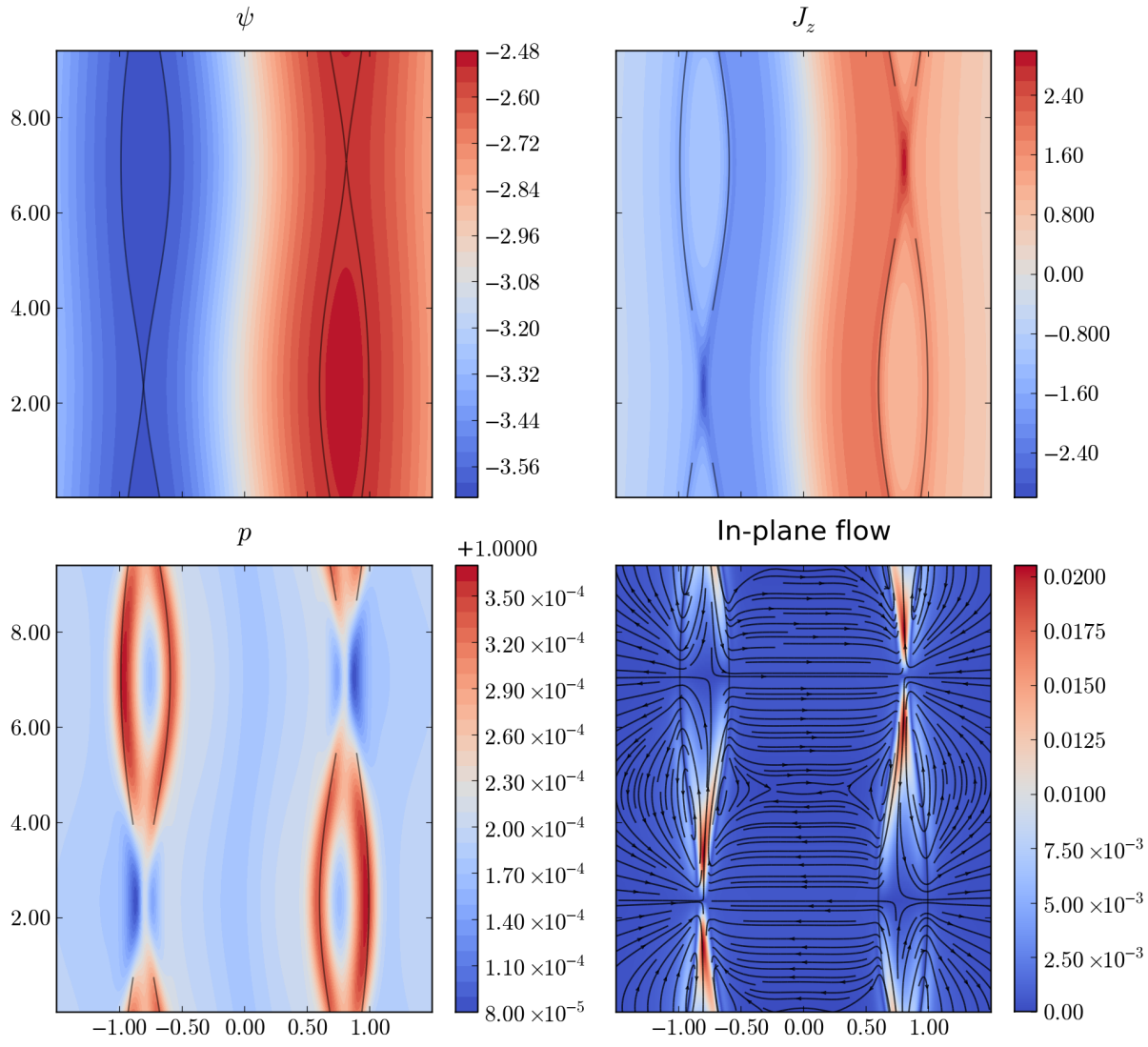

Figure 8-4: A sech DTM with $x_s = 0.8$ and $k = 0.667$ is firmly within the nonconstant ψ regime during the island growth phase. The separatrix (black line) has a more Y point and an extended current sheet is visible at the reconnection site. Streamlines of the plasma flow show strong coupling between the two resonant surfaces. (simulation time $t = 480$, resistivity $\eta = 1 \times 10^{-4}$, $D = DT = \nu = 0.1\eta$)

neither Rutherford-like nor Waelbreock-like. To the author's knowledge this region of the DTM parameter space has not been extensively studied, and the theoretical mechanism behind this strongly coupled nonlinear phase is unclear. We recall from Chap. 3, however, that in this system the slab kink mode is marginally stable. The nonlinear development of strongly coupled DTMs may, therefore, be governed by the nonlinear evolution of the ideal MHD mode. This interpretation is supported by the streamlines of the plasma velocity in Fig. 8-5 which show extremely strong coupling between the fluid flows created by the two reconnecting layers. It is not, in this case, appropriate to consider the DTM within the framework of two nonlinear STM modes, as we have for weak and intermediate coupling. Instead we should consider it a single reconnecting instability.

In this section we have presented only a cursory overview of the island growth regime. Although the presence of this phase of DTM evolution is a necessary precursor to later disruptive explosive growth, very few comprehensive studies of its behavior exist. We have shown that at smaller wavenumbers the separatrix structure transitions from saturated Rutherford-type X-points to Waelbroeck-like current sheets and Y-points. These results show that it is inappropriate to apply the term 'Rutherford regime' to the island growth phase (as is common in the literature) except in very specific cases. In fact, we suspect all truly constant ψ double-tearing modes (for which the theory of Ref. [42] might apply) will saturate before the explosive phase. A comprehensive scaling study of the island growth regime would allow better understanding of how the mode develops throughout this phase. Such an effort would, however, face several significant hurdles which we will address at the end of this chapter.

When the coupling parameter kx_s is very small the island growth regime is absent. Instead exponential growth continues until the free energy between the surfaces is consumed and complete reconnection is achieved. This branch of the nonlinear DTM has not been well studied, and the boundary between closely coupled behavior and nonconstant ψ intermediate modes is unexplored. Based on our work in the linear and nonlinear phases thus far, however, we believe that a clear threshold between the two behaviors may not exist. From the linear

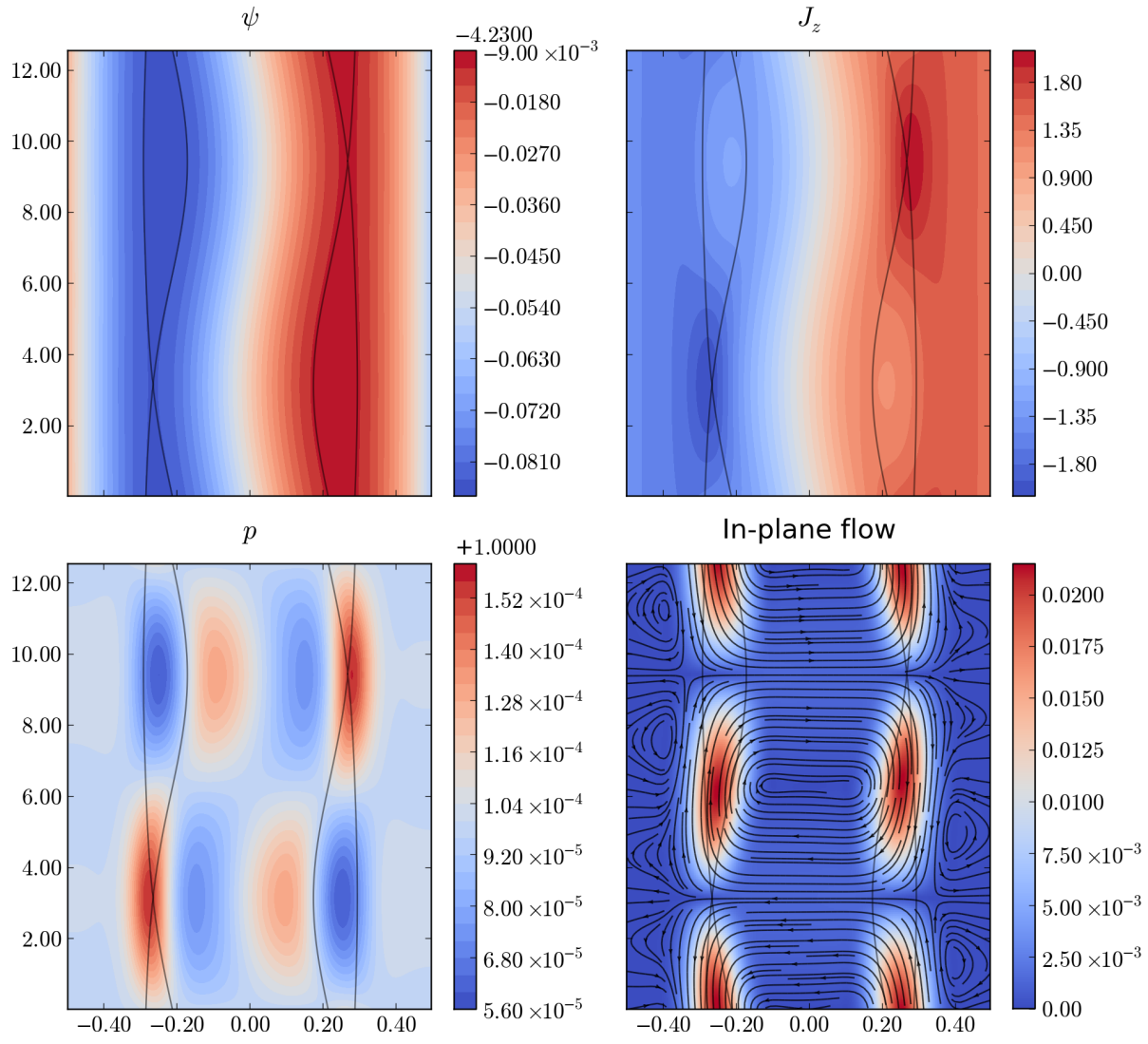

Figure 8-5: The strongly coupled $k = 0.5$, $x_s = 0.25$ DTM does not resemble either the Rutherford of Waelbroeck tearing mode theories. The current J_z is not a function of the magnetic flux ψ except far away from the resonant surfaces. Current sheets are not clearly visible anywhere in the domain, and streamlines of the plasma flow show significant interaction between the two tearing layers. (simulation time $t = 140$, resistivity $\eta = 1 \times 10^{-4}$, $D = DT = \nu = 0.1\eta$)

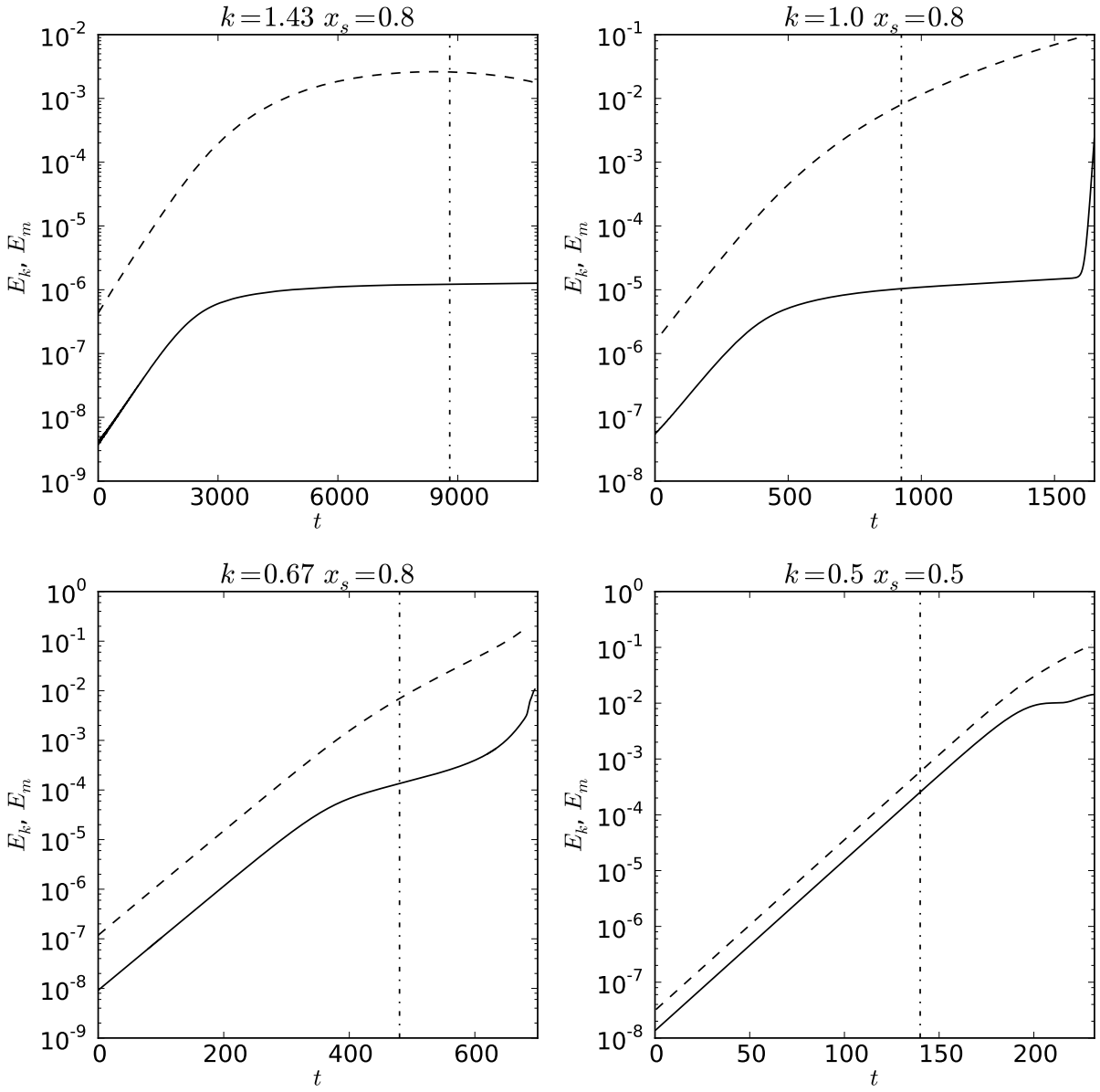

Figure 8-6: Integrated kinetic (E_k solid lines) and magnetic (E_m dashed lines) for the Cartesian double-tearing modes plotted in Figures 8-2(top left), 8-3(top right), 8-4(bottom left), and 8-5(bottom left) representing the different classes of island growth regime. Vertical dash-dot lines indicate the time at which the 2D images are plotted. These time series terminate during the explosive phase as simulating through this regime is numerically challenging.

theory it is known that as the wavenumber of the DTM decreases the eigenfunctions broaden and the coupling increases. Examining the nonlinear evolution of the kinetic energy for the nonconstant ψ mode (Figure 8-6) we observe that development of the mode during the island growth phase occurs at an appreciable fraction of the linear rate, and the onset of the explosive growth is smooth compared to the higher wavenumber modes. It is possible, therefore, that as the DTM wavenumber decreases and the coupling strength increases the island growth regime develops exponential growth and smoothly transitions in the form shown in Fig. 8-5. This transition would be consistent with the short lived behavior of the Waelbroeck regime in $m = 1$ kink-tearing modes [51]. As we will see, the current understanding of the explosive growth triggering mechanism may also support this hypothesis.

8.2 Explosive growth

Moderately coupled DTMs that do not saturate feature an inflection point in energy evolution during the island growth regime, after which the system accelerates into explosive growth. Using sech type equilibria Janvier et al. [31] found that the maximum wavenumber k^c at which the explosive phase occurs is independent of resistivity for a given x_s. By comparing the shape of the magnetic islands at the inflection point for DTMs of different size but equivalent kx_s, they found that the separatrices have structural similarity independent of the absolute island width. From this result they concluded that the explosive phase is triggered by a secondary instability dependent on the separatrix geometry, later confirmed via quasilinear analysis and simulations [32]. This secondary mode appears, in the weakly coupled limit, to be independent of resistivity. A detailed account of MHD forces above and below the stability threshold shows that at this late stage the pressure forces ($\nabla\pi$, $\pi = B^2/2 + p$) dominant the dynamics, with convective ($\mathbf{U} \cdot \nabla\mathbf{U}$) and field-line bending ($\mathbf{B} \cdot \nabla\mathbf{B}$) terms being of a lower order [33]. In particular, the appearance of the secondary instability seems to correlate with an imbalance in magnetic pressure on two sides of an

island. In cases leading to explosive growth the magnetic pressure at the 'inner' separatrix of an island (between the two tearing surfaces) is less than at the 'outer' (the side open to the boundary). This imbalance is generated by the development of triangular separatrix structure between the two resonant surfaces and is not evident in cases leading to saturation. We note that the strongly coupled islands in Fig. 8-9 are highly asymmetric at small island widths, suggesting that this pressure imbalance develops at small amplitudes and the distinct island growth and explosive regimes are replaced by a single fast reconnection phase. This strong coupling regime has not, however, been well studied and we will restrict our current discussion to Janvier's study of the marginally unstable domain.

Based on this description of the triggering mechanism we can now develop a picture of how the explosive growth regime emerges from the island growth phase in moderately coupled double-tearing modes. As the DTM enters the island growth regime the reconnection process slows but continues to reduce the magnetic field between the two tearing surfaces. If the structure of the mode is such that enough flux is reconnected before saturation is reached ($k < k^c$ for a given x_s) the pressures on both sides of the island boundary become imbalanced and a secondary instability is triggered. A key feature of this description (that the dominant behavior of the secondary instability is evident in the momentum equation) is consistent with observations that the kinetic energy growth increases before the magnetic [32]. The remaining flux is then driven into the current sheets by island motion, increasing the reconnection rate and generating a feedback loop that further decreases the pressure. The manifestation of this feedback loop is the explosive growth regime.

While the islands begin to bulge outward toward the opposite tearing surface the current sheets are compressed and the outflow jets are directed along the separatrices (point D in Fig. 8-1), resulting in large shears. As the remaining magnetic flux between the surfaces is reconnected the pressure within the islands becomes large enough to drive the center of the island toward the opposite tearing layer, causing a large increase in the system kinetic energy. After this shift the inner separatrices merge (point E) and the islands are slowly

consumed by the reconnection sites.

The explosive regime presents several challenges to numerical simulations. In particular the compression of current sheets as the islands bulge outward requires very small grid scales to resolve, and the dynamic motions require this enhancement over a significant portion of the domain (compare the Y-point positions at times C, D, and E in Fig. 8-1). These factors have limited the number of detailed simulations of this phase, and the physical mechanism and role of magnetic resistivity are currently unclear.

Despite these challenges several authors have been successful examining the behavior of this regime across one of more decades of resistivity η. These studies find, however, different scalings of growth rate on resistivity ($\gamma \propto \eta^{\alpha}$) and thus draw different conclusions about the primary driving mechanism. Ishii et al. [27–30] examine an $m = 3$, $n = 1$ double tearing mode with $kx_s \approx 2.8$ across one decade of resistivity ($3 \times 10^{-6} \leq \eta \leq 2 \times 10^{-5}$) and find a scaling exponent $\alpha \sim 0$, from which they conclude a structure driven instability. Using the common sech slab equilibrium (Chap. 2.3) with $kx_s \approx 0.785$ Wang et al. [52] find the very different scaling of $\alpha \sim 1/5$ across the region $2 \times 10^{-6} \leq \eta \leq 2 \times 10^{-4}$, leading them to propose a flow driven process [52] as the primary driver. Finally Zhang and Ma [62] choose the 'double-tanh' equilibrium (Chap. 2.3) with coupling $kx_s \approx 0.785$, which results in a stronger magnetic shear at the tearing layer compared to the common sech equilibrium ($B_0' = 5.0$ and $B_0' = \pi/2$ respectively). They vary the out of plane magnetic field from $B_G = 0 \rightarrow 5$ times the asymptotic in-plane field instead of assuming a strong guide field as in the previous studies. Over this range, and varying resistivity $2 \times 10^{-5} \leq \eta \leq 3 \times 10^{-4}$, they find the scaling exponent decreases monotonically from $\alpha \approx 0.06$ for $B_G = 0$ to $\alpha \approx 0$ when $B_G = 5$. Ref. [62] does not discuss the consequence of their results with regards to the underlying physical mechanism.

Assuming that the differences between the above three studies are not a result of fitting methodology, they indicate that there are multiple mechanisms for the explosive phase depending on either the DTM configuration or the underlying model. The available information

does not, however, allows us to identify the domain for each mechanism. Ishii et al. use an incompressible reduced MHD model in curvilinear geometry with an assumed strong guide field; Wang et al. have compressible rMHD in slab geometry also with a strong guide field; and Zhang and Ma use compressible MHD with a variable guide field. The incompressible model is the weakest of the three, but its results match those of the Zhang and Ma model in the high guide field limit where one expects incompressibility to be approximately valid. It does not seem likely, therefore, that the choices of simulation models are responsible for the differences. The factor kx_s, which is an indicator of the linear coupling strength (Chap. 3), is the same for the latter two papers ($kx_s \approx \pi/4$), and thus cannot account for the difference in measured resistivity scaling. Therefore neither the model nor the coupling parameter can be used to explain the variation.

The best remaining candidate is properties of the tearing layer local to each surface, i.e. the wave number k and magnetic shear. Together these determine whether the linear tearing layer is in the constant or nonconstant ψ regime, and we propose that they may also be responsible for variation in the explosive phase. If it can be shown that the character of the explosive phase changes with changing wavenumber and coupling it would support our proposal that the transition between the explosive and strongly coupled DTM behavior is smooth. We currently lack, however, a clear metric by which to catagorize nonlinear DTMs, as these studies of the explosive regime show that the coupling kx_s is insufficient. Identifying such a measure is outside the scope of this thesis, but we will discuss it in more depth at the end of this chapter.

8.3 Decay phase

Both the strongly coupled and explosive variants of the double tearing mode are troublesome for fusion devices. Both evolution paths lead to a flattening of the magnetic field

between the tearing surfaces [53] which would, in a tokamak, result in a loss of plasma confinement. The additional violent evolution of the explosive-type DTMs present a further danger of disruptive events which could damage hardware. As a consequence, much of the research has been dedicated to understanding and halting the mode's evolution. Several authors have, however, proposed that DTM activity may have beneficial characteristics by generating strong sheared flows [35, 53] and turbulence [9] which could affect the transport properties of a configuration. Although our focus on this work is to stabilize the DTM we will, for completeness, briefly discuss how these sheared flows develop.

Typically during reconnection the strongest plasma flows are downstream of the tearing location. The reconnection process releases stored magnetic energy and accelerates plasma along the separatrix. In the late nonlinear, the separatrices on both tearing surfaces are highly deformed and the outflow jets from both reconnection sites can interact. Wang et al. [53] examined the evolution of these flows in detail and found that during the explosive phase strong, large scale vortices form between the two surfaces. When the initial flux between the two surfaces is consumed, the inner separatrices of each island merge and lines of strongly sheared flow are created that connect the reconnection sites to each other. As the decay regime continues, the islands are consumed at the opposite tearing surface from which they were born and the flow profiles relax into layered shear flows spanning the space between the surfaces. Xia et al. [35] investigated the strength of these residual flows by varying the resistivity for a fixed equilibrium and found that although the instability evolved much slower with smaller η the generated flows were the same in all simulations. These results suggest that the plasma motion in the final state of the DTM depends primarily on the free energy available in the initial magnetic field configuration. Supporting this conclusion, Wang [53] found that varying the initial magnetic shear and separation of the resonant surfaces has a significant impact on both the magnitude and shear of the resultant surfaces.

These sheared flow patterns may have some beneficial characteristics in tokamak devices [53], but it is unclear whether they outweigh the loss of stability. The complete consumption of the magnetic islands leads to a flattened magnetic field and a loss of confinement [17, 29, 53]. Additional coupling to higher order modes may also lead to a turbulent collapse of the annular current ring [9], the consequences of which are unknown. Therefore we will focus, for the remainder of this work, on stabilizing (or at least slowing) the double-tearing mode, which is beneficial to so called 'advanced tokamaks' that exploit the reverse magnetic shear configuration.

8.4 Classification of the $m = 2$, $n = 1$ cylindrical DTM

The above framework (drawn mostly from symmetric, slab Cartesian simulations) represents our current understanding of the DTM nonlinear growth. Based upon this description we will now classify the $q = 2$, $D \approx 0.26$ cylindrical mode examined in Chapter 6, which we will use for the remainder of this work. We argued that the linear eigenmodes of this system are an asymmetric mixing of the strongly and moderately coupled Cartesian DTMs on the outer and inner rational surfaces respectively. One might expect, therefore, that the nonlinear evolution of the system will be an intermediate form between Figures 8-4 and 8-5.

Plotting our resistive $m = 2$, $n = 1$ mode at finite island size confirms this prediction. Both the inner and outer rational surfaces in Figure 8-7 show extended current sheet structures. Following the separatrix at the inner surface, however, shows that even away from the singular layer the axial current J_h is not strictly a function of the magnetic flux ψ^*. Furthermore, the kinetic and magnetic energies (Fig. 8-10) maintain exponential growth while the islands are finite sized, akin to the closely coupled Cartesian mode. This cylindrical DTM may, therefore, be a mode between the intermediate and strong regimes, as is indicated linearly by its growth rate scaling as $\gamma \sim \eta^{0.48}$.

The peculiarities of cylindrical geometry, however, prevent us from asserting the presence

or lack of an explosive phase in this system. As exhibited by streamlines of the plasma flow in Fig. 8-7, the magnetic pressure near the axis is insufficient to prevent the inner rational surface from coupling to itself across $r = 0$. This interior flux continues to decrease as the mode reconnects, thereby further decreasing the magnetic pressure and causing the current sheets on the inner rational surface to approach across the axis. By the time at which the separatrices merge (Fig. 8-8) the interior region is small and deformed, and subsequently vanishes all together as the outer islands drive the inner current sheets together (Fig. 8-9). Although our simulations are well resolved throughout this current sheet merging event the unphysically high degree of symmetry in our cylindrical domain means that past this point the applicability of our results to realistic devices is suspect. We note, however, that other simulations of $q = 2$ DTMs have found the same behavior and good agreement to Tokamak Fusion Test Reaction (TFTR) discharges [17], suggesting that this consumption of the flux interior to the r_{s1} surface is a challenge for low safety factor reverse shear plasmas. Studies of higher mode number instabilities have not found this behavior [9, 29].

The late time behavior of our $m = 2$, $n = 1$ cylindrical simulations should not, therefore, be treated as characteristic of DTM behavior in every application. At times prior to merging of the separatrices (Fig. 8-8), however, our results agree broadly with studies of more narrow current rings [9, 29]. The $q = 2$ example we have chosen is, in some sense, a worst case scenario for cylindrical DTM activity. Higher mode numbers are generally less strongly coupled (see Chap. 6.1), and will have a strong enough field near the axis to prevent the merging of the inner current sheets. Our mode will therefore be more difficult to decouple via differential drifts (see Chap. 5.2) and stabilization will be more easy to detect. Thus we expect the stabilization mechanisms explored in this work to be more effective for higher safety factor equilibria.

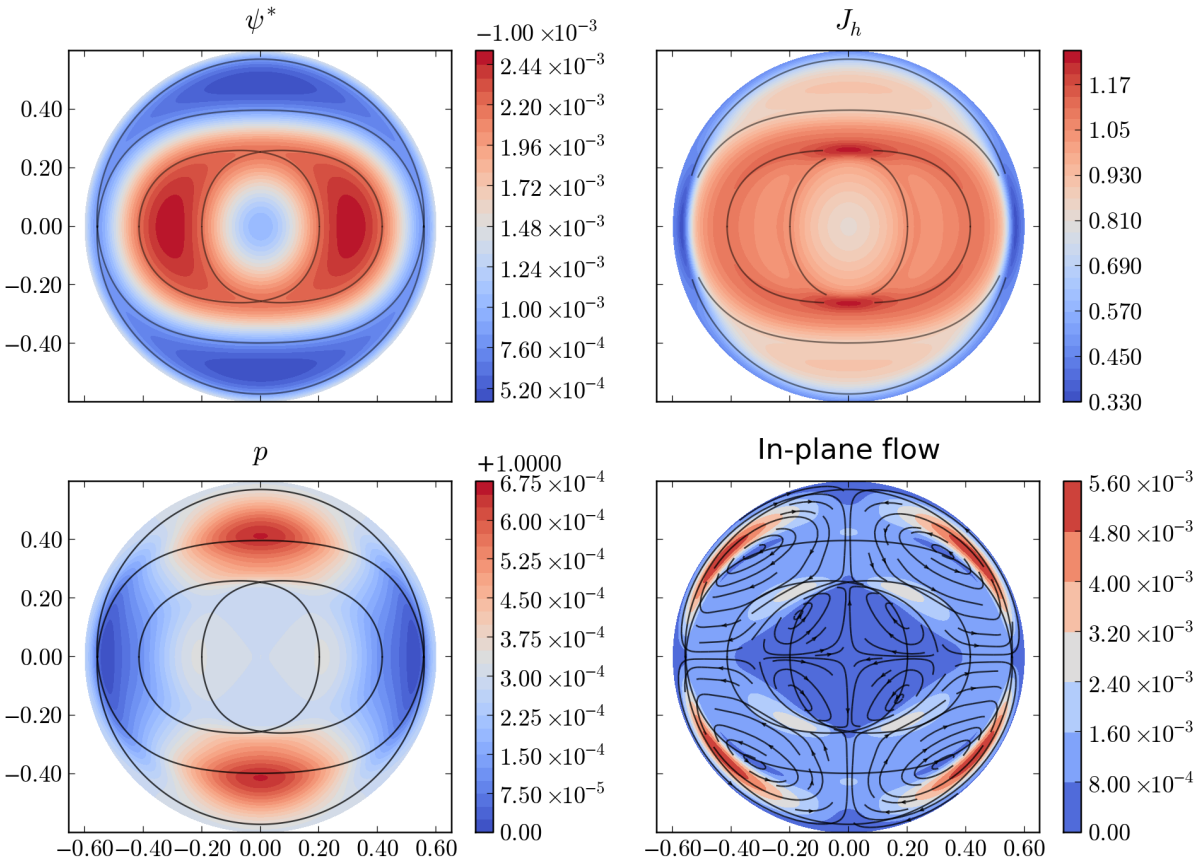

Figure 8-7: The $m = 2$, $n = 1$ cylindrical DTM is an asymmetric example of the transitional regime between moderate and strong coupling. Current sheets are visible at both rational surfaces but the island growth regime exhibits exponential energy growth. (simulation time $t = 600$, resistivity $\eta = 2 \times 10^{-5}$, $D = DT = \nu = 0.5\eta$)

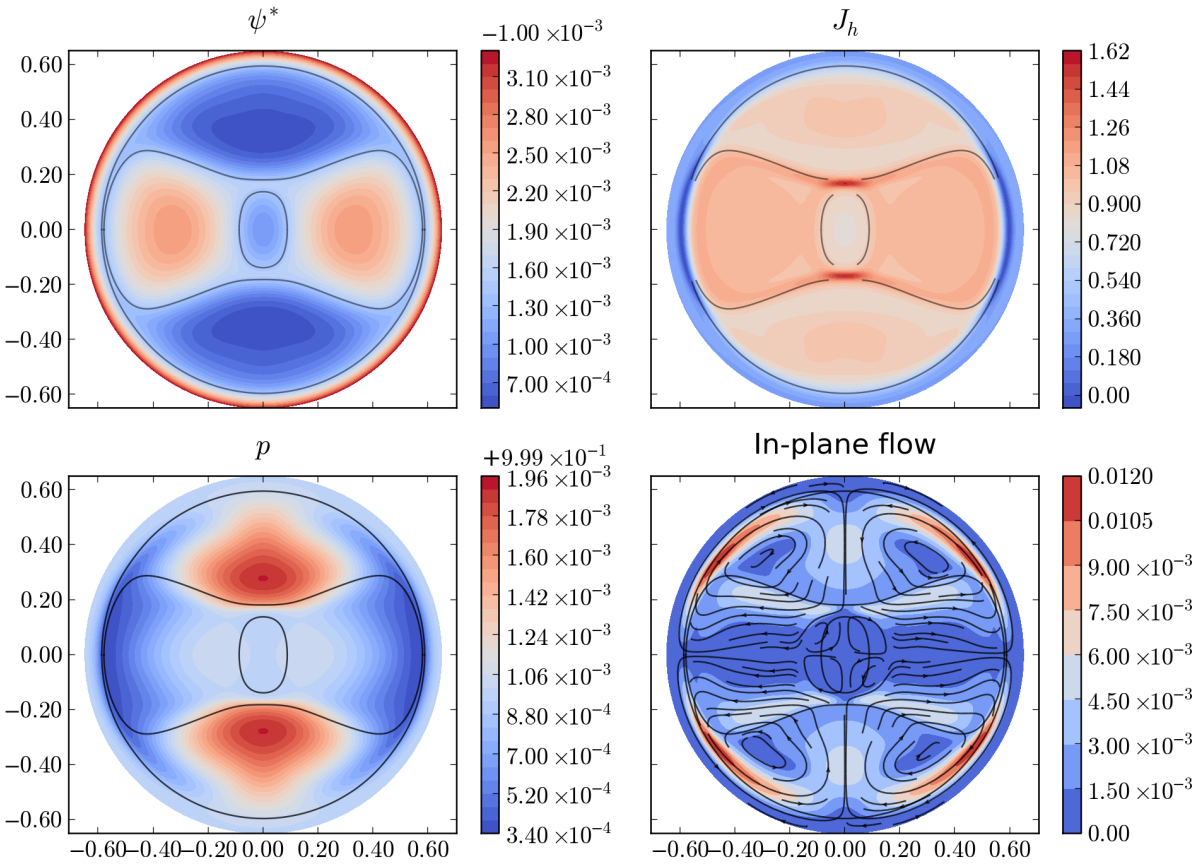

Figure 8-8: By the time at which the inner and outer separatrices merge the r_{s2} islands push the r_{s2} current sheets toward each, resulting in significant deformation of the magnetic field near the axis. Note that separatrix locations (solid black lines) plotted here are approximate due to the merging event interfering with our usual numerical saddle-point location technique. (simulation time $t = 690$, resistivity $\eta = 2 \times 10^{-5}$, $D = DT = \nu = 0.5\eta$)

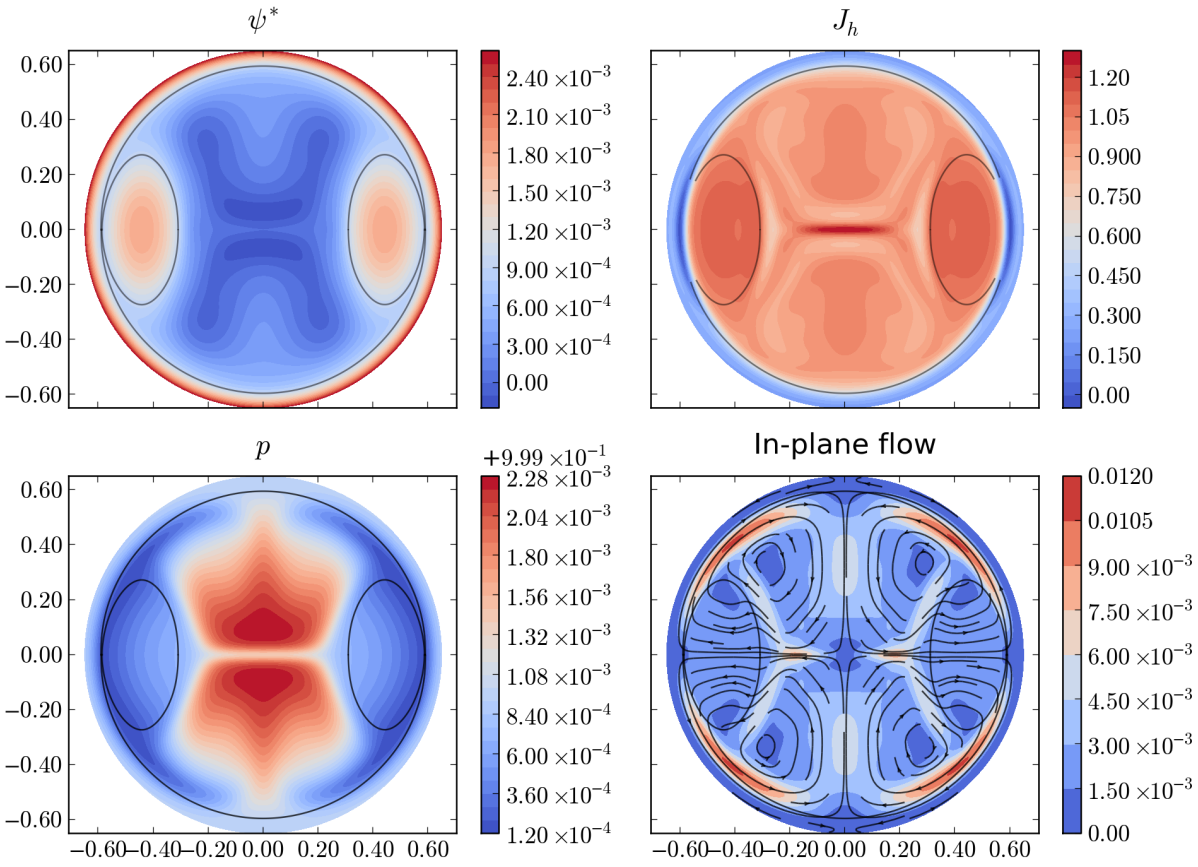

Figure 8-9: As reconnection continues the magnetic pressure along the axis is insufficient to prevent the inner current sheets from merging into a single structure. This behavior is likely an artifact of the unrealistically high symmetry in our simulations. The islands are consumed and confinement has been degraded. (simulation time $t = 770$, resistivity $\eta = 2 \times 10^{-5}$, $D = DT = \nu = 0.5\eta$)

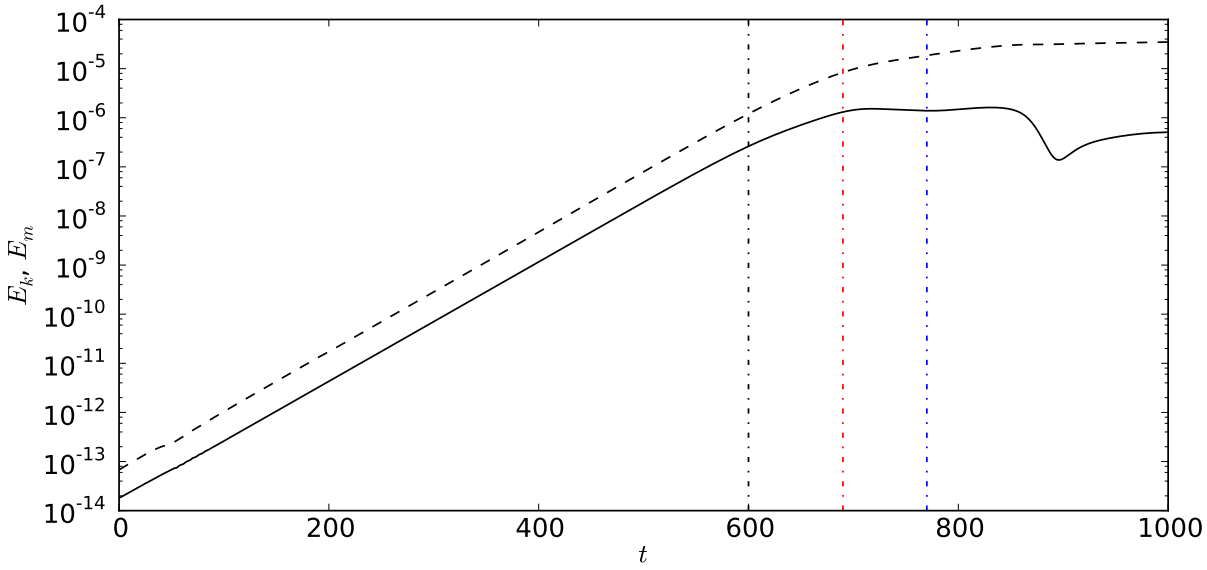

Figure 8-10: Evolution of kinetic (solid) and magnetic (dashed) energies for the $m = 2$, $n = 1$ cylindrical DTM. Dot-dashed lines indicate times for Figures 8-7 (black), 8-8 (red), and 8-9 (blue). The mode continues to evolve at the linear growth rate until the separatrices merge.

8.5 Discussion

In this chapter we have summarized the current understanding of the nonlinear double-tearing mode, from the slow island growth regime to the onset of explosive growth and finally complete reconnection. From this discussion it should be clear that much is not known about DTM evolution. Two important factors make studying this instability difficult. Numerically the nonlinear DTM is extremely challenging. The presence of two current sheets requires high resolution in at least two regions of the simulation domain, and during the explosive phase the current sheets commonly move as the islands drive them outwards. Furthermore, the explosive phase typically triggers at very late times, which is computationally expensive. These numerical challenges may, in principle, be overcome but doing so requires sophisticated techniques that are not widely available.

The second, and more difficult, challenge to DTM study is the wide parameter space. We have, at minimum, three potential final states of the nonlinear double-tearing mode: saturation at finite sized islands; explosive growth leading to complete reconnection; exponential

growth until complete reconnection without an explosive phase. It is unclear whether there are multiple classes of explosive phases or saturated islands, and the relationship between strongly coupled modes with and without an explosive phase has (to the author's knowledge) not been studied. To further complicate matters, both the sech and double-tanh equilibrium types are common, and thus there are significant variations in magnetic shear, spacing, and free energy in nearly all studies. Fundamentally, the problem reduces to an over-reliance on the linear coupling parameter kx_s as a descriptor of the double-tearing mode. A crucial component of nonlinear DTM work, going forward, should be a systematic mapping of the evolution with regards to spacing, magnetic shear, and free energy between the tearing surfaces. The recent work of Janvier et al. [31–33] has begun this process by exploring the boundary between saturated and explosively unstable DTMs in the constant ψ branch of the linear dispersion relation, but much of the parameter space remains unexplored. Such studies will require, however, addressing the numerical problems mentioned above so that scalings over resistivity may be conducted.

Despite the gaps in our understanding of the nonlinear DTM, some predictions can still be made concerning effective stabilization techniques. Our goal is to prevent complete collapse of the annular current ring due to either an explosive phase or fast exponential growth, both of which are weakly dependent on resistivity. Because it is not strongly current driven, it is not likely that a mechanism such as differential diamagnetic drifts will be able to stop the explosive phase once it is triggered. We will focus our efforts, therefore, on using diamagnetic drifts to slow the island growth regime and prevent development of structural instability and merging of the separatrices at each surface. As we will see in the following chapter, this will require overcoming not only the reconnection enhancements caused by the Hall term but also the tendency of the islands to re-lock the tearing surfaces nonlinearly.

Chapter 9

FLR effects on nonlinear DTMs

We have now categorized the nonlinear state of our force-free, resistive, $m = 2$, $n = 1$ cylindrical double-tearing mode and shown how the nonlinear growth of magnetic islands can lead to collapse of the annular current ring. In this chapter we will investigate the effect of electron diamagnetic drifts on this process. Linearly we found that differential diamagnetic drifts can significantly decrease the growth rate through a combination of global decoupling and local stabilization effects. We will see that finite sized magnetic islands modify this mechanism in both beneficial and detrimental ways. Growth of large islands tend to recouple the tearing surfaces (allowing faster evolution), but can also enhance the pressure gradients (and thus ω_* drifts) and increase stabilization. The competition between these two processes, as well as the ideal MHD destabilizing properties of the pressure gradient, will determine the final state of the Hall MHD DTM.

Using the machinery developed in previous chapters we will dissect the cylindrical $m = 2$, $n = 1$ double-tearing mode to understand the benefits and shortcomings of ω_* drifts as a stabilization mechanism. To begin we examine the impact of the FLR effects on the force-free DTM we categorized in Chapter 8.4. Using this force-free Hall MHD mode as a baseline we will then consider configurations with equal equilibrium ω_* at both rational surfaces. In Chapter 6 the linear growth rate of this class of profile increased with increasing pressure gradient, but we will show that the growth of large magnetic islands can enhance the local diamagnetic drift and stabilize the DTM. In light of this discovery we will briefly examine equilibria with ∇p localized at the inner r_{s1} rational surface, which are the most linearly unstable systems, and find that without an initial ω_* drift at the r_{s2} surface the outer islands disrupt the annular current ring before the nonlinear pressure enhancements can develop.

Finally we consider the class of DTMs with a steep pressure gradient at the r_{s2} rational surface, which we found to be most linearly stabilized. We will show two examples that have significantly slower nonlinear development compared to the force-free mode. Of these two examples, one will progress toward complete reconnection and the other will effectively saturate. We will propose an explanation for this different behavior.

In this chapter we will closely follow the linear work of Chapter 6, choosing characteristic equilibria to simulate nonlinearly. As before, we will run in the cold-ion regime ($\tau = 0$) and set the equilibrium electron temperature constant at $T = 1$. Initial diamagnetic drifts will be generated by equilibrium density profiles of the form:

$$\rho(r) = N_0 \left\{ 1 - (1 - N_b) \frac{\tanh(r_0/\delta_N) + \tanh[(r - r_0)/\delta_N]}{\tanh(r_0/\delta_N) + \tanh[(1 - r_0)\delta_N]} \right\} \tag{9.1}$$

This density is the same introduced in Equation 2.22 and used throughout Chapter 6.

9.1 Nonlinear simulation techniques and analysis

The simulations in this chapter are generated, as before, by the `MRC-3d` simulation code using helically symmetric, two-dimensional, periodic cylindrical geometry. The behavior of the double-tearing mode changes substantially during its nonlinear evolution and simulating to the important late times at sufficient resolution is computationally expensive. To alleviate this cost somewhat we follow the common practice of seeding a large initial perturbation, typically 1×10^{-4} times the equilibrium field. We have verified, for a subset of equilibria, that the final behavior of the mode is the same whether we use this large perturbation or allow the system to develop linearly. To further reduce the computational cost we rely heavily on `MRC-3d`'s implicit time-integration capabilities, which allows us to take comparatively large time steps. Our implicit solver is not adaptive and manual adjustment of Δt is necessary when the algorithm fails to converge. To save computation time we will typically not continue a simulation if the we observe that the inner and outer separatrices have merged, as we

consider this point to be a sufficient marker of disruption. All important simulation results have been tested for convergence in both time and spatial resolution, and we are confident these techniques do not affect the validity of our results.

Nonlinear simulations at realistic resistivities require unfeasibly high spatial resolution and we follow the common practice of using a larger value ($\eta = 2 \times 10^{-5}$ for this study). To further enhance stability, we also exploit the additional diffusion parameters available in `MRC-3d` by setting them to half the resistivity ($D = DT = \nu = 1 \times 10^{-5}$). These parameters may have a physical impact (in particular for the locking of magnetic islands [50]), however in our experience their primary effect is a small reduction in observed growth rates. The more substantial consequence of these large parameters (including resistivity) is that the characteristic timescales of the DTM growth and diffusion of the equilibrium are not as widely separated as in a more realistic system. To balance this we enable the `MRC-3d` 'source term' (see Appendix A), which is equivalent to introducing an external electric field that drives the system toward equilibrium. The evolution of the DTM at early times is sufficiently fast and depends weakly enough on resistivity that our results remain physically relevant. After complete reconnection, however, or when a saturated state is reached this source electric field has the effect of 'pumping' the system with energy. When we feel this effect is important to our results we will discuss it explicitly.

Before presenting our results it is useful to explain one feature of our data analysis technique and plot generation. In previous chapters we have used a numerical saddle-point identification algorithm to determine the magnetic separatrices and plot them explicitly. The strong diamagnetic drifts examined in this chapter interfere with this technique. When possible we have determined the saddle points via inspection, but this process is time consuming and frequently impractical. In any event, our two-dimensional, cylindrical simulations involve enough approximations that direct quantitative comparison to true tokamak devices is not possible. Therefore when automatic separatrix tracking fails we will instead plot contours of the flux function through the region of interest. This method will still allow qualitative

evaluation of the state of the DTM evolution and discernment of important characteristics.

Having established the basic techniques and caveats we may now proceed to our Hall MHD simulation results.

9.2 Nonlinear Hall DTMs

The evolution of the current layers during the multiple phases of nonlinear DTM reconnection allow for the Hall term to have a time-dependent influence normally absent from steady state STM systems. As the magnetic islands grow, they compress the current sheet at the opposite resonant surface. If the layer thickness falls below the characteristic ion scale (ρ_s for non-zero guide field, otherwise d_i) the reconnection site will collapse from a current sheet (Y-point geometry) toward the characteristic Hall current point (X-point configuration) [18]. The associated acceleration of the reconnection rate will not only hasten the onset of the explosive phase but also increase its maximum growth rate and the amount of kinetic energy generated. This effect has been confirmed in systems both with [1] and without [63] guiding magnetic fields. In force-free systems, therefore, the addition of Hall physics alters the seperatrix morphology and allows more efficient conversion of magnetic energy to kinetic but does not fundamentally alter the progression of the DTM, though it is unclear how quasilinear stability thresholds might be affected.

While these accelerating properties of the Hall term will likely be a factor in advanced tokamaks with high safety factor and small aspect ratio (and therefore weaker toroidal field) we find that the current sheets in our $m = 2$, $n = 1$ cylindrical DTM do not undergo collapse for the parameters of $\eta = 2 \times 10^{-5}$ and $d_i = 0.1$ that we use for nonlinear simulations. Due to the strong guide field in this equilibrium the ions decouple a distance $\rho_s = \sqrt{\beta} d_i = 0.014$ away from the rational surfaces, which is not large enough to cause enhancement unless the resistivity is very small. As a consequence the linear and early nonlinear growth of the Hall MHD mode is only barely faster than the resistive system, as shown in Figure 9-1.

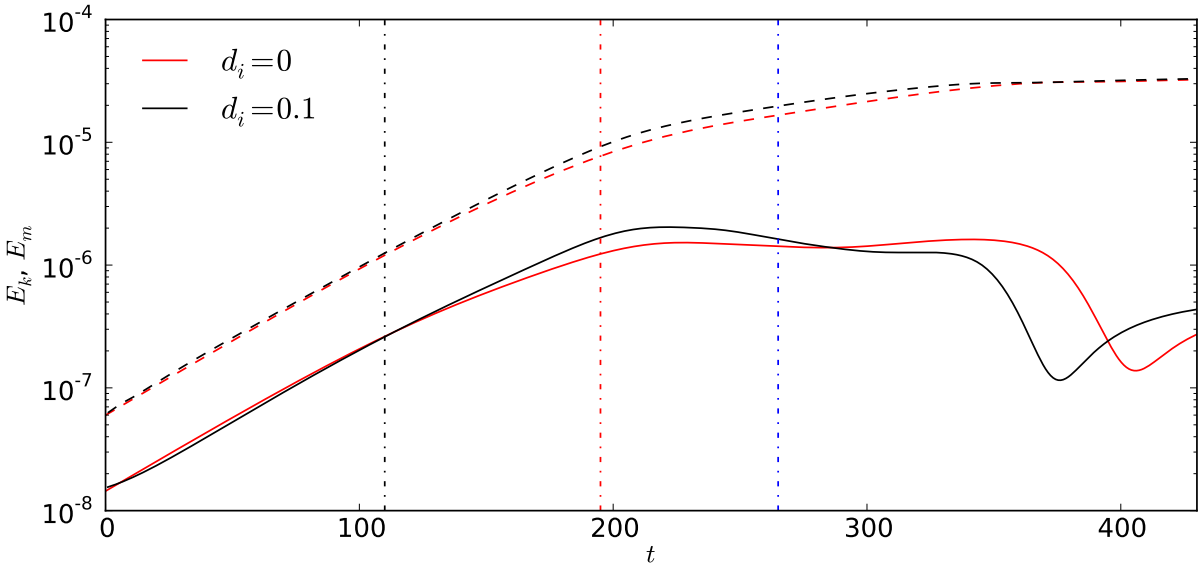

Figure 9-1: Evolution of kinetic (solid) and magnetic (dashed) energies for the $m = 2$, $n = 1$ force-free cylindrical DTM. Dot-dashed lines indicate times for Figures 9-5 and 9-6 (black), 9-7 (red), and 9-8 (blue). The ion inertial length of $d_i = 0.1$ results in a Hall DTM with slightly faster growth than the resistive DTM.

The separatrix and current morphology in the early nonlinear show weaker FLR effects than those discussed for STMs in Section 7.3. Figures 9-5 and 9-6 show the state of the resistive ($d_i = 0.0$) and Hall MHD ($d_i = 0.1$) systems at time $t = 110$ in each simulation, indicated by the dashed line in Fig. 9-1 where E_k is equal for both models. The axial current J_h, separatrix geometry, and plasma flow are nearly identical in both cases, with the caveat that the current sheets at the inner and outer reconnection sites are slightly more peaked in the Hall MHD run. As the islands grow, therefore, this systems stays in the weak to moderate Hall regime.

As the inner and outer separatrices merge the two models begin to deviate more substantially. The small enhancement of the reconnection rate in the Hall MHD simulation is sufficient for the total E_k and perturbed E_m to rise above their resistive MHD counterparts. In particular the peak E_k occurs earlier in the simulation, and the merging of the inner current sheets is accelerated. However the overall magnetic field and current sheet geometry during the merging of the inner and outer seperatrices (Fig. 9-7) and after the collision of the inner current sheets (Fig. 9-8) is not significantly impacted by the presence of FLR effects.

Our force-free $m = 2$, $n = 1$ can be considered, therefore, to be in the weak or moderate Hall regime throughout the entirety of its evolution. We will use this case as the baseline DTM for our nonlinear stabilization study.

9.3 Equal drifts at both $q = 2$ rational surfaces

In order to isolate the effects of diamagnetic drifts without considering the complications of DTM decoupling we will begin by introducing a broad pressure profile that generates equal ω_* at both $q = 2$ rational surfaces. Linearly the destabilizing contribution of the pressure gradient dominated over the FLR effects local to tearing layers (Fig. 6-10). In other reconnecting systems, however, the nonlinear growth of the magnetic islands has been shown to steepen the pressure gradients local to each layer and increase the stabilizing diamagnetic drift [41]. To examine whether such an effect is present for the double-tearing mode we consider two example equilibria: a shallow profile which produces a drift of $\omega_* = 2 \times 10^{-2}$ and has a linear growth rate only marginally greater than the force-free value (Fig. 6-10); and a steep profile with $\omega_* = 1 \times 10^{-1}$ that resulted in stronger liner growth. For reference the 2D shapes of these pressure profiles are shown in Figure 9-9.

The kinetic and magnetic energy growth for these two drift values is plotted together with the force-free Hall MHD mode growth in Figure 9-2. Let us first consider the $\omega_* = 2 \times 10^{-2}$ mode. The system kinetic energy (red line) is nearly an order of magnitude larger than the non-drifting mode (black line) at all times. E_m, in contrast, has approximately the same growth rate and magnitude until $t \approx 100$, after which the $\omega_* = 2 \times 10^{-2}$ DTM grows slightly faster. Because the electron diamagnetic drift is the same at both rational surfaces the mode is rotating, which results in a larger integrated kinetic energy. E_m better represents the comparative evolution of the DTM, and its behavior is consistent with the growth rates of the linear modes being approximately the same. The state of the drifting simulation near the merging of the inner and outer separatrices is shown in Figure 9-11, and can be compared

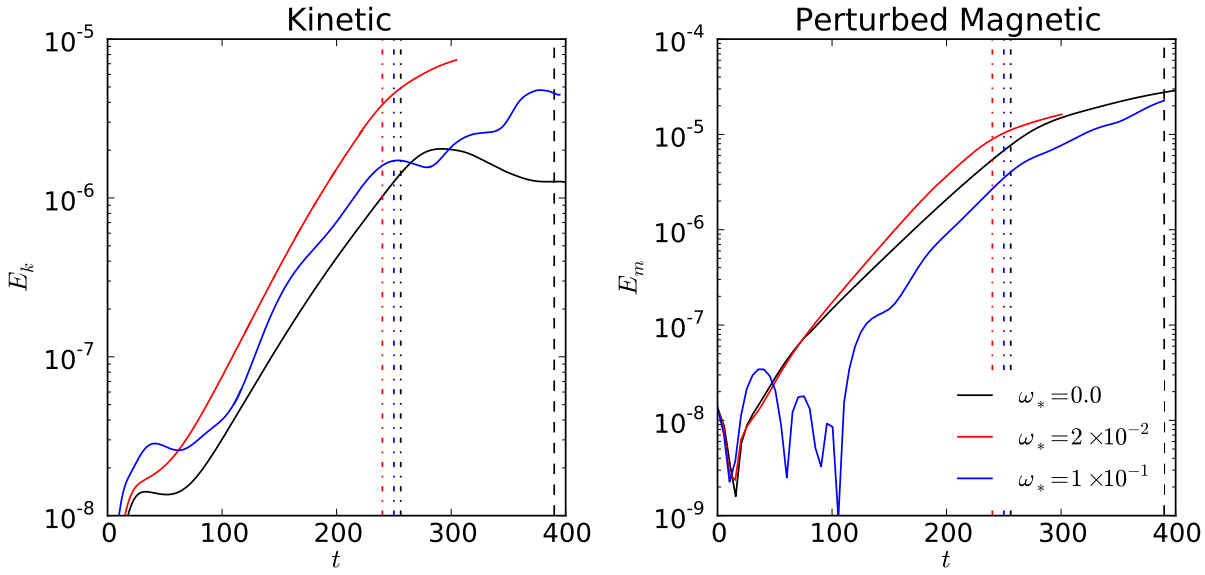

Figure 9-2: Evolution of kinetic (E_k) and perturbed magnetic (E_m) energies for the $m = 2$, $n = 1$ cylindrical DTM with equal initial electron diamagnetic drifts at both rational surfaces. The black and red dot-dashed lines indicate the separatrix merging point for the force-free ($\omega_* = 0$) and weak drift ($\omega_* = 2 \times 10^{-2}$) DTMs respectively, and the states of the simulations at these times are shown in Figures 9-7 and 9-11. The blue dot-dashed indicates the approximate time at which the growth of the $\omega_* = 1 \times 10^{-1}$, strong drift DTM slows, and is plotted in Figure 9-12. This time is not indicative of the separatrix merging event. Instead nonlinear enhancement of the pressure gradients local to each layer have stabilized the mode. Even at time $t = 390$ (black dashed line, Fig. 9-13) some flux remains unreconnected between the inner and outer separatrices.

to a similar state of the force-free equilibrium in Figure 9-7. Although the overall structure of the magnetic islands is similar, the diamagnetic drift has several important impacts. The outflow jets from the reconnection sites are biased strongly in the direction of the diamagnetic drift ($\hat{u} \sim \hat{\theta}$, see Eqn. 6.7), and the magnetic structures are sheared with the drift local to the surfaces. This elongation is, however, not uniform. Considering the upper half plane, the peaks of the inner and outer current sheets are separated by an angle of 76° rather than the 90° observed in the force-free case. Radials of the pressure across the two current sheets (Figure 9-10) show that the growth of the magnetic islands flattens the pressure gradient between the $q = 2$ rational surfaces and steepens it asymmetrically at the current sheets, introducing a slight differential drift and shearing the DTM structure. This effect is not, however, sufficient to either decouple the two surfaces or locally stabilize the reconnection process.

The nonlinear evolution of the pressure gradient becomes more important in the case of

the steeper profile that gives a drift of $\omega_* = 1 \times 10^{-1}$ at both surfaces. Previously we found the linear growth rate of this system to be faster than both the force free and $\omega_* = 2 \times 10^{-2}$ equilibria (Sec. 6.3). The DTM eigenmode, however, emerges slowly from the initial nonlinear perturbation, as shown by the early fluctuations in E_m on Figure 9-2. It eventually develops with a growth rate comparable to the other two equilibria (Fig. 9-2), suggesting that the quasilinear evolution is significantly different than the linear. The growth of the kinetic and magnetic energies slow near simulation time $t = 250$, and at a lower amplitude than the previously examined systems. At this rollover point a significant region of unreconnected flux exists between inner and outer separatrices (Fig. 9-12), thus this change in behavior is not associated with the separatrix merging event observed in the previous examples. Plotting radials of the pressure profile at this time (Fig. 9-10) we observe a substantial increase in the gradient at both the inner and outer surfaces as the growing islands drive the core plasma toward the opposite reconnection site. The resulting enhancement to the local diamagnetic drift significantly slows the growth the instability. This process has been observed in other reconnecting systems [41] and has been proposed as a mechanism for the appearance of large, saturated magnetic islands during incomplete $m = 1$ sawtooth crashes [8].

The inner and outer separatrices have not merged as of time $t = 390$ (Fig. 9-13) even though the kinetic and magnetic energies have grown larger than the force-free DTM (Fig. 9-2). Development in this late stage is sufficiently slow that the source electric field is likely significant and may be driving the continued growth of E_k and E_m. We cannot, therefore, claim that the state of this system is representative of the DTM behavior in a true reactor. It is apparent, however, that amplification of the pressure gradient has had a strong stabilizing effect on the double-tearing mode evolution. Further investigation may show that this mechanism can result in saturated, finite size double-tearing mode islands. As this enhancement of the pressure gradient only occurs in the late nonlinear phase, however, the DTM has already generated strong current sheets and large magnetic islands. The impact these structures may have on confinement and stability is unclear. Continuing this work further

will require better modeling of tokamak conditions, and is outside the scope of this thesis. We will instead proceed to configurations with differential drift, which were linearly more fruitful, and consider the implications of nonlinear pressure gradient enhancement there.

9.4 Concentrated ω_* at the inner surface

Linearly we found that localization of a pressure gradient (and thus diamagnetic drift) at the inner rational surface increased the growth rate of the double-tearing mode (Sec. 6.3). The energy growth of two example profiles with $\Delta\omega_*$ of 2×10^{-2} and 1×10^{-1} generated by a pressure gradient of width $\delta_N = 0.10$ are plotted in Figure 9-3, and show that this class of profile is similarly destabilizing for the nonlinear DTM. It holds nonlinearly, therefore, that some mechanism must be applied near the dominant, outer rational surface in order to slow the mode growth.

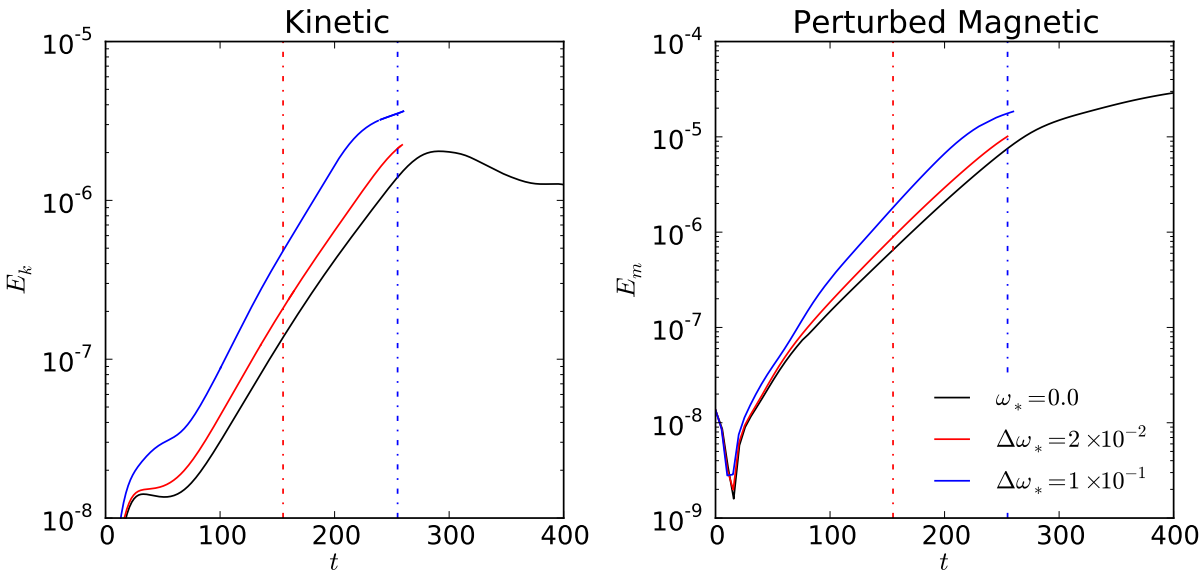

Figure 9-3: Evolution of kinetic (E_k) and perturbed magnetic (E_m) energies for the $m = 2$, $n = 1$ cylindrical DTM with a pressure gradient localized at $r_0 = r_{s1}$, on the inner rational surface. The inner surface experiences an equilibrium diamagnetic drift and the outer surface does not, resulting in a differential drift $\Delta\omega_*$. Both dot-dashed vertical lines indicate times for which we have generated 2D plots of the $\Delta\omega_* = 1 \times 10^{-1}$ DTM: red is time $t = 155$ and the early nonlinear state plotted in Fig. 9-14; blue is time $t = 255$ and shows the system state just prior to the inner current sheets colliding across the $r = 0$ axis, shown in Fig. 9-15. We have chosen not to extend the simulations once it is clear that the annular current has been disrupted.

As the focus of this work is primarily on stabilization mechanisms we will not examine this type of profile in great detail. We will note, however, that the evolution of the pressure gradient also affects the DTM final state in this class of equilibrium. At time $t = 155$ the state of the $\Delta\omega_* = 1 \times 10^{-1}$ (Fig. 9-14) resembles the force-free mode (Fig. 9-6) except that the diamagnetic drift at the inner surface causes the current sheets to be elongated and the islands to be sheared. The core plasma remains, at this time, bound by the inner separatrix. At the later time of $t = 255$, however, the separatrices have merged and the inner islands are being reconnected at the outer rational surface (Fig. 9-15). The pressure profile spans the entire diameter between $\theta = 0$ and π, and as such is able to impact the current sheets at r_{s2} and may slow the progression towards complete reconnection. This state requires, however, a merging of the separatrices and the disruption of the pressure core and annular current.

9.5 Concentrated ω_* at the outer surface

We have consistently found that the steeper magnetic shear at the outer rational surface of this $q = 2$ cylindrical equilibrium results in the r_{s2} layer dominating the DTM evolution. The most effective linear stabilization came from localizing a strong pressure gradient at this outer surface (Sec. 6.3), exploiting both differential drift and local ω_* properties. In this section we choose two equilibrium pressure profiles centered on the outer rational surface that produce the same differential diamagnetic drift of $\Delta\omega_* = 1 \times 10^{-1}$. Recall that in our linear study we found that increasing $\Delta\omega_*$ localized at the r_{s2} would decrease the growth rate until some threshold, after which an ideal MHD instability would begin driving the growth (Fig. 6-12). For the gradient width $\delta_N = 0.1$ a differential drift of $\Delta\omega_* = 1 \times 10^{-1}$ is above this threshold, and has a γ less than the force-free value but increasing. For $\delta_N = 0.05$, however, this drift is the minimum of γ, as well as being the lowest growth rate achieved in our linear study. Nonlinearly the promising stabilization features of this class of equilibrium persist, and we find the growth of the kinetic and magnetic energies to be significantly slower

than the force-free DTM.

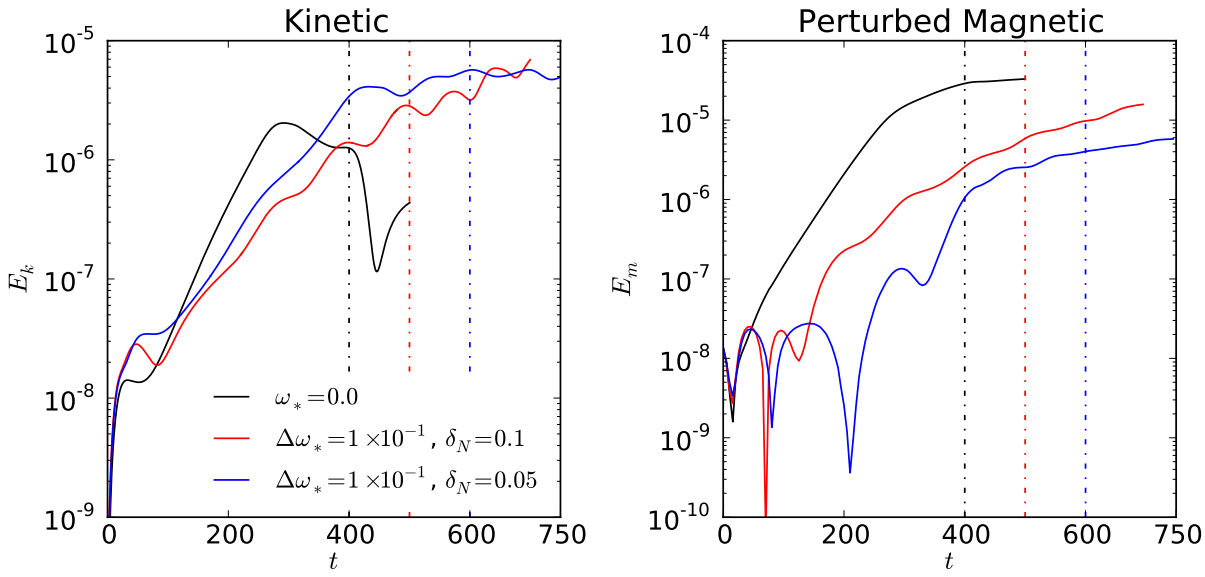

Figure 9-4: Evolution of kinetic (E_k) and perturbed magnetic (E_m) energies for the $m = 2$, $n = 1$ cylindrical DTM with a pressure gradient localized at $r_0 = r_{s2}$, on the outer rational surface. The outer surface experiences an equilibrium diamagnetic drift and the inner surface does not, resulting in a differential drift $\Delta\omega_*$. Linearly the two surfaces are decoupled by differential drift and the magnetic energy growth shows that some time is required before the islands at the outer, suppressed rational surface grow large enough to lock the mode. Both the drifting DTMs are stabilized with respect to the force-free example. The black dot-dashed vertical line indicates simulation time $t = 400$ at which we plot the state of both the broad $\delta_N = 0.1$ (Fig. 9-16) and localized $\delta_N = 0.05$ (Fig. 9-17) simulations. The red and blue dot-dashed lines indicate important times for the broad $\delta_N = 0.1$ simulation: red is near the separatrix merge point ($t = 500$, Fig. 9-18); blue is just after the inner current sheets collide across $r = 0$ ($t = 600$, Fig .9-19). Neither of these events occur within our $\delta_N = 0.05$ simulation.

The perturbed magnetic energy of the drifting profiles is highly oscillatory in the early nonlinear (Fig. 9-4), with the apparent frequency decreasing as the mode grows. These fluctuations can be related to the (de)coupling of the magnetic islands. Linearly the differential drift is sufficient to decouple the two reconnecting surfaces. As the islands reach finite size, however, they interlock [50] and again drive each other. At late times our simulations also show higher frequency oscillations of the energies, in particular for the $\delta_N = 0.1$ profile. Inspection of time series plots and comparison to similar behavior for strongly stabilized 'equal drift' runs (Fig. 9-2) suggests these fluctuations are caused by intermittent reconnection as the pressure gradients around each tearing layer shift, however we have not examined this phenomenon in detail.

Comparing both the $\delta_N = 0.10$ (Fig. 9-16) and $\delta_N = 0.05$ (Fig. 9-17) DTMs at simulation time $t = 400$, we observe that the outer magnetic islands are highly elongated while the inner

islands are merely sheared, consistent with the relative diamagnetic drifts at each surface. In both simulations the nonlinear locking of the inner and outer surfaces has 'spun-up' the islands at r_{s1}, but because the pressure gradient is not significant at the inner reconnection sites they do not experience the ω_* effects which cause the biased outflow jets and elongation seen at r_{s2}. We note, however, that the current peaks and outflow jets at each surface of the $\delta_N = 0.05$ DTM appear to have split. Two reconnection sites are visible for each wavelength. This suggests that the elongated current sheets may have become unstable to some secondary process such as plasmoid instability, which has been observed in DTMs previously [62]. Our ability to determine and track the separatrices is not, however, precise enough in this high drift regime to confirm this conclusion.

Although its growth is slowed significantly, the $\delta_N = 0.10$ is not completely stabilized. Near time $t = 500$ (Fig. 9-18) the inner outer and separatrices merge, and at $t = 600$ (Fig. 9-19) the magnetic field near the $r = 0$ axis is consumed and the inner current sheets approach each other. The steeper $\delta_N = 0.05$ profile is, by contrast, intact even at time $t = 750$ (Fig. 9-20). The kinetic energy has saturated, and the magnitudes of the current sheets and maximum plasma flows are less than or equal their counterparts at time $t = 400$ (Fig. 9-17). Finite sized magnetic islands are visible, but because the inner and outer separatrices have not merged the pressure profile remains intact. Accounting for the source electric field (which slowly pumps magnetic energy into the simulation, attempting to restore equilibrium) we consider this system a nonlinearly saturated DTM.

The key to understanding why the $\delta_N = 0.05$ profile saturates and the $\delta_N = 0.10$ system does not may lie in understanding how the ideal MHD stability depends on the details of the pressure profile, and how the ∇p driving changes with the nonlinear evolution. The islands at time $t = 400$ of the $\delta_N = 0.10$ profile are of approximately the same size as the saturated $t = 750$ state of the more localized $\delta_N = 0.05$ DTM, however radials of the pressure at the extrema of the current on each surface reveal substantial differences (Fig. 9-21). For the unstable $\delta_N = 0.10$ mode the gradient at r_{s2} is steeper than its equilibrium counterpart, and the

growth of the outer islands has broadened the profile wide enough to have finite gradient at the inner surface. The more localized, stabilized $\delta_N = 0.05$ mode, in contrast, does not show significant enhancement of ∇p at r_{s2} and the outer magnetic islands are not large enough to cause enhanced ω_* at the inner surface. We cannot, therefore, attribute the stabilization to nonlinear steepening of the pressure profiles as in Section 9.3. We propose, therefore, that for both the linear and nonlinear cylindrical DTM the efficacy of diamagnetic drifts can be characterized as a competition between the stabilizing, reconnection site local FLR effects and the destabilizing, ideal MHD mode. Without understanding how the pressure gradient drives the DTM growth it is difficult to determine how these modes will behave in actual tokamak reactors.

9.6 Discussion

Building on the linear work of Chapter 6 we have identified two profiles which are good candidates for nonlinear DTM stability. The most successful of these is a steep equilibrium pressure gradient with $\delta_N = 0.05$ centered at the r_{s2} rational surface. In our simulations an initial differential drift of $\Delta\omega_* = 1 \times 10^{-1}$ results in a saturated mode that maintains good confinement of the core plasma and preservation of the annular current ring. A similar differential drift produced by a wider $\delta_N = 0.1$ profile is also suppressed but does not saturate. The difference between the evolution of these two double-tearing modes, and their relevance to realistic tokamak configurations, will require a better understanding of the ideal MHD behavior.

A broad pressure profile with equal diamagnetic drifts of $\omega_* = 1 \times 10^{-1}$ at both rational surfaces was shown to be unexpectedly stable nonlinearly, given that the linear growth rate of this DTM was higher than the force-free baseline. As the magnetic islands grew they enhanced the pressure gradients, and thus diamagnetic drifts, at the current layers. This enhancement drastically reduced reconnection in the system, although it is unclear

whether this DTM can be considered saturated. The pressure gradients needed to generate this stability are only able to form at late times when the magnetic islands have grown to substantial size. It is possible, therefore, that the continued growth of the kinetic and perturbed magnetic energies in this example is due to a structure driven secondary instability similar to that discussed in Chapter 8. If this is the case then this nonlinear enhancement of the drifts may not be sufficient to prevent disruption. Regardless, this unexpected stability of an equal drift mode suggest that (contrary to the linear predictions) a sufficiently strong diamagnetic drift may be able to stabilize the DTM without first decoupling the tearing surfaces.

These nonlinearly stabilized profiles are the primary result of this thesis and their relevance to actual tokamak configurations relies on the validity of the work presented in the previous chapters. We will delay, therefore, further analysis and discussion of future work until the final chapter.

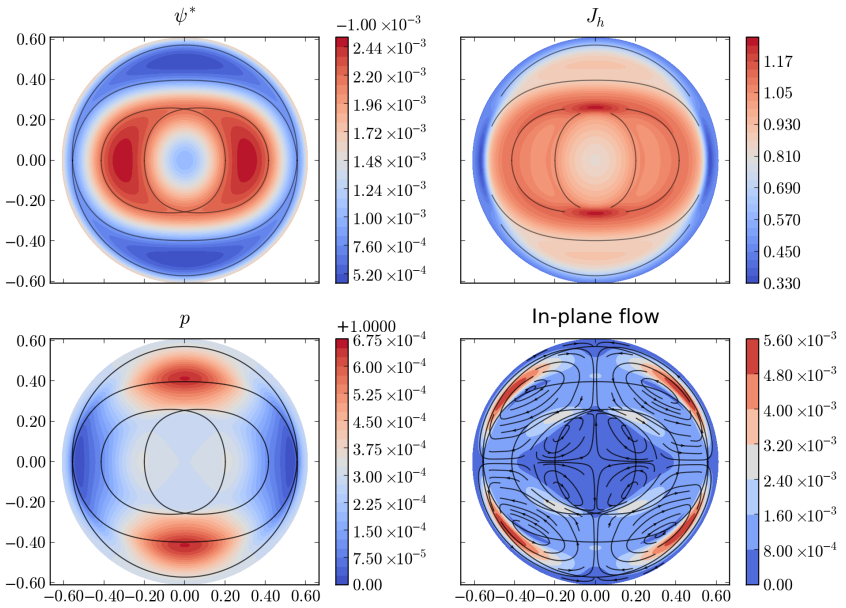

Figure 9-5: State of the resistive (d_i=0) DTM at time $t = 110$ (black dot-dashed line in Fig. 9-1).

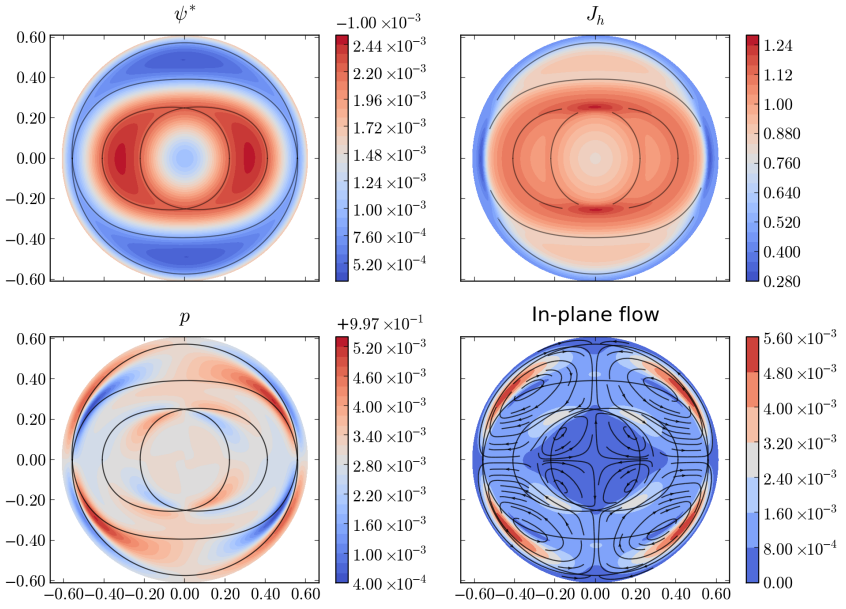

Figure 9-6: State of the Hall (d_i=0.1) DTM at time $t = 110$ (black dot-dashed line in Fig. 9-1).

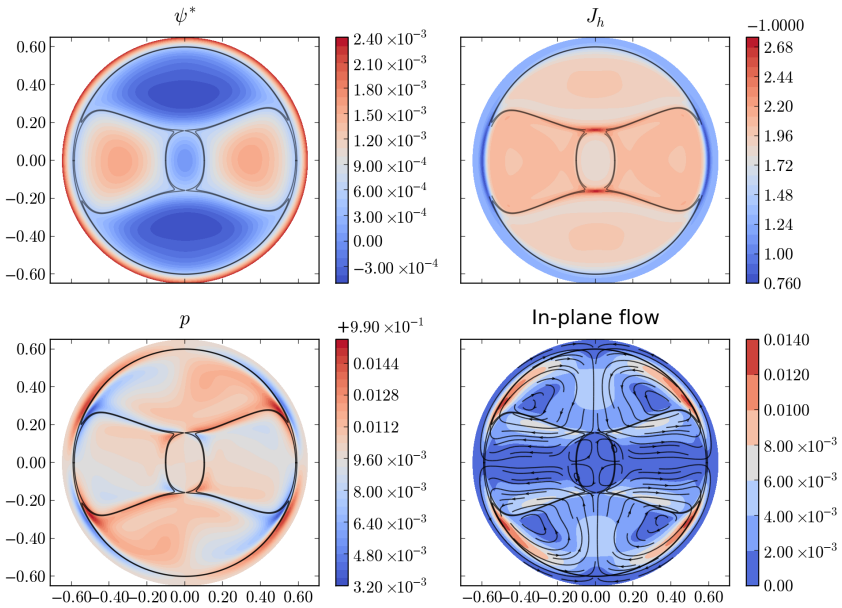

Figure 9-7: State of the Hall (d_i=0.1) DTM at time $t = 195$ (red dot-dashed line in Fig. 9-1), at which point the inner and outer separatrices merge. The magnetic field and current geometry is not significantly different than the resistive DTM (Fig. 8-8).

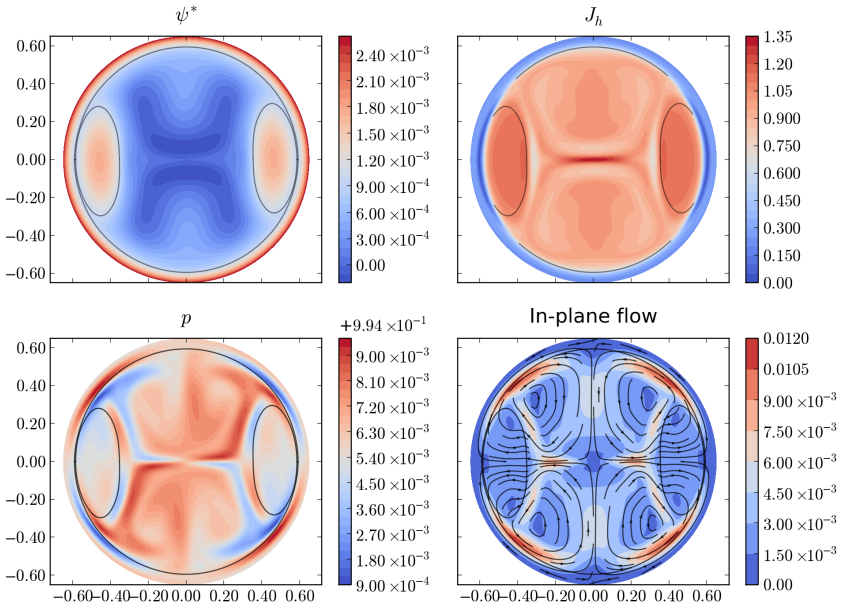

Figure 9-8: State of the Hall (d_i=0.1) DTM at time $t = 265$ (blue dot-dashed line in Fig. 9-1) after the current sheets at the inner rational surface have collapsed across the $r = 0$ axis.

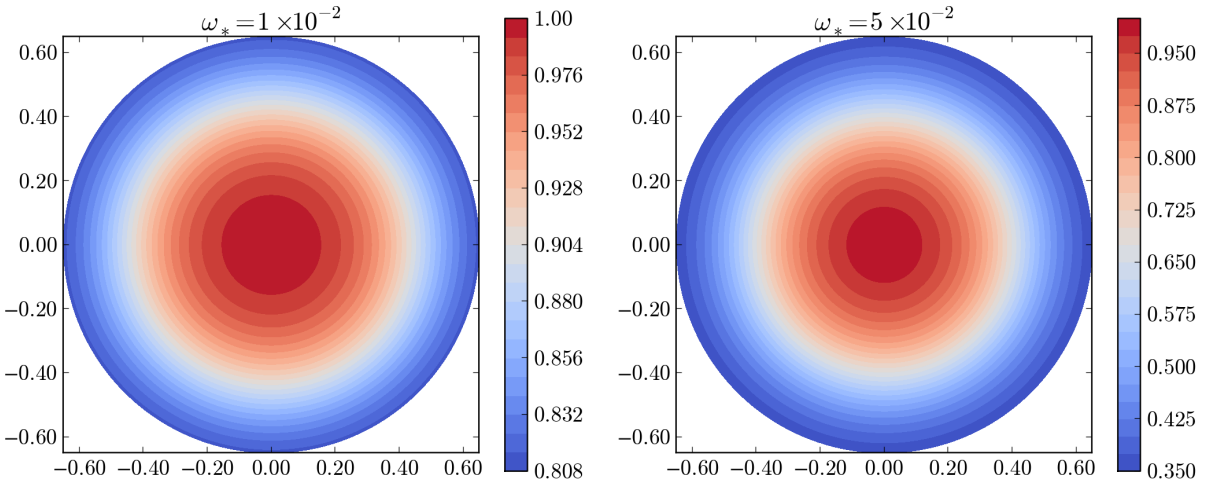

Figure 9-9: Two dimensional form of the equilibrium pressure profiles used to generate an equal diamagnetic drift at both $q = 2$ rational surfaces. The peak pressure gradient is centered at $r_0 = (r_{s1} + r_{s2})/2$, the profile width is set at $\delta_N = 0.2$, and the core pressure is fixed at $N_0 = 1$. We adjust the edge pressure N_b to achieve the desired electron diamagnetic drifts of $\omega_* = 2 \times 10^{-2}$ (left) and $\omega_* = 1 \times 10^{-1}$ (right).

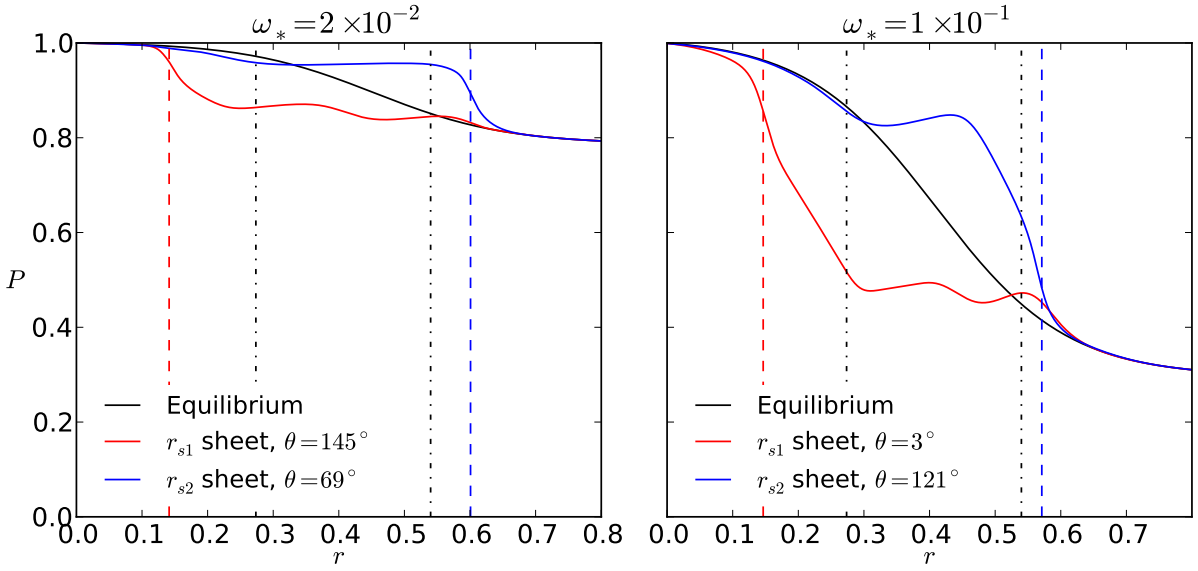

Figure 9-10: Radials of the pressure profile at the seperatrix merging time of the $\omega_* = 2 \times 10^{-2}$ equal drift DTM (Fig. 9-11), and the time at which the energy growth of the $\omega_* = 1 \times 10^{-1}$ slows (Fig. 9-12). Vertical dashed lines indicate radii of the current sheets: black are the equilibrium $q = 2$ rational surface positions; red is peak of the inner current sheet at the later time; blue is the peak of the outer current sheet at the later time. Solid red lines are radial cuts across the inner current sheet, solid blue lines are cuts across the outer current sheet, and black lines are the equilibrium profiles. Nonlinear growth of the magnetic islands increases the pressure gradient at the reconnection sites for both simulations.

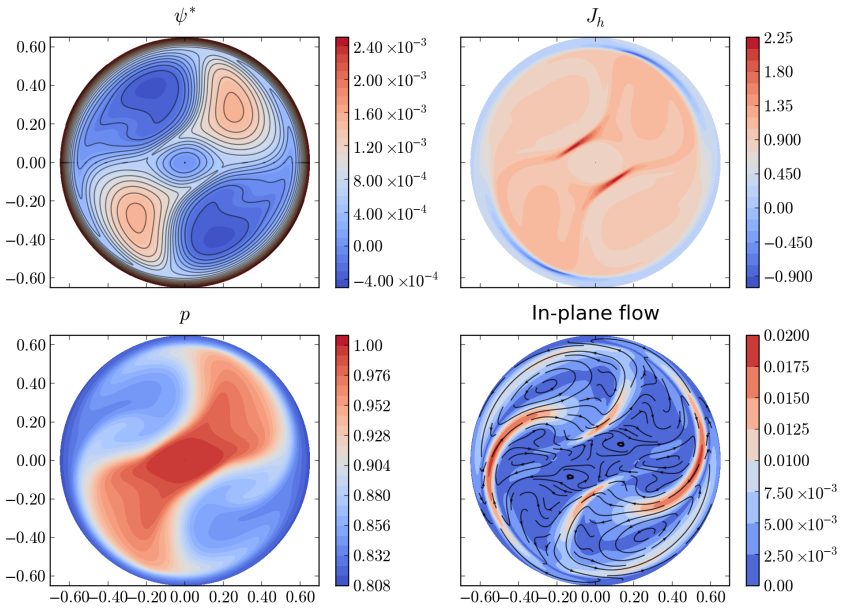

Figure 9-11: $\omega_* = 2 \times 10^{-2}$ equal drift DTM at simulation time $t = 240$ (red dot-dashed line in Fig. 9-2). The inner and outer separatrices are merging together, which decreases the growth the kinetic and magnetic energies.

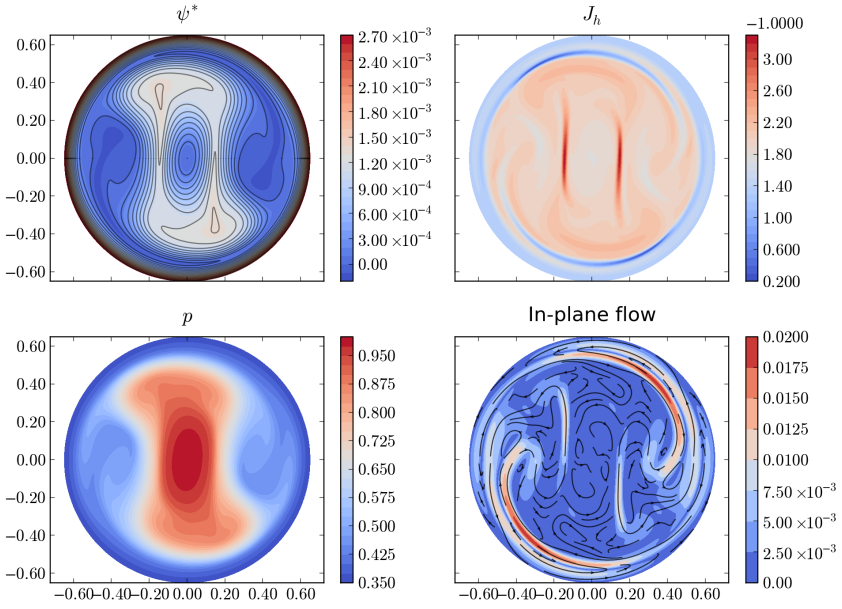

Figure 9-12: $\omega_* = 1 \times 10^{-1}$ equal drift DTM at simulation time $t = 250$ (blue dot-dashed line in Fig. 9-2). A significant amount of flux remains between the inner and outer separatrices, showing that the decrease in perturbed energy growth is not related a seperatrix merging event. Instead the nonlinear growth of the magnetic islands has significantly increased the pressure gradient, and thus diamagnetic drift, near the inner and outer reconnection sites.

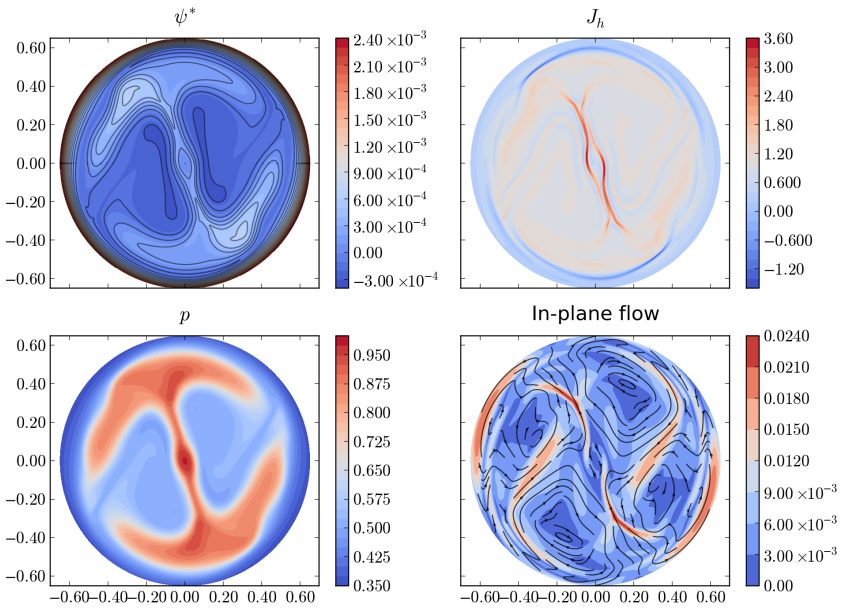

Figure 9-13: $\omega_* = 1 \times 10^{-1}$ equal drift DTM at simulation time $t = 390$ (black dashed line in Fig. 9-2). At this late time the plasma pressure and magnetic fields are highly deformed but the inner and outer separatrices still have not merged. The nonlinear enhancement of the diamagnetic drifts has resulted in a significant reduction in the reconnection rate of this DTM.

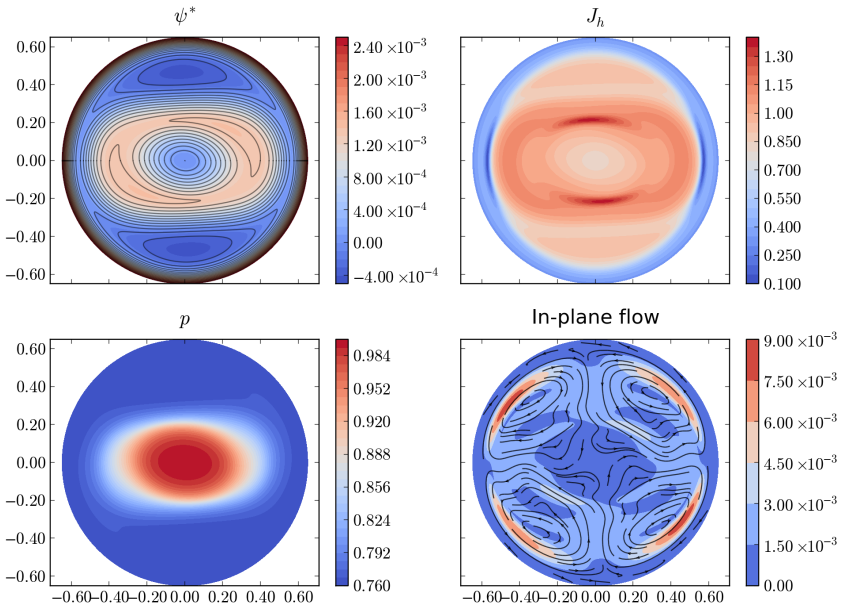

Figure 9-14: $\Delta\omega_* = 1 \times 10^{-1}$ differentially drifting DTM with the equilibrium pressure gradient localized near the inner rational surface. In this early nonlinear plot ($t = 155$, red dot-dashed line in Fig. 9-3) the inner and outer tearing surfaces, which are linearly decoupled, have been locked by the growing magnetic islands. The inner surfaces shows shearing and island elongation due to the local diamagnetic drift but the outer surface is unaffected.

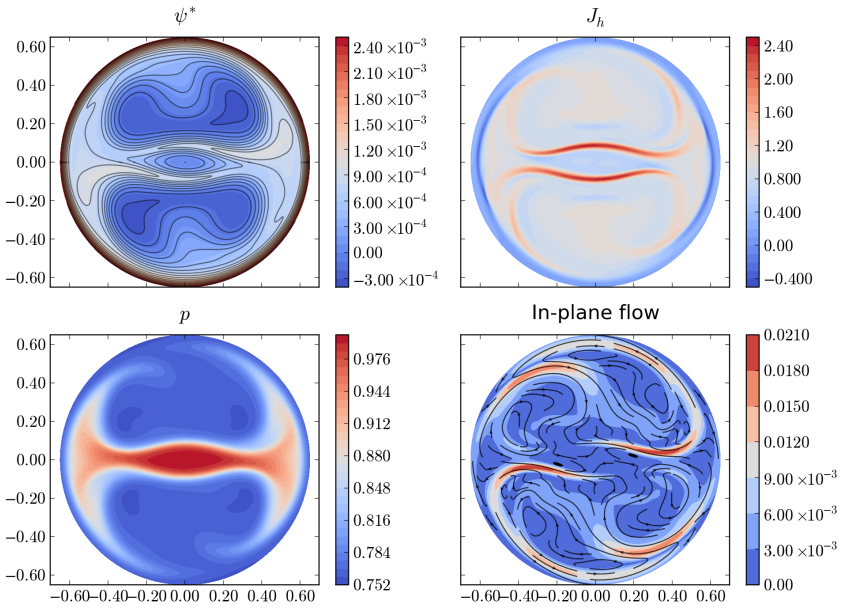

Figure 9-15: $\Delta\omega_* = 1 \times 10^{-1}$, $\delta_N = 0.10$ differentially drifting DTM with the equilibrium pressure gradient localized near the inner rational surface. At time $t = 335$ (the final output time of this simulation, indicated by the blue dot-dashed line in Fig. 9-3) the inner current sheets are nearing collision across the $r = 0$ axis. The growth of the inner magnetic islands has been strongly suppressed by the local diamagnetic drift and the current sheets at this surface are elongated.

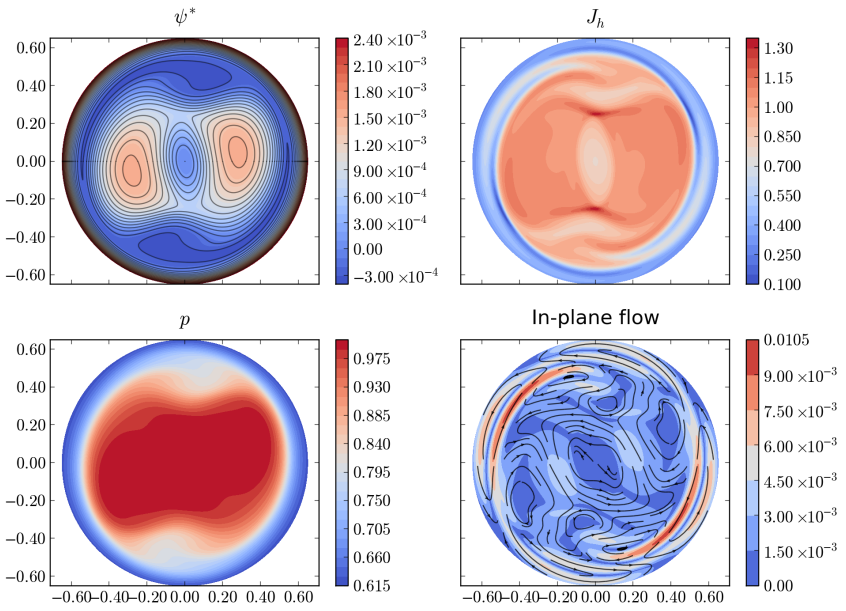

Figure 9-16: State at simulation time $t = 400$ (black dot-dashed line in Fig. 9-4) of the $m = 2$, $n = 1$ DTM with a broad equilibrium pressure gradient ($\delta_N = 0.10$) centered at the outer, r_{s2} rational surface. This profile results in an equilibrium differential diamagnetic drift of $\Delta\omega_* = 1 \times 10^{-1}$.

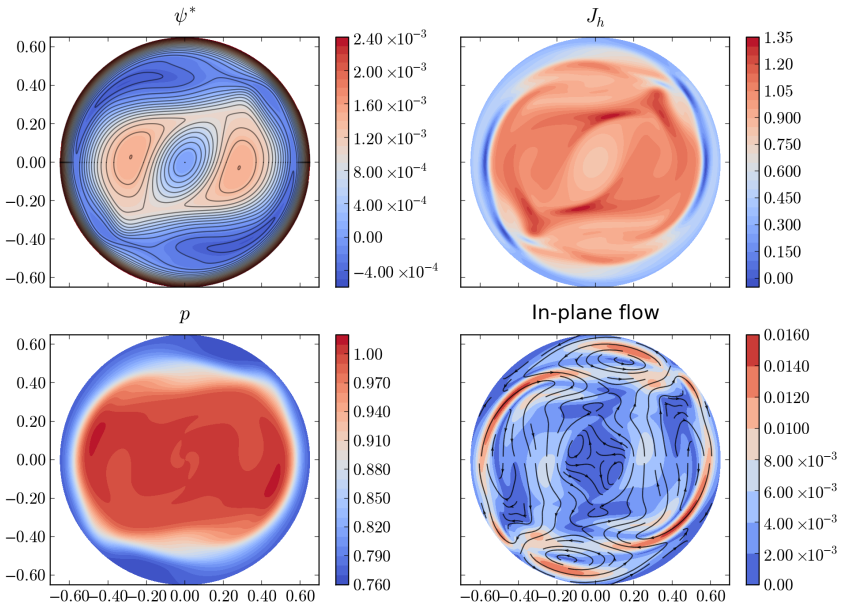

Figure 9-17: State at simulation time $t = 400$ (black dot-dashed line in Fig. 9-4) of the $m = 2$, $n = 1$ DTM with a localized equilibrium pressure gradient ($\delta_N = 0.05$) centered at the outer, r_{s2} rational surface. This profile results in an equilibrium differential diamagnetic drift of $\Delta\omega_* = 1 \times 10^{-1}$.

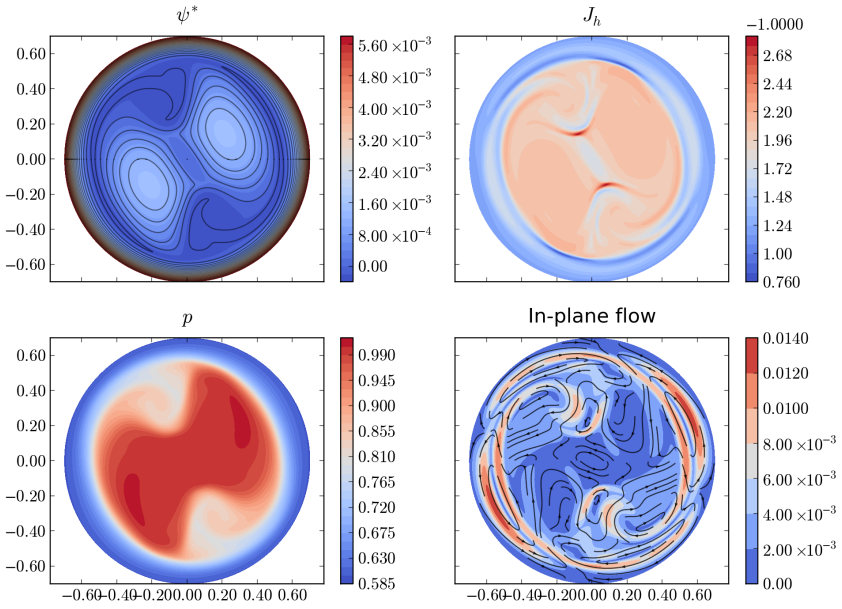

Figure 9-18: Near the separatrix merge time of DTM with a broad equilibrium pressure gradient of $\delta_N = 0.1$ centered at the r_{s2} rational surface, producing a differential diamagnetic drift of $\Delta\omega_* = 1 \times 10^{-1}$. The simulation time of this plot is $t = 500$ and corresponds to the red dot-dashed vertical line on Figure 9-4.

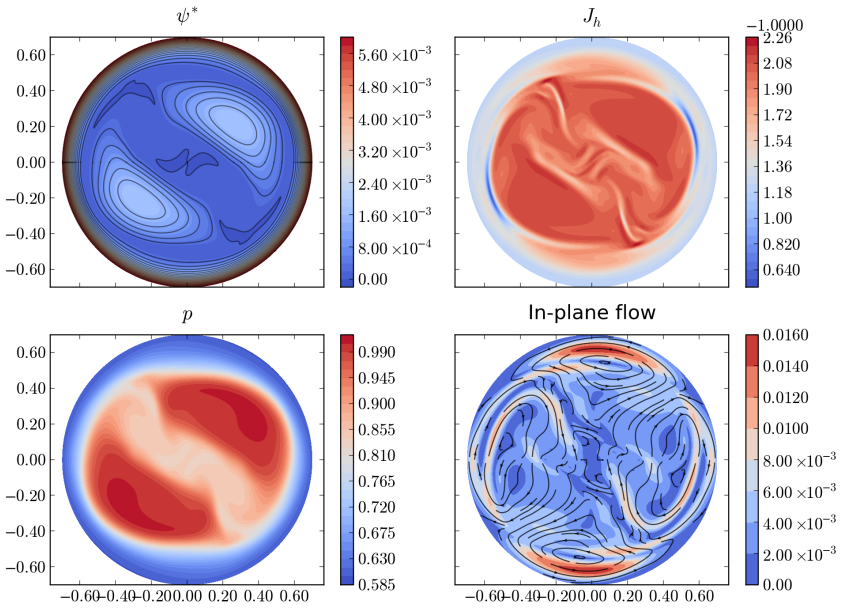

Figure 9-19: Near the time at which the inner current sheets collide across $r = 0$ for a DTM with a broad equilibrium pressure gradient of $\delta_N = 0.1$ centered at the r_{s2} rational surface, producing a differential diamagnetic drift of $\Delta\omega_* = 1 \times 10^{-1}$. The simulation time of this plot is $t = 500$ and corresponds to the blue dot-dashed vertical line on Figure 9-4.

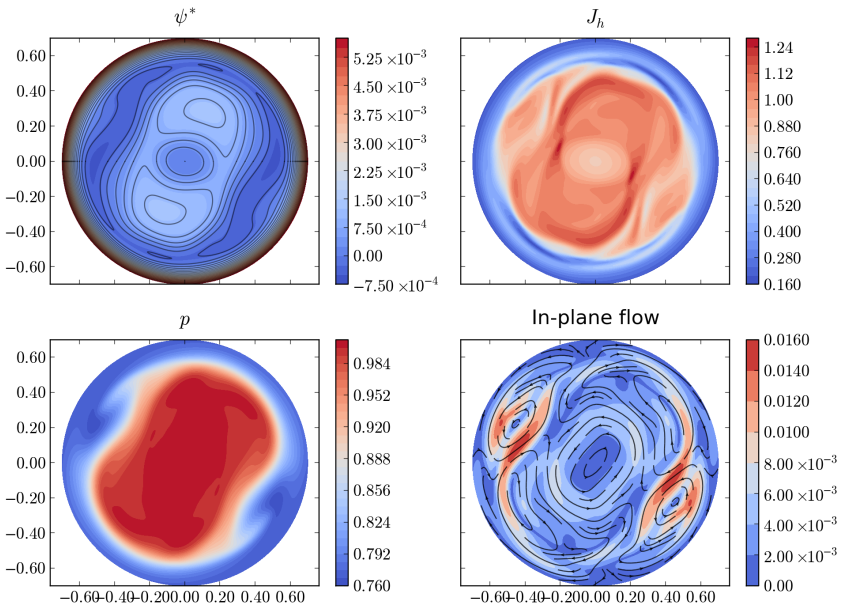

Figure 9-20: The saturated state of the $\Delta\omega_* = 1 \times 10^{-1}$, $\delta_N = 0.05$, $r_0 = r_{s2}$ DTM at time $t = 750$ (the last time we simulate). The magnetic islands are not significantly larger than they were at $t = 400$ (Fig. 9-17) and the current sheets have decreased in amplitude. The pressure profile is still well confined, and has not changed substantially from its equilibrium form (see Fig. 9-21).

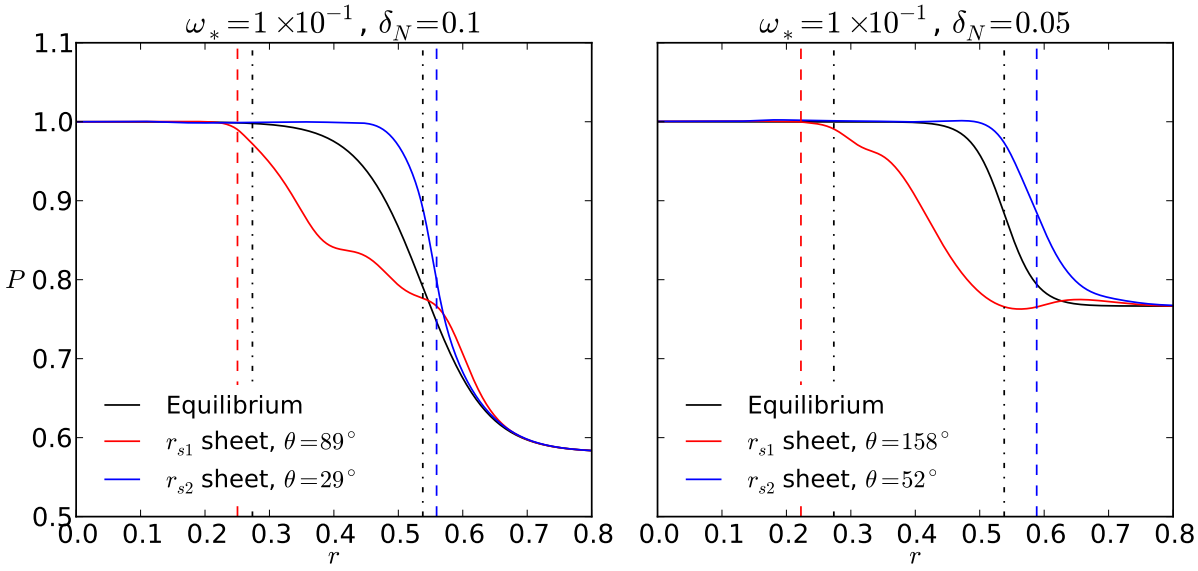

Figure 9-21: Radial cuts across the peaks of the inner and outer current sheets of the $\Delta\omega_* = 1 \times 10^{-1}$ inner-drift DTM with the two equilibrium pressure profiles: broad $\delta_N = 0.1$ at time $t = 400$ (left, 2D plot in Fig. 9-16) and localized $\delta_N = 0.05$ at time $t = 750$ (right, 2D plot in Fig. 9-20). The magnetic islands are approximately the same size in both simulations at the given times. The saturated $\delta_N = 0.05$ mode does not show significant enhancement of the pressure gradients at the current sheets, whereas the unstable $\delta_N = 0.10$ DTM does.

Chapter 10

Conclusion

The promising confinement properties of reverse-magnetic shear tokamak configurations has lead to recent interest in the double-tearing mode instability. The reversal of the poloidal magnetic field generates a non-monotonic safety factor profile with two rational surfaces of the same q spanning the annular current ring. If these two surfaces are close enough they can linearly couple and form the reconnecting DTM, which is a quickly growing instability only weakly dependent on resistivity. Nonlinearly the two reconnecting surfaces consume the magnetic flux separating them, resulting in the merging of their magnetic separatrices, disruption of the annular current ring, and loss of plasma confinement. The avoidance of this catastrophic nonlinear state is important to the future use of such advanced tokamak profiles, and there has been significant recent exploration of methods to stabilize the DTM. In this work we have examined the use of equilibrium diamagnetic drifts, which have been effective at slowing and saturating similar reconnecting instabilities in conventional tokamak designs. Understanding the impact of the diamagnetic drifts on the nonlinear DTM first requires understanding how the interaction of the two resonant surfaces impacts the mode growth, and then considering how the introduction of ω_* drifts may interfere with this growth.

10.1 Summary of important linear results

The linear behavior of the double-tearing mode is well understood in the simplest limit of symmetric, static, force-free, Cartesian systems. In Chapter 3 we reviewed the existing boundary layer theory and verified that it accurately describes DTM behavior in the `MRC-3d` simulation code. The presence of two resonant surfaces couples the reconnecting tearing

mode to a slab kink mode that is deeply stable when the surfaces are far apart and marginally stable when they are close. The driving energy of this underlying ideal MHD structure affects the dependence of the DTM linear growth rate on resistivity, with the instability growing as $\gamma \sim \eta^{3/5}$ in the weakly coupled, deeply ideally stable regime and as $\gamma \sim \eta^{1/3}$ in the strongly coupled, marginally stable domain. This behavior has also been confirmed in numerous cylindrical and toroidal simulation studies, where the interaction between the resonant surfaces is sufficiently strong that the annular region containing the DTM is (to lowest order) Cartesian.

The key to slowing the growth of the linear DTM relies, therefore, in decoupling the two resonant surfaces so that they cannot drive each other. In Chapter 4 we showed how an equilibrium antisymmetric sheared flow can force the DTM tearing layers to decouple and drift. Provided that there exists a differential equilibrium flow at the resonant surfaces, they cannot interact while drifting and tearing layers become isolated, thereby behaving more like single tearing modes with much lower growth rates. We showed through linear boundary layer analysis and simulations that the critical differential flow required to decoupling the resonant surfaces is directly related to the growth rate of the mode, and proposed a continuation of the existing linear theory in order to determine this critical point analytically. Past this decoupling point, however, the equilibrium sheared flow is not able to further decrease the DTM growth rate until Alfvén resonance layers appear at large velocities.

The inability of equilibrium flows to decrease the linear growth rate after DTM decoupling motivates the introduction of diamagnetic drifts, which can produce not only differential drift at the resonant surfaces but also interfere with reconnection within the resonant layers. In Chapter 5 we enabled the finite Larmor radius terms in the `MRC-3d` Ohm's law and introduced electron diamagnetic drifts via an equilibrium pressure gradient. These differential ω_* drifts were less effective than sheared flow at decoupling the tearing surfaces, but continued to slow the mode growth after decoupling. At very high drift values, however, we observed that the growth rate again began to increase. For strongly coupled $x_s = 0.25$ DTMs we

found that the diamagnetic drift necessary to decouple the surfaces was so large that the growth began to climb immediately after separation. Thus diamagnetic drifts are not the most effective linear stabilization mechanism in every system, but are more effective than equilibrium sheared flows for weak and moderately coupled double tearing modes.

These Cartesian analytic and numerical results are important from a theoretical standpoint, but predicting the efficacy of diamagnetic drifts in tokamak devices requires understanding the DTM behavior in asymmetric, curvilinear equilibria. In Chapter 6 we applied the prior slab linear results to a cylindrical DTM with poloidal and toroidal mode numbers $m = 2$, $n = 1$ and found several differences. The asymmetric magnetic shear at the two $q = 2$ rational surfaces results in the eigenmode resembling a strongly coupled DTM near the outer, dominant surface. Around the less sheared, sub-dominant, inner surface, however, the mode resembles a weakly coupled DTM. By examining these eigenmodes and measuring the resistive scaling of the growth rate to be $\gamma \sim \eta^{0.48}$, we concluded that this cylindrical double-tearing mode is in the moderately coupled regime.

Additional deviations from the Cartesian DTM emerge from the pressure gradients in tokamak configurations. We chose to use a density profile peaked at the magnetic axis which falls off with increasing radius, in order to represent the profiles associated with internal transport barriers (ITBs) in reverse-shear tokamak devices. We found that applying this pressure gradient to our $q = 2$ cylindrical equilibrium destabilized an ideal MHD mode. This couples to the reconnecting DTM, similar to the $m = 1$, $n = 1$ kink-tearing mode in conventional tokamaks. The nature of this instability is not currently understood, nor whether it will be stabilized by higher order toroidal corrections. In our simulations, however, its presence means the pressure gradients necessary to generate diamagnetic drifts will have an additional, ideal MHD destabilizing component not present in Cartesian geometry.

Our choice of a monotonic, ITB-like pressure profile only generates electron diamagnetic drifts in the $\hat{u}$ ($\sim \hat{\theta}$) direction. Therefore we were not able to consider equal and opposite drifts at both resonant surfaces, as in Chapter 5. We instead considered three classes of

pressure gradient centered at different points in the domains, and compared their behavior in resistive (no diamagnetic drifts) and Hall MHD (diamagnetic drifts) simulations. In order to isolate the efficacy of local diamagnetic stabilization without a differential drift we centered a broad pressure profile between the two rational surfaces, so that the ω_* drift was equal at both tearing layers. We found that the local diamagnetic drift resulted in lower growth rates compared to the resistive MHD simulations, but in both cases increasing the pressure gradient increased γ. Therefore in the absence of differential rotation the diamagnetic drifts are not able to overcome the destabilizing contributions of the pressure gradient.

Reintroducing differential rotation effects, we then localized a pressure gradient near the inner, weaker rational surface. The influence of the ideal MHD instability was felt even more strongly in this case, and the measured Hall MHD growth rates were uniformly larger than their resistive counterparts. We also found that although the system showed signs of mode decoupling, we were only able to extract a single, stationary eigenmode via Fourier analysis. Taken together, these observations indicate that the growth of the system was controlled by the outer resonant surface, which experienced the destabilizing effects of the pressure gradient without any of the beneficial drift effects.

Our lowest linear growth rates came from localizing a pressure gradient near the outer rational surface. These simulations showed decoupling behavior similar to that of Chapter 5, as well as significant decreases in γ after decoupling. At higher values of ω_* the ideal MHD instability again began to control the mode evolution, but the growth rates remained significantly lower than their resistive counterparts. The outer surface is clearly the dominant layer in this cylindrical equilibrium, and decreasing the linear growth rate requires that this surface be stabilized.

Some elements of our linear study may not persist in actual tokamak experiments. In particular, the ideal MHD instability observed in this work may not play as large a role in toroidal geometry. The most important result of our cylindrical simulations is, however, that the efficacy of diamagnetic drifts as a stabilization mechanism depends largely on where the

pressure gradient is located. The asymmetry inherent in curvilinear geometry results in one of the rational surfaces being the dominant driver of the mode evolution. The outer surface was dominate in our equilibrium, and we were able to observe slower linear growth (compared to resistive MHD) when this surface experienced a diamagnetic drift. Our best results came from combining differential drift decoupling effects with local stabilization of the outer surface, in which case the growth rate was reduced compared to the force-free configurations. These variations in stability based on the location of the pressure profile may explain why some reverse-shear tokamak discharges show DTM activity and others don't, and possibly even provide a mechanism to prevent disruptions. We were not, however, able to reduce the linear growth rate to zero, so the utility of these results will depend on how well they predict the nonlinear DTM behavior.

10.2 Summary of important nonlinear results

There are many different paths of evolution available to the nonlinear double-tearing mode, and very few analytic theories of its behavior are available. Most of our current understanding of large amplitude DTMs comes from simulation studies, and the lack of a clear classification mechanism makes them difficult to compare. In Chapters 7 and 8 we reviewed the existing DTM and STM literature in order to summarize the current understanding of nonlinear double-tearing mode evolution. We identified three distinct phases of growth: the island growth regime; the explosive phase; and the decay regime. Rather than reviewing this entire discussion here, we will instead highlight the key parts of our analysis which we feel have not been stated elsewhere in the literature.

The period of slow island growth, which we call the 'island growth regime' in this work, is commonly referred to as the 'Rutherford' regime elsewhere in the literature, in reference to the existing single-tearing mode quasilinear theories that we reviewed in Chapter 7. Based on examination of `MRC-3d` simulation results, we argued that the constant ψ singular

layer behavior required by Rutherford's quasilinear analysis [42] is not evident in nonlinear double-tearing modes except in cases leading to saturation. DTMs marginally below the nonlinear stability threshold may, to lowest order, be described by this theory, but small mode wavenumbers or closer spacings results in the formation of extended current sheets. The formation of this sheet is described by Waelbroeck's nonconstant ψ tearing mode theory [49], but the asymmetry of the magnetic fields and DTM inter-resonant driving should modify his predictions of the reconnection rate. We also showed that for strongly coupled surfaces the kinetic and magnetic energy growth does slow as the islands reach finite size, and we proposed that the nonlinear behavior of the slab kink mode should be considered a fundamental element of the DTM evolution. The underlying physics of early nonlinear DTM growth is currently undetermined, and thus we prefer the more general label of 'island growth regime'.

We also briefly considered the explosive growth regime, which is the period of fast, highly disruptive evolution that has attracted interest to the double-tearing mode. Simulation studies addressing this late nonlinear phase are somewhat limited, as the dynamics involved are numerically challenging. The few available studies do not, unfortunately, agree on the behavior of the DTM during this period, with particular disagreements revolving around the dependence of the mode evolution on resistivity. We proposed that there may be different mechanisms underlying the explosive phase, and that the DTM transitions between regimes smoothly based on the coupling between the resonant surfaces, instability wave number, and local magnetic shear. Verifying this prediction will, however, require additional analytic or simulation studies. Thus we delay discussion until the following section.

Based on this review of the literature we classified our $m = 2, n = 1$ cylindrical DTM as a moderate to strongly coupled nonlinear DTM, which is consistent with our linear evaluations. Normally double-tearing modes are classified by whether or not they feature an explosive growth phase, but it is not possible to observe this stage in our $q = 2$ equilibrium. The magnetic flux interior to the inner rational surface is rapidly consumed in our simulations.

By the time the inner and outer separatrices merge together, the interior flux is significantly reduced. Eventually the inner rational surfaces reconnect all the axial flux, and they merge across the axis. After this point we do not feel our simulations accurately reflect DTM behavior in any laboratory device, as our equilibrium is unrealistically symmetric. Prior to the current sheet collision, however, our results are similar to simulations of TFTR, off-axis sawtooth behavior [34]. While the islands are growing (but before the separatrices merge) the kinetic and magnetic energies continue to increase at the linear growth rate, similar to the Cartesian strongly coupled mode. Extended current sheets are, however, visible at each surface, similar to nonconstant ψ Cartesian modes that do feature an explosive phase. We cannot, therefore, precisely determine the classification of the $m = 2$, $n = 1$ DTM. In our Cartesian study of drifting DTMs (Chaps. 4 and 5) we found that more strongly coupled modes are harder to decouple and stabilize, thus we expect our stabilization study will be even more effective for higher mode number, less strongly coupled double-tearing modes.

In Chapter 9 we extended the linear, cylindrical diamagnetic drift study of Chapter 6, using the same pressure gradients and locations in the nonlinear. We will not discuss the class of pressure gradients localized near the inner resonant surface any further, as they performed as poorly in the nonlinear as they did linearly. Instead we briefly review the equal and outer drift cases that were strongly nonlinearly stabilized, albeit for different reasons.

The DTM with equal diamagnetic drifts of $\omega_* = 1 \times 10^{-1}$ at both rational surfaces was unexpectedly stabilized in the nonlinear regime, given that its linear growth rate was larger than the force-free case. As the magnetic islands grew they steepened the pressure profile local to the tearing layers. The increased gradient resulted in a faster diamagnetic drift, which was then sufficient to prevent the inner and outer separatrices from merging. This nonlinear drift enhancement process has been observed in other reconnecting systems, in particular it is known to be an important factor in the appearance of saturated $m = 1$ islands in conventional tokamaks [8]. In our simulations, however, the islands must grow very large before this effect becomes significant. As a consequence, the magnetic fields and

pressure profile are highly deformed. It is not clear whether this state is preferential to complete reconnection.

Using a differential diamagnetic drift of $\Delta\omega_* = 1 \times 10^{-1}$ localized with $\delta_N = 0.05$ at the outer rational surface, we were able to nonlinearly saturate the double-tearing mode. In this case enhancement of the pressure gradient does not appear to be a significant factor. Instead, the differential drift and suppression of the dominant, outer surface work to delay locking of the rational surfaces until a late time. Even after the tearing layers recouple, the outer surface is so strongly stabilized that it does not form large islands and appears unable to drive the inner surface. Without this strong coupling, the inner surface saturates at finite time, even though it does not experience a significant ω_*. Magnetic islands are visible, but the core plasma is largely intact and undeformed. Although this particular configuration may not manifest in actual tokamaks, we feel this result is strong evidence that the DTM can be avoided in reverse magnetic shear configurations. Stabilization requires, however, that the pressure profile be in the appropriate location to suppress the dominant rational surface. It is outside the scope of this thesis to speculate whether such control is possible in an actual device, but we suspect this result will be more useful to explain why DTM activity is or is not present in a given experiment.

10.3 Future directions

In this thesis we have focused largely on the underlying mechanisms behind double-tearing mode growth, and how equilibrium diamagnetic drifts can be used to suppress DTM activity. Much is not understood about the double-tearing mode, and there are many opportunities for future research. To conclude this thesis we will describe a small number of topics which we feel are important to explore.

In Chapter 4 we laid the foundations of a boundary layer theory describing the effect of equilibrium sheared flows on diamagnetic drifts. Expanding this theory would be beneficial

not only to future investigations of diamagnetic stabilization but also to work on differential rotation and Alfvén resonance techniques. The use of an eigensolver code would allow us to better resolve the antisymmetric branch of the DTM system, and perhaps gain insight into how this solution emerges from the boundary layer analysis. If the boundary layer theory can be completed, at least as far at the ideal MHD layer, we expect that the decoupling point will emerge. We cannot currently predict whether the decoupling behavior will be associated with a bifurcation, a failure to match across the boundary layers, or some other mechanism.

Whether or not the decoupling behavior can be understood, another useful research direction would be to combine equilibrium sheared flows and diamagnetic drifts. Equilibrium flows are more effective at decoupling the resonant layers, but diamagnetic drifts can continue to stabilize the isolated layers without the large amplitudes needed for Alfvén resonances. In slab Cartesian geometry these two effects could be achieved either by considering both equilibrium flows and pressure gradients, or by considering higher ion temperatures so that the ion diamagnetic drift is present.

In linear curvilinear geometry, it is important to understand what the observed ideal MHD instability is and how the pressure gradient affects it. The best way to approach this problem is likely through a variational principle or δW method, similar to the earliest $m = 1$ kink mode theories. The toroidal corrections should be evaluated, and it should be determined whether they are stabilizing or destabilizing. We expect that even if the ideal MHD mode is not linearly unstable in full toroidal geometry it will still play a role in driving DTM activity both linearly and nonlinearly.

Nonlinearly we suggest two different types of studies. The first of these focuses on the fundamental understanding and classification of double-tearing mode behavior. Even with the recent abundance of nonlinear DTM simulation work, we currently lack a method to predict whether or not an equilibrium will support an explosive DTM. The work of Janvier et al. [31] has explored the saturation threshold for equilibria with weak magnetic shears, but

a significant region of the parameter space remains unexplored. We suggest that conducting a survey of the DTM behavior in k, x_s, and magnetic shear B_0 might illuminate the possible behaviors of the island growth and explosive regime. At first such a study could be conducted at fixed resistivity, as the existing work consistently shows that the triggering of explosive growth is independent of η. Once the boundaries between stabilized, explosive, and strongly coupled systems are determined, however, the resistivity dependence of the linear, island growth, and explosive phases should be determined for characteristic modes. Such a study could be conducted in slab geometry, but will still require significant computational resources. A simulation code with implicit time integration and adaptive mesh refinement would be a large benefit. If possible, the double tanh equilibrium should be used in order to avoid the unpredictable variations in magnetic free energy cause by the sech profile.

The second nonlinear direction is to make better contact with experimental tokamak results. We feel it is not productive to continue with cylindrical simulations of this $q = 2$ equilibrium, as it does not reproduce enough features of tokamak geometry to be directly comparable to laboratory experiments. Some utility may exist in higher mode number simulations, but it would be better to move toward toroidal geometry. New reactors are trending towards smaller aspect ratios where toroidal corrections become more significant. Even in systems where the plasma core is approximately cylindrical plasma rotation caused by gravity and variations in magnetic curvature will likely play a roll in decoupling the DTM. We note, however, that toroidal equilibria are less flexible than cylindrical, and it may be difficult to isolate the contributions of the various effects. An important starting point for toroidal simulations would, therefore, be to establish how diamagnetic stabilization of the $m = 2$, $n = 1$ DTM in toroidal geometry is different from the cylindrical results we have presented here. We expect that the overall behavior of the nonlinear DTM is the same in both geometries, and this would allow the flexibility of cylindrical simulations to inform future toroidal studies.

Appendix A

The MRC-3d simulation code

The MRC-3d simulation code was originally written by Kai Germaschewski and updated to use the LIBMRC [21] library for data management, output, and time-stepping by Stephen Abbott. In this appendix we will briefly summarize the primary structure and features of the code. Full documentation, including information on how to obtain and use the code, is available at Reference [2].

MRC-3d is built on the LIBMRC library developed at the University of New Hampshire. LIBMRC provides the capability to define objects in parallel for use on high performance computing clusters. MRC-3d is designed using this object orientated programming model. Data objects are distributed in parallel across many processors with LIBMRC handling communication. It also writes output of simulation data using the HDF5 hierarchical data format [47], which allows for portability and efficient storage. Time integration is implemented using the Portable, Extensible Toolkit for Scientific Computation (PETSc) [4–6] via the unified LIBMRC time-stepping interface. PETSc provides a wide variety of algorithms useful for scientific computing. In MRC-3d we use, in particular, its explicit and implicit nonlinear methods and distributed, sparse matrix linear solvers.

The MRC-3d model is variant of the conservative, $\nabla \cdot \mathbf{B} = 0$ preserving, finite-volume MHD model given in Ref. [16], modified to include the Hall and electron pressure gradient terms. This model is written in a manifestly covariant form so that it applies in arbitrary curvilinear geometries. To exploit this flexibility, MRC-3d uses a Python based code generator built around the SymPy [45] package for symbolic mathematics. Metric tensors and differential operators are defined symbolically. The model equations are then written in simple pseudo-code. Symbolic manipulation is used to generate the full discretized equations in C, which are

then wrapped in a function and attached to a `MRC-3d` object. These objects can be chosen at run-time, allowing a single build of `MRC-3d` to perform simulations in many different coordinate systems. This code generation process has many benefits. First, the model pseudo-code is substantially simpler than the full discretized equations. For example in the current version of `MRC-3d` the right hand side equations require 729 characters of pseudo-code. The resulting C code is 23,336 characters in Cartesian geometry and 53,047 characters in cylindrical. Second, boundary conditions can also be handled in this fashion, and at boundaries where no data is exchange (e.g. conducting walls) the code generator can back-substitute the boundary condition into the r.h.s. equations. Finally, and most importantly, this symbolic manipulation process is also used to generate a full Jacobian of the discretized system that is necessary for the use of the `PETSc` implicit time-steppers.

One feature of `MRC-3d` is particularly useful for studies of reconnecting systems. The 'source term' is a mechanism for forcing an equilibrium to not decay, and is equivalent to applying a weak external electric field driving the system toward equilibrium. In physical systems the characteristic timescales of reconnection are much faster than the resistive decay time. In simulation studies, however, it is common to use unrealistically high values for the resistivity so that current layers are wider and lower spatial resolutions may be used. In these more diffusive systems the growth and decay timescales are much closer. The source term mitigates this by evaluating the r.h.s. equations on the equilibrium at initialization, then subtracting this contribution from each time step. In this fashion the equilibrium is prevented from decaying. Care should be taken in the use of this term, however, as it does represent an external electric field and may change results. When the instability growth is fast the source term does a good job of preventing anomalous decay due to high resistivity, and we have verified in select simulations that at very low resistivity the difference between runs with and without the forced equilibrium is minimal. However when the mode growth is very slow (either because the system is decaying or a saturated state has been reached) then the external electric field effectively 'pumps' the simulation back toward equilibrium. When

considering certain laboratory plasmas this situation may, in fact, be appropriate, but it is not desirable in every case. Thus this feature of `MRC-3d` can be disabled by a command line option at runtime.

In addition to the full, nonlinear Hall MHD model, `MRC-3d` also contains a one-dimensional linear simulation code. This linear model uses the same discretization as the full model in one dimension and applies the Fourier ansatz ($F(\boldsymbol{x}) = \exp(\boldsymbol{k} \cdot \boldsymbol{x})$) to the other two. This capability is also enabled by the code generation process. The usual 8 component MHD state vector is expanded to 16 components to contain both the real and imaginary parts of each field. A new complex field type is defined in the code generator as the sum of the real part of each field plus i times the imaginary, where i is the imaginary unit. The linearized equations are then written in pseudo-code using differential operators which encapsulate the Fourier decomposition. `SymPy` is capable of symbolic manipulation of complex numbers and we use it to expand the pseudo-code to the full discretized equations.

The final major feature of `MRC-3d` is its analysis package `pymrc`. We use the Cython utility [7] to wrap the top level `MRC-3d` objects within Python classes. Data can then be loaded directly into Python scripts for analysis. To aid in this process we have also wrapped a variety of useful functions. For example, the discretized expression for the current density $\mathbf{J}$ can be called from a script so that the returned field can be calculated during analysis in the same fashion as it was during the simulation. This ability is of particular important when the metric tensor is non-trivial. This package has many useful features, and we recommend consulting the documentation at Ref. [2] for more information.

List of References

[1] S. Abbott, K. Germaschewski, and A. Bhattacharjee, "Diamagnetic Effects on Double Tearing Modes in Hall-MHD and PIC Simulations," in *APS Meeting Abstracts*, Oct. 2011, 9019P.

[2] S. Abbott and K. Germaschewski. (2014). The Magnetic Reconnection Code (MRC) documentation, [Online]. Available: `http://fishercat.sr.unh.edu/mrc-v3` (visited on 05/28/2015).

[3] G. Ara *et al.*, "Magnetic reconnection and m = 1 oscillations in current carrying plasmas," *Annals of Physics*, vol. 112, pp. 443–476, 1978.

[4] S. Balay *et al.*, "Efficient management of parallelism in object oriented numerical software libraries," in *Modern Software Tools in Scientific Computing*, E. Arge, A. M. Bruaset, and H. P. Langtangen, Eds., Birkhäuser Press, 1997, pp. 163–202.

[5] S. Balay *et al.*, "PETSc users manual," Argonne National Laboratory, Tech. Rep. ANL-95/11 - Revision 3.5, 2014.

[6] ——, *PETSc Web page*, `http://www.mcs.anl.gov/petsc`, 2014.

[7] S. Behnel *et al.*, "Cython: the best of both worlds," *Computing in Science Engineering*, vol. 13, no. 2, pp. 31–39, 2011.

[8] M. T. Beidler and P. A. Cassak, "Model for Incomplete Reconnection in Sawtooth Crashes," *Physical Review Letters*, vol. 107, no. 25, p. 255 002, Dec. 2011.

[9] A. Bierwage *et al.*, "Dynamics of resistive double tearing modes with broad linear spectra," *Physics of Plasmas*, vol. 14, no. 2, p. 022 107, 2007.

[10] A. Bierwage *et al.*, "Fast growing double tearing modes in a tokamak plasma," *Physics of Plasmas*, vol. 12, no. 8, pp. 082 504–+, Aug. 2005.

[11] J. Birn *et al.*, "Geospace Environmental Modeling (GEM) Magnetic Reconnection Challenge," *Journal of Geophysical Research*, vol. 106, no. A3, pp. 3715–3719, 2001.

[12] D. Biskamp, *Nonlinear Magnetohydrodynamics*. Cambridge University Press, 1993.

[13] ——, *Magnetic reconnection in plasmas*. Cambridge University Press, 2005, vol. 3.

[14] M. N. Bussac *et al.*, "Internal kink modes in toroidal plasmas with circular cross sections," *Phys. Rev. Lett.*, vol. 35, pp. 1638–1641, 24 Dec. 1975.

[15] P. A. Cassak and M. A. Shay, "Scaling of asymmetric magnetic reconnection: General theory and collisional simulations," *Physics of Plasmas*, vol. 14, no. 10, p. 102 114, 2007.

[16] L. Chacón, "A non-staggered, conservative, , finite-volume scheme for 3D implicit extended magnetohydrodynamics in curvilinear geometries," *Computer Physics Communications*, vol. 163, no. 3, pp. 143–171, Nov. 2004.

[17] Z. Chang *et al.*, "Off-Axis Sawteeth and Double-Tearing Reconnection in Reversed Magnetic Shear Plasmas in TFTR," *Physical Review Letters*, vol. 77, pp. 3553–3556, Oct. 1996.

[18] Z. Chenglong, M. Zhiwei, and D. Jiaqi, "A Simulation Study of Hall Effect on Double Tearing Modes," *Plasma Science and Technology*, vol. 10, no. 4, pp. 407–411, Aug. 2008.

[19] J. Q. Dong, S. M. Mahajan, and W. Horton, "Double tearing mode in plasmas with anomalous electron viscosity," *Physics of Plasmas*, vol. 10, pp. 3151–3159, Aug. 2003.

[20] H. P. Furth, J. Killeen, and M. N. Rosenbluth, "Finite-Resistivity Instabilities of a Sheet Pinch," *Physics of Fluids*, vol. 6, no. 4, p. 459, 1963.

[21] K. Germaschewski. (2011). libmrc: a library for parallel pde solvers, [Online]. Available: `http://fishercat.sr.unh.edu/trac/libmrc` (visited on 05/28/2015).

[22] G. Giruzzi, "Advances in the physics of steady-state plasmas by long pulse experiments on Tore Supra," *Plasma Physics and Controlled Fusion*, vol. 47, no. 12B, B93–B105, Dec. 2005.

[23] D. Grasso, M. Ottaviani, and F. Porcelli, "Linear stability and mode structure of drift tearing modes," *Physics of Plasmas*, vol. 8, pp. 4306–4317, Oct. 2001.

[24] B. Green *et al.*, "Iter: burning plasma physics experiment," *Plasma physics and controlled fusion*, vol. 45, no. 5, p. 687, 2003.

[25] D. Gurnett and A. Bhattacharjee, *Introduction to Plasma Physics: With Space and Laboratory Applications*. Cambridge University Press, 2005.

[26] R. D. Hazeltine, C. T. Hsu, and P. J. Morrison, "Hamiltonian four-field model for nonlinear tokamak dynamics," *Physics of Fluids*, vol. 30, no. 10, p. 3204, 1987.

[27] Y. Ishii, M. Azumi, and Y. Kishimoto, "Structure-Driven Nonlinear Instability of Double Tearing Modes and the Abrupt Growth after Long-Time-Scale Evolution," *Physical Review Letters*, vol. 89, no. 20, pp. 205 002–+, Oct. 2002.

[28] ——, "Current point formation and magnetic reconnection process in nonlinearly destabilized double tearing modes," *Physics of Plasmas*, vol. 10, pp. 3512–3520, Sep. 2003.

[29] Y. Ishii *et al.*, "Nonlinear evolution of double tearing modes," *Physics of Plasmas*, vol. 7, pp. 4477–4491, Nov. 2000.

[30] Y. Ishii *et al.*, "Long timescale plasma dynamics and explosive growth driven by the double tearing mode in reversed shear plasmas," *Nuclear Fusion*, vol. 43, pp. 539–546, Jul. 2003.

[31] M. Janvier, Y. Kishimoto, and J. Li, "Critical parameters for the nonlinear destabilization of double tearing modes in reversed shear plasmas," *Nuclear Fusion*, vol. 51, no. 8, p. 083 016, 2011.

[32] M. Janvier, Y. Kishimoto, and J. Li, "Structure-Driven Nonlinear Instability as the Origin of the Explosive Reconnection Dynamics in Resistive Double Tearing Modes," *Physical Review Letters*, vol. 107, no. 19, pp. 1–5, Oct. 2011.

[33] M. Janvier *et al.*, "Role of the pressure force in the explosive dynamics of magnetic islands in double tearing modes," *Physics of Plasmas*, vol. 18, no. 10, p. 102 112, 2011.

[34] F. Levinton *et al.*, "Stabilization and Onset of Sawteeth in TFTR," *Physical review*, 1994.

[35] X. X. Li, X. Y. Gong, and X. Q. Lu, "Nonlinear Evolution of Shear Flows in Double Tearing Modes," *IEEE Transactions on Plasma Science*, vol. 40, no. 5, pp. 1416–1420, May 2012.

[36] Z. W. Ma and A. Bhattacharjee, "Hall magnetohydrodynamic reconnection: The Geospace Environment Modeling challenge," *Journal of Geophysical Research*, vol. 106, no. A3, pp. 3773–3782, 2001.

[37] A. Mao *et al.*, "Eigenmode characteristics of the double tearing mode in the presence of shear flows," *Physics of Plasmas*, vol. 20, no. 2, p. 022 114, 2013.

[38] L. Ofman, "Double tearing instability with shear flow," *Physics of Fluids B*, vol. 4, pp. 2751–2757, Sep. 1992.

[39] P. L. Pritchett, Y. C. Lee, and J. F. Drake, "Linear analysis of the double-tearing mode," *Physics of Fluids*, vol. 23, pp. 1368–1374, Jul. 1980.

[40] S. Rauf and J. A. Tataronis, "On the Alfvén resonance and its existence," *Physics of Plasmas*, vol. 2, no. 1, pp. 340–342, Jan. 1995.

[41] B. Rogers and L. Zakharov, "Nonlinear ω_*-stabilization of the m=1 mode in tokamaks," *Physics of Plasmas*, vol. 2, no. 9, p. 3420, 1995.

[42] P. Rutherford, "Nonlinear growth of the tearing mode," *Physics of Fluids*, vol. 14, no. 11, 1973.

[43] D. D. Schnack, *Lectures in Magnetohydrodynamics: With an Appendix on Extended MHD*. Springer Science & Business Media, 2009, vol. 780.

[44] M. Swisdak *et al.*, "Diamagnetic suppression of component magnetic reconnection at the magnetopause," *Journal of Geophysical Research (Space Physics)*, vol. 108, p. 1218, May 2003.

[45] SymPy Development Team, *Sympy: python library for symbolic mathematics*, 2014.

[46] E. Synakowski *et al.*, "The national spherical torus experiment (NSTX) research programme and progress towards high beta, long pulse operating scenarios," *Nuclear Fusion*, vol. 1653, no. 43, 2003.

[47] The HDF Group. (1997-NNNN). Hierarchical Data Format, version 5, [Online]. Available: `http://www.hdfgroup.org/HDF5/`.

[48] T. Voslion *et al.*, "Impact of a shear flow on double tearing nonlinear dynamics," *Physics of Plasmas*, vol. 18, no. 6, p. 062 302, 2011.

[49] F. L. Waelbroeck, "Current sheets and nonlinear growth of the m=1 kink-tearing mode," *Physics of Fluids B: Plasma Physics*, vol. 1, no. 12, p. 2372, 1989.

[50] X.-Q. Wang *et al.*, "Compressibility effects on double tearing mode interlocking in differentially rotating plasmas," *Physics Letters A*, vol. 376, no. 4, pp. 505–509, Jan. 2012.

[51] X. Wang and a. Bhattacharjee, "Exponential nonlinear growth of a resistive m=1 island," *Physics of Plasmas*, vol. 6, no. 5, p. 1674, 1999.

[52] X. Wang, Z. W. Ma, and A. Bhattacharjee, "Fast magnetic reconnection and sudden enhancement of current sheets due to inward boundary flows," *Physics of Plasmas*, vol. 3, no. 5, p. 2129, 1996.

[53] Z.-X. Wang *et al.*, "Shear flows induced by nonlinear evolution of double tearing modes," *Physics of Plasmas*, vol. 15, no. 8, p. 082 109, 2008.

[54] Z.-X. Wang *et al.*, "Self-suppression of double tearing modes via Alfvén resonance in rotating tokamak plasmas," *Physics of Plasmas*, vol. 18, no. 5, p. 050 701, 2011.

[55] Z. Wang *et al.*, "Fast Resistive Reconnection Regime in the Nonlinear Evolution of Double Tearing Modes," *Physical Review Letters*, vol. 99, no. 18, pp. 185 004–+, Nov. 2007.

[56] R. B. White *et al.*, "Saturation of the tearing mode," *Physics of Fluids*, vol. 20, no. 5, p. 800, 1977.

[57] L. Wu *et al.*, "The effects of a shear flow on nonlinear evolutions of double tearing mode in Hall magnetohydrodynamics," *Physics Letters A*, vol. 377, no. 37, pp. 2373–2377, Nov. 2013.

[58] Q. Yu, "Nonlinear growth of the double tearing mode," *Physics of Plasmas*, vol. 3, pp. 2898–2902, Aug. 1996.

[59] H. Y. Yuh *et al.*, "Internal transport barriers in the National Spherical Torus Experiment," *Physics of Plasmas*, vol. 16, no. 5, p. 056 120, 2009.

[60] L. Zakharov and B. Rogers, "Two-fluid magnetohydrodynamic description of the internal kink mode in tokamaks," *Physics of Fluids B: Plasma Physics*, vol. 4, no. 10, p. 3285, 1992.

[61] G. P. Zank and W. H. Matthaeus, "The equations of reduced magnetohydrodynamics," *Journal of Plasma Physics*, vol. 48, no. 01, p. 85, 1992.

[62] C. L. Zhang and Z. W. Ma, "Nonlinear evolution of double tearing mode with guiding magnetic field," *Physics of Plasmas*, vol. 18, no. 5, p. 052 303, 2011.

[63] C. Zhang and Z. Ma, "Nonlinear evolution of double tearing mode in Hall magnetohydrodynamics," *Physics of Plasmas*, vol. 16, no. 12, p. 122 113, Dec. 2009.

[64] X. M. Zhao *et al.*, "Double tearing modes in the presence of internal transport barrier," *Physics of Plasmas*, vol. 18, no. 7, p. 072 506, 2011.